The Response and Optimisation of Hybrid Wind Turbine Towers

Alan Kenna

Trinity College Dublin

A thesis submitted for the degree of

Doctor of Philosophy

2019

I declare that this thesis has not been submitted as an exercise for a degree at this or any other university and it is entirely my own work.

I agree to deposit this thesis in the University's open access institutional repository or allow the Library to do so on my behalf, subject to Irish Copyright Legislation and Trinity College Library conditions of use and acknowledgement.

Alan Kenna

January 2019

Acknowledgements

The work presented in this thesis was part funded by Bord na Mona plc.

My work was supervised by Professor Biswajit Basu. I would like to thank Professor Basu for all of the knowledge and encouragement he has given me throughout my years working with him. I would also like to thank him for being open to my proposal to complete a Ph.D. on a part-time basis. I later realised that this required patience and an openness towards acting as a mentor in a flexible, non-traditional manner as compared to full-time supervision.

I wish to acknowledge the faculty of the Department of Civil, Structural and Environmental Engineering at Trinity College Dublin for their help in carrying out this work and preparing the Thesis. I wish to thank Dr. Breiffni Fitzgerald in particular for his help in the later stages of the work.

I am grateful to my colleagues in the Department of Civil Engineering at Bord na Mona for taking the time to review and critique some of my work. I also want to thank my Line Manager in accommodating me to attend lectures and meetings with my supervisor as required.

This Ph.D. is dedicated to my family: my parents, Kate and Paddy, my wife Jennine and our four children Daniel, James, Luke and Annalise. This work was completed on a part time basis, which meant time spent at study rather than with my family and for this, I want to thank Jennine. I want to thank my parents for always encouraging me to continue to learn and develop wherever my interests lay.

Abstract

This thesis investigates the response and optimisation of wind turbine tower structures with a particular emphasis on hybrid steel-concrete towers. The wind turbine blades with tower interaction are represented through equations of motion where mass, stiffness and damping properties have a time varying component. This thesis investigates the response and optimisation of these towers in a global and local sense through review of global tower top behaviour as well as the response at selected local locations from around the tower shell. Structural models of the tower are presented and used in analysing the response. An exact, closed form analytical model was developed using classical beam bending theory, with boundary and compatibility conditions imposed to generate a system of homogeneous linear equations with non-trivial solutions. Approximate, Finite Element models of the tower were constructed using both modified Euler-Bernoulli beam elements and also Reissner-Mindlin shell finite elements of varying numbers of degrees of freedom.

Two reduced order dynamic multi-degree of freedom (MDOF) models for an overall wind turbine assembly are then presented using a mixed formulation approach including Finite Element models incorporated into Euler-Lagrangian based systems. Discrete, global interpolation functions are used to reduce the total number of degrees of freedom (DOF) of the tower models to a selected reduced number of DOF. Continuous mode shapes are used to reduce the blade elements to selected DOF. Rotating blades are exposed

to time varying load application through aerodynamic load and periodicity introduced by gravity. Axial effects through gravity and centrifugal stiffening act on the blades to vary their stiffness. Aerodynamic loading has been simulated using the modified blade element momentum (BEM) algorithm which accounts for the angle of attack, blade pre-twist, pitch angle and wind shear. Turbulence was generated from a Kaimal spectrum.

The closed form analytical model was used to assess tower free vibration response and MDOF dynamical models were used to investigate forced vibration response of towers of varying properties. The nacelle mass and hybrid interface height had the most significant impact on the first natural frequency of the tower. This was observed through free vibration response but also through frequency domain review of the forced response. Hybrid interface height was strongly correlated with the mean displacement but to a lesser extent on the velocity and acceleration response. Concrete compressive strength and structural damping properties had an influence on the tower response. The first and second natural frequency of the tower was slightly reduced when introducing and increasing a prestress into the models. The global forced vibration response of the tower showed insignificant change as a result of the introduction of prestress. The effect of prestress was more significant at a local finite element level on review of strain response in three principal directions. Separately, the frequency content of local finite element strain response was significantly different to the frequency content of the global tower top response. This was deemed to be due to the effects of combined deformation through all tower global DOF.

A methodology has been proposed for the optimisation of hybrid concrete-steel wind turbine towers. This methodology incorporates the generalisation of free and forced vibration results of such towers using a configuration of Artificial Neural Networks, which are embedded within an optimisation algorithm which itself is a hybrid of a Genetic Algorithm and a Pattern

Search Algorithm. Objective functions are defined in terms of both structural and non-structural criteria. Fundamental fore-aft frequency was maximised, peak tower displacement was minimised, as was a weighted sum of concrete and steel stress utilisation ratios. Levelised Cost of Energy (LCoE) was set as an objective and was minimised for a series of load cases and hub heights. Concrete and prestressed reinforcement contributed most significantly to the breakdown of LCoE. The Climate Change Potential (CPP) was also set as an objective to be minimised and followed similar patterns to the LCoE in terms of sensitivity to change in wind speed and height. Contributions to the overall CCP are much more equally spread than was the case in LCoE, with each contributing similar amounts. Multi-objective optimisation was carried out using the epsilon constraint method.

A method was proposed to utilise and process spatial strain and acceleration signals as a means of damage detection around the shell of the finite element model of the wind turbine tower. Processing involved passing the signals through the Discrete Wavelet Transform (DWT) signal processing technique. The spatial signals were all transformed and co-efficients were found for low and high frequency components. GIS spatial images were presented to represent aerodynamic loading and tower responses generated using BEM and the 11 DOF structural models described earlier in the thesis. By generalising the loading and response quantities as a function of spatially distributed environmental exposure conditions, it is possible to plot these loading and response quantities spatially.

Contents

List of Figures

LIST OF FIGURES

List of Tables

LIST OF TABLES

LIST OF TABLES

Chapter 1

Introduction

1.1 Historical

Historically, wind energy has been captured by mankind to serve a wide range of purposes. Wind has been used to propel sail ships, to power windmills used to process grain and to pump water from wells. Whilst wind was used for energy for at least the past 3000 years, it was used specifically as a source of mechanical energy to power windmills by the seventh century BC, where such windmills were constructed in Afghanistan. These windmills were vertical axis machines, based on drag loading. Evidence of the first horizontal axes turbines can be found in historical documents from Persia, Tibet and China dating from circa 1000 AD (Ackermann and Söder [2000]).

Windmills were developed in Europe in the middle ages and at the time were used to power a range of devices in terms of providing a source to carry out mechanical tasks such as grinding grain, pumping water and cutting timber (Manwell et al. [2010]). In Ireland, the earliest recorded windmill dates from 1281 at Kilscanlon, Co. Wexford. By 1840, there were 250 windmills in place across Ireland.

From the 12th to the 19th century, around the time of the industrial revolution, wind-

mills continued to be of great use to society and continued to be developed technically. Their demise did occur during the industrial revolution and this is attributed to a number of factors. The steam engine had been developed by this time by engineers and, along with coal as a fuel source, was providing energy which was effectively mobile and could be dispatched. This was in contrast to the energy available from windmills which was fixed to the local site of the windmill. Energy from the steam engine could also be adjusted by adjusting the rate of fuel input, again, providing more flexibility than windmills. Despite the perceived redundancy of wind energy by this time, there were a number of technical advancements made which contributed to the design of modern machines. For example, the blades of windmills had developed to take on the shape of an efficient airfoil.

The towers were constructed as fixed structures and a manually operated yaw mechanism allowed for the orientation of the rotor to be adjusted to face the wind. In addition, the blades had taken on a twist to improve lift performance. An English Civil Engineer, John Smeaton (credited as being the founder of the civil engineering profession in Great Britain) had also observed three important characteristics which are still relevant today. These include; the speed of the blade tips is ideally proportional to the wind speed, the maximum torque is proportional to the wind speed squared and finally, the maximum power is proportional to the wind speed cubed. During the period of the 18th century, windmills were also in development in the United States (US), being especially useful in western states to pump water for agricultural purposes and used by early settlers in the area. The US Department of Agriculture by that time had developed a standard design of a so-called 'fan mill', which was known for its multiple blades. This windmill included a simple regulation system which allowed for its unattended use for prolonged periods and can be described as a forerunner to modern control systems (Manwell et al. [2010]). This self-regulating system turned the rotor windward during periods of high wind to avoid damage.

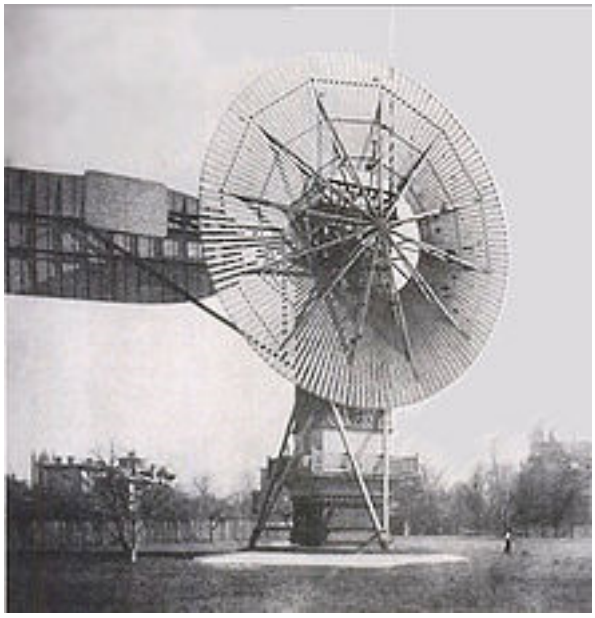

Figure 1.1: Turbine Built by Charles F. Brush (Danish Wind Industry Association [2010])

1.2 Wind Energy for Electrical Power

By the late 19th century, efforts were being made to convert wind energy to electricity. Charles F. Brush was the first to construct a wind turbine used to generate electricity in Cleveland, Ohio, in 1888 (Righter [1996]). This machine was capable of generating 12 kW, with notable features including a 17m diameter rotor which was constructed using multiple blades and a 'picket-fence' design, as shown in fig 1.1. It was also the first windmill to incorporate a step-up gearbox. In 1891, Poul LaCour built the first wind turbine machine which had an electrical output in Askov, Denmark (Ackermann and Söder [2000]). This turbine was more aerodynamically efficient given a low solidarity ratio compared to that of Charles F. Brush and by the end of World War I was in widespread use across Denmark.

Wind turbines used to generate electricity were now being developed both in the US and Europe. Small machines capable of generating 1-3 kW were available from companies like Parris-Dunn and Jacobs Wind-electric and were in widespread use across rural parts

of the US. While new installations of these small systems effectively ceased by the 1950s due to the availability of the electricity grid in the US, their use continued in Europe, Asia and parts of Africa and Australia.

Large scale wind turbines became of interest internationally when in 1931 a 100kW wind generator was constructed in Russia at the Caspian Sea. This machine produced power for 2 years. In 1941, the 1.25 MW Smith-Putnam machine was constructed in Vermont. This turbine was a horizontal axis machine, with two blades and a rotor which was 175 feet (approximately 58m) in diameter. This operated until 1945, when a blade failed apparently as a result of fatigue damage. Although this machine operated only intermittently, it showed, along with other large scale turbines, that large scale power generation could be achieved.

In the 1960s, work carried out in Denmark and Germany laid the way prior to when wind energy production would again become competitive due to the oil crisis of the 1970's. Work in Denmark around this time included design of the three-bladed upwind rotor concept, where blades had a fixed pitch. Aerodynamic design and controls were being incorporated by this time. Development in blade designs by this stage meant most designers were using blades of fibreglass, which were shaped like airfoils and based on propeller design of the period.

As noted, interest in energy production from wind resources increased in the early 1970s with the onset of the oil crisis. Funding was put in place by governments of the time in the US and Europe whereby multi-megawatt prototype machines would be developed. Wind farms were being constructed to achieve large scale energy production using turbines of rated capacities of between 50kW and 200kW. Development in multi-megawatt machines was hampered by technical difficulties, particularly around blade pitching.

The European Wind Energy Association (EWEA) was formed in 1982 in Stockholm at a time considered to be the beginning of the modern wind energy industry. That

same year, a group of agricultural machinery manufacturers travelled from Europe to California to assess the market for wind energy (European Wind Energy Association [2012]). As a result of this assessment, orders were received for 25-30 turbines. The following year, 350 turbines with a total capacity of 20MW were installed. This period became known as the 'California wind rush'. Although development in the 1990s slowed in the US, it continued apace in Europe. Part of the reason for this was the imposition by European governments of feed-in tariffs for suppliers of renewable energy/wind energy to national electricity grids. Similarly in India, tax deductions were put in place for the same purposes, again stimulating research and development in the industry.

In the period since the establishment of the EWEA a number of basic features and performance indicators have changed drastically. Two such features include individual turbine rated capacities and rotor diameters. Turbine rated capacities have increased from 55kW to modern day machines which can achieve 5000kW. Similarly, rotor diameters have increased from just 15m up to 126m.

1.3 Present Day Industry

Since the first testing of multi megawatt machines in the 1970s and 1980s, they have now become a well-established machine in terms of their rating in industrial wind farm applications, with onshore machines typically rated between 2MW and 3MW. The growth of wind energy over the past decade has been remarkable. The global total installed capacity for wind power at the end of 2017 was 539.8 GW (Global Wind Energy Council [2017]), representing an increase of almost ten-fold compared to the 2005 figure of 59.1 GW (Global Wind Energy Council [2006]). This exponential increase in installed capacity in only ten years has been made possible due to developments in wind turbine technology and design. A visual presentation of the trend in installed capacity is provided in fig 1.2. Wind is now an established source of electricity for the global market and contributes 5% of the global electricity demand. Countries including Ireland, Denmark, Spain, Portugal, United Kingdom and Germany have actually already exceeded

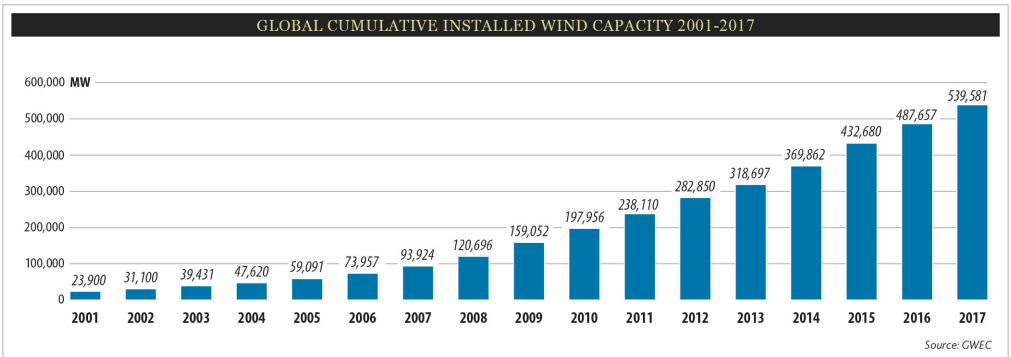

Figure 1.2: Global Cumulative Installed Capacity, 2011-2017 (Global Wind Energy Council [2017])

10% in terms of the amount of their electricity demand produced by wind. Europe's installed power by 2012 accounted for 7% of the total demand for European countries at 106 GW (European Wind Energy Association [2012]).

The European Union is working towards achieving a target of 20% of its total energy demand, provided from renewable resources by the year 2020. This has been set out in the EU's Renewable Energy Directive. Looking to the future, all EU countries have agreed to a target amount of 27% of demand being provided by renewables by the year 2030. In terms of the target for 20% by 2020, it is estimated by the EWEA that by that stage, wind will have reached an installed capacity of 230 GW. In Ireland, there are is currently a total of 233 wind farms in place, which contributes slightly over 3 GW to the national electricity grid. In 2014, 18.3% of Ireland's electricity demand was provided by wind energy.

In terms of turbines currently on the market, the MHI Vestas V164 turbine has a rated capacity of 9.5 MW and was designed for the offshore market. It has a rotor diameter of 164m and is the largest machine in terms of capacity, since its construction in 2014. This turbine has been chosen to power part of the Walney Extension project in the Irish Sea, due to go online in summer 2018. The Enercon E-126 wind turbine has a slightly lower capacity of 7.5 MW. It has a hub height of 135m and a rotor diameter of 126m and unlike many of the other turbines at this scale, has been developed for onshore applications. Fig 1.3 taken from Premalatha et al. [2014] outlines the increasing size in

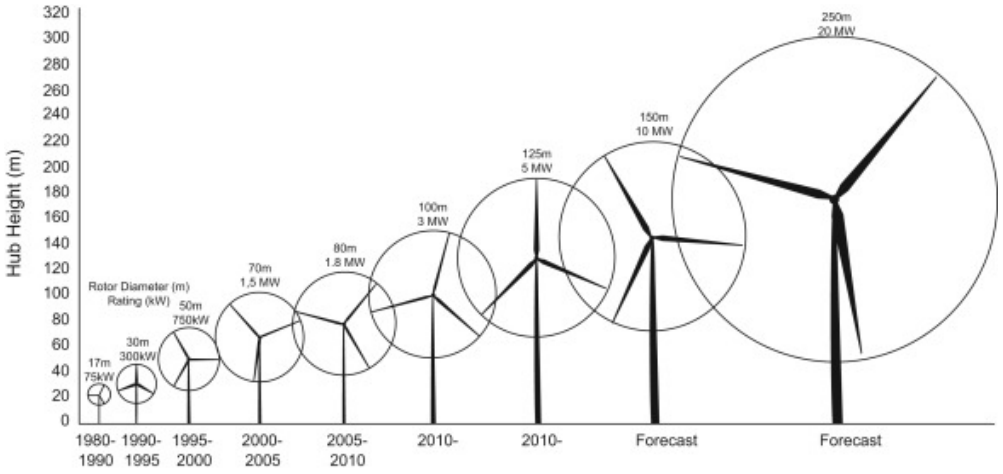

Figure 1.3: Historical Increase in Industrial Turbine Size

turbines in recent years and some predition for the future.

1.4 Research Aims

Given the increasing demand to improve the efficiency of wind turbines around the world to harness as much energy as possible from available sites, there is a need to consider the design of supporting towers to heights in excess of 100m. Although tubular steel towers have been the traditional tower design up to heights of this order, there is a need to assess the viability of other solutions due to transportation and relative stiffness limitations when using steel alone. Given the well-established concrete design and construction techniques utilised in industrial chimney applications, designers have been looking to incorporating concrete into wind turbine tower configurations to overcome some of the difficulties presented at hub heights of the order of 100m (Lanier [2005]).

In the literature, authors have cited the availability of hybrid concrete-steel towers and its cost-competitiveness in terms of Cost of Energy (CoE), which compares favourably to towers consisting of steel alone at high hub-height levels. The cost of the tower has been reported to be between 20-30% of the overall capital cost of the wind turbine (Colherinhas et al. [2016]). This cost contribution adds to the need to investigate the various costs and performance measures attributed to hybrid towers.

In order for engineers to design wind turbines, there is a need both to have suitable numerical and analytical models to carry out the design and in addition, there is a need to understand the key response characteristics. The design of a turbine or a component such as the tower will often be carried out within an environment of optimising a particular objective, be that a structural performance characteristic or some monetary function. As such, there is a need to develop suitable optimisation strategies and algorithms to contribute to understanding and expand on available tools for the wind energy industry.

This research will address these problems in four ways -

- Derivation and construction of analytical and finite element models to establish the free vibration response characteristics of hybrid towers and utilise these models to interrogate responses.
- Derivation of multi-degree of freedom (MDOF) mixed-formulation reduced order models of wind turbines including hybrid towers to establish forced vibration characteristics and utilise these models to interrogate responses.
- Development and application of optimisation strategies to allow for the design and optimisation of hybrid concrete-steel towers whilst accounting for dynamic model responses in a computationally efficient manner.
- Application of models developed to local and global applications including structural health monitoring at a local level and spatial response review at a geographically global level.

1.5 Organisation of the Thesis

The thesis has eight chapters in total including **Chapter 1** and seven further chapters outlined below.

Chapter 2 covers the literature review section of the thesis. General wind turbine features and properties will be introduced. Fundamental concepts around finite element modelling, structural dynamics and structural optimisation will be introduced. Turbine towers and the development of hybrid steel and concrete towers are to be outlined.

Chapter 3 is concerned with the modelling of tower structures. It will broadly include the derivation and benchmarking of analytical and discretised finite element models of hybrid towers.

Chapter 4 consists of modelling wind turbine assemblies as Multi-Degree of Freedom (MDOF) models capable of being subjected to coherent, turbulent wind field drag forces. Two 11 DOF mixed formulation Finite Element (FE) and Euler-Lagrangian models will be developed. The aerodynamic loading, including the derivation of lift and drag forces and the generalisation of forces according to the Principal of Virtual Work is also outlined.

In **Chapter 5**, the response of hybrid concrete-steel towers is examined in detail using the models developed in Chapters 3 & 4. Global and local strain responses are examined in the time and frequency domains under variable design criteria and exposure conditions.

In **Chapter 6**, the development of an optimisation algorithm to arrive at a near global optimum design for a hybrid tower under conditions of dynamic load application and imposition of structural constraints is carried out. Optimisations are conducted under single and multiple objective problems, which themselves consist of structural and non-structural goals.

Chapter 7 presents two distinct applications of the MDOF models developed. The first application is to use the high-fidelity nature of the tower model to examine its potential in detecting damage through signal processing of local signals. The second application is to couple the MDOF model with a Geographical Information Systems (GIS) model to present turbine load and response solutions spatially.

Finally, **Chapter 8** is used to present some discussion and conclusions which can be taken from the work. Some suggestions for areas which could be developed through further research are given.

Chapter 2

Literature Review

2.1 Introduction

This chapter proposes to outline the literature review carried out in the work. Some of the fundamental features of wind turbine assemblies will be presented. In addition, the fundamental engineering considerations in terms of design such as free and forced vibration characteristics and time varying loading and structural response. A review of the published literature is also given, describing the current state of knowledge around the modelling, response and optimisation of hybrid wind turbine towers, with an emphasis on works investigating the response and optimisation of these towers and wind turbine support structures.

2.2 Wind

Wind can be defined as a body of moving air in the earth's atmosphere, moving in three dimensions but primarily moving parallel to the ground. Wind occurs as a result of pressure differences caused by uneven heating of the earth's surface by the sun between regions around the equators and the regions around the poles. It is also caused by the rotation of the earth, an effect known as the Coriolis effect. As the earth rotates at a

faster rate around the equators than at the poles, this will affect the movement of air between the two extremities.

2.2.1 Wind Shear

In engineering applications, wind is described using a number of measures. The most important measure is that of wind speed. Wind speed at any point in time and space is defined by a mean wind speed component and a turbulent wind speed component. The mean component will vary as a function of height and a parameter known as shear exponent. This change in wind speed with height is known as wind shear. The steady state or mean wind speed, $\bar{v}(h)$ can be found using the two available mathematical approaches. One is known as the Power Law and the other the Logarithmic Law. The Power Law is given in Eq 2.1 and an example of a typical profile is given in fig 2.1.

$$\bar{v}(h) = \bar{v}(h_{\text{ref}}) \left(\frac{h}{h_{\text{ref}}} \right)^{\alpha} \tag{2.1}$$

Where, in Eq 2.1, $\bar{v}(h_{\text{ref}})$ is the wind speed at a reference height and α is the shear exponent value, which defines the surface roughness. Typical values of the shear exponent values range from 0.15-0.25.

2.2.2 Turbulence

For any one site, wind speeds will vary over short term and long term periods. In both cases, probability distribution functions are used to express the probability of occurrence of any given wind speed over the expected range of speeds. For long-term applications, a Rayleigh or Weibull probability distribution function can be used (annual) (International Electrotechnical Commission [2005]). In the case of short term predictions (up to one hour), a Gaussian probability distribution function is appropriate.

Turbulence occurs in the atmosphere and causes the wind speed to change on a continual

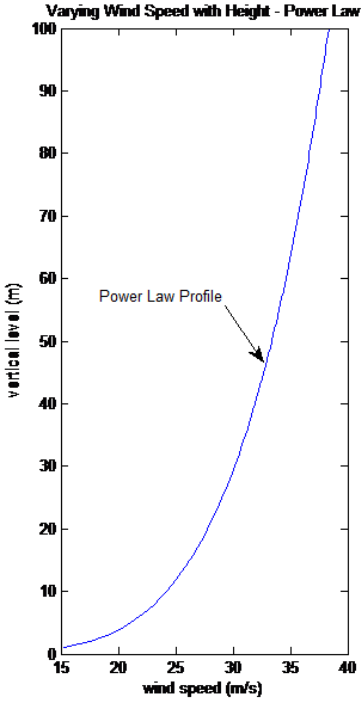

Figure 2.1: Varying Mean Wind Speed with Height (Wind Shear)

basis. This turbulence creates the fluctuating component of wind speed. The energy present which causes this turbulence is described using a spectral density function, which outlines the energy content in the frequency domain. One model is the Kaimal PSDF, presented in Eq 2.2

$$PSD(f) = \frac{4\sigma_w^2 L_w / v(h_{\text{hub}})}{(1 + 6fL_w / v(h_{\text{hub}}))^{\frac{5}{3}}} \tag{2.2}$$

An important property of the PSDF plot is that the integral of power over the frequency range will equal the total variance (Manwell et al. [2010]). The variance in this expression is a function of some specified wind turbulence intensity, I and the mean wind speed. Turbulence intensity is defined as per Eq 2.3. Other variables in Eq 2.2 include an Integral Scale Length, L_w and frequency, f.

$$I = \frac{\sigma_w}{\bar{v}(h)}\% \tag{2.3}$$

Wind turbulence intensity is directly related to the surface roughness at any specific site. Turbulence intensity will increase as the surface roughness increases due to the increased friction experienced by the moving air. An example of a turbulent wind speed time history, $v_t(t)$, for two different shear exponent values is given in fig 2.2.

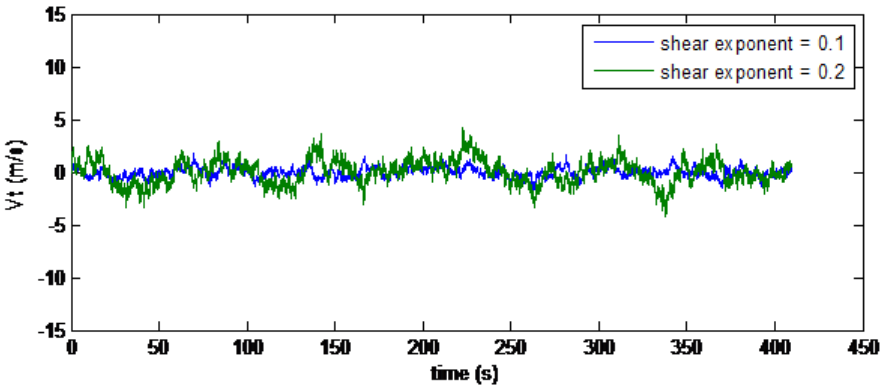

Figure 2.2: Turbulent Component of Wind Speed

2.2.3 Capture of Kinetic Energy

Wind is essential to the operation of wind turbines. The law of conservation of energy states that the total energy in an isolated system remains constant and so cannot be created nor destroyed. It can only be transformed from one state to another. This is the fundamental principle which makes the generation of electrical Potential Energy possible, by virtue of harnessing the Kinetic Energy (T) present in the wind and using this to create mechanical energy, which is then transformed to electrical Potential Energy.

It is possible to determine the amount of energy available in the body of moving air which passes through the wind turbine rotor through simple derivations of the Kinetic Energy present, as follows in Eq 2.4. The terms A_r, ρ_a and m_a refer to the swept rotor area, density of air and mass of air respectively.

$$T = \frac{1}{2} m_a \bar{v}^2 = \frac{1}{2} A_r \bar{v} t \rho_a \bar{v}^2 = \frac{1}{2} A_r t \rho_a \bar{v}^3 \tag{2.4}$$

$$\text{Power(wind)} = \frac{dT}{dt} = \frac{1}{2} A_r \rho_a \bar{v}^3 \tag{2.5}$$

Power is simply a measure of energy per unit time, which is given in Eq 2.5. This is a fundamental equation in terms of the wind energy industry. It can be seen that power is a multiple of the rotor area (or in other words the square of the rotor diameter) and of the wind speed cubed and so these two variables are key in assessing the wind energy resource at any location for a given rotor diameter.

Eq. 2.5 presents the total amount of power available from the wind as it passes through the rotor disk. However, not all of this power can be captured by the wind turbine due to the fact that the air will not be stopped by the rotor, rather it will pass through the rotor and some of this Kinetic Energy will be passed to the rotor blades generating lift and drag. The maximum amount of energy which can theoretically be extracted from

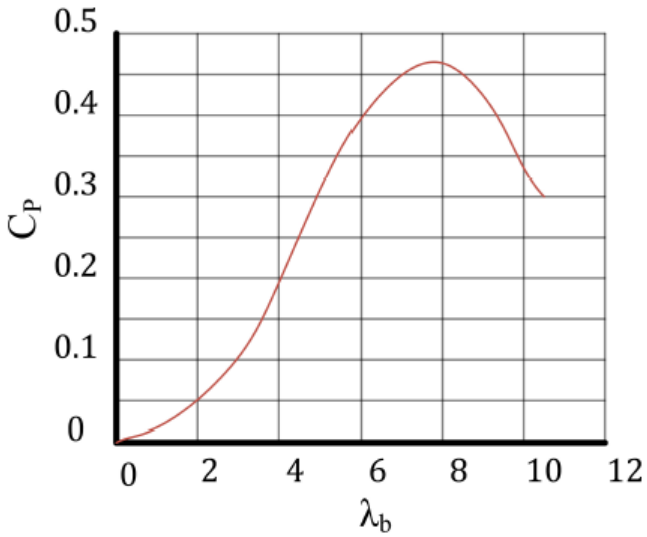

Figure 2.3: Power Co-efficient vs Tip Speed Ratio

the wind is 59% of the total Kinetic Energy and this limit is known as the Betz limit. A power co-efficient (C_p), with an upper limit of 0.59 is therefore introduced as per Eq. 2.6. The value of C_p is also known to be a function of the Tip Speed Ratio (TSR), which is the ratio of the speed of the tip of the blade to the prevailing wind speed. Figure 2.3 gives a typical plot of C_p vs TSR for a modern horizontal axis wind turbine (HAWT).

$$\text{Power(turbine)} = \frac{1}{2} C_p A_r \rho_a \bar{v}^3 \tag{2.6}$$

The rated power output of modern HAWTs are often described using power curves. These are two dimensional plots of the power output which can be achieved at a given wind speed.

An example of a HAWT power curve is given in Figure 2.4, taken from Hall et al. [2011]. The curve is divided into three distinct regions, which are delineated by defined wind speeds, namely the cut-in wind speed, the rated wind speed and the cut-out wind speed. Below the cut-in wind speed, there is not enough energy available from the wind to cause sufficient lift for the blades to rotate. Once the cut-in speed is exceeded, some

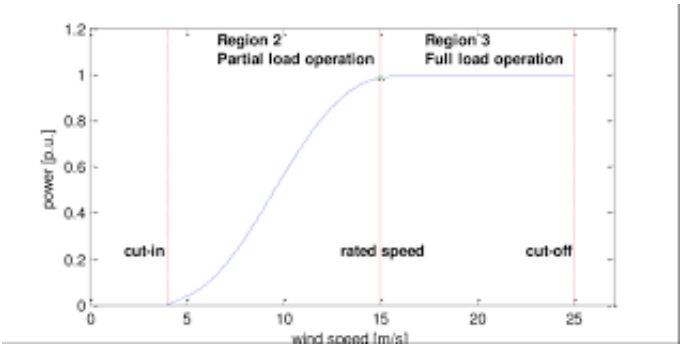

Figure 2.4: Sample Turbine Power Curve

rotation and power generation will occur. From this point, rated power will increase non-linearly with wind speed until the rated wind speed is reached. At this speed, the turbine is operating at its optimum efficiency and in order to maintain the required speed of rotation and lift force, modern turbines will use pitch control to alter the angle of attack of the blades. The power output between the rated wind speed and the cut-out speed is held constant on this basis. Finally, if wind speeds increase above the cut-out speed, the turbine will cease to operate as it will have reached its operating and structural capacity. In order to bring the rotation to rest, blades will pitch to a point where stall is induced and lift is eliminated, with a braking mechanism then used to hold the rotor in a fixed position.

2.2.4 Wind Turbine General Properties

Wind turbines have been going through engineering development in terms of form and shape since the first windmills were constructed to grind grain in 1000 AD. At the present time, there are two dominant forms of turbine, namely the Vertical Axis Wind Turbine (VAWT) and the Horizontal Axis Wind Turbine (HAWT). The latter will be used in detail in this work. A VAWT consists of a central vertical tower, with blades which rotate around the tower which also acts as a vertical axis. The blades have a fixed pitch and the generator and gearbox typically sit at ground level.

A HAWT consists of a vertical tower and a number of blades which radiate from a rotor

which is supported at the top of the tower. The rotor has a horizontal axis. This type of turbine can either be an upwind turbine with the rotor/blades located on the upwind side of the tower or a downwind turbine with the rotor/blades on the downwind side of the tower. The former has been optimised over time to include three blades, with the latter formed using two blades.

2.2.4.1 Rotor

In the majority of modern HAWT, there are three blades connected to a hub. The assembly of the three blades and the hub are known as the rotor and this sits at the top of the tower. Blades are one of the most expensive components of the overall wind turbine. The blades are designed to achieve optimal structural and aerodynamic performance. Structurally, they must have a high strength to mass ratio. Aerodynamically, they are designed such that the amount of Kinetic Energy extracted from the wind is maximised. Drag and lift are generated as a result of their shape and effective pitching of the blades by the wind turbine controller.

2.2.4.2 Nacelle

The nacelle houses a number of components. These components include the rotating shaft from the hub, the emergency brake, the gear box and high speed shaft and the generator. The nacelle housing is placed onto a nacelle yawing mechanism which can rotate the entire assembly so that the plane of the rotor is perpendicular to the wind direction. All of the rotating parts will have associated couplings and bearings also housed in the nacelle.

Modern turbines include a braking system in order to hold the rotor in position in the event of an emergency shut-down of the machine. In such an event, typical pitch controlled rotors will pitch the blades such that the rotor moves from a condition of generating lift to one where dynamic stall is induced and rotation is stopped. The brake would then be activated to hold the idle blades in position.

2.2.4.3 Tower

The tower of a HAWT provides the elevation required by the hub such that the plane of rotation for the blades is sufficiently clear of ground level and any obstacle above ground. Towers are typically 1 to 1.5 times as tall as the diameter of the rotor. As with any component, the height will vary from one supplier to the next and will be selected to suit the characteristics of the site and the required rated power output of the turbine.

The tower must be sustain different types of loading during its lifetime, all of which have a dynamic component in their application. These include axial forces and bending moments in various directions, generally applied at the tower top.

Towers have been historically constructed as masonry structures in early windmills. Other forms of construction have included lattice and cable stayed structures. Modern forms of construction include tubular steel, timber, lattice construction, reinforced concrete or some hybrid of concrete and steel. The choice of tower construction will depend on its suitability to the site environment, the structural demand and its monetary and environmental cost.

2.2.4.4 Foundations

The foundations must transfer all structural load to the underlying soils. Onshore turbine foundation types include gravity based spread foundations and piled foundations. These foundations have been discussed in many texts including Tricklebank et al. [2007]. Subject to the availability of suitably stiff ground conditions, spread foundations are the most economical form of foundation. In this case, the large overturning moment and vertical loading is transferred to the underlying soils across a large footprint, thus reducing bearing pressure to within the prevailing allowable soil bearing pressures and avoiding unwanted uplift.

Offshore foundations are an area of significant research effort, with a wide variety of

types under development. These can broadly be described as those which are fixed to the sea floor and those which are buoyant and semi-submersed in the water. A review paper by Schaumann and Wilke [2005] provides a summary of the different types in use. Gravity based offshore foundations are application in depths up to 10m. From 10-30m, a monopile foundation is the most popular type. In deeper waters or where a wind turbine of relatively large size is proposed, a monopile becomes impractical. Multi-pile foundations, suction-bucket foundations, jacket and floating foundations are all options for deeper or large turbine applications.

2.3 Dynamical Numerical Modelling of Wind Turbines

Research on the subject of forced simulations of wind turbines has been presented to date under a broad range of themes. These themes include review papers, tower analysis and design papers, condition monitoring papers, structural control and aerodynamic and hydrodynamic load description papers among others. In the case of most works, authors have either presented a new mathematical description of the turbine (or local element), or constructed a model using well established engineering tools such as the Finite Element Method (FEM) and then followed with a numerical study to investigate some aspect of the theme in question.

2.3.1 Model Formulations

In terms of established model formulation approaches, these formulations can be broadly split in three categories (Hansen et al. [2006]), 1) Full FEM modelling, 2) multi-body modelling where the flexible members are divided into rigid elements connected with springs and dampers and 3) reduced order models such as the use of virtual work and modal functions where physical movements can be described using a linear combination of realistic modes of vibration. Recently, authors have produced models which have consisted of mixed-formulations where combinations of the above three approaches have been utilised. These mixed approaches propose to capture the benefits of FEM and

multi-body modelling in terms of accuracy and ability to account for non-linearity, whilst also utilising assumed shapes of vibration to minimise computational effort. (Wang et al. [2010], Gebhardt and Roccia [2014]). Most works to date have accounted for the tower component of the assembly using the analogy of an Euler-Bernoulli beam element or series of beam elements. Whilst this allows for the derivation of global structural responses, it means that a further step of computation is required to establish local shell strains and stresses. This is significant in the sense that structural health monitoring of local connections will require collection and analysis of strain or stress time histories. It is also significant in terms of the analysis and design of towers before construction. Another consequence of simplified tower modelling is often that deformations attributed to shear deformation are omitted. Finally, in terms of improving accuracy in defining dynamic performance, simplified tower definition can also reduce the accuracy in defining modal mass quantities.

2.3.2 Numerical Modelling Applications

Authors have established the importance of considering the dynamic response of the tower as a result of its interaction with the rotor and nacelle in the literature (Murtagh et al. [2005]) and the increased displacement which occurs due to this interaction. As such, there has been an effort to construct multi-degree of freedom (MDOF) models when considering the deformation of these structures. As well as studying tower deformations, reasons behind constructing holistic models range from the study of foundations (Ramachandran et al. [2014]) to the study of vibration suppression applications (Zhang et al. [2015]) to developing techniques for the structural health monitoring of various components.

2.4 The Finite Element Method

2.4.1 Introduction

In solid mechanics, an expression for the response of a body can be derived using a combination of ordinary and partial differential equations, with exact solutions to these equations then found through either numerical or analytical means. However, in the case of irregular solid shapes, the task of deriving such expressions can become impractical if not impossible. Finite Element Analysis (FEA) developed out of the need to find approximate solutions to such problems, which were either impossible or impractically time-consuming to solve exactly by analytical means. In simple terms, the Finite Element Method (FEM) is a means of creating a discretized model of a continuous structural body or system by describing that system using a definite number of nodes and associated degrees of freedom. The exact differential equations are replaced by a system of approximate algebraic equations with a view to solving the problem. Cook et al. [2007] describes it as a method for numerical solution of a field problem, which is said to be a problem which requires us to find the spatial distribution of one or more dependent variables.

In terms of the development of the FEM, a piece of work by Schellbach in 1851 is seen as being the origins of discretizing a continuous domain to derive an approximate solution to degrees of freedom at node points. In 1943, Courant et al. [1943] described the torsional rigidity of a hollow shaft by discretising the cross section and then interpolating a stress function over each 'element'. At this time, the FEM was seen as a sort of engineering method rather than something with a sound mathematical basis, however, in the early 1960s it was given academic respectability, having been seen as a form of the classical approximation method known as the Rayleigh-Ritz method (Clough and Penzien [1993]), shortly after the term 'finite element' had been proposed by Clough. The Rayleigh-Ritz method itself originated in the 1870's when Lord Rayleigh was working in the area of vibrations. Ritz then extended the method in 1909, with it being a

method whereby responses of a continuum can be found without the need to explicitly solve the governing differential equations of that continuum.

2.4.2 Mathematical Formulation

In the FEM, individual 'finite elements' are assembled to describe the behaviour of an overall structural model and are connected at node points, all of which combine to form a finite element mesh. The behaviour of each element is described mathematically using some generalisation, such as the use of polynomials to portray the spatial distribution of displacement or rotation across the element. In structural mechanics, the most widely used elements are displacement elements, where assumed displacement fields are used to derive a response. In these cases however, the displacement solution over the domain will be closer to the exact solution than in the case of the stress solution given that stresses will be taken from derivatives of the displacement. The description for each local elements are initially generated by way of a characteristic or 'stiffness' matrix, before each elements' stiffness matrix is combined into a global structural description. Such elemental stiffness matrices are at the basis of any FEM model and can be found using one of the following approaches –

- Direct formulation
- Virtual work
- Variational arguments applied to functionals
- Weighted residual methods

Direct formulation is the most elementary approach to the formation of a set of algebraic equations with respect to system degrees of freedom and is based on a physical understanding of the external and internal forces which must be at equilibrium for the existence of a stable system. An example would be in the direct application of Hooke's

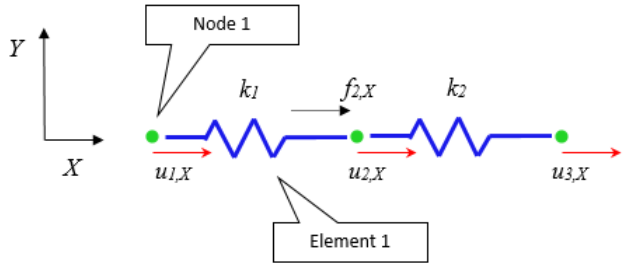

Figure 2.5: Bar/Spring Elements - Direct Formulation of Stiffness Matrix

Law to construct a set of equations for a pair of springs in series. Translational degrees of freedom are assigned to three nodes as shown in Figure 2.5. After an external force is applied, the system will be at equilibrium after some displacement and internal force has developed. In this case, each spring can be considered as a local finite element, connected at node points to form the complete system. For equilibrium to exist, the internal forces at each node must balance. Assembling these equations into matrix form yields vectors for the force and displacement quantities and also what is known as the elemental stiffness matrix. At this point it is worth understanding that the elemental stiffness matrix is symmetric and singular in linear algebra terminology. This process can be repeated for the second spring, using nodes 2 and 3 and building another associated stiffness matrix.

$$[k]\{u\} = \{F\} \tag{2.7}$$

$$\begin{bmatrix} k_1 & -k_1 \\ -k_1 & k_1 \end{bmatrix} \begin{Bmatrix} u_1 \\ u_2 \end{Bmatrix} = \begin{Bmatrix} F_1 \\ F_2 \end{Bmatrix} \tag{2.8}$$

Application of the principle of virtual work is a slightly more rigorous method in formulating finite element matrices than the use of direct formulation only. The principle

of virtual work can be written as

$$\int \{\delta\varepsilon\}^T \{\sigma\} dV = \int \{\delta u\}^T \{F\} dV + \int \{\delta u\}^T \{\Phi\} dS \tag{2.9}$$

Where $\{\delta\varepsilon\}^T = [\delta\varepsilon_x, \delta\varepsilon_y, \delta\gamma_{xy}]$ is a three dimensional strain vector produced by imposing a virtual displacement $\{\delta u\}$. This equation states that for any admissible virtual displacement from equilibrium, the strain energy stored is equal to the work done by body forces F in the volume, V. The last term in the above equation defines the virtual displacement times the surface tractions on the surface S. The displacements can be interpolated over a finite element as

$$\{u\} = [N]\{d\} \tag{2.10}$$

In this expression, $\{d\}$ represents the nodal displacement degrees of freedom and $[N]$ is a matrix of elemental shape (also known as interpolation) functions, which describe the expected deformed shape of the element. The strain can be found using Eq. 2.11.

$$\{\varepsilon\} = [B]\{d\} = [\delta][N]\{d\} \tag{2.11}$$

In this expression, $[B]$ is known as a strain-displacement matrix. From the above and from basic stress-strain relations of structural mechanics, the elemental stiffness matrix can be determined as follows.

$$\{\sigma\} = [E]\{\varepsilon\} \tag{2.12}$$

$$\{\delta u\}^T = \{\delta d\}^T [N]^T \tag{2.13}$$

$$\{\delta\varepsilon\}^T = \{\delta d\}^T [B]^T \tag{2.14}$$

Taking equations 2.12, 2.13 and 2.14 and inserting into 2.9, the following expression is found

$$\{\delta d\}^T \int [B]^T [E][B] dV \{d\} = \{\delta d\}^T \int [N]^T \{F\} dV + \{\delta d\}^T \int [N]^T \{\Phi\} dS \tag{2.15}$$

In the case of loads applied only at nodal points and not across the surface of the body, this expression can be shortened to read

$$[k]\{d\} = \{f\}, [k] = \int [B]^T [E][B] dV \tag{2.16}$$

Variational methods in the context of formulating finite element matrices are most commonly based on the functional of Potential Energy. The Rayleigh-Ritz method is one such method. The total Potential Energy of any structural system is equal to the strain energy of the system, less the Potential Energy of applied loads. Once an external force has been applied to a body, at some point afterwards, when the change in Potential Energy is zero, the strain energy in the body is equal to the Potential Energy of the applied loads. This stationary position in the total Potential Energy of the system is found by differentiating the Potential Energy with respect to the system degrees of freedom. In simple terms, at equilibrium, the change in strain energy generated in a body will be equal to the change in Potential Energy of the applied loading (leading to distortion of the body and hence strain energy).

The total Potential Energy of any system is described symbolically by the equation below, including terms for strain energy, U, and potential due to applied loads Φ.

$$\Pi = U + \Phi \tag{2.17}$$

The strain energy held in a linear elastic body with volume V, is defined as

$$U = \frac{1}{2}\int \{\varepsilon\}^T [E]\{\varepsilon\} dV \tag{2.18}$$

By relating the strain to the displacement by way of a strain-displacement entity, as Eq. 2.18 can be written as

$$\begin{aligned} U &= \frac{1}{2}\int \{d\}^T [B]^T [E][B]\{d\} dV \\ &= \frac{1}{2}\{d\}^T [k]\{d\} \end{aligned} \tag{2.19}$$

$$[k] = \int [B]^T [E][B] dV \tag{2.20}$$

The matrix $[k]$ is known as the elemental stiffness matrix. The equation for strain energy is also valid in a larger sense where a global structure is comprised of many local finite elements. In this case, the equation can be written as

$$U = \frac{1}{2}\{D\}^T [K]\{D\} \tag{2.21}$$

With regards to the Potential Energy of applied loads acting on the global system, this is defined in structural mechanics as being the work done by an applied force, or

$$\Pi = \{D\}^T \{F\} \tag{2.22}$$

Using the principle of stationary Potential Energy, when the change in total Potential Energy with respect to the system degrees of freedom is at zero, the system has reached

equilibrium.

$$\frac{d\Pi}{d\{D\}} = \frac{d}{d\{D\}}\left(\frac{1}{2}\{D\}^T[K]\{D\}\right) + \frac{d}{d\{D\}}\left(-\{D\}^T\{F\}\right) = 0 \tag{2.23}$$

From matrix linear algebra, and because of the symmetry inherent in the global stiffness matrix, this equation reduces to

$$\begin{aligned} [K]\{D\} - \{F\} &= 0, \\ [K]\{D\} &= \{F\} \end{aligned} \tag{2.24}$$

This equation appears to be the same as that given by Hooke's Law in the simple case of a spring elements. However, this form can now be used for any global stiffness matrix assembly in order to solve for the unknown degrees of freedom.

2.4.3 Forms of Finite Element

The choice of a suitable form of finite element is dependent on a number of concerns, primarily, the anticipated physical behaviour of the structure and the required fidelity of the model. In the case of a truss structure where all elements are expected to sustain axial loading only, then a suitable element could be a 1-D bar element. In the case of a long, slender element which is expected to bend out-of-plane due to out-of-plane loading, a 1-D beam element might be preferred. Planar structures such as slabs and membranes can also be described using 2-D membrane, plate or shell elements. Finally, solid, 3-D elements may be applied to problems where highly complex three dimensional stresses are expected, such as local steel-steel connection details.

2.4.3.1 Bar/Spring Elements

The example provided of spring elements used in determining the system equations through the direct method is also an example of 1-Dimensional bar elements. These

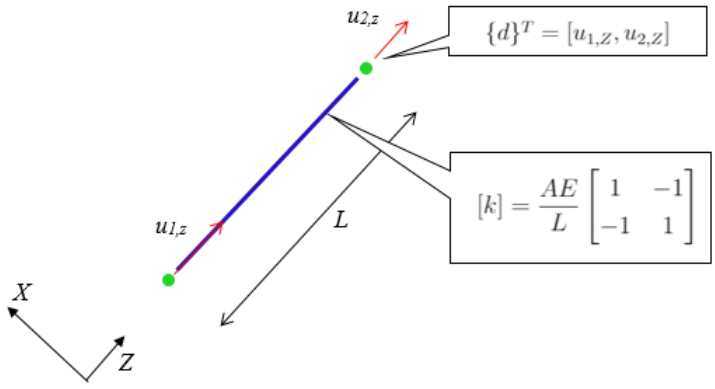

Figure 2.6: Bar Element, Axial DOF

elements include a bar, which possesses axial stiffness only and an element node at each end of the bar. With 1 degree of freedom (DOF) per node, it has a total of 2 DOF and has an elemental displacement vector, $\{d\}$ of $\{d\}^T = [u_{1,Z}, u_{2,Z}]$. Figure 2.6 identifies these DOF and the elemental stiffness matrix.

The stiffness matrix for the element can be constructed by using linear shape functions to relate the nodal displacements to the nodal degrees of freedom. This stiffness matrix is given in Eq. 2.25.

$$[k] = \frac{AE}{L}\begin{bmatrix} 1 & -1 \\ -1 & 1 \end{bmatrix} \tag{2.25}$$

2.4.3.2 Beam Elements

In terms of beam elements, these are a well-established form of finite element and can be used to describe structures which deform primarily in flexure as a result of out-of-plane loading. This is the case in terms of the flexible elements of wind turbines including the tower and blades. In a finite element model, a beam element consists of an element connecting two end nodes. These nodes will each have corresponding degrees of freedom depending on the type of beam element in question. Beam elements are often

described in the literature as being 'Euler-Bernoulli' beam elements or 'Timoshenko' beam elements. The former is an element which conforms to classical beam bending theory, whereas the latter incorporates shear deformation into its composition as well as flexure. The stiffness matrix for an Euler-Bernoulli element can be derived as follows on the basis of the fourth order equation of the out-of-plane displacement of a uniform beam element.

$$F = EI\frac{d^4u}{dz^4} \tag{2.26}$$

$$M = EI\frac{d^2u}{dz^2} \tag{2.27}$$

In these equations, the force F is the applied out of plane force, u is the resulting displacement and M is the applied and internally developed bending moment. For this beam element, degrees of freedom are given at each node and include a translation and rotation degree of freedom. Local shape functions are used in describing the assumed deformed shape of the element and in the case of a beam element, cubic curve functions are fitted to the deflected profiles of the beam when subjected to a unit displacement/rotation in the case of each degree of freedom.

$$\{u\} = [N]\{d\}, \qquad \frac{d^2u}{dz^2} = [B]\{d\} \tag{2.28}$$

$$[N] = [N_1, N_2, N_3, N_4] \tag{2.29}$$

$$
\begin{aligned}
N_1 &= 1 - \frac{3z^2}{L^2} + \frac{2z^3}{L^3} \\
N_2 &= z - \frac{2z^2}{L} + \frac{z^3}{L^2} \\
N_3 &= \frac{3z^2}{L^2} - \frac{2z^3}{L^3} \\
N_4 &= \frac{z^2}{L} + \frac{z^3}{L^2}
\end{aligned}
\tag{2.30}
$$

It is noted that N_1 and N_3 refer to displacement degrees of freedom and N_2 and N_4 refer to the rotational degrees of freedom. Using these expressions and in this case the principle of virtual work,

$$
[B] = \frac{d^2}{dz^2}[N] \tag{2.31}
$$

$$
[k] = \int_0^L [B]^T EI[B]dz = \frac{EI}{L^3}\begin{bmatrix} 12 & 6L & -12 & 6L \\ 6L & 4L^2 & -6L & 2L^2 \\ -12 & -6L & 12 & -6L \\ 6L & 2L^2 & -6L & 4L^2 \end{bmatrix} \tag{2.32}
$$

This beam element has an elemental displacement vector, $\{d\}^T = [u_{1,X}, \theta_{1,Y}, u_{2,X}, \theta_{2,Y}]$. Figure 2.7 identifies these DOF and the elemental stiffness matrix.

An extension of this element is possible in terms of extending the number of DOF available to the element by also considering either axial DOF or torsion-rotation DOF. Axial DOF may be added in the manner of the 1-D bar elements described above. Torsional DOF may be added by considering the DOF identified in Figure 2.8. This element torsional stiffness matrix is given in Eq. 2.33, where G and J refers to the

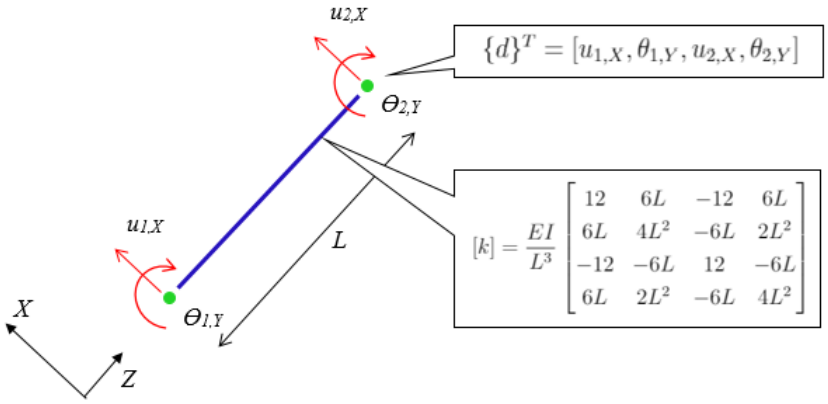

Figure 2.7: Beam Element, Flexural DOF

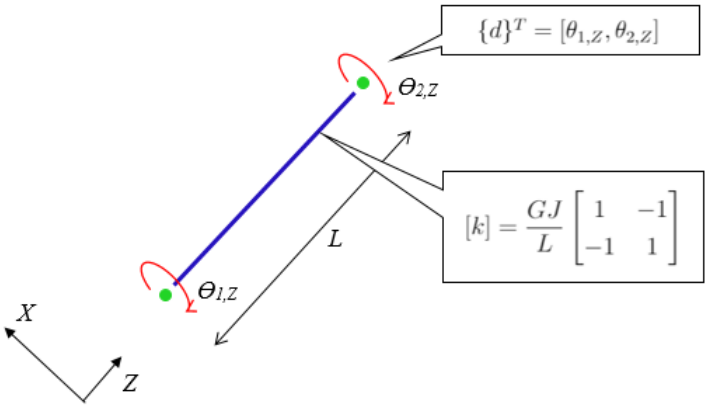

Figure 2.8: Beam Element, Torsional DOF

Modulus of Rigidity (or Shear Modulus) and the Torsional Constant respectively.

$$[k] = \frac{GJ}{L}\begin{bmatrix} 1 & -1 \\ -1 & 1 \end{bmatrix} \tag{2.33}$$

This torsional element has an elemental displacement vector, $\{d\}^T = [\theta_{1,Z}, \theta_{2,Z}]$ where the rotational DOF are seen to be about the Z axis identified in Figure 2.8.

2.4.4 Global System Matrices

It has been noted that the basis of the FEM is to take a system which is described using exact differential equations and represent it by a system of approximately equivalent algebraic equations. To this end, it is required to take the representative matrices from each local finite element and compile global system matrices which can be used to solve for the unknown degrees of freedom at a structural level as per Eq. 2.24.

In Eq 2.24 the global stiffness matrix is assembled by first writing a global vector of the system degrees of freedom, $\{D\}$. An example is given in the case of the system of two spring (bar) elements connected in series. The combined stiffness matrix is given below. This was assembled through overlaying entries of each of the local finite elements into the global matrix at locations associated with the global degrees of freedom. It can be seen that the entries for element 1, associated with degree of freedom u_1 and u_2 are found in the upper left corner of the matrix. Entries for element 2, associated with u_2 and u_3 are given in the lower right, with an overlapping term in the centre of the matrix. This approach is replicated in the form of global matrices with many thousands of degrees of freedom through careful book-keeping practices.

At this point, externally applied forces can be input as they are applied to the global system and the equations can be solved through linear algebra to derive the unknown displacements in this case.

$$\begin{Bmatrix} F_1 \\ F_2 \\ F_3 \end{Bmatrix} = \begin{bmatrix} k_1 & -k_1 & 0 \\ -k_1 & k_1 + k_2 & -k_2 \\ 0 & -k_2 & k_2 \end{bmatrix} \begin{Bmatrix} u_1 \\ u_2 \\ u_3 \end{Bmatrix} \tag{2.34}$$

Eq. 2.34 can be re-written by isolating the unknown displacements and inverting the

stiffness matrix as follows

$$\begin{Bmatrix} u_1 \\ u_2 \\ u_3 \end{Bmatrix} = \begin{bmatrix} k_1 & -k_1 & 0 \\ -k_1 & k_1 + k_2 & -k_2 \\ 0 & -k_2 & k_2 \end{bmatrix}^{-1} \begin{Bmatrix} F_1 \\ F_2 \\ F_3 \end{Bmatrix} \tag{2.35}$$

2.4.5 Finite Elements in Structural Dynamics

The Equation of Motion for a discretised system, in matrix form is given in Eq. 2.36.

$$[M]\{\ddot{u}\} + [C]\{\dot{u}\} + [K]\{u\} = \{F\} \tag{2.36}$$

The matrices $[M]$ and $[C]$ represent the global mass and damping matrices respectively. Once local mass matrices are determined, these can be compiled into a global matrix as outlined in the case of stiffness matrices in 2.4.4 The global damping matrix can be found by way of proportional damping, which will be described below.

2.4.5.1 Mass

Mass matrices are described in the FEM in terms of structural dynamics as being either 'lumped element mass matrices' or 'consistent mass matrices'. The difference being that lumped mass attributes mass to each node of the element, primarily for the purposes of accounting for translational inertia only. As such, lumped mass matrices are often diagonal. An example is in the case of bar element, whose stiffness and lumped mass matrices are given as follows

$$[k] = \frac{AE}{L} \begin{bmatrix} 1 & -1 \\ -1 & 1 \end{bmatrix} \tag{2.37}$$

$$[m] = \frac{m}{2}\begin{bmatrix} 1 & 0 \\ 0 & 1 \end{bmatrix} \tag{2.38}$$

The consistent mass matrix can be formed by using the same shape functions as are applicable in defining the stiffness matrix and which describe the expected deformed shape of the element. Using the shape functions applicable to a bar element, the consistent mass matrix is given as

$$[N] = \left[\frac{L-z}{L}, \frac{z}{L}\right] \tag{2.39}$$

$$[m] = \int_0^L [N]^T[N]\rho AL dz = \frac{m}{6}\begin{bmatrix} 2 & 1 \\ 1 & 2 \end{bmatrix} \tag{2.40}$$

In the case of an Euler-Bernoulli beam element and all other elements described using shape functions, the same principle can be applied to find the consistent mass matrix.

2.4.5.2 Damping

The damping quantity is defined to take account of the various forms of energy dissipation present within the structure, whether inherent in the construction or added to suppress vibrations. Damping is described in finite element applications using Proportional or Rayleigh Damping. The damping matrix is found to be a linear combination of the global stiffness and mass matrices

$$[C] = a_0[M] + a_1[K] \tag{2.41}$$

The terms a_0 and a_1 are found on the basis of the frequency range of interest and

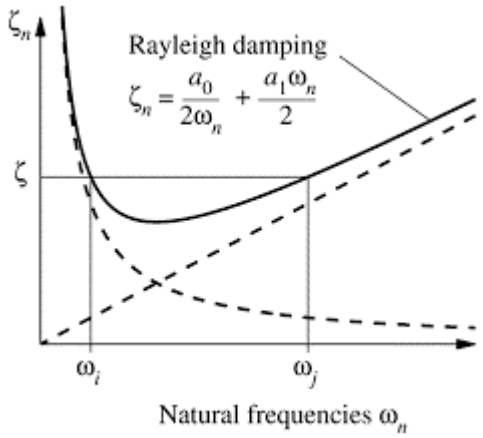

Figure 2.9: Rayleigh Damping & Frequency Dependence

the damping is therefore said to be frequency dependent. Expressions for finding these terms are given in Appendix B. The frequency dependence for a typical system can be seen in fig 2.9, taken from Chopra [1995].

2.4.6 Use of Finite Element Method in Wind Industry

The FEM is widely used in the design of flexible and rigid components in wind turbine towers. It can be applied to situations where loading is applied statically or dynamically, however typically it has been used in static loading scenarios given the inherent high-fidelity nature of such models. In terms of the finite element modelling of wind turbine towers, authors have modelled the towers using beam elements and as shell/membrane elements. Studies have been presented in papers by Lavassas et al. [2003] and Bazeos et al. [2002] of towers constructed using shell elements. Lavassas et al. [2003] modelled the tower and foundation as a meshed finite element continuum, with 5208 4-noded quadrilaterals used to represent the tower. Bazeos et al. [2002] modelled the tower using 8-noded quadrilateral shell elements. These models were used in static analysis of the tower in question and lead to resulting membrane stresses around the tower continuum. They were also used to determine free vibration properties of the towers. These finite element models were effective and accurate in providing free vibration properties of the towers in question.

Authors have utilised the FEM as a tool to optimise the design of wind turbine components. AlHamaydeh and Hussain [2011] used the FEM in order to optimise a wind turbine foundation by preparing several designs and assessing patterns in results to determine optimal conditions. Formal optimisation algorithms have also been utilised with the FEM included as a nested function. Cai et al. [2012] and Zhu et al. [2014] used the FEM in the deterministic optimisation of a wind turbine blade mass, by applying static loading and conducting the accompanying analysis at each iteration of the optimisation. Perelmuter and Yurchenko [2013] used the FEM in optimising wind turbine towers, again assessing the performance of the tower through loading and analysis at each iteration.

2.5 Optimisation in Engineering Applications

2.5.1 Introduction

In engineering problems, it is often the case that a certain goal is to be either maximised (for example design life) or minimised (for example, cost). The goal to be optimised is known as the objective function, and this can be selected according to the problem at hand. In many design situations, this objective function will be optimised by carrying out a limited number of iterations of that design (three or four) and by using each iteration to modify one of the design variables in an ad-hoc manner in order to converge on a 'near-optimal' solution. In the literature, (Yang et al. [2013]) this type of approach has been called the 'expert-based optimisation' approach as the optimisation is carried out on the basis of expert judgement as to the most suitable combination of design variables and how constraints are to be managed and weighted. Formal mathematical algorithms were then developed to provide for the rigorous optimisation of an objective function such as cost, mass or other, which is dependent on a set of design variables and often constrain conditions.

2.5.2 Mathematical Formulation

It is possible to write the optimisation problem in a format known as Nonlinear Programming (NLP).

Minimise $f(x)$, subject to

$$\begin{aligned} g_j(x) &\geq 0, \quad \text{and} \quad j = 1, 2, \cdots, J \\ h_k(x) &= 0, \quad \text{and} \quad k = 1, 2, \cdots, K \\ x_i^{(L)} &\leq x_i \leq x_i^{(U)}, \quad \text{and} \quad i = 1, 2, \cdots, N \end{aligned} \tag{2.42}$$

The objective function is written as $f(x)$, with $\{x\}$ denoting a vector of design variables such that $\{x\}^T = [x_1, x_2, x_3, \ldots, x_N]$. In this formulation, $g(x)$ are inequality constraints and $h(x)$ are equality constraints. The above formulation is written such that the objective function is to be minimised, however it is noted that it can equally be written to maximise the objective using the duality principle.

2.5.3 Traditional Optimisation Methods

Traditional optimisation methods were developed on the basis of optimising a continuous, differentiable objective function dependent on a limited number of independent design variables. Such methods rely on the ability to assess the objective function value (also known as objective fitness) on an iterative basis, from at least two consecutive locations in the solution space and then use this information to form a path to a location of improved objective fitness. Iterations are repeated until a point where a global optimum has been converged upon. Various texts on the subject (Koziel and Yang [2011],Deb [2012]) define some of the better known traditional methods.

Gradient based methods use the gradient of the objective function line or surface to move in the direction of the optimum solution.

Direct search methods have been used where a gradient is not available. Although not as efficient as gradient based methods, they can prove to be successful in converging on local minima. They are based up searching a number of points at the same time in order to converge on an optimum on the basis of discrete point objective functions.

Region elimination methods are used in the case of single variable problems, whereby zones of the solution space are sequentially eliminated based on proven fitness of objective functions, thus allowing convergence on an optimum.

Finally, the Generalised reduced gradient method has been used in constrained optimisation problems and is a variant of the gradient methods used in unconstrained problems.

2.5.4 Non-Traditional Optimisation Methods

Optimisation in complex engineering applications often means considering an objective function which is not a continuous or differentiable function. Similarly, constraints on the design variables or the objective may be either continuous or otherwise and may be implicit rather than explicit, requiring numerical calculation within the optimisation routine. This is a fundamental problem in terms of applying traditional gradient-based methods.

Non-traditional methods have developed in light of the above challenges and are known as nature-inspired metaheuristic algorithms (Yang et al. [2013]). These algorithms attempt to mimic facets of nature on the basis that optimisation is continually happening in nature in search of a better solution than the one at hand. These optimisation algorithms have been used extensively in the literature (Karpat [2013], Kusiak et al. [2010]) and include techniques such as Genetic Algorithms, Greedy Algorithms (GA's), Particle Swarm Optimisation, Fire Fly Optimisation and Cuckoo Search Optimisation. A subset of these algorithms are described as Evolutionary Algorithms (EA). The Genetic Algorithm is one such EA given the concept of taking a population of design points within

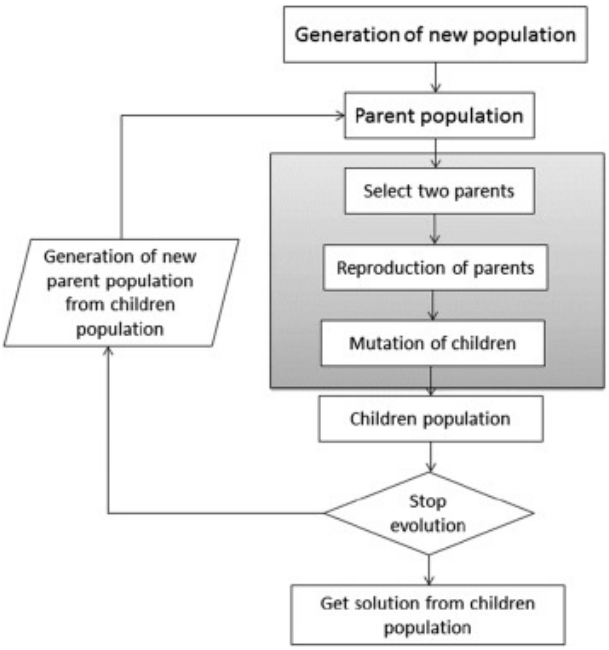

Figure 2.10: Flow Diagram of Typical Genetic Algorithm

a domain and using features of genetic evolution to create a next generation of search points on the basis of assessment of objective fitness and selection of those of higher level of fitness. In this way, the objective function is used as a performance indicator at each population point and its fitness is used as a measure of the probability of a global optimal point being present in its vicinity. A flow diagram of a typical GA is provided in fig 2.10, taken from a paper by Taghavifar et al. [2015].

The ability to search multiple points without gradient information and converge on a global optimal location is one of the advantages held by EAs over traditional methods. However, there are a number of disadvantages to these algorithms including the requirement to adjust factors such as population size, and the rates of evolutionary factors such as mutation and gene crossover, which are problem-specific and require an amount of trial and error. A second issue is that an exact optimum is difficult to achieve, rather a 'near-optimum' location will be found. To overcome this, practitioners have sometimes used EAs to arrive at a location close to the optimum and then use this location as a start point for a more traditional approach to arrive closer to the global optimum.

2.6 Optimisation in Wind Energy

2.6.1 Optimisation of Wind Turbine Towers

In terms of wind turbines, a substantial amount of work has been carried out into the optimisation of dynamically sensitive components such as the blades, tower and recently foundations. A single objective function is typically defined in works in the literature and this is usually element mass, which was assumed to have the most significant impact on cost. Perelmuter and Yurchenko [2013] optimised the mass of a steel wind turbine tower subject to operational and survival loading conditions and a series of performance constraints. The rotor diameter and tower height were both design variables in this work.

Studies have been carried out into assessing which forms of objective function perform best in terms of wind turbine optimisation. Objectives used in the literature include structural measures such as maximising stiffness or minimising vibrations (Colherinhas et al. [2016], Negm and Maalawi [2000]), minimisation of mass or construction cost (Fylling and Berthelsen [2011]), maximisation of Annual Energy Production (AEP) (Zahle et al. [2015]) or some combination of these objectives.

In terms of mathematically optimising the solution in a domain of feasible solutions, engineers have used a number of optimisation algorithms. Both evolutionary methods and traditional methods have been used either in isolation or within a hybrid approach to initially establish a 'near-global' optimum using one algorithm and then refining the solution using a second. Evolutionary algorithms have been used extensively in the literature (Karpat [2013],Kusiak et al. [2010]). Gradient descent methods have been used successfully elsewhere (Ashuri et al. [2014]) in the optimisation of Cost of Energy, however this requires generalisation of objective and constraint functions to allow for differentiation which is not always possible.

One common feature in terms of optimising the structural or aerodynamic performance

of any element has been the need to assess the performance of selected points in the search space by using some nested tool, for example a finite element analysis tool. Lee et al. [2016] optimised the topology of a jacket foundation of an offshore wind turbine by using a nested finite element step. Yang and Zhu [2015] studied the probabilistic optimisation, again of an offshore foundation, using metamodels and evolutionary algorithms. A critical simplification which is often imposed is that loadings imposed on these nested models are applied statically, such that the assessment of a search point's fitness against constraints (such as stress or displacement) can be achieved in a computationally acceptable manner. Wind turbine towers have been optimised in the literature by imposing static rotor loading and tower wind loading (Lagaros and Karlaftis [2015]). This has the effect of potentially underestimating the dynamic deformation of the tower which can result from interaction of the tower with the coupled rotor, as well as removing any time-history loading information from the optimisation routine which is required to assess fatigue damage accumulation.

2.7 Wind Turbine Tower Design

In terms of the design of wind turbine towers including hybrid concrete-steel towers, designers must account for a wide range of actions and ensure structural capacities can sustain all actions. What follows are the key design criteria.

2.7.1 Primary Design Situations

The primary force the tower must sustain is lateral bending. Bending will occur during operation as a result of drag forces acting on the blades and these forces coupled with the inertial forces of the vibrating blades are then transferred to the top of the tower. In addition, wind will create a drag force on the tower itself over the height of the tower. This condition is known as a normal operating condition, and is included in IEC 61400-1 (International Electrotechnical Commission [2005]) as one of a number of 'Power Production' design situations. In the event of cut-out wind speed being reached,

the blades will cease to attract any drag force and so this thrust will become negligible at the top of the tower. This design situation is referred to as 'Shutdown'. Although thrust from the rotor has been eliminated in this case, there will be a marked increase in the drag created over the height of the tower as a result of the high wind speeds, with the result being a lateral load and bending moment of similar scale to that created during operating conditions.

2.7.2 Global Design Criteria

Global design criteria include the global buckling strength of the tower, the free vibration properties of the tower and overall displacement and rotation. Global buckling failure has occur as a result of exceeding the permissible axial or lateral load of the tower and is seen as a severe failure mechanism, resulting in the collapse of the tower. Authors have studied buckling based on numerical models and on physical tower failures in the literature (Chen et al. [2015],Guo et al. [2011]). There are examples of this failure occurring as a direct result of typhoon wind speeds acting on the tower alone, with rotor blades having been pitched to avoid any lift or drag.

Free vibration properties include the natural frequencies and mode shapes of the global tower structure. In order to avoid resonance, there must be adequate separation between the natural frequencies of the tower and those of other components as well as the frequencies of load application. The free vibration properties are gathered through carrying out an Eigenanalysis of the tower structure, including the mass placed on top from the nacelle and rotor. In practical terms, designers will initially seek to ensure that the fundamental frequency is sufficiently removed from the $1P$ and $3P$ frequencies of the rotation of the overall rotor and individual blade respectively. Mode shapes of the towers are often utilised in dynamic simulations where modal analysis is undertaken.

Tower top displacement is another important design criteria to be met. Historically, displacement would have been found by applying a static load to the top of the tower in a numerical model and applying some dynamic amplification factor to find the equiv-

alent dynamic displacement. Given the established dynamic coupling effect between the blades and the tower (Murtagh et al. [2005]), modern tall towers are analysed in a dynamic simulation model with the result that more accurate dynamic displacements are generated. It is important to limit the lateral displacement at the top of the tower primarily to avoid contact between the rotating blades and the face of the tower. Although IEC 61400-1 does not limit the amount of displacement which can occur, an established limit of height/100 has been used.

2.7.3 Local Design Criteria

Local design criteria include local stresses and strains, local buckling, local fatigue damage estimates and in the case of multi-member towers such as lattice towers, local free vibration and response properties. Stresses and strains will be incurred in the structure as it deforms in response to applied forces. Lateral bending of the tower will lead to tensile and compressive stresses on opposing sides of the tower over its height. Torsion transferred at the connection to the yawing mechanism will also lead to a torsional stress within the tower. Stresses in many different directions must be taken and transformed into principal stresses. In the case of a homogenous material such as steel, operating in its linear elastic region, stresses can be transformed into a single stress entity by using various hypotheses such as the Von Mises hypothesis. In the case of reinforced or prestressed concrete, stresses must be considered in perpendicular directions given the structures heterogeneous nature. Areas particularly susceptible to high stress concentrations are areas around doors and connections.

Local buckling can occur where a local member or shell element experiences a level of stress in excess of its buckling capacity, which may also be below its yield capacity. In the case of a tubular steel tower, local buckling can occur within the shell in regions between ring stiffeners, given the high length to thickness ratios present within the plates. In the case of concrete, this length to thickness ratio is greatly reduced with the result that local buckling will not occur. Lattice towers with many members can

experience local buckling given the use of members with high slenderness ratios.

Fatigue damage will occur over the lifetime of the tower given the high number of oscillations the tower will experience. Locally sensitive areas include those which experience high stress levels such as around doors and in the region of section connections. Fatigue damage can lead to the formation of cracks which can propagate and result in a global failure if not detected locally. Wind turbines are typically designed to achieve a twenty year lifespan as minimum and as such, each component must achieve this lifespan prior to failure as a result of fatigue damage.

Local free vibration properties are important in the case of lattice towers. In the same way as high slenderness ratios will increase sensitivity to local buckling of members, this characteristic can also lead to local resonance if local member frequencies coincide with other structural or forcing function frequency.

2.8 Hybrid Concrete-Steel Towers

Given the established engineering practice of using concrete in forming industrial chimneys, this has lead engineers to study the practicalities and nuances present in adopting concrete into the tower design. Concrete provides a relatively thick shell which in turn leads to improvements in the local and global stiffness of the tower structure. Given its heightened structural damping properties, it will offer inherent damping in ambient operational vibrations. Any improvement in stiffness or improvement in vibration suppression can be seen to benefit the entire assembly as the reduced peak vibrations will not only improve the fatigue life and stress level of the tower but also of any connected vibrating elements within the turbine assembly. Concrete can be either poured on site or fabricated using precast elements and so addresses transportation difficulties as compared to steel.

Recent publications have studied the emergence of hybrid towers as a conceptual solution in applications where tall wind turbines are desired (Agbayani and Vega [2012],

Figure 2.11: ATS Hybrid Concrete-Steel Tower

(Tricklebank et al. [2007], Lanier [2005]). Many of the above advantages offered by concrete as a partial replacement for steel in the lower section of the tower are cited by these authors. A report by LaNier (Lanier [2005]) was prepared on behalf of the National Renewable Energy Laboratory (NREL) in the US as a study of the cost competitiveness of hybrid towers, particularly in locations of low wind speed (mean annual wind speed of 5.8m/s at 10m). The authors designed hybrid towers for rated turbine capacities of 1.5MW, 3.6MW and 5.0MW but also designed fully concrete and fully steel options for each machine. For the 1.5MW machine, the authors found the cost of the three types were within 33% of each other. For the 3.6MW machine and the 5MW machine, the hybrid towers were found to be significantly more expensive than the other options. In the case of each rated machine, the fully concrete (cast in-situ) towers were the most cost-effective. The 1.5MW towers were more economical than the larger machines in terms of absolute costs, whereas in terms of cost per kW, the 3.6MW and 5.0MW concrete towers were said to be more effective.

Analyses of hybrid towers was carried out by Lee et al. [2010] with a view to establishing an optimum hybrid interface level when considering the initial capital cost of the tower. A Finite Element Analysis (FEA) is carried out including modal, buckling and static analysis for a series of 100m high hybrid towers.

Brughuis [2006] carried out a study which accounted for the cost of hybrid towers and drew comparisons against steel towers of the same height. It was found that hybrid towers become more economical than steel towers in terms of the Cost of Energy associated with the towers, from a height of 90m. Transportation costs were included in the Cost of Energy calculations and this was found to affect the results. At sites in India and the US, where transportation costs of steel are significant, hybrid tower fitness proved better than where transportation costs were lower.

Quilligan et al. [2012] studied the performance of concrete and steel towers from the point of view of fragility analyses. The performance of steel and concrete towers at different hub heights is presented through the use of fragility curves, based on response

time histories of the tower top displacement when turbines are subjected to turbulent, coherent wind fields. Fragility curves are given which show the probability of any peak tower top displacement exceeding an imposed limit level. The steel towers display consistently higher probability of limit state exceedance.

Other literature has also been published to investigate the performance of concrete wind turbine towers (Harte and Van Zijl [2007], BI et al. [2011]). Harte and Van Zijl [2007] presented the key criteria of tower frequency placement relative to other dominant component and loading frequencies as well as the difference in assessing concrete fatigue life compared to steel fatigue life. BI et al. [2011] presented a study of the performance of prestressed concrete towers when excited seismically. A door was included in the model to assess its affect on dynamic performance and the authors found this effect to be minimal.

Work has been published which examines the performance of high strength cementitious materials and the implications of their use in hybrid tower configurations (Wu et al. [2013]). Compressive strengths of $200N/mm^2$ were said to be possible from these materials. The authors propose their use in tall wind turbine towers. The authors carry out some numerical modelling to assess the performance of different thicknesses over the height of the tower and include recommendations for future limitations on shell thickness in design standards.

An example of a hybrid concrete-steel tower is given in Figure 2.11, provided by Dywidag (Dywidag Systems International). This tower is supplied by Dutch companies MECAL Engineering and HURKS BETON have developed this design, consisting of a 74m tall lower concrete section and 55m tall steel section.

Chapter 3

Wind Turbine Towers - Numerical and Analytical Models

3.1 Introduction

This chapter proposes to describe a number of structural models which can be used to represent a hybrid wind turbine tower in isolation. Models of the tower structure are to be presented in a number of different formulations, all of which can be used to examine free and forced vibrations of such a structure.

3.2 Closed Form Analytical Model

3.2.1 Transverse Vibrations of Uniform Beam Element

A uniform beam consisting of homogenous, isotropic, linear elastic material is presented here. The well-known governing partial differential equation of motion of a beam ele-

ment, sometimes known as the Euler-Bernoulli differential equation, is given as

$$\frac{\partial^2}{\partial z^2}\left(EI(z)\frac{\partial^2 u(z,t)}{\partial z^2}\right) + \rho(z)A(z)\frac{\partial^2 u(z,t)}{\partial t^2} = r(z,t) \tag{3.1}$$

In the case of uniform beam elements, where free vibration only is under consideration such that there is no externally applied load, Eq. 3.1 can be simplified to a fourth order homogeneous equation, with flexural rigidity and mass density distribution held constant

$$EI\frac{\partial^4 u(z,t)}{\partial z^4} + \rho A\frac{\partial^2 u(z,t)}{\partial t^2} = 0 \tag{3.2}$$

The unknown transverse displacement in Eq. 3.2 is said to vary both spatially and temporally. Assuming that the shape of vibration will be harmonic, it is possible to re-write Eq. 3.2 such that the transverse displacement varies only in space, transforming it from a Partial Differential Equation (PDE) to an Ordinary Differential Equation (ODE). This method is known as the separation of variables and has been used in a number of works (Auciello [1996], Posiadała [1997], Naguleswaran [2002]).

$$u(z,t) = \phi(z)e^{-i\omega t} \tag{3.3}$$

In Eq. 3.3, $\phi(z)$ is a function of z alone so refers to the spatially varying shape of vibration. The resulting ODE can be manipulated such as to arrive at a special form of second order ODE which has a known, general solution as per Eq. 3.4

$$EI\frac{d^4\phi(z)}{dz^4} - \rho A\omega^2\phi(z) = 0 \tag{3.4}$$

$$\frac{d^4\phi(z)}{dz^4} - \beta^4\phi(z) = 0 \tag{3.5}$$

Where, the non-dimensional term β is defined as

$$\beta^4 = \frac{\rho A\omega^2}{EI} \tag{3.6}$$

The general solution to Eq. 3.5 reads

$$\phi_n(z) = C_1\cosh(\beta_n z) + C_2\sinh(\beta_n z) + C_3\cos(\beta_n z) + C_4\sin(\beta_n z) \tag{3.7}$$

This equation includes four unknown constants, $C_1 - C_4$. Using known boundary conditions at points along the beam, it is possible to determine the unknowns in this equation and plot mode shapes. Typical mode shape plots are provided in Appendix E. It is also possible to show that non-trivial solutions exist only if

$$\cosh(\beta_n L)\cos(\beta_n L) + 1 = 0 \tag{3.8}$$

This transcendental equation can then be solved numerically to give the roots $\beta_1 L = 1.875, \beta_2 L = 4.694....$ From this, circular frequencies are found from

$$\omega_n = \beta_n^2\sqrt{\frac{EI}{\rho A}} \tag{3.9}$$

3.2.2 Transverse Vibrations of a Hybrid Tower with Lumped Mass

3.2.2.1 Introduction

In the literature there is an extensive amount of work in the area of proposing exact solutions to practical vibration problems involving flexible structural members. These problems typically included the introduction of some variance in terms of support condition, variation of profile or rigidity over its length or additional imposed mass attachments or externally applied loading in the preparation of solutions and review of resulting vibrations.

Authors have presented work on the subject of variable cross sectional area, rigidity and mass over the length of a beam. Kirchhoff et al. [1879] presented a seminal paper in 1879 which gave the solution to the motion of a particular form of tapered beam using Bessel Functions to solve the governing ordinary differential equations (ODEs). Other authors have since extended this work using other methods to solve the ODEs including Frebonious method, (Naguleswaran [1994]) and the Feldholm integral equation, (Huang and Li [2010]). Approximate methods were also presented for beams of variable profile, rigidity or mass in the form of Rayleigh-Ritz formulations (Klein [1974]).

Authors have considered the attachment of additional masses in the vibration of beams (Auciello [1996], Posiadała [1997]). In these cases, authors have made use of kinetic and potential energy expressions to find exact solutions for natural frequencies.

Authors have also considered the motion of beams consisting of two connected but distinctly different elements. Auciello and Ercolano [1997] considered a beam a part of which was uniform in profile and a part of which was tapered. Uściłowska and Kołodziej [1998] presented a solution for the free vibration of a column which was partially immersed in water, describing the motion using two connected uniform beam elements with continuity enforced through the applied boundary conditions at the interface.

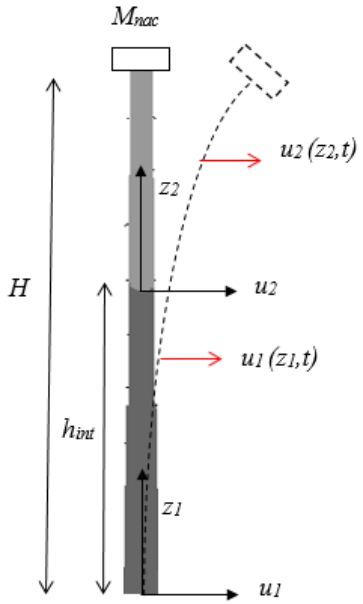

Figure 3.1: Closed Form Model - Displacement/Axes Convention

Specifically in terms of wind turbine towers, authors have presented solutions to describe their free vibration properties in closed form in recent years. Murtagh et al. [2004] described a lattice tower with mass on top. Adhikari and Bhattacharya [2012] provided a solution to a tower with an applied axial force, tower top mass, uniform cross section and also a spring rather than fixed base connection. A simple equation was provided by van der Tempel and Molenaar [2002] to find the natural frequency of a uniform tower with lumped mass on top to represent the nacelle.

3.2.2.2 Governing Equations & Transformation

A closed form solution is developed here on the basis of a hybrid tower with two uniform tower sections, one of concrete and one of steel, with an elevated lumped mass at the top of the tower to represent the nacelle and hub. The interface height between the steel and concrete segments will be a variable within the resulting expression. A schematic for this model is presented in Figure 3.1. Based on the co-ordinate system presented, two governing equations can be written to describe the motion of each portion of the

tower.

$$\frac{d^4u_1}{dz_1^4} - \beta^4 u_1 = 0 \qquad 0 \leq z_1 \leq h_{\text{int}} \tag{3.10}$$

$$\frac{d^4u_2}{dz_2^4} - \alpha^4 u_2 = 0 \qquad 0 \leq z_2 \leq H - h_{\text{int}} \tag{3.11}$$

In Eqs. 3.10 and 3.11, the terms α and β are co-efficients defined as per Eqs. 3.12 and 3.13,

$$\beta^4 = \frac{\rho_c A_c \omega^2}{E_c I_c} \tag{3.12}$$

$$\alpha^4 = \frac{\rho_s A_s \omega^2}{E_s I_s} \tag{3.13}$$

Having established these equations, the next step is to introduce some dimensionless quantities which can be used to normalise the lengths of both the concrete and the steel segments of the tower, thus allowing for the direct differentiation of terms within the general solutions for displacement which are expressed in terms of segment length.

$$\xi = \frac{z_1}{h_{\text{int}}} \qquad 0 < \xi < 1 \tag{3.14}$$

$$\eta = \frac{z_2}{H - h_{\text{int}}} \qquad 0 < \eta < 1 \tag{3.15}$$

Using these expressions and the Chain Rule, Eq 3.10 and Eq 3.11 can be transformed

as follows to create ODEs which are functions of the dimensionless quantities ξ and η.

$$\frac{\partial^4 u_1}{\partial z_1^4} = \frac{\partial^4 u_1}{\partial \xi^4}\left(\frac{\partial \xi}{\partial z_1}\right)^4 + 6\frac{\partial^3 u_1}{\partial \xi^3}\left(\frac{\partial \xi}{\partial z_1}\right)^2\frac{\partial^2 \xi}{\partial z_1^2} + \frac{\partial^2 u_1}{\partial \xi^2}\left(4\frac{\partial \xi}{\partial z_1}\frac{\partial^3 \xi}{\partial z_1^3} + 3\left(\frac{\partial^2 \xi}{\partial z_1^2}\right)^2\right) + \frac{\partial u_1}{\partial \xi}\frac{\partial^4 \xi}{\partial z_1^4} \tag{3.16}$$

Eq. 3.16 reduces to Eq. 3.17 on introduction of derivatives $\frac{\partial \xi}{\partial z_1}, \frac{\partial^2 \xi}{\partial z_1^2}$ and higher derivatives.

$$\frac{\partial^4 u_1}{\partial z_1^4} = \frac{\partial^4 u_1}{\partial \xi^4}\left(\frac{1}{h_{\text{int}}}\right)^4 \tag{3.17}$$

Thus the dimensionless ODEs read

$$\left(\frac{1}{h_{\text{int}}}\right)^4 \frac{d^4 u_1}{d\xi^4} - \beta^* u_1 = 0 \tag{3.18}$$

$$\left(\frac{1}{H - h_{\text{int}}}\right)^4 \frac{d^4 u_2}{d\eta^4} - \alpha^* u_2 = 0 \tag{3.19}$$

where

$$\beta^{*4} = \frac{\rho_c A_c \omega^2}{E_c I_c} h_{\text{int}}^4 \tag{3.20}$$

$$\alpha^{*4} = \frac{\rho_s A_s \omega^2}{E_s I_s}(H - h_{\text{int}})^4 \tag{3.21}$$

General solutions to Eq 3.20 and Eq 3.21 are written as

$$u_1(\xi) = C_1 \cosh(\beta^* \xi) + C_2 \sinh(\beta^* \xi) + C_3 \cos(\beta^* \xi) + C_4 \sin(\beta^* \xi) \tag{3.22}$$

$$u_2(\eta) = C_5\cosh(\alpha^*\eta) + C_6\sinh(\alpha^*\eta) + C_7\cos(\alpha^*\eta) + C_8\sin(\alpha^*\eta) \tag{3.23}$$

3.2.2.3 Boundary & Continuity Conditions

Eq. 3.22 and Eq. 3.23 describe the displaced shape of each section of the tower in terms of the circular frequency and unknown constants of integration. In order to progress to a solution of the unknowns, the boundary and continuity conditions can be applied which will enforce the known properties in terms of the mode shape and various derivatives of the shape, at the base of the tower, hybrid interface location and tower top. There are two boundary conditions for the base of the tower, which are given in Eq. 3.24 .

$$\begin{aligned} u_1(0) &= 0 \\ \frac{du_1(0)}{d\xi} &= 0 \end{aligned} \tag{3.24}$$

There are four continuity conditions which exist at the hybrid interface height accounting for continuity in shape, rotation, moment and shear force across this connection. These are given in Eq. 3.25.

$$\begin{aligned} u_1(1) &= u_2(0) \\ \frac{du_1(1)}{d\xi} &= \frac{du_2(0)}{d\eta} \\ -E_cI_c\frac{d^2u_1(1)}{d\xi^2} &= -E_sI_s\frac{d^2u_2(0)}{d\eta^2} \\ -E_cI_c\frac{d^3u_1(1)}{d\xi^3} &= -E_sI_s\frac{d^3u_2(0)}{d\eta^3} \end{aligned} \tag{3.25}$$

In order to enforce the application of mass at the top of the tower in terms of the transverse vibration, an applied shear force is imposed instead of the normal assumption of zero shear force at a cantilever free end. The shear force is equal to the mass of the nacelle times the acceleration of the tower at this location. The two tower top boundary equations are given in Eq. 3.26. Figure 3.2 indicates the boundary conditions and

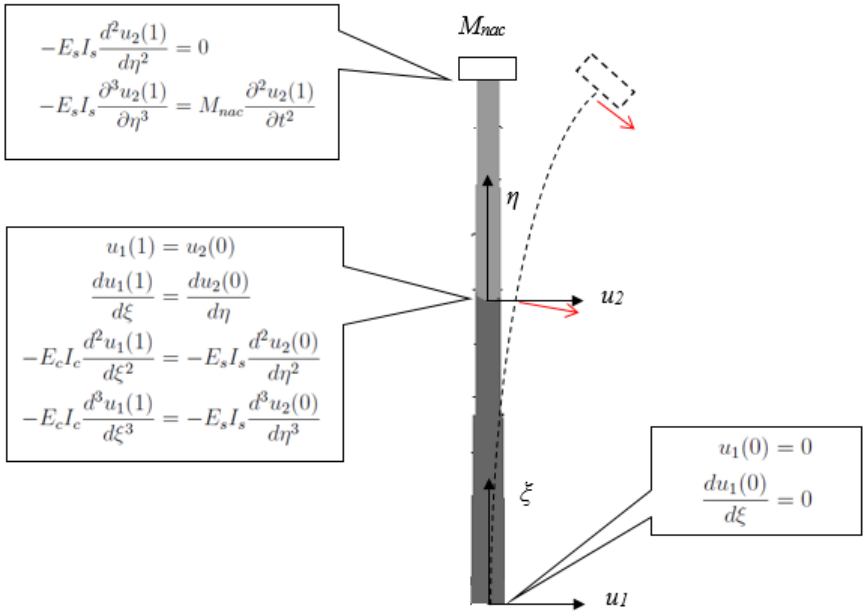

Figure 3.2: Closed Form Model - Boundary Conditions

locations.

$$\begin{aligned} -E_sI_s\frac{d^2u_2(1)}{d\eta^2} &= 0 \\ -E_sI_s\frac{\partial^3u_2(1)}{\partial\eta^3} &= M_{\text{nac}}\frac{\partial^2u_2(1)}{\partial t^2} \end{aligned} \tag{3.26}$$

Eq. 3.26 is a PDE which contains terms which vary both temporally and spatially. The right hand side of this expression can be transformed to be a function of space only using the method of seperation of variables as follows in Eq. 3.27.

$$M_{\text{nac}}\frac{\partial^2\phi(z)}{\partial t^2} = M_{\text{nac}}\omega^2\phi(z) \tag{3.27}$$

Thus

$$-E_sI_s\frac{\partial^3u_2}{\partial\eta^3}(1) = M_{\text{nac}}\omega^2u_2(1) \tag{3.28}$$

3.2.2.4 Transcendental Equations

After applying the boundary conditions at the base of the tower, it is possible to find that $C_1 = -C_3$ and $C_2 = -C_4$. By applying all other boundary and continuity conditions, it is possible to collect the constant terms and realise the following equation,

$$[A]\{C\} = 0 \qquad \{C\}^T = \begin{bmatrix} C_1 & C_2 & C_5 & \cdots & C_8 \end{bmatrix} \tag{3.29}$$

It is noted that there is now one unknown quantity, β, which has an infinite number of possible solutions, all of which are valid roots of this expression. The matrix, $[A]$ is given as

$$\begin{bmatrix} (\cosh(\beta^*) - \cos(\beta^*)) & (\sinh(\beta^*) - \sin(\beta^*)) & -1 & 0 & -1 & 0 \\ (\sinh(\beta^*) + \sin(\beta^*)) & (\cosh(\beta^*) - \cos(\beta^*)) & 0 & -c_1 & 0 & -c_1 \\ (\cosh(\beta^*) + \cos(\beta^*)) & (\sinh(\beta^*) + \sin(\beta^*)) & -c_1^2 c_2 & 0 & c_1^2 c_2 & 0 \\ (\sinh(\beta^*) - \sin(\beta^*)) & (\cosh(\beta^*) + \cos(\beta^*)) & 0 & -c_1^3 c_2 & 0 & c_1^3 c_2 \\ 0 & 0 & \cosh(c_3) & \sinh(c_3) & -\cos(c_3) & -\sin(c_3) \\ 0 & 0 & c_5 & c_6 & c_7 & c_8 \end{bmatrix} \tag{3.30}$$

In order for there to be a non-trivial solution to this expression, the determinant of the matrix shown must equate to zero. In Linear Algebra, this expression is often written as

$$[A]\{C\} = 0, \qquad [A] \neq 0 \tag{3.31}$$

Co-efficient terms c_1 to c_8 are listed as follows.

$$c_1 = \left(\frac{E_c I_c}{\rho_c A_c} \times \frac{\rho_s A_s}{E_s I_s} \right)^{\frac{1}{4}} \tag{3.32}$$

$$c_2 = \frac{E_s I_s}{E_c I_c} \tag{3.33}$$

$$c_3 = \beta^* \frac{H - h_{\text{int}}}{h_{\text{int}}} c_1 \tag{3.34}$$

$$c_4 = \frac{M_{\text{nac}} c_3}{\rho_s A_s (H - h_{\text{int}})} \tag{3.35}$$

$$c_5 = -\sinh(c_3) - c_4 \cosh(c_3) \tag{3.36}$$

$$c_6 = -\cosh(c_3) - c_4 \sinh(c_3) \tag{3.37}$$

$$c_7 = -\sin(c_3) - c_4 \cos(c_3) \tag{3.38}$$

$$c_8 = \cos(c_3) - c_4 \sin(c_3) \tag{3.39}$$

It can be seen from Eq 3.26 that the mass of the nacelle is accounted for by its inclusion within the boundary conditions, rather than explicitly including it in the equation of motion. This is a simplification of sorts and does not account for the fact that the nacelle will impart an axial force as well as a shear force. The effects of this axial force on the free vibration properties is expected to be minimal in comparison to the effects of the shear force and so is ignored.

Having solved for the unknown quantity β from Eq. 3.30, it is possible to solve for the

circular frequencies and the unknown constants of integration C_1 to C_8. There are an infinite number of roots to these equations and so each solution, β_n is associated with an n^{th} circular frequency of the hybrid tower, ω_n.

3.2.2.5 Evaluation of Mode Shapes

Mode shapes corresponding to each natural frequency of the hybrid tower, ω_n, can be found by finding solutions to the constants of integration, C_1 to C_8 and by then solving Eqs. 3.22 and 3.23. Work in this area has been carried out by authors such as Mao [2011] and Naguleswaran [2002]. Naguleswaran [2002] presented a work providing the mode shapes of a beam with a single step in distributed properties. The author used a technique of applying the known boundary conditions to express certain constants of integration in terms of others and then imposed a unit displacement to each mode shape at the location of the step in properties. The author noted this does not lead to any loss in generality. The same technique is adopted in this section, using the characteristic equations written in Eqs. 3.24 to 3.26.

By considering the two boundary conditions at the base of the tower and the four continuity equations at the interface location, it is possible to write the following equations.

$$\begin{aligned}
&C_1\Big(\cosh(\beta^*)-\cos(\beta^*)\Big)+C_2\Big(\sinh(\beta^*)-\sin(\beta^*)\Big)-C_5-C_7=0\\
&C_1\Big(\sinh(\beta^*)+\sin(\beta^*)\Big)+C_2\Big(\cosh(\beta^*)-\cos(\beta^*)\Big)-c_1C_6-c_1C_8=0\\
&C_1\Big(\cosh(\beta^*)+\cos(\beta^*)\Big)+C_2\Big(\sinh(\beta^*)+\sin(\beta^*)\Big)-c_1^2c_2C_5+c_1^2c_2C_7=0\\
&C_1\Big(\sinh(\beta^*)-\sin(\beta^*)\Big)+C_2\Big(\cosh(\beta^*)+\cos(\beta^*)\Big)-c_1^3c_2C_6+c_1^3c_2C_8=0
\end{aligned} \tag{3.40}$$

Through a linear combination of the first and third expression within Eq. 3.40, constant C_7 can be eliminated to find an expression for C_5 alone. The same can be achieved in the case of finding an expression for C_7. The second and fourth expressions may be

combined to find equations for C_6 and C_8. These formulations are given in Eq. 3.41.

$$\begin{aligned}
C_5 &= C_1\left(\frac{c_{10}}{2} + \frac{c_{12}}{2c_1^2c_2}\right) + C_2\left(\frac{c_{11}}{2} + \frac{c_{13}}{2c_1^2c_2}\right) \\
C_6 &= C_1\left(\frac{c_{13}}{2c_1} + \frac{c_{11}}{2c_1^3c_2}\right) + C_2\left(\frac{c_{10}}{2c_1} + \frac{c_{12}}{2c_1^3c_2}\right) \\
C_7 &= C_1\left(\frac{c_{10}}{2} - \frac{c_{12}}{2c_1^2c_2}\right) + C_2\left(\frac{c_{11}}{2} - \frac{c_{13}}{2c_1^2c_2}\right) \\
C_8 &= C_1\left(\frac{c_{13}}{2c_1} - \frac{c_{11}}{2c_1^3c_2}\right) + C_2\left(\frac{c_{10}}{2c_1} - \frac{c_{12}}{2c_1^3c_2}\right)
\end{aligned} \tag{3.41}$$

The terms c_{10} to c_{13} introduced above are given as the following trigonometric functions

$$\begin{aligned}
c_{10} &= \cosh(\beta^*) - \cos(\beta^*) \\
c_{11} &= \sinh(\beta^*) - sin(\beta^*) \\
c_{12} &= \cosh(\beta^*) + \cos(\beta^*) \\
c_{13} &= \sinh(\beta^*) + \sin(\beta^*)
\end{aligned} \tag{3.42}$$

Eq. 3.41 can be re-written in shortened form as

$$\begin{aligned}
C_5 &= C_1c_{20} + C_2c_{21} \\
C_6 &= C_1c_{22} + C_2c_{23} \\
C_7 &= C_1c_{24} + C_2c_{25} \\
C_8 &= C_1c_{26} + C_2c_{27}
\end{aligned} \tag{3.43}$$

Eqns 3.22 and 3.23 can now be re-written in terms of C_1 and C_2 to describe the shape of both the concrete and the steel sections of the tower, u_1 and u_2.

$$u_1(\beta^*\xi) = C_1c_{10}(\beta^*\xi) + C_2c_{11}(\beta^*\xi) \tag{3.44}$$

$$
\begin{aligned}
u_2(\alpha^*\eta) &= C_5\cosh(\alpha^*\eta) + C_6\sinh(\alpha^*\eta) + C_7\cos(\alpha^*\eta) + C_8\sin(\alpha^*\eta) \\
&= \Big(C_1c_{20} + C_2c_{21}\Big)\cosh(\alpha^*\eta) + \Big(C_1c_{22} + C_2c_{23}\Big)\cos(\alpha^*\eta)\cdots \\
&+ \Big(C_1c_{24} + C_2c_{25}\Big)\sinh(\alpha^*\eta) + \Big(C_1c_{26} + C_2c_{27}\Big)\sin(\alpha^*\eta) \\
&= C_1\Big(c_{20}\cosh(\alpha^*\eta) + c_{22}\cos(\alpha^*\eta) + c_{24}\sinh(\alpha^*\eta) + c_{26}\sin(\alpha^*\eta)\Big)\cdots \\
&+ C_2\Big(c_{21}\cosh(\alpha^*\eta) + c_{23}\cos(\alpha^*\eta) + c_{25}\sinh(\alpha^*\eta) + c_{27}\sin(\alpha^*\eta)\Big)
\end{aligned}
\tag{3.45}
$$

In order to solve for the final remaining constants of integration, C_1 and C_2, two equations with two unknowns can be written, which will enforce known properties of both sections of the tower. For the lower concrete section, the mode shape given in Eq. 3.44 is taken and the magnitude of the mode shape at the interface height ($\xi = 1$) is set to unity. For the upper section of the tower, the bending moment is set to zero at ($\eta = 1$). Thus the following equations are written in terms of C_1 and C_2.

$$
C_1c_{10} + C_2c_{11} = 1 \tag{3.46}
$$

$$
\begin{aligned}
&C_5\cosh(c_3\eta) + C_6\sinh(c_3\eta) - C_7\cos(c_3\eta) - C_8\sin(c_3\eta) = 0 \\
&\therefore \Big(C_1c_{20} + C_2c_{21}\Big)\cosh(c_3\eta) - \Big(C_1c_{22} + C_2c_{23}\Big)\cos(c_3\eta) \\
&+ \Big(C_1c_{24} + C_2c_{25}\Big)\sinh(c_3\eta) - \Big(C_1c_{26} + C_2c_{27}\Big)\sin(c_3\eta) = 0 \\
&\therefore C_1\Big(c_{20}\cosh(c_3\eta) - c_{22}\cos(c_3\eta) + c_{24}\sinh(c_3\eta) - c_{26}\sin(c_3\eta)\Big) \\
&+ C_2\Big(c_{21}\cosh(c_3\eta) - c_{23}\cos(c_3\eta) + c_{25}\sinh(c_3\eta) - c_{27}\sin(c_3\eta)\Big) = 0
\end{aligned}
\tag{3.47}
$$

The terms c_{30} and c_{31} are used to represent the multipliers to C_1 and C_2 in the previous

equation,

$$\begin{aligned} c_{30} &= \Big(c_{20}\cosh(c_3\eta) - c_{22}\cos(c_3\eta) + c_{24}\sinh(c_3\eta) - c_{26}\sin(c_3\eta) \Big) \\ c_{31} &= \Big(c_{21}\cosh(c_3\eta) - c_{23}\cos(c_3\eta) + c_{25}\sinh(c_3\eta) - c_{27}\sin(c_3\eta) \Big) \end{aligned} \tag{3.48}$$

$$C_1 c_{30} + C_2 c_{31} = 0 \tag{3.49}$$

By combining Eqs. 3.46 and 3.49, values for C_1 and C_2 are written as

$$C_1 = \frac{1}{c_{11}\left(\frac{c_{10}}{c_{11}} - \frac{c_{30}}{c_{31}}\right)} \tag{3.50}$$

$$C_2 = \frac{1}{c_{10}\left(\frac{c_{11}}{c_{10}} - \frac{c_{31}}{c_{30}}\right)} \tag{3.51}$$

Figure 3.3 provides an example of mode shapes associated with the first and second natural frequency of a sample hybrid tower, with shapes found using the closed form expressions given above. Note the value of unity of each shape at the interface location of 60% of the beam length.

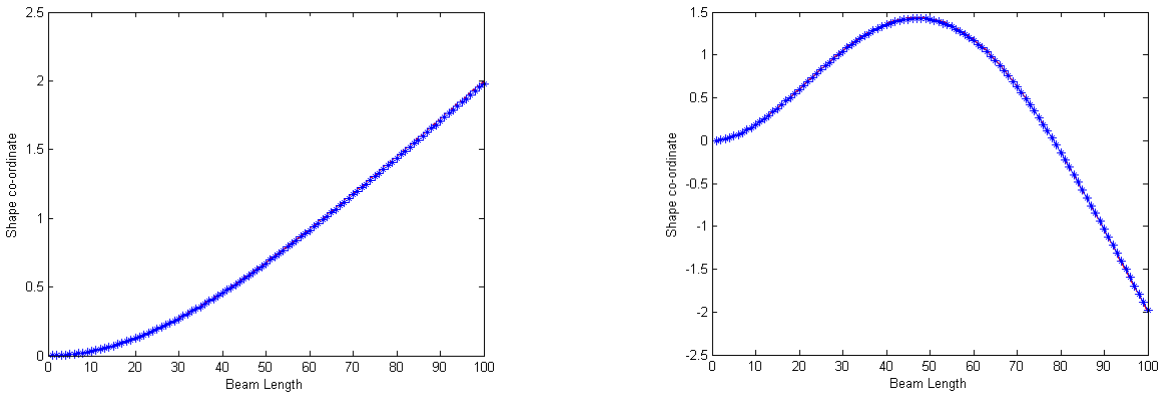

(a) 1^{st}ModeShape (b) 2^{nd}ModeShape

Figure 3.3: Closed Form Model - Sample Tower Modes Shapes

3.3 Global Beam (Modified Euler-Bernoulli) Finite Element Model

3.3.1 Introduction

Authors have proposed the use of finite element modelling in describing wind turbine towers in a number of works, specifically in terms of approximating the tower behaviour using beam finite elements. Yan et al. [2012] described a model of a wind turbine consisting of a tower and three blades which used beam elements to describe these components. Xiong et al. [2010] presented a model of a tower using the finite element method and Euler-Bernoulli beam elements. This was then used to find the free vibration properties of a 1MW wind turbine. A software code made available by the National Renewable Energy Laboratory (NREL) known as BModes, Bir [2005] uses beam elements within a finite element domain to calculate the free vibration properties of towers and blades in isolation.

Here, a Global Beam Finite Element (GBFE) model of a tower is proposed, consisting of beam elements with five degrees of freedom per node.

3.3.2 Beam Element Stiffness Matrix

In this section, the hybrid tower will be described using an approximation of the exact solution through the use of the finite element method (FEM). Euler-Bernoulli beam elements have been augmented such that the represent out-of-plane displacement and also rotational degrees of freedom along their longitudinal axes in two orthogonal directions. Each element node offers five degrees of freedom. The displacement vector for each element is given as $\{d\}$, as per Eq. 3.52.

$$\{d\}^T = [u_{1,X}, u_{1,Y}, \theta_{1,X}, \theta_{1,Y}, \theta_{1,Z}, u_{2,X}, u_{2,Y}, \theta_{2,X}, \theta_{2,Y}, \theta_{2,Z}] \tag{3.52}$$

The local stiffness matrix for the element is given in Eq. 3.53.

$$[k] = \frac{EI}{L^3} \begin{bmatrix} 12 & 0 & 0 & 6L & 0 & -12 & 0 & 0 & 6L & 0 \\ 0 & 12 & 6L & 0 & 0 & 0 & -12 & 6L & 0 & 0 \\ 0 & 6L & 4L^2 & 0 & 0 & 0 & -6L & 2L^2 & 0 & 0 \\ 6L & 0 & 0 & 4L^2 & 0 & -6L & 0 & 0 & 2L^2 & 0 \\ 0 & 0 & 0 & 0 & \frac{GJL^2}{EI} & 0 & 0 & 0 & 0 & -\frac{GJL^2}{EI} \\ -12 & 0 & 0 & -6L & 0 & 12 & 0 & 0 & -6L & 0 \\ 0 & -12 & -6L & 0 & 0 & 0 & 12 & -6L & 0 & 0 \\ 0 & 6L & 2L^2 & 0 & 0 & 0 & -6L & 4L^2 & 0 & 0 \\ 6L & 0 & 0 & 2L^2 & 0 & -6L & 0 & 0 & 4L^2 & 0 \\ 0 & 0 & 0 & 0 & -\frac{GJL^2}{EI} & 0 & 0 & 0 & 0 & \frac{GJL^2}{EI} \end{bmatrix} \tag{3.53}$$

3.3.3 Beam Element Mass Matrix

The local beam mass matrix for the element is given in Eq. 3.54.

$$[m] = \frac{\rho AL}{420}\begin{bmatrix} 156 & 0 & 0 & 22L & 0 & 54 & 0 & 0 & -13L & 0 \\ 0 & 155 & 22L & 0 & 0 & 0 & 54 & -13L & 0 & 0 \\ 0 & 22L & 4L^2 & 0 & 0 & 0 & 13L & -3L^2 & 0 & 0 \\ 22L & 0 & 0 & 4L^2 & 0 & 13L & 0 & 0 & -3L^2 & 0 \\ 0 & 0 & 0 & 0 & 2\Gamma_{tor} & 0 & 0 & 0 & 0 & \Gamma_{tor} \\ 54 & 0 & 0 & 13L & 0 & 156 & 0 & 0 & -22L & 0 \\ 0 & 54 & 13L & 0 & 0 & 0 & 156 & -22L & 0 & 0 \\ 0 & -13L & -3L^2 & 0 & 0 & 0 & -22L & 4L^2 & 0 & 0 \\ -13L & 0 & 0 & -3L^2 & 0 & -22L & 0 & 0 & 4L^2 & 0 \\ 0 & 0 & 0 & 0 & \Gamma_{tor} & 0 & 0 & 0 & 0 & 2\Gamma_{tor} \end{bmatrix} \tag{3.54}$$

The term Γ_{tor} defines the torsional entries and is defined as $\Gamma_{tor} = \frac{70(I_x+I_y)}{A}$. This matrix has been formed by combining the co-efficients of the Euler-Bernoulli beam element of 4 DOF which was derived in a consistent manner and adding torsional stiffness and mass inertia derived directly.

Although not part of the structural mass of the tower, it is important to account for the mass of the nacelle at the top of the tower as it will influence the free and forced vibration responses. In order to include this mass (M_{nac}) at the top of the tower, it can be considered as a lumped mass and directly summed to the relevant co-efficients ($u_{N,X}, u_{N,Y}$) at this node. The mass moment of inertia (I_{nac}) of the nacelle is assumed to be constant around each axis and is summed to rotational degrees of freedom ($\theta_{N,X}, \theta_{N,Y}$ and $\theta_{N,Z}$) co-efficients associated with this top node. Thus, the local element at the

top of the tower, $[m]_{N_{\text{els}}}$, is amended to incorporate this lumped mass as per Eq. 3.55.

$$[m]_{N_{\text{els}}} = [m]_{N_{\text{els}}} + \begin{bmatrix} [0]_{5\times5} & & [0]_{5\times5} & & \\ & \begin{bmatrix} M_{\text{nac}} & 0 & 0 & 0 & 0 \\ 0 & M_{\text{nac}} & 0 & 0 & 0 \\ 0 & 0 & I_{\text{nac}} & 0 & 0 \\ 0 & 0 & 0 & I_{\text{nac}} & 0 \\ 0 & 0 & 0 & 0 & I_{\text{nac}} \end{bmatrix} & \\ [0]_{5\times5} & & & & \end{bmatrix} \tag{3.55}$$

3.3.4 Global Matrix Assembly

The construction of global mass and stiffness matrices is required prior to carrying out free or forced vibration analyses on an overall tower. The steps involved in constructing the tower hybrid model using these beam elements such that global matrices are assembled include -

- Determine the number of local beam elements to be used to describe the tower and assign local lengths to each beam
- Split the tower into elements and assign global structural node numbers to each node
- Based on local element material and geometrical properties, establish local elemental matrices
- Populate global matrices with degree of freedom entries from local matrices

Each local matrix must first be expanded such that their elemental co-efficients are aligned with the global structure node numbers and associated degrees of freedom. The

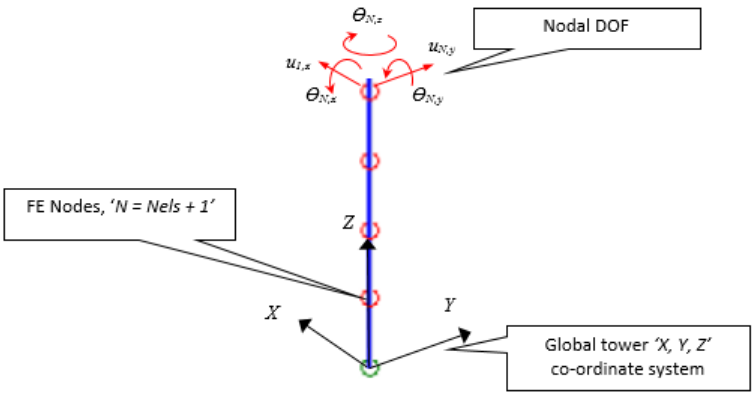

Figure 3.4: GBFE Tower Model - Axes and Nodal DOF

global structure displacement vector for a tower of N_{els} elements is given in Eq. 3.56.

$$\{D\}^T = [u_{1,X}, u_{1,Y}, \theta_{1,X}, \theta_{1,Y}, \theta_{1,Z}, u_{2,X}, \cdots, u_{N,Y}, \theta_{N,X}, \theta_{N,Y}, \theta_{N,Z}] \tag{3.56}$$

For a tower consisting of N_{els} elements, there will be $N = N_{\text{els}} + 1$ nodes and $5N$ DOF. A schematic for this model is provided in Figure 3.4 which also identifies the nodal degrees of freedom.

Assembling this global matrix requires superposition of entries of each local element matrix co-efficient into the global matrix, such that co-efficients associated with local nodes are assigned to their global node position. Once local elements have been transformed, they will each now be aligned with the global displacement vectors and so can be directly summed to find the global matrices, as outlined in Eqs. 3.57 and 3.58.

$$[K_{g,T}] \in \mathbb{R}^{5N \times 5N} = \sum_{i=1}^{N_{\text{els}}} [k] \tag{3.57}$$

$$[M_{g,T}] \in \mathbb{R}^{5N \times 5N} = \sum_{i=1}^{N_{\text{els}}} [m] \tag{3.58}$$

In the case of a model consisting of two beam elements ($N_{\text{els}} = 2$), there will be three nodes ($N = N_{\text{els}} + 1$) and thus $5N$ DOF. As a result the global matrices will each be of size $5N \times 5N$.

In order to generate a global damping matrix, $[C_{g,T}]$, Rayleigh damping may be used whereby the damping matrix is found to be a linear combination of the global stiffness and mass matrices and is frequency dependent. As such, a free vibration analysis of the tower must first be carried out to determine relevant frequencies.

$$[C_{g,T}] = a_0[M_{g,T}] + a_1[K_{g,T}] \tag{3.59}$$

In the same manner as the exact solution methodology, in order to solve for free or forced vibration properties, boundary conditions must be enforced on the model. For this tower, the conditions of zero displacement and zero rotation exist at the base of the structure. Refer to Appendix B for further details. In the FEM, these conditions are enforced numerically by assigning zero values to the known responses at the base of the tower.

3.4 Local Shell (Reissner-Mindlin) Finite Element Model

3.4.1 Introduction

Authors have used two dimensional elements to describe towers where the form of tower construction chosen is to be a tubular form. By making use of these types of elements, it is possible to create a continuous, densely discretised, three dimensional shell model of a tower, which offers distinct advantages over more simplistic beam-column type models.

Some of the benefits offered by shell element based models over beam element models include -

- Potential to extract local strains and stresses,
- Potential to incorporate initial stresses in shell structure,
- Potential to conduct local condition monitoring
- Incorporation of features such as opes and ring stiffeners,
- Potential to carry out local and global buckling analysis,
- Eigenanalyses leading to three dimensional modes of vibration,
- More accurate reflection of changing tower material and geometric profiles.

Lavassas et al. [2003] modelled a tower for a prototype tower which was 44m in height and used to support a 1MW turbine. The tower was modelled using 5208 4-noded quadrilateral elements and was used in vibration and stress analyses. In a similar way, Bazeos et al. [2002] described a wind turbine tower structure using 8-noded quadrilateral shell elements. The shell nature of the finite element model allowed the authors to study in detail the stresses present around door opes and also to determine stresses and free vibration properties. Local stresses around the door opening at the base of the tower were studied by Long and Wu [2012].

Hu et al. [2014] put forward a study on the effects of internal ring stiffeners and wall thickness on the response characteristics of towers at various heights. A steel tubular tower is studied using the FEM with the towers described as shell structures. Von Mises stress and displacement results are given for each tower configuration modelled.

Makarios et al. [2015] used three dimensional FE models of towers to study the torsional-translational responses. The authors cite a number of tower collapses which have been attributed to torsional effects. A continuous model method is used to simulate the structural response of the tower.

Shell models have been used in terms of condition monitoring in review of potential damage to local areas of the structure. Kenna and Basu [2015a] presented a technique

whereby strain signals were extracted from defined circumference locations from a shell model of a wind turbine tower and then processed using a Discrete Wavelet Transform (DWT) such that damage could be identified.

3.4.2 Reissner-Mindlin Shell Elements

The total potential energy within each shell element includes strain energy held within the body under consideration and the potential of all applied loads. The total strain energy held in a body is as follows

$$U = \frac{1}{2}\int \{\varepsilon\}^T [E]\{\varepsilon\} dV \tag{3.60}$$

By relating the strain to the displacement by way of a strain-displacement entity, $\{\varepsilon\} = [B]\{d\} = \partial[N]\{d\}$, Eq. 3.60 can be re-written as shown in Eq. 3.61. Reference is made to Appendix A for the derivation of the strain-displacement matrix in the case of a four node membrane element.

$$U = \frac{1}{2}\int \{d\}^T [B]^T [E]\{d\}[B] dV = \frac{1}{2}\{d\}^T [K]\{d\} \tag{3.61}$$

The elemental stiffness matrix, k is extracted from the elemental strain energy equation and reads

$$[k] = \int [B]^T [E][B] dV \tag{3.62}$$

The element form used in defining the tower continuum in this section is an isoparametric bilinear quadrilateral, with membrane and plate bending properties to give the element shell capabilities. A sketch of the membrane and plate elements combined to form the complete shell element is given in Figure 3.5. The membrane

part of the element accounts for the in-plane displacement degrees of freedom at each node, in the local x-y plane of the element. The vector of membrane degrees of freedom reads $\{d_m\}^T = [u_{1,x}, u_{1,y}, u_{2,x}, \cdots, u_{4,y}]$. As such, there are co-efficients for eight degrees of freedom defined for the membrane action. Part of the definition of a shell element is its ability to account for out-of-plane actions in addition to in-plane actions and as such, a Mindlin plate element is used to account for these actions and degrees of freedom. The associated vector of plate degrees of freedom reads $\{d_p\}^T = [u_{1,z}, \theta_{1,x}, \theta_{1,y}, u_{2,z}, \cdots, u_{4,z}, \theta_{4,x}, \theta_{4,y}]$. In total, there are 20 DOF per shell element on summation of these two components.

When the membrane and plate degrees of freedom are all incorporated, each shell element will have a displacement vector, $\{d\}$ as per Eq. 3.63.

$$\{d\}^T = [u_{1,x}, u_{1,y}, u_{1,z}, \theta_{1,x}, \theta_{1,y}, u_{2,x}, \cdots, u_{4,z}, \theta_{4,X}, \theta_{4,y}] \tag{3.63}$$

The element is referred to as being "bilinear" because of the nature of its shape functions, which are products of one dimensional linear polynomial functions. The complete displacement field for the element degrees of freedom, $\{u\} = [N]\{d\}$, is given as

$$\begin{Bmatrix} u_x \\ u_y \\ u_z \\ \theta_x \\ \theta_y \end{Bmatrix} = \begin{bmatrix} N_1 & 0 & 0 & 0 & 0 & N_2 & 0 & \cdots & 0 & 0 \\ 0 & N_1 & 0 & 0 & 0 & 0 & N_2 & \cdots & 0 & 0 \\ 0 & 0 & N_1 & 0 & 0 & 0 & 0 & \cdots & 0 & 0 \\ 0 & 0 & 0 & N_1 & 0 & 0 & 0 & \cdots & N_4 & 0 \\ 0 & 0 & 0 & 0 & N_1 & 0 & 0 & \cdots & 0 & N_4 \end{bmatrix} \begin{Bmatrix} u_{1,x} \\ u_{1,y} \\ u_{1,z} \\ \theta_{1,x} \\ \vdots \\ u_{4,z} \\ \theta_{4,x} \\ \theta_{4,y} \end{Bmatrix} \tag{3.64}$$

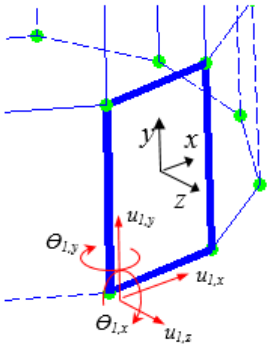

Figure 3.5: Local Shell Element - Axes and Nodal DOF

The shape functions themselves are given as

$$\begin{aligned} N_1 &= \frac{1}{4}(1-\xi)(1-\eta) \\ N_2 &= \frac{1}{4}(1+\xi)(1-\eta) \\ N_3 &= \frac{1}{4}(1+\xi)(1+\eta) \\ N_4 &= \frac{1}{4}(1-\xi)(1+\eta) \end{aligned} \tag{3.65}$$

3.4.3 Shell Element Stiffness Matrix

Eq. 3.62 is written in terms of a two dimensional element with a constant thickness t, as

$$[k] = t \iint [B]^T [E][B] dA \tag{3.66}$$

In order to integrate each element over its area, Gauss-quadrature numerical integration is used (see Appendix A), where the element is first mapped to a local co-ordinate system. The membrane part of the shell element stiffness matrix expressed in Cartesian co-ordinate space of x and y is transformed as

$$[k_m] = t \iint [B_m]^T [E_m][B_m] dx dy \tag{3.67}$$

This principle is outlined by Moaveni [2003], explaining numerical implementation of the finite element method. The subscript m here denotes the application to the membrane degrees of freedom of the element. In local co-ordinates, where it is mapped in ζ and η, the element stiffness matrix is

$$[k_m] = t \iint [B_m]^T [E_m][B_m] |J| d\xi d\eta \tag{3.68}$$

where J denotes the Jacobian matrix, used to transform derivatives of displacements with respect to x and y to those with respect of ξ and η (see Appendix A). Notwithstanding the requirement for transformation to a local axis system in order to numerically integrate, mapping the element to a local system with nodes at $\xi = +/\text{-}1$ and $\eta = +/\text{-}1$ also means that the element does not need to be rectangular and can take any quadrilateral shape. This suits the case of a tapered cylinder where elements will become truncated towards the top of the tower.

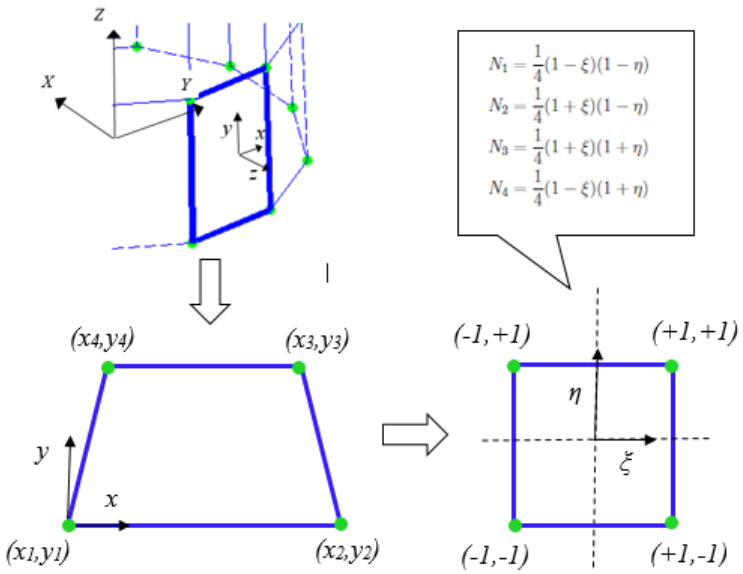

Figure 3.6: Local Shell Element - Co-ordinate Transformation

In terms of the plate part of the shell element stiffness matrix, the same form of integral is used to define this section of the element stiffness matrix as was used to define the membrane part. One important difference is that separate strain-displacement matrices need to be used for the bending and shear degrees of freedom.

The Mindlin plate stiffness matrix is thus defined as follows

$$[k_p] = t \iint [B_{pb}]^T [E_{pb}][B_{pb}]|J|d\xi d\eta + t \iint [B_{ps}]^T [E_{ps}][B_{ps}]|J|d\xi d\eta \tag{3.69}$$

where in Eq. 3.69, the subscripts *pb* and *ps* refer to bending and shear strain-displacement of the plate respectively. It is noted that although the strain-displacement matrices are slightly lengthier to set up, the same shape functions are used throughout to generate all membrane and plate co-efficients. Once the membrane and plate co-efficients are in place for each element, they are then combined to form the shell element elastic stiffness

matrix as follows.

$$[k] \in \mathbb{R}^{20\times 20} = [k_m] \oplus [k_p] = \begin{bmatrix} [k_m] & [0] \\ [0] & [k_p] \end{bmatrix} \tag{3.70}$$

Note that there are no coupling terms between the membrane and plate co-efficients in this matrix. The material constitutive matrices used in defining the membrane and plate co-efficients are as follows

$$[E_m] = \frac{E}{(1-\nu^2)} \begin{bmatrix} 1 & \nu & 0 \\ \nu & 1 & 0 \\ 0 & 0 & \frac{(1-\nu)}{2} \end{bmatrix} \tag{3.71}$$

$$[E_b] = \frac{Et^3}{12(1-\nu^2)} \begin{bmatrix} 1 & \nu & 0 \\ \nu & 1 & 0 \\ 0 & 0 & \frac{(1-\nu)}{2} \end{bmatrix} \tag{3.72}$$

$$[E_s] = \frac{Et\frac{5}{6}}{2(1+\nu)} \begin{bmatrix} 1 & 0 \\ 0 & 1 \end{bmatrix} \tag{3.73}$$

In Eq 3.73 an empirical value of $\frac{5}{6}$ is included, which is a shear correction value. This is applied to correct for a limitation in Reissner-Mindlin plate theory which assumes a constant shear strain distribution across the thickness of the plate, rather than the parabolic distribution expected in reality. This correction ensures a more accurate reflection of the shear strain energy which is present.

3.4.4 Shell Element Mass Matrix

The mass matrices are generated in a consistent manner using the same shape functions used to derive the stiffness matrices. The expression for the consistent mass matrix of

a membrane element reads

$$\begin{aligned}[m_m] &= \rho t \iint [N]^T [N] dA \\ &= \rho t \iint [N]^T [N] |J| d\xi d\eta \end{aligned} \tag{3.74}$$

while the expression for a plate element reads

$$\begin{aligned}[m_p] &= \rho t \iint [N]^T [\kappa][N] dA \\ &= \rho t \iint [N]^T [\kappa][N] |J| d\xi d\eta \end{aligned} \tag{3.75}$$

$$[\kappa] = \begin{bmatrix} 1 & 0 & 0 \\ 0 & \frac{t^2}{12} & 0 \\ 0 & 0 & \frac{t^2}{12} \end{bmatrix} \tag{3.76}$$

Again, as was the case for the element stiffness matrix, the mass matrix is found numerically using Gauss-quadrature integration. The complete shell element mass matrix, with entries from the membrane and plate locations reads

$$[m] \in \mathbb{R}^{20\times 20} = [m_m] \oplus [m_p] = \begin{bmatrix} [m_m] & [0] \\ [0] & [m_p] \end{bmatrix} \tag{3.77}$$

In order to include the nacelle mass (M_{nac}) at the top of the tower, it can be considered as a lumped mass and directly summed to the relevant co-efficients for elements at the top of the tower. The mass moment of inertia (I_{nac}) of the nacelle is assumed to be constant around each axis and is summed to rotational degrees of freedom for elements at the top of the tower. Thus, each local element located around the circumference of the top of the tower was amended to incorporate a portion of these quantities. These

shell elements were amended as per Eq. 3.78 and 3.79.

$$[m_{\text{nac}}] = \begin{bmatrix} \frac{M_{\text{nac}}}{\text{seg}\times 2} & 0 & 0 & 0 & 0 & 0 \\ 0 & \frac{M_{\text{nac}}}{\text{seg}\times 2} & 0 & 0 & 0 & 0 \\ 0 & 0 & \frac{M_{\text{nac}}}{\text{seg}\times 2} & 0 & 0 & 0 \\ 0 & 0 & 0 & \frac{I_{\text{nac}}}{\text{seg}\times 2} & 0 & 0 \\ 0 & 0 & 0 & 0 & \frac{I_{\text{nac}}}{\text{seg}\times 2} & 0 \\ 0 & 0 & 0 & 0 & 0 & \frac{I_{\text{nac}}}{\text{seg}\times 2} \end{bmatrix} \tag{3.78}$$

In this equation, the term *seg* refers to the number of elements around the circumference of the tower. The total mass and inertia are divided as given to account for overlap between each element in constructing the overall mass matrix, such that the total mass and inertia achieved when considering all tower top nodes is M_{nac} and I_{nac} respectively.

$$[m]_n = [m]_n + \begin{bmatrix} [0]_{6\times 6} & [0]_{6\times 6} \\ [m_{\text{nac}}] & [m_{\text{nac}}] \end{bmatrix}, \qquad (N_{\text{els}} - \text{seg} \leq n \leq N_{\text{els}}) \tag{3.79}$$

3.4.5 Global matrix assembly

As outlined in Chapter 2, a required step in forming the overall tower model is to establish global descriptive matrices to account for stiffness, $[K_{l,T}]$ in the case of static analysis and extended to stiffness $[K_{l,T}]$, mass $[M_{l,T}]$ and damping $[C_{l,T}] \in \mathbb{R}^{6N\times 6N}$ matrices in the case of dynamic analysis. Appendix C outlines steps in constructing these matrices. A plot of the assembled tower using the Cartesian co-ordinates for each local element is provided in Figure 3.7.

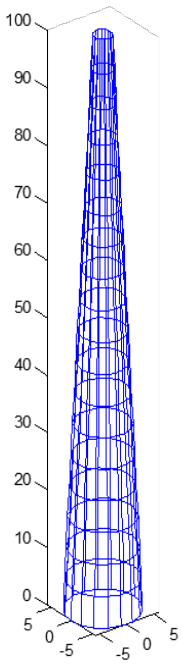

Figure 3.7: 3D Plot of Local Shell Finite Element Model

3.5 Local Shell Finite Element Model - Prestressed or Post-Tensioned

3.5.1 Introduction

The numerical modelling of prestressed concrete structures has been of great interest to civil engineers for many years. The structures examined in the literature were of historical importance in construction and remain of importance today – consisting mainly of prestressed simply supported beams, prestressed bridge decks and containment structures.

Law and Lu [2005] modelled a prestressed concrete beam for the purpose of system identification using Bernoulli-Euler assumptions. In this work, the elastic and geometric stiffness matrices of the beam element were defined, with geometric stiffness being a function of the prestress force. The tendon was not included in terms of the overall system stiffness and prestress is accounted for as an externally applied load.

Saiidi et al. [1994] carried out laboratory and field testing of prestressed beams. It was found, contrary to simple 'compression-softening' estimations that the first bending frequency of the beams increased with increasing prestress force. This is attributed to the fact that micro-cracks present in the physical beams are closed as a result of prestress, leading to stiffer sections. This non-linear behaviour of the concrete, the presence of the tendon and also the magnitude of prestress were thus shown to influence the dynamic properties of the section. These factors are all to be built into the model proposed here.

Kerr [1976] studied the dynamic response of prestressed beams and concluded that where the prestressing cable passes through the centroid of the member and where the cable is supported by the member laterally, that the magnitude of prestress does not affect its natural frequency.

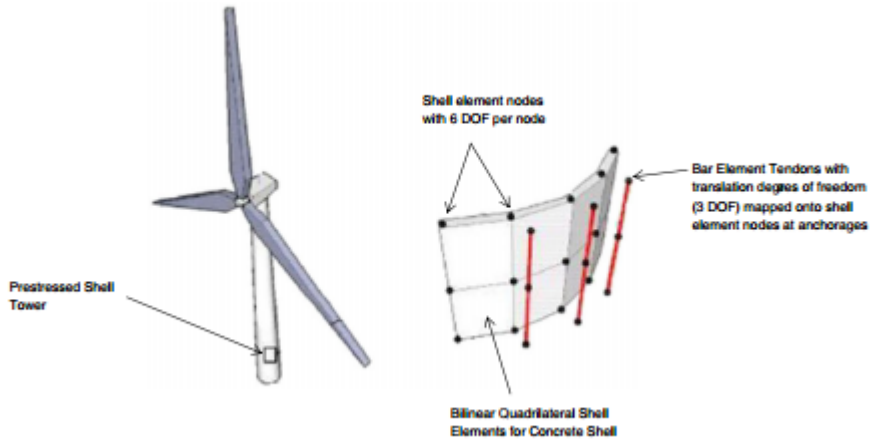

Figure 3.8: Mapping of Post-tensioning Tendons onto LSFE Model at Element Nodes

Chan and Yung [2000] proposed a method of identifying axle loads of moving vehicles from responses of prestressed concrete bridges. It was concluded that ignoring the effects of prestress in the identification process introduces inaccuracies which increase with increasing prestress. Material non-linearity was not included in the study, nor was the prestressed tendon(s) included in the model stiffness descriptions.

Kenna and Basu [2015b] presented a finite element shell model of a wind turbine tower where prestressed tendons were imposed as 1-D bar elements. The work presented in this paper is described in detail in the current section of this thesis.

3.5.2 Bar Element Stiffness Matrix

The tendons to be modelled are those of post-tensioned towers and are to be unbonded to the ducts they pass through. Kwak and Filippou [1990] described how steel reinforcement can be mapped directly onto the nodes of a shell or membrane element to include them in the overall structure stiffness. This method is used here, where the tendons are modelled as bar elements, with their end nodes mapped onto the shell element nodes used as anchorage locations. Figure 3.8 identifies how such bar elements are overlaid onto the tower model.

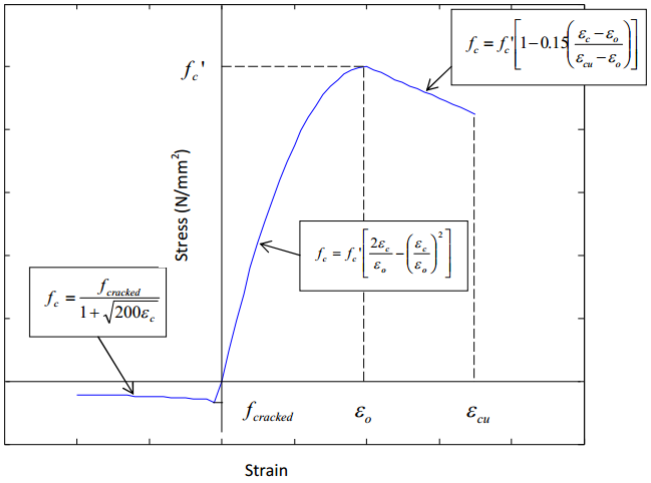

Figure 3.9: Concrete Constitutive Model in Tension (Vecchio [1989] and Compression (Eurocode 3, British Standards Institution [1993]

3.5.3 Material Non-linearity

In order to model non-linear behaviour of the concrete the modified Hognestad model was chosen, as described by Kwak and Filippou [1990]. This model is based on the behaviour of concrete under uniaxial loading. The shell elements in this model will generate biaxial stress results; however, as the principal stresses are not expected to be close to each other in magnitude, a constitutive model based on uniaxial loading will be applied. In tension, the concrete is assumed to have a linear stiffness until the point of cracking at its tensile strength and then to exhibit strain softening until ultimate failure. A strain softening curve suggested by Vecchio [1989] for cracked membrane elements is used. Expressions for stress at various levels of strain are shown in Figure 3.9. Values for the compressive strength, f_c'; the tensile strength, $f_{cracked}$; the yield strain, ε_0 and ultimate compressive strain ε_{cu} are available in Eurocode 3 (British Standards Institution [2004]). The prestressed steel in the model is assumed to behave in an elastic-perfectly plastic manner, with a bilinear curve.

3.5.4 Initial Stress (Prestress) Condition

The effect of applying a prestress needs to be accounted for in terms of the stiffness of the shell continuum. Prestress will be applied by externally applied loads to the concrete structure. The imposition of the prestress into the system will have implications for the global stiffness of the tower in that it will result in a stress stiffening effect on the tendons but a stress-softening effect on the shell continuum. In order to describe how this is represented in a finite element framework, some background is given in Appendix F.

In order to describe the lateral displacements of elements, Green Strain is used. This is a measure of strain used in finite element methods where deformations lead to a change in stiffness of the structure, as described by Cook et al. [2007]. The stiffness in such global structures is directly related to the deformed shape of the structure/element. With this approach, strains are described as follows in the normal and shear directions respectively

$$\varepsilon_x = \frac{\delta u_x}{\delta x} + \frac{1}{2}\left(\left(\frac{\delta u_x}{\delta x}\right)^2 + \left(\frac{\delta u_y}{\delta x}\right)^2 + \left(\frac{\delta u_z}{\delta x}\right)^2\right) \tag{3.80}$$

$$\gamma_{xy} = \frac{\delta u_x}{\delta y} + \frac{\delta u_y}{\delta x} + \left(\left(\frac{\delta u_x}{\delta x}\right)\left(\frac{\delta u_x}{\delta y}\right) + \left(\frac{\delta u_y}{\delta x}\right)\left(\frac{\delta u_y}{\delta y}\right) + \left(\frac{\delta u_z}{\delta x}\right)\left(\frac{\delta u_z}{\delta y}\right)\right) \tag{3.81}$$

where u_x, u_y and u_z are the displacements along the three orthogonal X, Y and Z directions respectively. The membrane strain energy for any element is equivalent to the work carried out by a membrane force (or axial force in the case of a 1-D bar) in lengthening or shortening an element by an infinitesimal length described by the strain in that particular direction. Thus for a bar element, the strain energy reads

$$U_m = \frac{1}{2}\int_0^L P\varepsilon_m dz \tag{3.82}$$

where P equals the applied axial load and ε_m is the axial strain. When the only displacement is through the in-plane degrees of freedom, Greens Strain states

$$\varepsilon_m = \frac{1}{2}\left(\frac{\delta u_y}{\delta x}\right)^2 \tag{3.83}$$

As such, the geometric stiffness, at an element level, is derived as follows

$$\begin{aligned} U_m &= \frac{1}{2}\int_0^L P\left(\frac{\delta u_y}{\delta x}\right)^2 dx \\ &= \frac{1}{2}\int_0^L \left(\frac{\delta u_y}{\delta x}\right)^T P\left(\frac{\delta u_y}{\delta x}\right) dx \\ &= \frac{1}{2}\{d\}[k_{\text{geo}}]\{d\} \end{aligned} \tag{3.84}$$

In terms of a physical interpretation of the effect of stress stiffening/softening on the overall tower, it is assumed that the out-of-plane stiffening experienced by the tendon is of no benefit to the concrete shell. As it is unbonded to the concrete, it is free to vibrate laterally between restraint locations. Any increase in its out of plane stiffness does not therefore offset the softening experienced by the concrete shell. As such, for the purpose of this thesis, the geometric stiffness of the tendons will not be included.

3.5.5 Shell Element Geometric Stiffness & Non-linearity

The principle of work performed by membrane forces carried through small changes in length owing to lateral displacements describes the change in strain energy and is used in defining the geometric stiffness of the shell elements. The membrane forces in the normal (i.e. X and Y) and shear (X–Y) directions are R_x, R_y and R_{xy}. The strain energy is thus

$$U_m = \int \left(\frac{1}{2}R_x\left(\frac{\delta u_z}{\delta x}\right)^2 + \left(\frac{1}{2}R_y\left(\frac{\delta u_z}{\delta y}\right)^2 + \left(\frac{1}{2}R_{xy}\left(\frac{\delta u_z}{\delta x}\right)\left(\frac{\delta u_z}{\delta y}\right)\right)dA \tag{3.85}$$

which can alternatively be written as

$$U_m = \frac{1}{2} \iint \begin{Bmatrix} \frac{\delta u_z}{\delta x} \\ \frac{\delta u_z}{\delta y} \end{Bmatrix}^T \begin{bmatrix} R_x & R_{xy} \\ R_{xy} & R_y \end{bmatrix} \begin{Bmatrix} \frac{\delta u_z}{\delta x} \\ \frac{\delta u_z}{\delta y} \end{Bmatrix} dxdy \tag{3.86}$$

The lateral displacement is again described by the shape functions and degrees of freedom. The derivatives of the displacement is expressed as

$$\begin{Bmatrix} \frac{\delta u_z}{\delta x} \\ \frac{\delta u_z}{\delta y} \end{Bmatrix} = [G]\{d\} \tag{3.87}$$

where $[G]$ is the matrix denoting the derivative of the shape function matrix. Manipulation of the above equations leads to an expression for the geometric stiffness of the local shell element of

$$[K_{\text{geo}}] = \iint [G]^T \begin{bmatrix} R_x & R_{xy} \\ R_{xy} & R_y \end{bmatrix} [G] dxdy \tag{3.88}$$

It can be seen from Eqs. 3.87 and 3.88 that the only coefficients resulting from this description are those relating to the out-of-plane displacements of each element node. Where the applied membrane loads are tensile or compressive in the shell element, this will lead to an increase or reduction in the membrane stiffness of the shell.

The first-order derivatives of the out-of-plane displacements have been used here to generate the geometric stiffness. Other works on this subject, particularly in the area of large-displacement theory, have also included the first-order derivatives of the bending degrees of freedom in describing the geometric stiffness. As the members to be analysed by this model are assumed to develop small lateral displacements without coupling of bending and membrane actions at any point prior to buckling, the bending degrees of freedom are not considered in the geometric stiffness matrices.

3.5.6 Prestress Losses

Losses will take place in the transfer of the tendon force to the concrete element, which needs to be accounted for in any analysis of such structural members. Some of these losses will occur during construction, whilst others will occur slowly over time. Losses occur because of friction, anchorage draw-in, elastic deformation of concrete, shrinkage, creep and relaxation.

In applying tension to the pre-stressed tendons, a certain amount of this force will be lost through friction between the tendon and the duct that the tendon passes through. This will result in the force present in the tendon varying along the length of the duct and thus along the height of the tower. In this work, it will be assumed that the tendon force is applied at the base of the tower. The expression for calculating the change in tendon force due to friction at a distance from the base is given in Eurocode 3 (British Standards Institution [2004]) as

$$\Delta P(x) = P_{max}(1 - \exp^{-\mu(\vartheta + \upsilon x)}) \tag{3.89}$$

where P_{max} is the maximum value of the force, μ is the friction coefficient and ϑ is the change in tendon angle along its length. The coefficient υ is known as a 'wobble' coefficient of friction (dependent on type of tendon). The values incorporated in this model for μ and υ are taken from a report by Concrete Society [2005] and are 0.06 and 0.05 rad/m, respectively. Elastic deformation of the concrete as it takes up stress will lead to losses in tendon force. Time-dependent sources of loss of force in the tendons include creep and shrinkage of the concrete and relaxation of the tendons themselves. Expressions for all of the aforementioned losses are available in Eurocode 2 (British Standards Institution [2004]), and will be used in this model. Figure 3.10 shows how the tendon force would typically vary over the height of the tower.

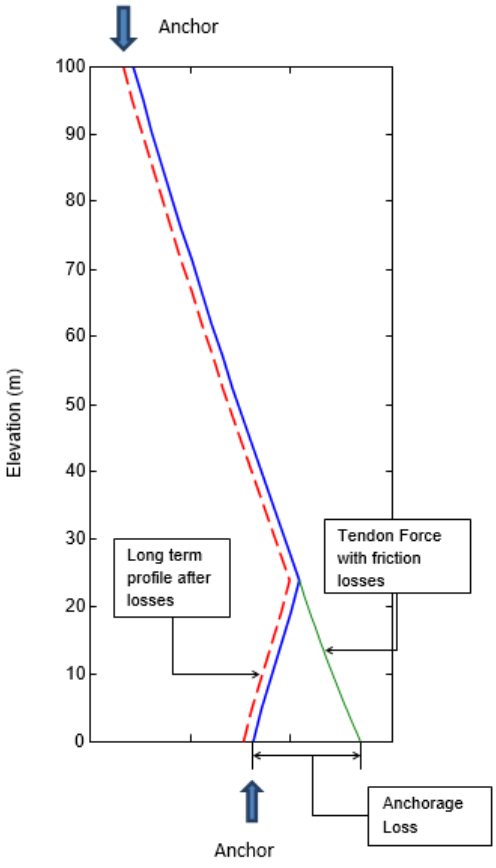

Figure 3.10: Immediate and Long Term Losses in Prestress Force over Tower Height

Properties	Sym	BM Tower 1	BM Tower 2	BM Tower 3
Height (m)	H	100	100	100
Interface (m)	h_{int}	20	60	N/A
Base Dia (m)	D_c	7	7	6
Base Shell (mm)	t_c	300	300	24
Top Dia (m)	D_s	3	3	3.87
Top Shell (mm)	t_s	25	25	24
Density (steel) (kg/m^3)	ρ_s	7890	7890	7890
Youngs Mod (steel)(GPa)	E_s	205	205	205
Poissons ratio (steel)	ν_s	0.3	0.3	0.3
Density (conc)(kg/m^3)	ρ_c	2450	2450	N/A
Youngs Mod(conc)(GPa)	E_c	30	30	N/A
Poissons ratio (conc)	ν_c	0.15	0.15	N/A
Mass Ratio (%)	$\frac{M_{nac}}{M_{Tower}}$	25	50	0

Table 3.1: Sample Towers used in Benchmarking - Model Properties

3.6 Benchmarking

3.6.1 Free Vibration Response

Validation of the closed form, analytical model and global beam FE model was carried out by completing a number of free-vibration analyses of sample benchmark hybrid towers and comparing resulting eigen-pairs of frequencies and mode shapes. Two sample benchmarking towers were chosen and are given as BM Tower 1 and BM Tower 2 in Table 3.1.

The results of this comparison are presented in Table 3.2 and fig 3.11. Both the mode shapes and frequencies are in good agreement.

Validation of the shell model was carried out in terms of its ability to generate the free vibration properties of a tower. Tower stiffness and mass matrices were assembled based on the input properties listed as BM Tower 3 in Table 3.1 (note this is a fully steel tower) and an Eigenanalysis was carried out to obtain frequencies and associated mode shapes. A comparison between the output of the shell model and the commercially available software is included below in Table 3.3. Figure 3.12 provides plots of the first

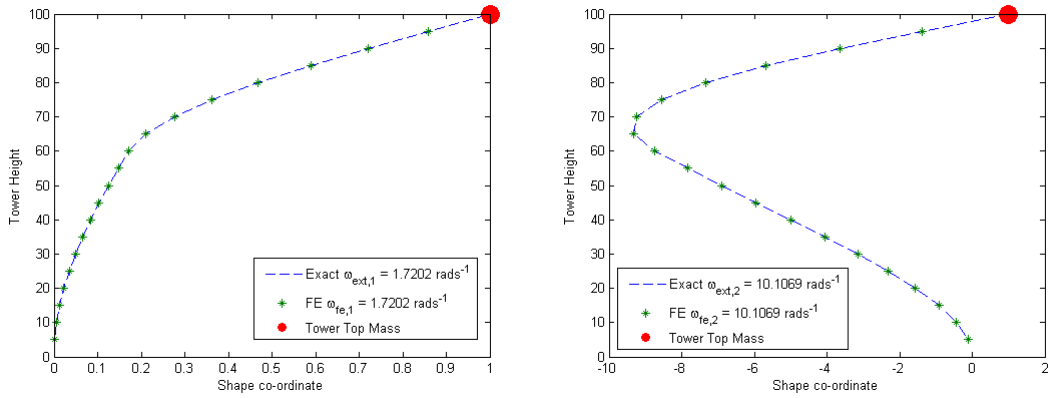

(a) BM Tower 2, 1st Mode, Closed Form & GBFE Models

(b) BM Tower 2, 2nd Mode, Closed Form & GBFE Models

Figure 3.11: Benchmarking Results 1 (Mode Shapes); Closed Form & GBFE Model Free Vibration

Model	BM Tower	f_1(Hz)	f_2(Hz)	f_3(Hz)
Closed Form Model	1	0.2252	2.1222	6.3338
Global Beam FE Model	1	0.2252	2.1222	6.3339
Closed Form Model	2	0.2738	1.6086	7.0146
Global Beam FE Model	2	0.2738	1.6086	7.0148

Table 3.2: Benchmarking Results 1 (Natural Frequencies); Closed Form & GBFE Model Free Vibration

three benchmarked mode shapes from the LSFE model.

3.6.2 LSFE Model Stress Analysis

Finally, a stress analysis was carried out using the LSFE model and the commercial FE package Autodesk Robot and the results compared, using a steel tower defined by BM Tower 3 as the input. This was carried out by applying a static lateral load to the top of the tower. For the local response, a local finite element was considered at the base of the tower. In the case of both models, a mesh density equating to 20 elements around the

Model	BM Tower	f_1(Hz)	f_2(Hz)	f_3(Hz)
Local Shell FE Model	3	0.817	4.213	10.8133
Autodesk Robot	3	0.82	4.2	10.7

Table 3.3: Benchmarking Results 2; LSFE Model Free Vibration

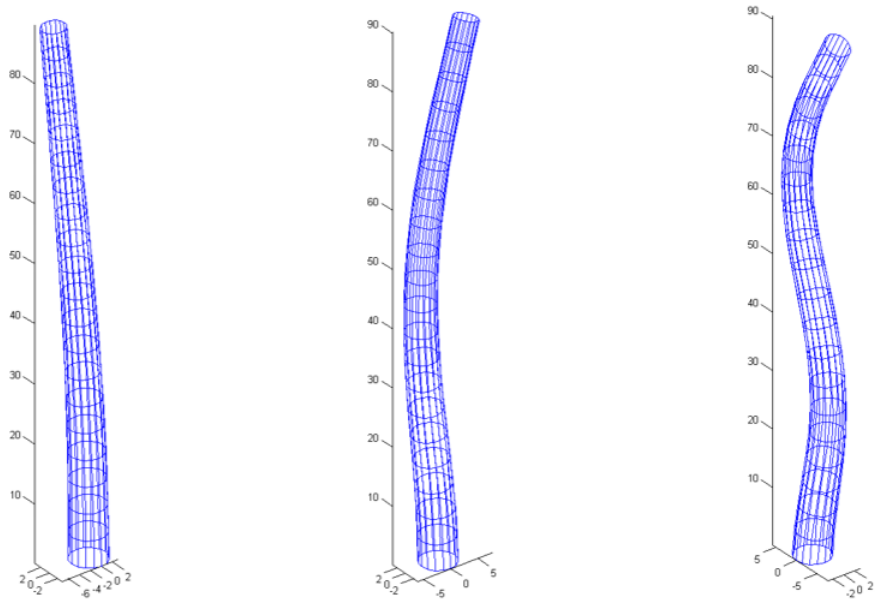

Figure 3.12: Benchmarking Results 2 (Mode Shapes); LSFE Model $1^{st}, 2^{nd}, 3^{rd}$ Mode Shapes

Model	P (kN)	$u_{N,X}$ (mm)	$\sigma_{1,x}$	$\sigma_{1,y}$	τ_{xy}
Local Shell FE Model	800	607.7	-2.24	98.38	-0.55
Autodesk Robot	800	604	-2.23	101.66	0.11

Table 3.4: Benchmarking Results 3; LSFE Model Stress Analysis

tower circumference and 25 elements along the height of the tower was chosen. Results for the stress vector $\{\sigma_1\}^T = [\sigma_{1,x}, \sigma_{1,y}, \tau_{xy}]$, for the first finite element at the base of the tower are given in Table 3.4. A plot of the LSFE elemental vertical stress, $\sigma_{1,y}$ is provided in Figure 3.13 as well as an overlay of the out-of-plane displacement, $u_{n,X}$ $(1 \leq n \leq N)$ profile for both models. Both sets of results are in good agreement.

3.7 Conclusions

A number of numerical models were developed to describe the structure of a hybrid concrete-steel wind turbine tower with nacelle and hub mass at its top. Models developed included an exact, analytical model, an approximate finite element model formulated using beam elements and a further finite element model formulated using bilinear shell elements.

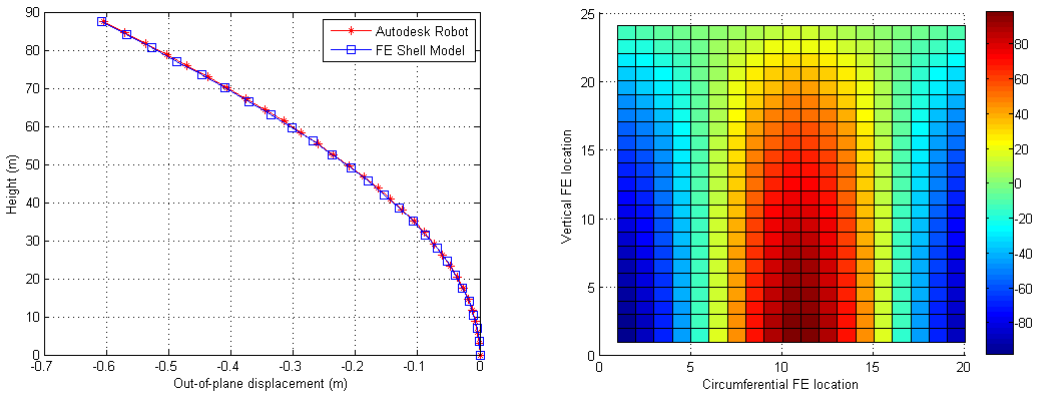

(a) Displacement, (u_x), LSFE & Autodesk Robot (b) Tower Stress Distribution (σ_y), LSFE Model

Figure 3.13: Benchmarking Results 3; Displacement & Stress Analysis Plots, LSFE Model and Autodesk Robot Model

The finite element models are given the names Global Beam Finite Element model (GBFE) and Local Shell Finite Element model (LSFE) based on their make-up.

Finally, a benchmarking exercise has shown that the response of the models developed are as expected and for cases selected, are in agreement with responses from commercially available software models. The approximate FE models will now be taken forward for inclusion in MDOF wind turbine models and will be used in applications such as optimisation and damage detection in other parts of the thesis. The GBFE model will be used in situations where only a global response is required, whereas where a local response is required, the LSFE model will be used.

Chapter 4

Multi Degree of Freedom Turbine Models - Formulation & Generalised Loading

4.1 Introduction

In this chapter, a mixed-formulation approach will be presented for the incorporation of finite element models of a tower into two MDOF models. The FE models will be incorporated into Euler-Lagrangian reduced order models where all turbine components follow deformation paths assigned by assumed shapes of vibration. The models will account for in-plane and out-of-plane deformation of the tower and three blades. They will account for tower-rotor dynamic interaction by way of deformation coupling within the equations of motion.

A Global Beam FE (GBFE) model will be used in one model to describe the tower. This will allow for the extraction of global responses of the tower and turbine at each degree of freedom to any external excitation. A second MDOF model, which will be called a

Local Shell FE (LSFE) model will then describe the tower using a highly discretised 3D shell. This second model will allow for the direct extraction of shell nodal deformations and shell element strains immediately after carrying out any simulations. Both models will also address the issue of variable structural damping properties between the concrete and steel sections of the tower.

This chapter will also introduce the concept of numerically describing the physical forces generated when a wind field passes around and against the wind turbine structural components, namely the rotating blades and the tower. Loading is applied to the model in each DOF to represent loading arising through the following mechanisms – aerodynamic load and gravitational load.

In the literature, the most common means of describing the turbine in terms of a dynamical model is to use a reduced order model. This allows for the representation of flexible components such as blades and the tower using modal co-ordinates and assumed shapes of vibration. Rigid component movement can be described using virtual work within the same model.

Lagrangian dynamics have been widely used as a means of describing turbine element motion and interaction where the total system Potential and Kinetic Energy descriptions can be put to use (Simani [2015]). Fitzgerald et al. [2013] presented an Euler-Lagrangian model to develop an active structural control scheme would include as Active Tuned Mass Damper (ATMD) to limit the responses of the nacelle/tower in the out of plane direction, based on an Energy formulation. Zhang et al. [2014] also studied the implications of a damper on a turbine assembly. The authors propose a 13 DOF model which includes tower-drive train-blade interaction to model the responses of the lateral vibrations of a tower subjected to wind and wave loading. The model is formulated using an Euler-Lagrangian approach.

One of the novelties of this thesis is the combination of continuous and discrete functions as assumed shapes in constructing the MDOF model. The use of continuous functions

would be a typical approach and have been used in the literature in works by Quilligan et al. [2012] and Harte and Basu [2013]. Discrete shapes are not apparent in the literature and are used here in order to incorporate a highly discretised three-dimensional FE model into a reduced order MDOF dynamical model.

4.2 Lagrangian Formulation

The Lagrangian formulation of the dynamic equations of motion is provided by Clough and Penzien [1993] as a function of a systems total Potential (U) and Kinetic (T) Energy expressions. This expression is given in Eq. 4.1.

$$\frac{\partial}{\partial t}\left(\frac{\partial T}{\partial \dot{q}_i}\right) - \frac{\partial T}{\partial q_i} + \frac{\partial U}{\partial q_i} = Q_i \tag{4.1}$$

In Eq. 4.1, Q_i refers to a generalised loading quantity and q_i defines the i^{th} generalised co-ordinate or degree of freedom of the system. The generalised co-ordinates are related to physical displacements through the use of assumed shapes of vibration, ϕ_i as in Eq. 4.2, which is a general form of this relationship. The assumed shapes are sometimes taken to be the mode shape associated with the frequency the structure is assumed to vibrate at. Alternatively, some other assumed shape which satisfies the elemental boundary conditions could be used.

$$u_i(z,t) = \phi_i(z)q_i(t) \tag{4.2}$$

4.3 Generalised Degrees of Freedom

The model presented here will include the structural components of wind turbine blades, nacelle and tower and each of the degrees of freedom associated with these members.

The vector of generalised co-ordinates for both the GBFE model and LSFE model will

read as given in Eq 4.3 to 4.5.

$$q_{11DOF}^T = \begin{bmatrix} q_B^T & q_T^T \end{bmatrix} \tag{4.3}$$

$$q_B^T = \begin{bmatrix} q_{b,1,x} & q_{b,1,y} & q_{b,2,x} & q_{b,2,y} & q_{b,3,x} & q_{b,3,y} \end{bmatrix} \tag{4.4}$$

$$q_T^T = \begin{bmatrix} q_7 & q_8 & q_9 & q_{10} & q_{11} \end{bmatrix} \tag{4.5}$$

Co-ordinates $q_{b,1,x}$ to $q_{b,3,y}$ will describe the flapwise and edgewise motion of the blades, while co-ordinates q_7 to q_{11} describe motion of the tower in translation and rotation, as shown in Figure 4.1. The tower DOFs include fore-aft (q_7) and side-side (q_9) displacement as well as tilting (q_8), rolling (q_{10}) and torsional (q_{11}) rotation of the tower. A local co-ordinate system (x, y, z) is used for each of the rotating blades, with its origin at the centre of rotation. The global co-ordinate system (X, Y, Z) is used for the tower, with its origin at the base of the tower. In terms of numerical descriptions of the main turbine components, the NREL 5MW baseline turbine (Jonkman et al.) was used for the blades and nacelle, whereas the tower properties were found through the optimisation design variables, which are outlined elsewhere in this work.

4.4 Tower Model Order Reduction

Harte and Basu [2013] used a beam element to represent a tower within a wind turbine assembly and used modal analysis, and tower mode shapes, to reduce the tower motion to a single fore-aft generalised DOF. Zhang et al. [2014] also used a beam element to represent the tower component of a wind turbine model but in this case used cubic shape functions to represent the tower response, with one shape function to describe tower top side-side response and a second to describe tower top rolling response.

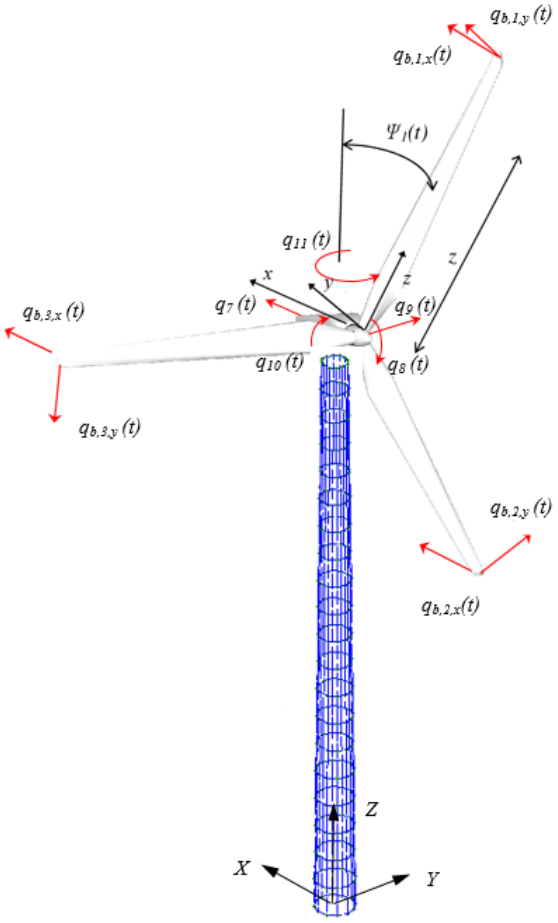

Figure 4.1: Turbine MDOF Model Co-ordinate Systems and Degrees of Freedom

In both 11 DOF models, the tower element of the model is initially constructed using a finite element description. In the case of the GBFE model, Euler-Bernoulli beam elements which have been extended to include torsional degrees of freedom are used to describe tower elements, such that its stiffness matrix is $[K_{g,T}] \in \mathbb{R}^{5N\times 5N}$. In the case of the LSFE model, a high-fidelity 3D tower model is constructed using Reissner-Mindlin shell elements, such that the tower stiffness matrix, $[K_{l,T}] \in \mathbb{R}^{6N\times 6N}$ is found. A description for the construction of both tower models is found in Chapter 3 of this thesis.

Discrete shape functions, $s_j(X, Y, Z)$ are used to reduce the FE DOF's to five DOF to represent tower top fore-aft (q_7), tilting (q_8), side-side (q_9), rolling (q_{10}) and torsion (q_{11}). These five directions are chosen due to the primary aerodynamic and inertial loading of the tower being in these directions at its top and as such, they are expected to dominate the real physical response.

It is important to differentiate these global shape functions from the local elemental shape functions used to describe the local displaced shape of a given finite element. This method of order reduction is similar to methods such as the use of Rayleigh-Ritz vectors.

In order to realise each tower shape function, s_j, a technique described in a text by Chopra [1995] is used. Chopra [1995] describes a means of establishing a shape which will automatically satisfy the boundary conditions of the model by using statically deformed shapes to represent each DOF. Boundary conditions of the tower shape include zero displacement and rotation of the tower at its base ($u_{i,X}, u_{i,Y}, u_{i,Z}, \theta_{i,X}, \theta_{i,Y}, \theta_{i,Z} = 0$, $1 \leq i \leq seg$ in the case of the LSFE model, where $'seg'$ refers to the number of elements at the base of the tower). Figures 4.2 and 4.3 provides some of the shape functions used for the tower in the case of both the GBFE and LSFE models.

The use of statically deformed shapes is a simplification which will lead to some measure of error, as tower mass inertia forces have not been included in their generation.

However, justification for this approach is found in the knowledge that the dominant inertia loading will occur at the tower top, through the motion of the nacelle. In addition to this, large shear and bending inertia forces will be applied to the tower by the nacelle/rotor, which will also occur at the tower top. Both of these forms of loading are expected to be far more significant than any inertia occurring over the height of the tower.

4.5 Rotating Blades

For both the GBFE model and LSFE model, the assumed shapes of vibration for the blades in their flapwise and edgewise directions are the mode shapes associated with their fundamental frequencies in these directions. Polynomial expressions to the order of six were fitted to the mode shapes, which themselves were extracted using the NREL finite element (FE) based code BModes (Bir [2005]). The flapwise motion occurs in the x direction, with edgewise motion occurring in the y direction. The z axis is in line with the longitudinal axis of the blade, with any point along the blade being at a distance (z) from its origin. Blade relative displacements in the flapwise and edgewise directions are given in Eq. 4.6.

$$u_{b,i,x} = \phi_{b,x}(z)q_{b,i,x}(t) \qquad u_{b,i,y} = \phi_{b,y}(z)q_{b,i,y}(t) \tag{4.6}$$

4.6 11 DOF Models

The 11 DOF models are constructed by first determining the assumed shapes of vibration of the tower associated with each of the generalised DOFs. Following this, the turbine assembly Potential and Kinetic Energy expressions are written. Finally, the system equations of motion are determined through incorporating the Potential and Kinetic Energy expressions into the Lagrangian Formulation.

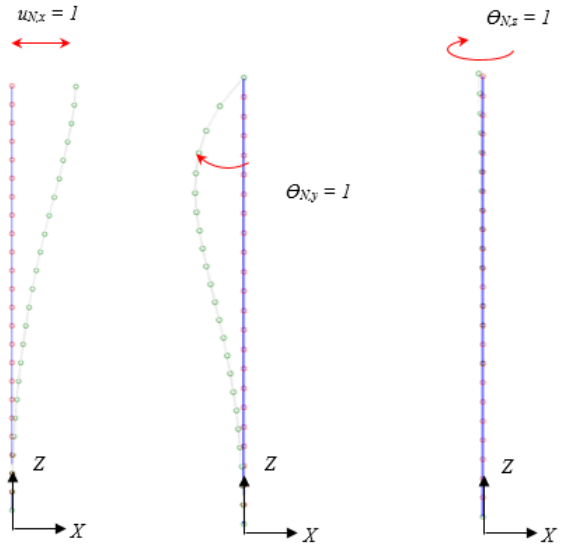

Figure 4.2: GBFE Model, Shapes of Vibration; Fore-aft (q_7), Tilting (q_8) and Torsional (q_{11}) DOFs

4.6.1 11 DOF GBFE Model - Assumed Shapes of Vibration

The shape functions for the 11 DOF GBFE model are found using the expression given in Eq. 4.7, where the vector $\{R_{g,j}\} \in \mathbb{R}^{5N}$ represents external load vectors applied to achieve the desired unit displacement/rotation for the j^{th} shape function.

$$\{s_{g,j}\} = [K_{g,T}]^{-1}\{R_{g,j}\} \qquad j \in [7, 8, 9, 10, 11] \tag{4.7}$$

The assumed shapes for the fore-aft (q_7), tilting (q_8) and torsional (q_{11}) DOFs for the 11 DOF GBFE model are given in Figure 4.2.

After undergoing any level of deformation, the physical deformed shape of the tower can be described using the form given in Eq. 4.8, which gives the response for each of

the physical FE DOF, $\{D_g\} \in \mathbb{R}^{5N}$.

$$\{D_g\}^T = [u_{g,1,X}, u_{g,1,Y}, \theta_{g,1,X}, \theta_{g,1,Y}, \theta_{g,1,Z}, u_{g,2,X}, \cdots, u_{N,Y}, \theta_{N,X}, \theta_{N,Y}, \theta_{N,Z}] \tag{4.8}$$

The shape function vectors, $\{s_{g,j}\}$, will each take the same form as that given in Eq. 4.8. The relationship between the physical FE response, the generalised tower DOF responses and these shape functions is given in Eq. 4.9.

$$\begin{aligned} \{D_g\} &= \{s_{g,7}\}q_7 + \{s_{g,8}\}q_8 + \{s_{g,9}\}q_9 + \{s_{g,10}\}q_{10} + \{s_{g,11}\}q_{11} \\ &= [S_g]\{q_T\} \end{aligned} \tag{4.9}$$

$$[S_g] \in \mathbb{R}^{5N\times 5} = \begin{bmatrix} \{s_{g,7}\}_{u_{g,1,X}} & \{s_{g,8}\}_{u_{g,1,X}} & \cdots & \{s_{g,11}\}_{u_{g,1,X}} \\ \{s_{g,7}\}_{u_{g,1,Y}} & \{s_{g,8}\}_{u_{g,1,Y}} & \cdots & \{s_{g,11}\}_{u_{g,1,Y}} \\ \{s_{g,7}\}_{\theta_{g,1,X}} & \{s_{g,8}\}_{\theta_{g,1,X}} & \cdots & \{s_{g,11}\}_{\theta_{g,1,X}} \\ \vdots & \vdots & \ddots & \vdots \\ \{s_{g,7}\}_{\theta_{g,N,Z}} & \{s_{g,8}\}_{\theta_{g,N,Z}} & \cdots & \{s_{g,11}\}_{\theta_{g,N,Z}} \end{bmatrix} \tag{4.10}$$

4.6.2 11 DOF LSFE model - Assumed Shapes of Vibration

The shape functions for the 11 DOF LSFE model are found using the expression given in Eq. 4.11, where the vector $\{R_{l,j}\} \in \mathbb{R}^{6N}$ represents external load vectors applied to achieve the desired unit displacement/rotation for the j^{th} shape function.

$$\{s_{l,j}\} = [K_{l,T}]^{-1}\{R_{l,j}\}, \qquad j \in [7, 8, 9, 10, 11] \tag{4.11}$$

The assumed shapes for the fore-aft (q_7), tilting (q_8) and torsional (q_{11}) DOFs for the 11 DOF LSFE model are given in Figure 4.3.

After undergoing any level of deformation, the physical deformed shape of the tower

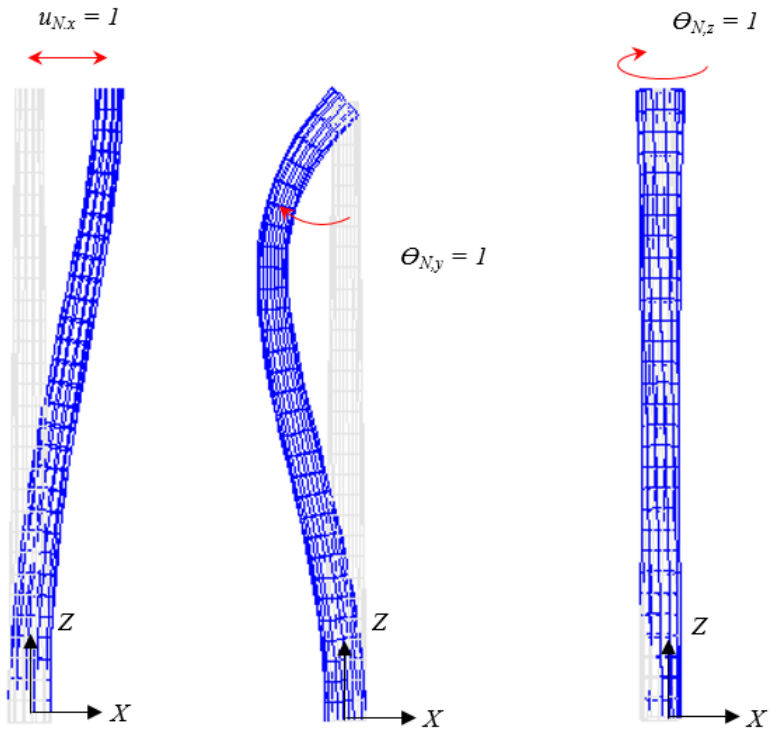

Figure 4.3: LSFE Model, Shapes of Vibration; Fore-aft (q_7), Tilting (q_8) and Torsional (q_{11}) DOFs

can be described using the form given in Eq. 4.12, which gives the response for each of the physical FE DOF, $\{D_l\} \in \mathbb{R}^{6N}$.

$$\{D_l\}^T = [u_{l,1,X}, u_{l,1,Y}, u_{l,1,Z}, \theta_{l,1,X}, \theta_{l,1,Y}, \theta_{l,1,Z}, u_{l,2,X}, \cdots, u_{l,N,Z}, \theta_{l,N,X}, \theta_{l,N,Y}, \theta_{l,N,Z}] \tag{4.12}$$

The shape function vectors, $\{s_{l,j}\}$, will each take the same form as that given in Eq. 4.12. The relationship between the physical FE response, the generalised tower DOF responses and these shape functions is given in Eq. 4.13.

$$\begin{aligned} \{D_l\} &= \{s_{l,7}\}q_7 + \{s_{l,8}\}q_8 + \{s_{l,9}\}q_9 + \{s_{l,10}\}q_{10} + \{s_{l,11}\}q_{11} \\ &= [S_l]\{q_T\} \end{aligned} \tag{4.13}$$

$$[S_l] \in \mathbb{R}^{6N\times 5} = \begin{bmatrix} \{s_{l,7}\}_{u_{l,1,X}} & \{s_{l,8}\}_{u_{l,1,X}} & \cdots & \{s_{l,11}\}_{u_{l,1,X}} \\ \{s_{l,7}\}_{u_{l,1,Y}} & \{s_{l,8}\}_{u_{l,1,Y}} & \cdots & \{s_{l,11}\}_{u_{l,1,Y}} \\ \{s_{l,7}\}_{u_{l,1,Z}} & \{s_{l,8}\}_{u_{l,1,Z}} & \cdots & \{s_{l,11}\}_{u_{l,1,Z}} \\ \vdots & \vdots & \ddots & \vdots \\ \{s_{l,7}\}_{\theta_{l,N,Z}} & \{s_{l,8}\}_{\theta_{l,N,Z}} & \cdots & \{s_{l,11}\}_{\theta_{l,N,Z}} \end{bmatrix} \tag{4.14}$$

4.6.3 Tower Potential Energy

The total Potential Energy of the tower structure can be written in terms of the physical DOF and stiffness matrix as per Eq. 4.15. Depending on which model is to be developed, the terms $\{D_T\}, [K_T]$ and $\{S_T\}$ are given by $\{D_T\} \in [\{D_g\}, \{D_l\}], [K_T] \in [[K_{g,T}], [K_{l,T}]]$ and $\{S_T\} \in [\{S_g\}, \{S_l\}]$

$$U_T = \frac{1}{2}\{D_T\}^T[K_T]\{D_T\} \tag{4.15}$$

By combining Eq. 4.10 and Eq. 4.15, the Potential Energy may now be re-written as

given in Eq. 4.16.

$$U_T = \frac{1}{2}\{q_T(t)\}^T[S_T]^T[K_T][S_T]\{q_T(t)\} = \frac{1}{2}\{q_T(t)\}^T[K_{TR}]\{q_T(t)\} \tag{4.16}$$

The matrix $[K_{TR}] \in \mathbb{R}^{5\times5}$ is a reduced order stiffness matrix. This reduced stiffness matrix, aligned with tower DOFs $\{q_T\}^T = [q_7, q_8, q_9, q_{10}, q_{11}]$ is given in Eq. 4.17.

$$[K_{TR}] = \begin{bmatrix} [K_{TR}]_{1,1} & [K_{TR}]_{1,2} & 0 & 0 & 0 \\ [K_{TR}]_{2,1} & [K_{TR}]_{2,2} & 0 & 0 & 0 \\ 0 & 0 & [K_{TR}]_{3,3} & [K_{TR}]_{3,4} & 0 \\ 0 & 0 & [K_{TR}]_{4,3} & [K_{TR}]_{4,4} & 0 \\ 0 & 0 & 0 & 0 & [K_{TR}]_{5,5} \end{bmatrix} \tag{4.17}$$

4.6.4 Tower Kinetic Energy

The total Kinetic Energy of the tower structure can be written in terms of the physical DOF and stiffness matrix as per Eq. 4.18. Depending on which model is to be developed, the term $[M_T]$ is given by $[M_T] \in [M_{g,T}], [M_{l,T}]$.

$$T_T = \frac{1}{2}\{\dot{D}_T\}^T[M_T]\{\dot{D}_T\} \tag{4.18}$$

By combining Eq. 4.9 and Eq. 4.18, the Kinetic Energy may now be re-written as given in Eq. 4.19.

$$\begin{aligned} T_T &= \frac{1}{2}\{\dot{q}_T(t)\}^T[S_T]^T[M_{TR}][S_T]\{\dot{q}_T(t)\} \\ &= \frac{1}{2}\{\dot{q}_T(t)\}^T[M_{TR}]\{\dot{q}_T(t)\} \end{aligned} \tag{4.19}$$

The matrix $[M_{TR}] \in \mathbb{R}^{5\times5}$ is a reduced order mass matrix. This reduced mass matrix, aligned with tower DOFs $\{q_T\}^T = [q_7, q_8, q_9, q_{10}, q_{11}]$ is given in Eq. 4.20, taking the

same form as Eq. 4.17.

$$[M_{TR}] = \begin{bmatrix} [M_{TR}]_{1,1} & [M_{TR}]_{1,2} & 0 & 0 & 0 \\ [M_{TR}]_{2,1} & [M_{TR}]_{2,2} & 0 & 0 & 0 \\ 0 & 0 & [M_{TR}]_{3,3} & [M_{TR}]_{3,4} & 0 \\ 0 & 0 & [M_{TR}]_{4,3} & [M_{TR}]_{4,4} & 0 \\ 0 & 0 & 0 & 0 & [M_{TR}]_{5,5} \end{bmatrix} \tag{4.20}$$

4.6.5 MDOF Equations of Motion

In order to couple the motion of the various degrees of freedom using Lagrangian dynamics, expressions for the systems Potential and Kinetic Energies are to be established. The total Potential Energy is written as

$$\begin{aligned} U = & \frac{1}{2}\{q_T(t)\}^T[K_{TR}]\{q_T(t)\} \\ & + \frac{1}{2}\sum_{i=1}^{3}\Bigg\{\int_0^{R_b}\Big[EI_{b,x}(z)(\frac{\delta^2\phi_{b,x}}{dz^2})^2 q_{b,i,x}^2 \\ & + EI_{b,y}(z)(\frac{\delta^2\phi_{b,y}}{dz^2})^2 q_{b,i,y}^2\Big]dz \\ & + U_g + U_c\Bigg\} \end{aligned} \tag{4.21}$$

The total Kinetic Energy allows for coupling of the blades and the tower through incorporating the tower top motion in finding the absolute velocity of the blades in any degree of freedom direction. In the fore-aft direction, the appropriate entry of the tower shape vector $\{s_7\}$ is used to describe the magnitude of deformation of the top of the tower. Any of the tower top nodes in the FE model can be used as they will all have the same magnitude of deformation. The 'N^{th}' node will be used for this purpose ($\{s_7\}_{u_{N,X}}$).

The total Kinetic Energy can be written as

$$\begin{aligned} T &= \frac{1}{2}\{\dot{q}_T(t)\}^T[M_{TR}]\{\dot{q}_T(t)\} \\ &= \frac{1}{2}M_{nac}\big(\{s_7\}_{u_{N,X}}\dot{q}_7(t)\big)^2 + \frac{1}{2}I_{nac,tilt}\big(\{s_8\}_{\theta_{N,Y}}\dot{q}_8(t)\big)^2 \\ &+ \frac{1}{2}M_{nac}\big(\{s_9\}_{u_{N,Y}}\dot{q}_9(t)\big)^2 + \frac{1}{2}I_{nac,roll}\big(\{s_{10}\}_{\theta_{N,X}}\dot{q}_{10}(t)\big)^2 \\ &+ \frac{1}{2}I_{nac,tor}\big(\{s_{11}\}_{\theta_{N,Z}}\dot{q}_{11}(t)\big)^2 \\ &+ \frac{1}{2}\sum_{i=1}^{3}\int_0^{R_b} m_b(z)(v_{b,i,x}^2 + v_{b,i,y}^2 + v_{b,i,z}^2)dz \end{aligned} \tag{4.22}$$

The terms $v_{b,i,x}, v_{b,i,y}$ and $v_{b,i,z}$ refer to the absolute velocity of the blades in their respective local co-ordinate axes. Numerical values for the nacelle mass, M_{nac}, and the moment of inertia associated with the nacelle in various directions ($I_{nac,tilt}, I_{nac,roll}$ and $I_{nac,tor}$) are provided in the appendices. The velocity of a point on the blade in each of the local blade directions are as follows

$$\begin{aligned} v_{b,i,x} &= \{s_7\}_{u_{N,X}}\dot{q}_7(t) + \phi_{b,x}(z)\dot{q}_{b,i,x}(t) \\ v_{b,i,y} &= \{s_9\}_{u_{N,Y}}\dot{q}_9(t)sin(\psi_i) - \Omega\phi_{b,y}(z)q_{b,i,y}(t) \\ v_{b,i,z} &= \{s_9\}_{u_{N,Y}}\dot{q}_9(t)cos(\psi_i) + \Omega z + \phi_{b,y}(z)\dot{q}_{b,i,y}(t) \end{aligned} \tag{4.23}$$

The absolute velocity of any location on a blade (z) in the x direction is found through the direct summation of the tower top fore-aft velocity and the blade flexural velocity. In the plane of the rotor, the velocity of any point on the blade is a function of the tower side-side velocity, the blade edgewise velocity and the rotational frequency of the rotor, Ω_r. It is noted that the tower top rotational motions are not included in the blade velocity expressions as these are expected to be insignificant in their effect on the blades motion.

$$\begin{aligned} \psi_i(t) &= \Omega_r t + \psi_i(t_0) \\ \psi_i(t_0) &= \frac{2\pi}{3}(i-1) \end{aligned} \tag{4.24}$$

Using Eqns. 4.21 to 4.23, equations of motion for the structure can be written. System matrices cater for each of the blade and tower DOF's.

$$[M(t)]\{\ddot{q}(t)\} + [C(t)]\{\dot{q}(t)\} + [K(t)]\{q(t)\} = \{Q(t)\} \tag{4.25}$$

$$[M(t)] \in \mathbb{R}^{11\times 11} = \begin{bmatrix} [M_b] & [0] & [0] & [M_{bt}(\psi_i)] \\ [0] & [M_b] & [0] & [M_{bt}(\psi_i)] \\ [0] & [0] & [M_b] & [M_{bt}(\psi_i)] \\ [M_{tb}(\psi_i)] & [M_{tb}(\psi_i)] & [M_{tb}(\psi_i)] & [\bar{M}_{TR}] \end{bmatrix} \tag{4.26}$$

$$[C(t)] \in \mathbb{R}^{11\times 11} = \begin{bmatrix} [C_b] & [0] & [0] & [0] \\ [0] & [C_b] & [0] & [0] \\ [0] & [0] & [C_b] & [0] \\ [C_{tb}(\psi_i)] & [C_{tb}(\psi_i)] & [C_{tb}(\psi_i)] & [C_{TR}] \end{bmatrix} \tag{4.27}$$

$$[K(t)] \in \mathbb{R}^{11\times 11} = \begin{bmatrix} [K_b] & [0] & [0] & [0] \\ [0] & [K_b] & [0] & [0] \\ [0] & [0] & [K_b] & [0] \\ [K_{tb}(\psi_i)] & [K_{tb}(\psi_i)] & [K_{tb}(\psi_i)] & [K_{TR}] \end{bmatrix} \tag{4.28}$$

The term $[\bar{M}_{TR}] = [M_{TR}] + [M_{TB}]$ incorporates the reduced order mass matrix of the tower, plus co-efficients derived where interaction with blades are included at relevant matrix entries. Equation of motion matrix entries are defined in Appendix D.

4.7 Structural Damping

Whilst damping in general refers to the Energy dissipation present within the system, whether inherent in the construction material, through some artificial damping device or through aero-elastic interaction, the Lagrangian formulation does not explicitly account

for all forms of damping. The effects of structural damping are not explicitly accounted for and so the associated quantities must be superimposed into the system equations of motion.

Structural damping is accounted for in the models using Proportional or Rayleigh Damping. The relationship between the critical damping ratio, ξ_n and natural frequency, ω_n of the n^{th} natural frequency is given as follows, showing that the damping ratio is a function of natural frequency.

$$\xi_n = \frac{1}{2\omega_n} a_0 + \frac{\omega_n}{2} a_1 \tag{4.29}$$

The values of a_1 and a_0 can be selected using experience such that the critical-damping ratio is given at two known frequencies. If the damping ratios (ξ_i and ξ_j) associated with two specific frequencies (ω_i and ω_j) are known, the two Rayleigh damping factors a_1 and a_0 can be evaluated by the solution of a pair of simultaneous equations.

$$\begin{Bmatrix} \xi_i \\ \xi_j \end{Bmatrix} = \frac{1}{2} \begin{bmatrix} \frac{1}{\omega_i} & \omega_i \\ \frac{1}{\omega_j} & \omega_j \end{bmatrix} \begin{Bmatrix} a_0 \\ a_1 \end{Bmatrix} \tag{4.30}$$

In order to simplify the derivation of a_1 and a_0 further, it may be assumed that $\xi = \xi_i = \xi_j$, such that

$$\begin{aligned} a_1 &= \frac{2\xi}{\omega_i + \omega_j} \\ a_0 &= a_1 \omega_i \omega_j \end{aligned} \tag{4.31}$$

Therefore, in the case of the blades, the superimposed structural damping quantity

reads as given in Eq. 4.32.

$$C_{b,i,x} = a_0 M_{b,i} + a_1 K_{b,i,x}$$
$$C_{b,i,y} = a_0 M_{b,i} + a_1 K_{b,i,y} \tag{4.32}$$

In the case of the tower, a global damping matrix is found using Eqns 4.30 and 4.31 on the basis of finding values for $a_{1,s}$ $a_{1,c}$ $a_{0,s}$ and $a_{0,c}$ (note subscripts c and s refer to the concrete and steel elemental properties) using the method prescribed here. Using the global damping matrix, a reduced version is then found for each of the tower modes of vibration, which is the superimposed structural damping quantity for these modes. Depending on which model is to be developed, the term $[C_T]$ is given by $[C_T] \in [C_{g,T}], [C_{l,T}]$.

$$[C_{TR}] = [S_T]^T [C_T][S_T] \tag{4.33}$$

4.8 Aerodynamic Loading

Loading is applied to each DOF of the structure in the form of generalised time-varying loading, $Q(t)$. The aerodynamic load onto the rotor is based on drag and lift forces created by the wind field acting on the rotating blades. The temporal variation in loading arises due to turbulence in wind speeds and also the rotation of the rotor, which changes the location of loaded blades.

In terms of realising the total wind speed at any elevation, h, this is the sum of the mean wind speed and a turbulent component, $v(t,h) = \bar{v}(h) + v_t(t,h)$. The mean wind speed can be found using the Powers Law, which allows for wind shear close to ground level, with speeds rising steadily with increasing height. The turbulent component is found through using a prescribed Power Spectrum Density Function (PSDF), which describes the frequency content of a given wind speed time-history. An Inverse Fourier Transform of a PSDF will provide the required turbulent signal. In this work, an algorithm made

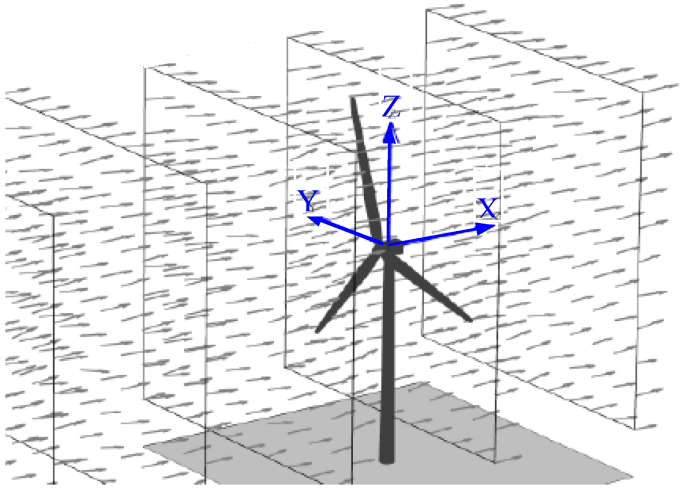

Figure 4.4: 2D Time-Marching Matrices of Along-Wind Wind Speed (TurbSim); source Jonkman [2009]

available by the National Renewable Energy laboratory (NREL), namely TurbSim, has been used (Jonkman [2009]) to simulate time series of three-component (X,Y & Z) wind-speed vectors at points in a two-dimensional vertical rectangular grid that is fixed in space.

Figure 4.4 provides a diagram which illustrates the time-marching time-series of wind speed vectors which are generated using TurbSIM. A 2D matrix of wind speeds is available at each time increment δt specified, for each global direction.

4.8.1 Blade Element Momentum Theory

Drag and lift forces acting on the blades are found using the Blade Element Momentum method (BEM). This is a well-established tool in wind turbine design, used extensively for this purpose. Aerodynamic properties of an airfoil (rotor blade) are utilised in tandem with the prevailing wind speeds and blade rotational speed (Ω_r) to generate nodal drag and lift loadings acting on elements of the blades. This theory has been used by a number of authors in preparing aerodynamic models used in the forced analysis

of wind turbine assemblies (Staino and Basu [2013], Harte and Basu [2013], Fitzgerald et al. [2013]).

BEM theory encompasses principles from areas such as three-dimensional aerodynamics, one-dimensional momentum theory and also incorporates a number of empirical correction factors to allow for fluid dynamic effects specific to wind turbine rotors. The form used here was put forward by Glauert (1935) and again presented by Hansen et al. [2006].

Each blade is to be divided into a number of elements, with the result being that at each time step, dt, a nodal drag and lift force is derived for that particular element of the blade. In dividing the swept path into annular elements, the following is assumed for each element –

- There is no radial dependency between elements, and
- The force imposed on the flow, from the blades, is constant in each annular element assuming an infinite number of blades. This will be corrected using Prandtl's tip loss factor.

The division of the swept path of the blade into annular elements of size dz, with blade chord width $c(z)$ is outlined in Figure 4.5.

In order to define the local element loads, the relative wind velocity acting on the blade, V_{rel}, must be found. This velocity is a function of the velocities seen by the blade in the normal and tangential directions, which are in turn functions of the blade rotational speed, the wind speed normal to the rotor and vortex effects created around the blade by virtue of the rotation. The vortex effects are accounted for by way of axial and tangential induction factors, a and a'. The vortex effects caused by blade rotation create wind flow in the normal and tangential directions which lead to a net rise in tangential flow but a net reduction in normal flow, which lead to the mathematical

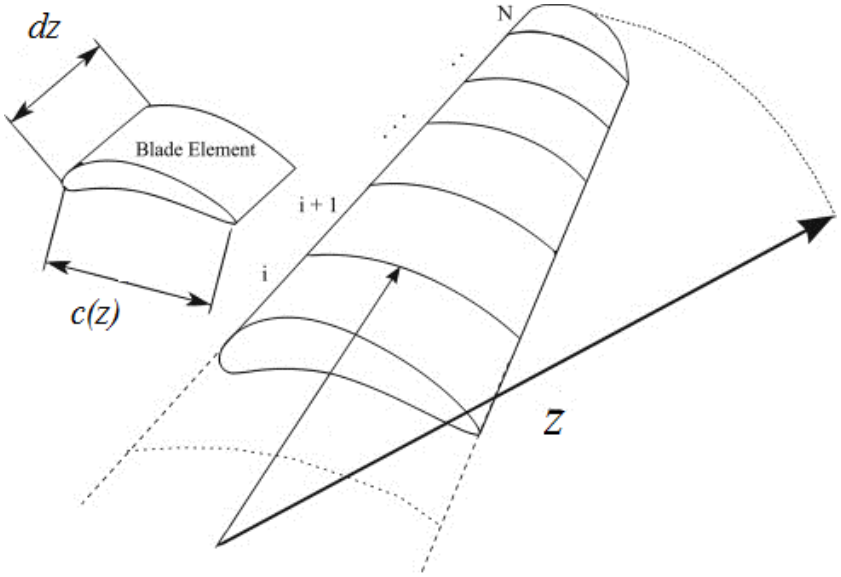

Figure 4.5: Blade Element Momentum; Blade Discretisation

expressions given.

$$V_{rel}(z,t) = \left(\left(\bar{v}(1-a) + v_t \right)^2 + \Omega_r^2 z^2 (1+a')^2 \right)^{\frac{1}{2}} \tag{4.34}$$

$$\begin{aligned} V_a &= \bar{v}(1-a) + v_t \\ V_{rot} &= \Omega_r z(1+a') \end{aligned} \tag{4.35}$$

The relative velocity, V_{rel} is then the resultant of the axial and tangential velocity components, V_a and V_{rot} respectively as provided in Eq. 4.34 and 4.35. The local flow angle, Φ, is found as per Eq. 4.36.

$$\begin{aligned} \Phi(z,t) &= tan^{-1}\left(\frac{\bar{v}(1-a) + \bar{v}_t}{\Omega_r z(1+a')} \right) \\ \varphi(z,t) &= \Phi(z,t) - \bar{\omega}_r(t) - \bar{\kappa}(z) \end{aligned} \tag{4.36}$$

The local 'angle of attack', φ is calculated using the flow angle ($\Phi(z,t)$) and the instantaneous blade pitching angle ($\bar{\omega}_r(t)$) and local pre-twist ($\bar{\kappa}(z)$) . If the lift and drag

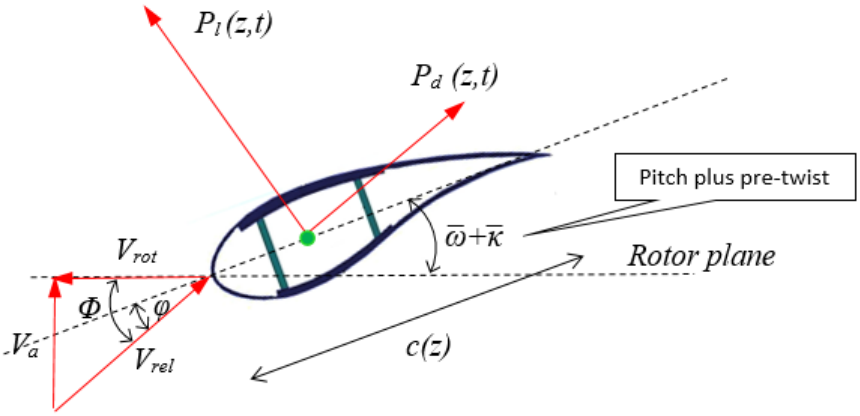

(a) BEM; Drag & Lift Loading

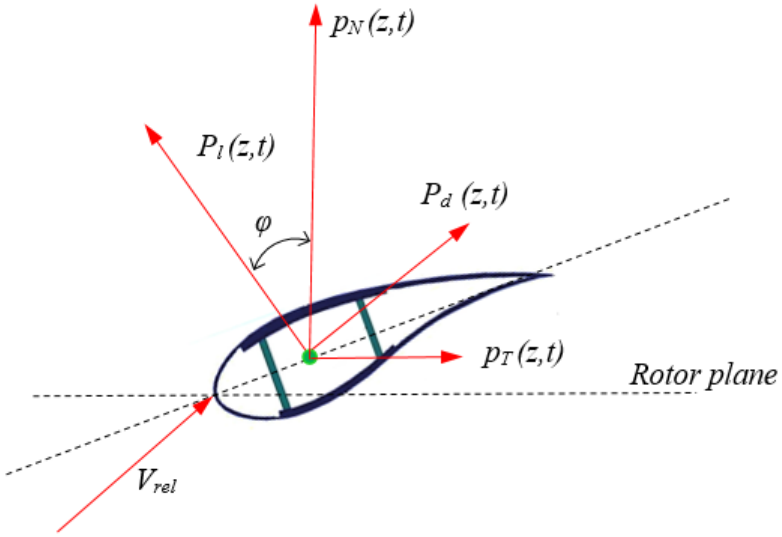

(b) BEM; Normal & Tangential Loading

Figure 4.6: Blade Element Momentum; Drag and Lift, Normal and Tangential Blade Element Loading

co-efficients, $C_l(\varphi)$ and $C_d(\varphi)$ are known for the particular airfoil in use, as well as the chord width $c(z)$, the lift and drag forces can be found, as per Eqs 4.37 and 4.38. The drag force acts parallel to the relative velocity component, V_{rel}, with the lift component acting perpendicular to this direction.

$$P_l(z,t) = \frac{1}{2}\rho_a V_{rel}^2(z,t)c(z)C_l(\varphi) \tag{4.37}$$

$$P_d(z,t) = \frac{1}{2}\rho_a V_{rel}^2(z,t)c(z)C_d(\varphi) \tag{4.38}$$

In order to convert these forces to normal and tangential directions which will align with the global axes directions of the wind turbine MDOF model, Eqs 4.39 and 4.40 can be used.

$$p_N(z,t) = P_l(z,t)cos(\varphi) + P_d(z,t)sin(\varphi) \tag{4.39}$$

$$p_T(z,t) = P_l(z,t)sin(\varphi) - P_d(z,t)cos(\varphi) \tag{4.40}$$

The mechanics of the BEM algorithm are aimed towards generating the axial and tangential induction factors, a and a' through in iterative procedure and then following Eqs 4.34 to 4.40. The drag and lift co-efficients are taken from known airfoil data tables and so do not have to be calculated within the algorithm. In calculating the induction factors, the method imposes the Prandtl tip loss factor to correct for the condition of a finite number of blades and the Glauert correction to account for unrealistically high values of a. The Glauert correction is required to adjust the induction factor to ensure the governing aerodynamic principles of the BEM are not violated.

4.8.2 Virtual Work & Aerodynamic Loading of Tower

As well as creating lift and drag forces on the rotor blades, the passage of the wind will also create drag forces on the surface of the tower. This load is small with respect to the load applied through the rotor under normal operating conditions, however, it can become significant under survival wind load conditions (when the rotor is not operating, $\Omega_r = 0$) where wind speeds are far in excess of operating wind speeds (IEC 61400 extreme wind speed of up to 70m/s at the hub under class I conditions).

4.8.2.1 11 DOF GBFE Model

The force generated on the surface of the tower in the case of the 11 DOF GBFE model, $F_T \in \mathbb{R}^{5N}$, is given in discrete terms as follows, expressed as the force applied to each tower FE node in its alongwind (X) direction, $1 \leq n \leq N$.

$$f_{Tu_{g,n,X}} = \frac{1}{2}\rho_a v(t,n)^2 A_n \tag{4.41}$$

$$\{F_T(t)\}^T \in \mathbb{R}^{5N} = [f_{Tu_{g,1,X}}, 0, 0, \cdots, 0, f_{Tu_{g,N,X}}, 0, 0, 0, 0] \tag{4.42}$$

Where in this expression the density of air is defined as ρ_a and the projected area of the tower attributed to each node is given as A_n. The wind speed v is given as $v = v(t,n)$. Using the principle of virtual work, the total work is found through assuming a virtual displacement experienced in line with the assumed shapes of vibration in the direction of wind application. The expression for this total work is given in Eq. 4.43.

$$\delta W_T = \{F_T\}^T \{s_{g,7}\} \delta q_7(t) + \{F_T\}^T \{s_{g,8}\} \delta q_8(t) \tag{4.43}$$

The tower shapes $\{s_{g,7}\}$ and $\{s_{g,8}\}$ are used to represent the displaced shapes in the fore-aft and tilting directions, which are influenced by the wind loading in these directions.

4.8.2.2 11 DOF LSFE Model

The force generated on the surface of the tower in the case of the 11 DOF LSFE model, $F_T \in \mathbb{R}^{6N}$, is given in discrete terms as follows, expressed as the force applied to each tower FE node, $n = [1, 2, \cdots, N]$.

$$f_{Tu_{l,n,X}} = \frac{1}{2}\rho_a v(t,n)^2 A_n \tag{4.44}$$

$$\{F_T(t)\}^T \in \mathbb{R}^{6N} = [f_{Tu_{l,1,X}}, 0, 0, \cdots, 0, f_{Tu_{l,N,X}}, 0, 0, 0, 0, 0] \tag{4.45}$$

The expression for this total work is given in Eq. 4.46.

$$\delta W_T = \{F_T\}^T \{s_{l,7}\} \delta q_7(t) + \{F_T\}^T \{s_{l,8}\} \delta q_8(t) \tag{4.46}$$

The tower shapes $\{s_{l,7}\}$ and $\{s_{l,8}\}$ are used in this case. The nodal loading attributed to each shell node is illustrated in Figure 4.7.

4.8.3 Gravity Loading

Virtual work carried out through gravitational load on blades in their edgewise direction can be written as per Eq. 4.47. This loading is to be applied to both 11 DOF models.

$$\delta W_{b,y,g} = \sum_{i=1}^{3} g \int_0^{R_b} m_b(z) \phi_{b,y}(z) \delta q_{b,i,y}(t) sin(\psi_i) dz \tag{4.47}$$

Gravity acts on the blades in the edgewise direction at all times, however the direction relative to the longitudinal axis of the blade varies as the blades rotate. This time dependency is captured by accounting for the azimuth angle of a given blade, ψ_i.

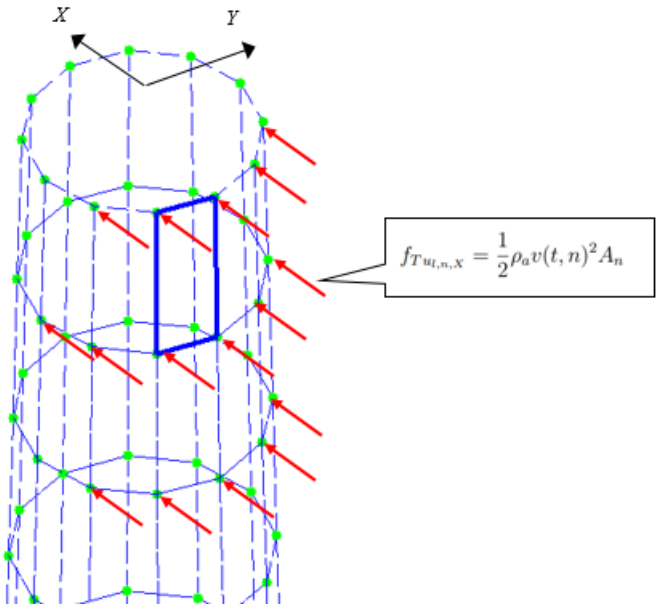

Figure 4.7: LSFE Model; Outline of Tower Nodal Loading

4.8.4 Generalised Loading

The virtual work expressions for the models are differentiated with respect to each generalised degree of freedom to find a generalised applied loading, which has a general form as per Eq. 4.48.

$$Q(t) = \frac{\delta W}{\delta q} \tag{4.48}$$

Generalised loading resulting from the above mechanisms of aerodynamic loading onto the rotor, aerodynamic loading onto the tower, gravity loading and the offset of the

tower and hub are listed in Eqs 4.49 and 4.50.

$$\begin{aligned}
\{Q_{11DOF}(t)\}^T &= \begin{bmatrix} Q_b(t) & Q_T(t) \end{bmatrix} \\
\{Q_b(t)\}^T &= \begin{bmatrix} Q_{b,1,x}(t) & Q_{b,1,y}(t) & Q_{b,2,x}(t) & Q_{b,2,y}(t) & Q_{b,3,x}(t) & Q_{b,3,y}(t) \end{bmatrix} \\
\{Q_T(t)\}^T &= \begin{bmatrix} Q_7(t) & Q_8(t) & Q_9(t) & Q_{10}(t) & Q_{11}(t) \end{bmatrix}
\end{aligned} \tag{4.49}$$

$$\begin{aligned}
Q_{b,i,x}(t) &= \int_0^{R_b} p_{N_{b,i}}(z,t)\phi_{b,x}(z)dz \\
Q_{b,i,y}(t) &= \int_0^{R_b} p_{T_{b,i}}(z,t)\phi_{b,y}(z)dz + g\int_0^{R_b} m_b(z)\phi_{b,y}(z)sin(\psi_i)dz
\end{aligned} \tag{4.50}$$

In the case of both the GBFE model and LSFE model, the entries to vector $Q_T(t)$ are as follows in Eq 4.51.

$$\begin{aligned}
Q_7(t) &= \sum_{i=1}^{3}\int_0^{R_b} p_{N_{b,i}}(z,t)\{s_7\}_{u_{N,X}}dz + \{F_T(t)\}^T\{s_7\} \\
Q_8(t) &= \sum_{i=1}^{3}\int_0^{R_b} p_{N_{b,i}}(z,t)\{s_8\}_{\theta_{N,Y}}zcos(\psi_i)dz + \big(M_{nac}g\big)\big(L_o\big)\{s_8\}_{\theta_{N,Y}} + \{F_T(t)\}^T\{s_8\} \\
Q_9(t) &= \sum_{i=1}^{3}\int_0^{R_b} p_{T_{b,i}}(z,t)\{s_9\}_{u_{N,Y}}cos(\psi_i)dz \\
Q_{10}(t) &= \sum_{i=1}^{3}\int_0^{R_b} p_{T_{b,i}}(z,t)\{s_{10}\}_{\theta_{N,X}}zdz \\
Q_{11}(t) &= \sum_{i=1}^{3}\int_0^{R_b} p_{N_{b,i}}(z,t)\{s_{11}\}_{\theta_{N,Z}}zsin(\psi_i)dz
\end{aligned} \tag{4.51}$$

The rolling moment applied to the tower top, Q_{10} is applied in this work assuming a direct drive machine, such that all of the shaft moment generated through blade edgewise loading is transferred through the generator into the nacelle and tower top.

4.9 Benchmarking

In order to validate the 11 DOF GBFE model and LSFE model, a global assessment of the NREL 5MW baseline turbine free vibration properties was carried out. This exercise was completed using the two established models, along with the NREL code FAST (Jonkman and Buhl Jr). Steady-state quantities are extracted from the 11 DOF model EOM about initial conditions, assuming no rotor rotation. One of the blades is set to the vertical position at an azimuth angle of 0^0. This results in the elimination of centrifugal stiffening from the EOM. By taking the system mass and stiffness matrices, it is then possible to carry out an eigen-analysis and to extract modal frequencies and mode shapes.

In order to introduce steady state conditions within the FAST model, a facility known as 'Linearization' can be used. Within the input properties for FAST, the rotor is to be set to a static state ($\Omega_r = 0$). The degrees of freedom activated are chosen as the fundamental tower fore-aft and side-side DOFs and the fundamental blade flapwise and edgewise DOF for each blade. All other DOFs are de-activated in FAST. Linearized state matrices are then produced by manipulating the system mass and forcing function matrices. The modal frequencies and shapes are extracted from the steady state matrices using MATLAB.

Table 4.1 provides results from both the developed 11 DOF models and FAST. These are in close agreement, particularly in the case of the towers. Differences in terms of blade frequencies are thought to be due to the allowance of blade pre-twist within FAST.

4.10 Conclusions

In this chapter, the approximate, finite element models developed in Chapter 3 have been incorporated into MDOF models based on Euler-Lagrangian dynamics. Tower finite element displacement vectors are expressed as functions of the reduced order tower DOF's and the global interpolation functions. Total Potential and Kinetic Energy

-	FAST (Hz)	11 DOF LSFE Model (Hz)	11 DOF GBFE Model (Hz)
Tower 1	0.325	0.328	0.324
Tower 2	0.315	0.331	0.326
Flapwise 1	0.674	0.682	0.697
Flapwise 2	0.677	0.682	0.697
Flapwise 3	0.693	0.699	0.714
Edgewise 1	1.085	1.046	1.067
Edgewise 2	1.085	1.046	1.067
Edgewise 3	1.116	1.06	1.081

Table 4.1: 11 DOF Model Benchmarking; NREL FAST, 11 DOF LSFE Model & 11 DOF GBFE Model

formulations are described for the model, which are used to derive the equations of motion. Damping is introduced directly as only conservative forces are included in the Euler-Lagrangian formulation.

Generalised loading was found for each DOF through the use of the principle of virtual work. The physical loading generated by the rotor, through the rotating blades has been numerically determined using the BEM method. Drag and lift forces are calculated for the blade aerfoil in an iterative manner and on the basis of a number of assumptions in terms of the behaviour of the wind field and its interaction with the rotor blades. Drag force developed through wind acting directly on the tower is also accounted for.

The 11 DOF GBFE Model was developed for use in situations where only global responses of the tower are required. Where review of local responses are required (for local design, damage detection, prestress application for example), the 11 DOF LSFE Model may be used. Both models will be applied to suitable scenarios in later parts of this thesis.

Chapter 5

Response of Hybrid Concrete - Steel Towers

5.1 Introduction

In this chapter, the models formulated to describe the towers, both in isolation and as part of overall turbine assemblies, will be used to examine the response of hybrid concrete and steel wind turbine towers, subjected to varying design configurations. In the first part of this chapter, a review of global and local response is carried out on the basis of varying the external loading exposure conditions.

Next, taking a number of load cases, response behaviour based on varying the design parameters specific to this hybrid form of construction are studied in detail. These include the influence of varying levels of structural damping offered by the steel and concrete parts of the tower, the influence of concrete compressive strength, and the influence of an applied prestress.

Properties	Symbol	Units	Tower 1
Tower Height	H	m	100
Base Diameter	D_c	m	8.8
Base Shell	t_c	mm	500-350
Top Diameter	D_s	m	3
Top Shell	t_s	mm	40-25
Interface lvl	h_{int}	m	60
Interface Dia	D_{int}	m	6.5
Fore-aft freq	f	Hz	0.53
Conc damping	ξ_c	-	0.05
Steel damping	ξ_s	-	0.02

Table 5.1: Hybrid Tower 1; Geometrical and Material Properties

5.2 Dynamic Response Simulations

In Chapter 4 the dynamic equations of motion for both the 11 DOF Global Beam FE (GBFE) Model and 11 DOF Local Shell FE (LSFE) Model models were described. In this section, the models will be exposed to a number of different load conditions and the time varying load and responses of the models will be presented. The global responses will be presented using the results of the 11 DOF GBFE model. Local element strain responses will be presented using the results of the 11 DOF LSFE model.

The NREL 5MW baseline turbine (Jonkman et al.) was used to develop and benchmark both coupled structural models. Properties of this turbine are given in Appendix G. For the purposes of modelling typical responses in this chapter, the tower segment of the NREL turbine was replaced with a hybrid steel and concrete tower taken from a study carried out as part of the Vindforsk project V-342 into design and construction approaches for such towers (Engström et al. [2010]). Whilst not all data required in terms of modelling has been provided by this report, sufficient data was provided to be able to tune input properties to match its given natural frequency of 0.53 Hz, allowing for the nacelle mass provided with the NREL baseline turbine data. For the purposes of use elsewhere in this thesis, it is termed Hybrid Tower 1. Geometrical and material properties of this tower are given in 5.1.

Loadcase	$\bar{v}$ (m/s)	I (%)	Ω_r (rpm)
LC 1	12	0	12.1
LC 2	16	0	12.1
LC 3	20	0	12.1
LC 4	12	14	12.1
LC 5	16	14	12.1
LC 6	20	14	12.1
LC 7	12	25	12.1
LC 8	16	25	12.1
LC 9	20	25	12.1
LC 10	50	14	0

Table 5.2: Forced Simulation Loadcases 1 to 10

A total of ten load cases were applied to both 11 DOF models, designed to review the variation in loading, global response and local response as a result of varying exposure and operating conditions. The details of these loadcases are provided in Table 5.2

5.2.1 Global Loading

For operating conditions (Loadcases LC 1 to LC 9), the blades of the turbine are rotating at a specified rate of rotation, with the result that an aerodynamic load is being developed and transferred to the tower top. Blade drag forces are derived using BEM theory. In the parked condition (Loadcase LC 10), blades are not rotating and are pitched out of the wind. In this case, there is no drag force developed on the blades. There is only a drag force developed over the surface of the tower.

5.2.1.1 Operating Conditions

Figure 5.1 identifies the generalised load applied in the fore-aft direction ($Q_7(t)$) both in the case of load cases LC 1 and LC 4, where in load case LC 1 there is no turbulence and in load case LC 4, turbulence has been introduced. A mean wind speed, $\bar{v}$, of 12m/s has been used.

The load applied in LC1 is clearly a sinusoidal load. The period of the signal is a

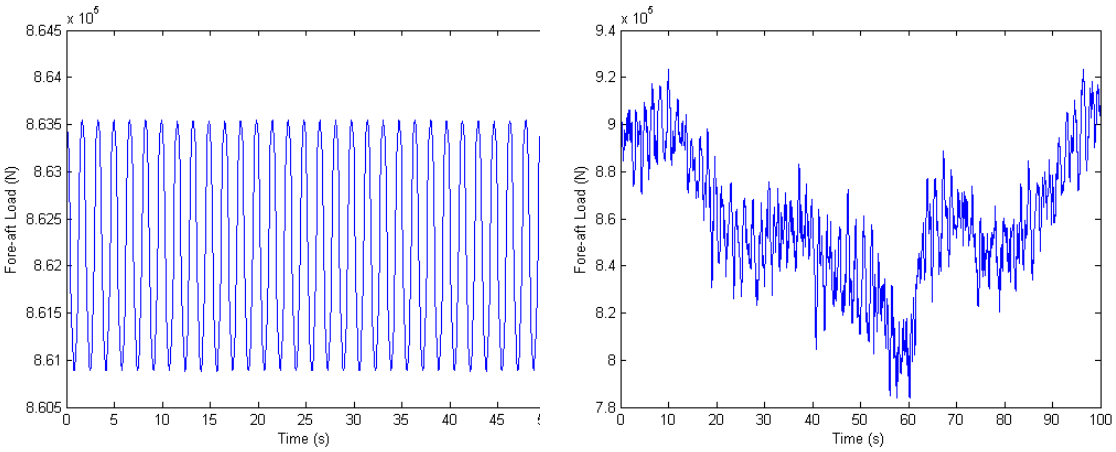

(a) $Q_7(t)$, LC 1 (b) $Q_7(t)$, LC 4

Figure 5.1: Fore-Aft Load $Q_7(t)$, LC 1 & LC 4, Variable Turbulence

function of the rotational speed of the rotor and is a result of a varying wind speed, and thus drag force, with height. There is no temporal variation in wind speed. Conversely, the introduction of turbulence in LC4 has produced a far more irregular loading time-history. Variations in this signal are as a result of a variation in mean wind speed with height and as a result of the turbulent part of the wind speed. It is apparent however that the mean load over time is the same for both LC1 and LC4.

The impact of a variation in mean wind speed, $\bar{v}$, and also turbulence level, I, can be reviewed by presenting the fore-aft displacement initially for LC1, LC2 and LC3 and then next for load cases LC2, LC5 and LC8. These plots are given in Figure 5.2.

The plots in the case of varying the mean wind speed illustrate the proportional increase in mean fore-aft loading. In the case of the increasing turbulence levels, it is clear that the mean fore-aft load is unaltered, however the temporal deviation in applied load increases with increase in wind speed turbulence.

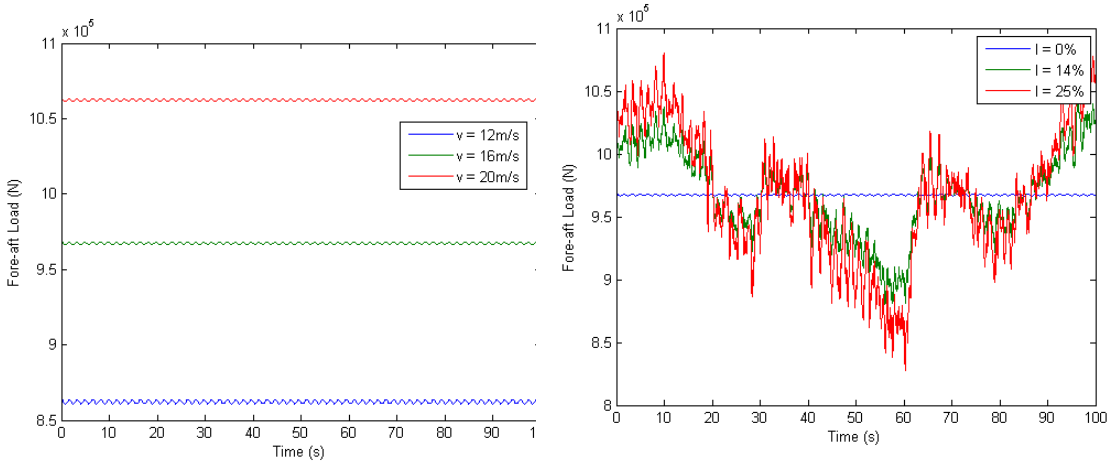

(a) Variable Wind Speed (LC 1, 2 & 3), $Q_7(t)$

(b) Variable Turbulence Intensity (LC 2, 5 & 8), $Q_7(t)$

Figure 5.2: Fore-aft Load $Q_7(t)$, Variable Wind Speed (LC 1, 2 & 3) and Turbulence (LC 2, 5 & 8)

5.2.1.2 Parked Conditions

The global load applied in the parked condition is due to wind drag forces generated on the surface of the tower alone.

Figure 5.3 provides the fore-aft loading for the parked condition. The dominant frequencies in this case are now clearly the frequencies in the turbulent wind speed, as there is no frequency component associated with drag loading of the rotating blades. Figure 5.3 also provides plots of this load for LC1 and LC10 to allow some comparison in terms of order of magnitude. In this case, the parked condition provides a load which is close to that of the operating condition, but does not exceed the loading in this case.

5.2.2 11 DOF GBFE Model - Global Response

Load cases LC1 to LC10 were each applied to the 11 DOF GBFE Model. The responses are summarised below for some of these load cases in terms of the responses of the top of the tower in its five degrees of freedom.

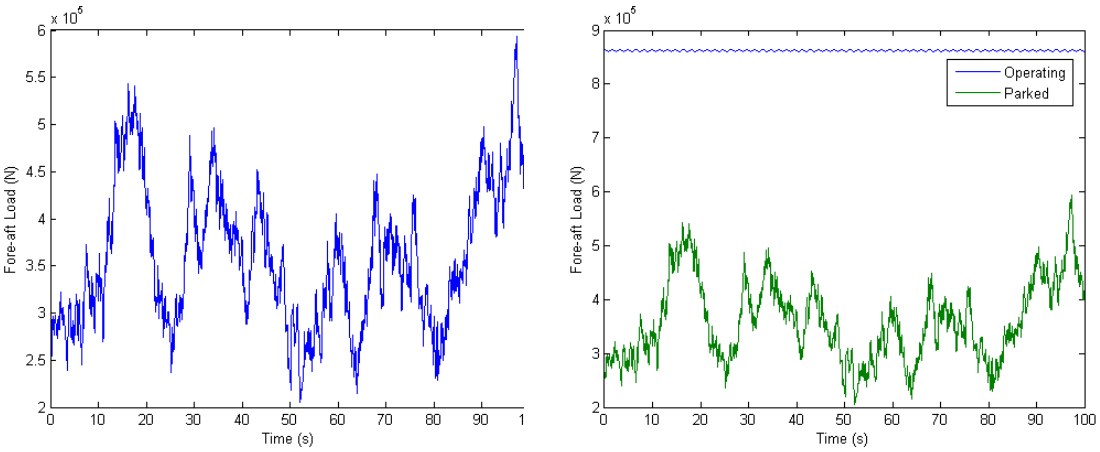

(a) Fore-aft load, $Q_7(t)$, LC 10

(b) Fore-aft load, $Q_7(t)$, LC 1 & LC10

Figure 5.3: Fore-Aft Load $Q_7(t)$, (LC 1 & LC 10), Operating and Parked Conditions

5.2.2.1 Operating Conditions

In this case, the blades are rotating at the rated speed for the NREL turbine, which is 12.1 rpm (Ω_r = 12.1 rpm). Figure 5.4 identifies the displacement experienced in the fore-aft direction ($u_{N,X}$) both in the case of load cases LC1 and LC4. Where turbulence is introduced, there is an ongoing level of vibration.

Figure 5.5 provides the displacement time histories for the tilting $\theta_{N,Y}$ and side-side $u_{N,Y}$ motion of node N at the top of the tower. The side-side displacement is initially large and through damping, dissipates to vibrate at a near mean level of 0.04m. The slower reduction in peak displacement levels compared to the fore-aft time history can be attributed to the lack of aerodynamic damping offered by the rotor blades in their edgewise direction.

In order to review the effect of a change in mean hub height wind speed, $\bar{v}$, the results in terms of fore-aft tower top displacement can be viewed together, for load cases LC1, LC2 and LC3 are presented in Figure 5.6.

The time histories shown in Figure 5.6 clearly show that the increase in mean wind

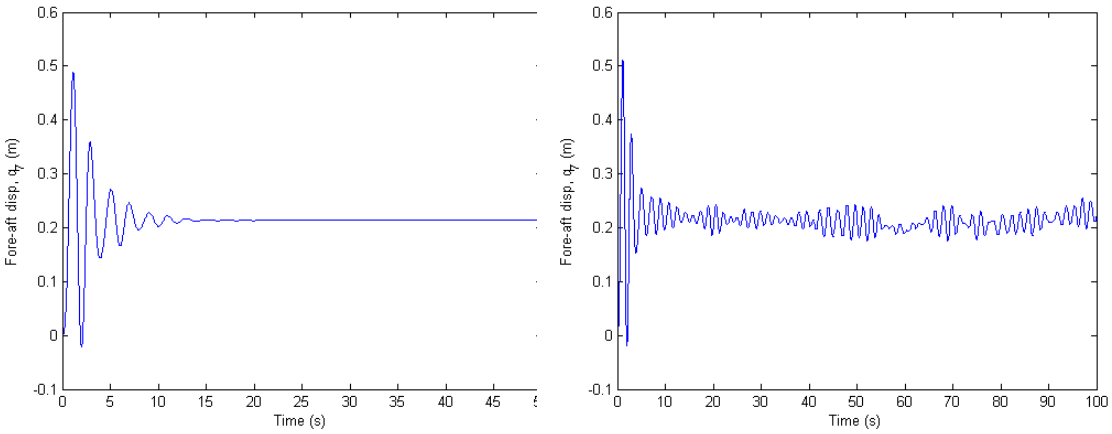

(a) Fore-aft disp, $u_{N,X}$, LC1

(b) Fore-aft disp, $u_{N,X}$, LC4

Figure 5.4: Fore-Aft Displacement $u_{N,X}(t)$, LC 1 & LC 4, Variable Turbulence

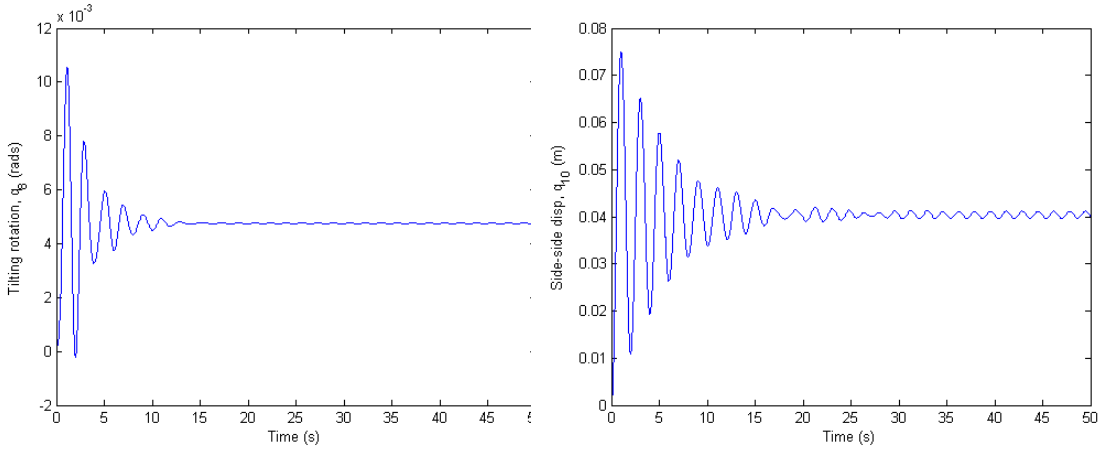

(a) Tilting rotation, $\theta_{N,Y}$, LC1

(b) Side-side disp, $u_{N,Y}$, LC1

Figure 5.5: Tilting Rotation $\theta_{N,Y}(t)$ and Fore-Aft Displacement $u_{N,Y}(t)$, LC1, Zero Turbulence

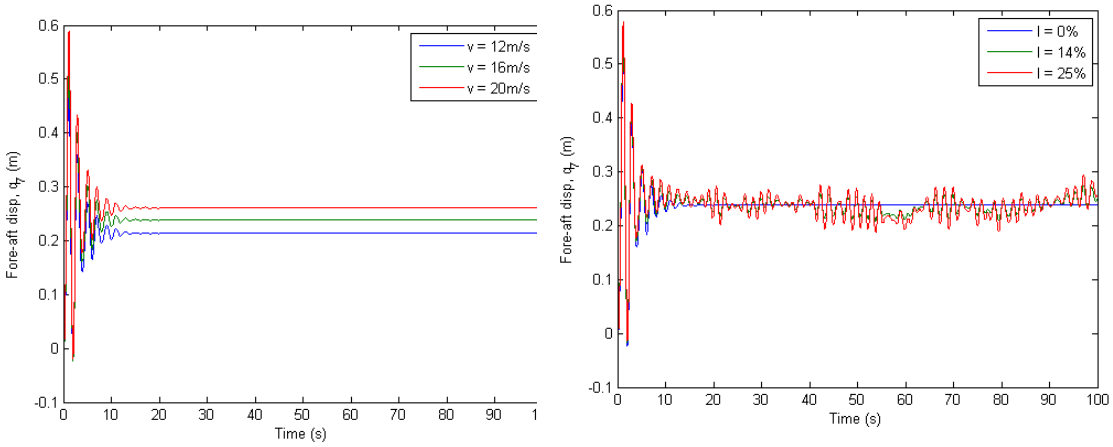

(a) $u_{N,X}$ (LC 1, 2 & 3), Variable Wind Speed

(b) $u_{N,X}$ (LC 2, 5 & 8), Variable Turbulence Intensity

Figure 5.6: Fore-Aft Displacement $u_{N,X}(t)$, Variable Wind Speed (LC 1, 2 & 3) and Turbulence (LC 2, 5 & 8)

speed leads to an increase in mean tower top displacement. The mean displacement increases from 0.21m/s to 0.27m/s on increase in mean wind speed, $\bar{v}$, from 12m/s to 20m/s.

In the same manner, it is possible to examine the effect of an increase in turbulence level on the fore-aft displacement time history. Load cases LC2, LC5 and LC8 are considered and the results presented in Figure 5.6 for this degree of freedom.

The time-histories presented indicate that the mean tower top displacement is consistent and is not impacted by the change in turbulence level, I. When the turbulence level is introduced and varied, there is an increase in peak displacement levels over the duration of the simulation.

5.2.2.2 Parked Conditions

The fore-aft displacement experienced in the parked condition can be found through applying loads generated for load case LC10.

Figure 5.7 provides the fore-aft displacement for the parked condition. The displacement

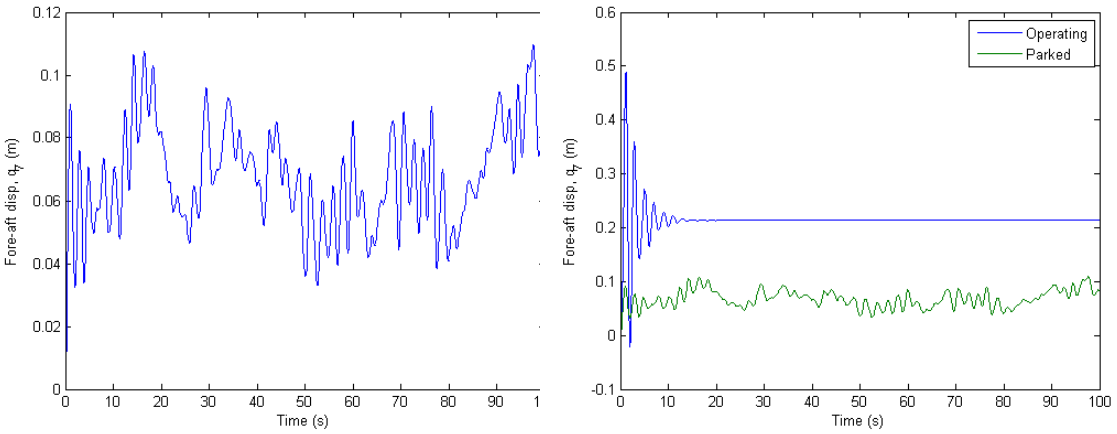

(a) Fore-aft disp, $u_{N,X}$, LC10

(b) Fore-aft disp, $u_{N,X}$, LC1 & LC10

Figure 5.7: Fore-Aft Displacement $u_{N,X}(t)$, Operating (LC1) and Parked (LC10) Conditions

time history indicates that whilst there is an initial unsteady period of vibration, similar to the time history of load cases both with and without turbulence under operating conditions, the peak displacement level occurs after this initial transient period ends.

Figure 5.7 also provides plots of the displacement for LC1 and LC10 to allow some comparison in terms of order of magnitude. In this case, the parked condition results in a displacement which is close to that of the operating condition, but does not exceed the loading in this case. However, ongoing vibration continues after the initial transient period, unlike that of LC1.

5.2.3 11 DOF LSFE Model - Local Response

Load cases LC1 to LC10 were also applied to the 11 DOF LSFE Model. The local responses were obtained for a shell element at the base of the tower, whose local out-of-plane axis is parallel with the fore-aft direction.

The results are reviewed in terms of local principal strain including vertical ϵ_x, circumferential, ϵ_y, and shear strain γ_{xy}. These quantities can be extracted from the 11 DOF model through steps outlined elsewhere in this thesis. The element chosen is the first of

the towers N elements and is denoted $\{\varepsilon_1\}^T = [\varepsilon_{1,x}, \varepsilon_{1,y}, \gamma_{1,xy}]$. The element is shown in more detail in Figure 5.13.

At the base of the tower, the vertical strain, $\varepsilon_{1,y}$, is the dominant strain in terms of magnitude when compared to the strain in the circumferential, $\varepsilon_{1,x}$, or shear, $\gamma_{1,xy}$, directions.

5.2.3.1 Operating Conditions

Figure 5.8 identifies the strain experienced by the selected local element initially without turbulence (LC1) and also with some level of turbulence (LC4).

Considering the strain time histories without turbulence initially, it is clear that the vertical strain is the primary form of strain relative to circumferential and shear strain. The vertical strain time history is similar to the fore-aft deflection time history in shape, however there are some differences. The circumferential strain time history is similar to that of the side-side global displacement time history, but again with some differences. When comparing the strain time histories with turbulence to the displacement time histories with turbulence, the strain histories appear to be vibrating over a broader range of frequencies than the displacement histories in any direction. This could be attributed to the fact that the strain at any point in time is a combination of the effects of the global displacements at that point in time.

In terms of the strain time histories where turbulence is present, the mean strain is the same as the mean strain without turbulence.

In order to review the effect of a change in mean hub height wind speed, $\bar{v}$, the results in terms of vertical strain, $\epsilon_{1,y}$, can be viewed together, for load cases LC1, LC2 and LC3 are presented in Figure 5.9. There is an increase in vertical strain proportionate with the increase in mean wind speed.

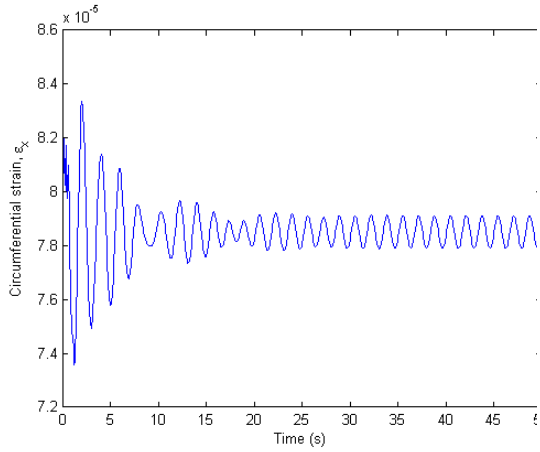

(a) Time v $\varepsilon_{1,x}$, LC1

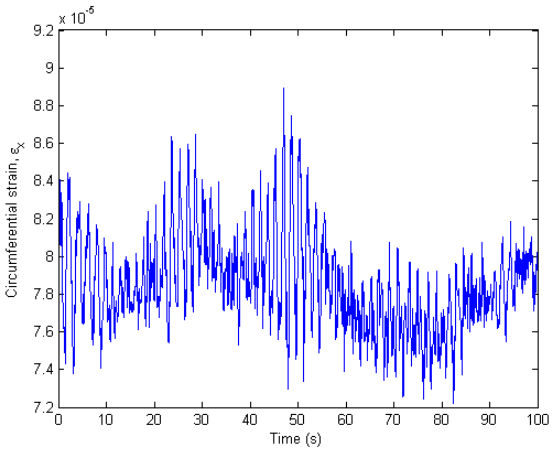

(b) Time v $\varepsilon_{1,x}$, LC4

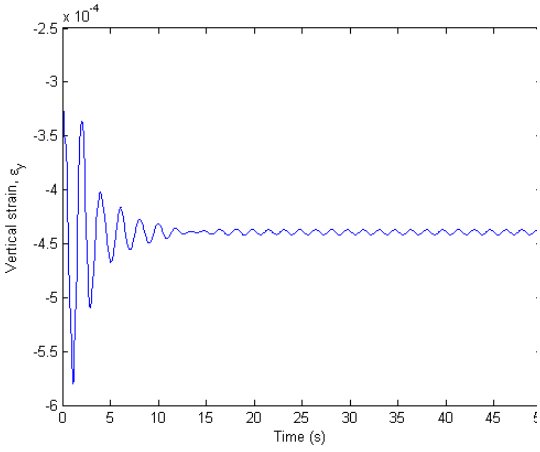

(c) Time v $\varepsilon_{1,y}$, LC1

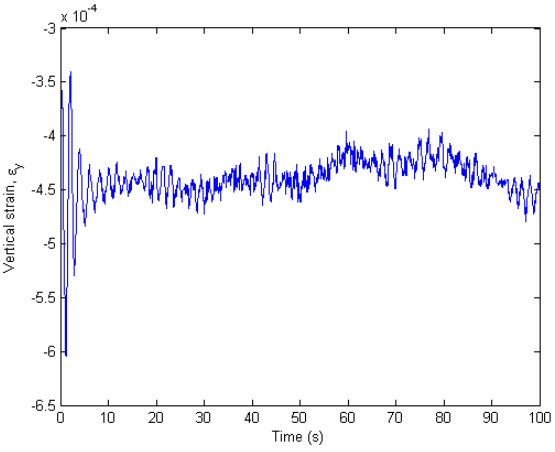

(d) Time v $\varepsilon_{1,y}$, LC4

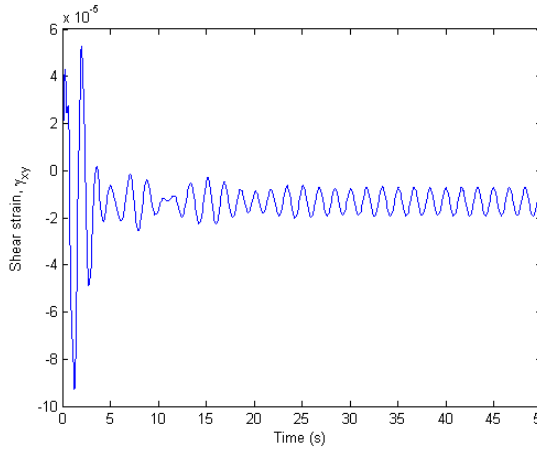

(e) Time v $\gamma_{1,xy}$, LC1

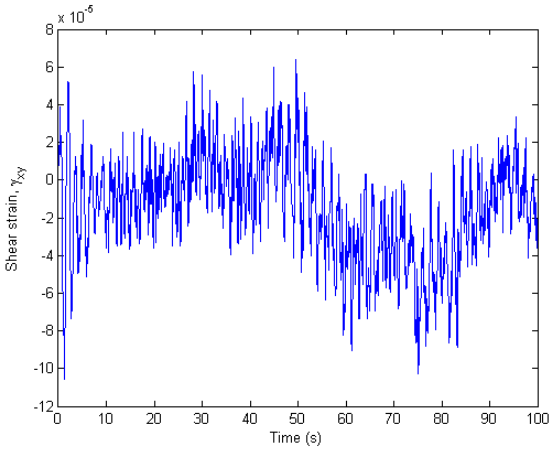

(f) Time v $\gamma_{1,xy}$, LC4

Figure 5.8: Vertical, Circumferential and Shear Strain $\varepsilon_1(t)$, With & Without Turbulence (LC 1 & LC 10)

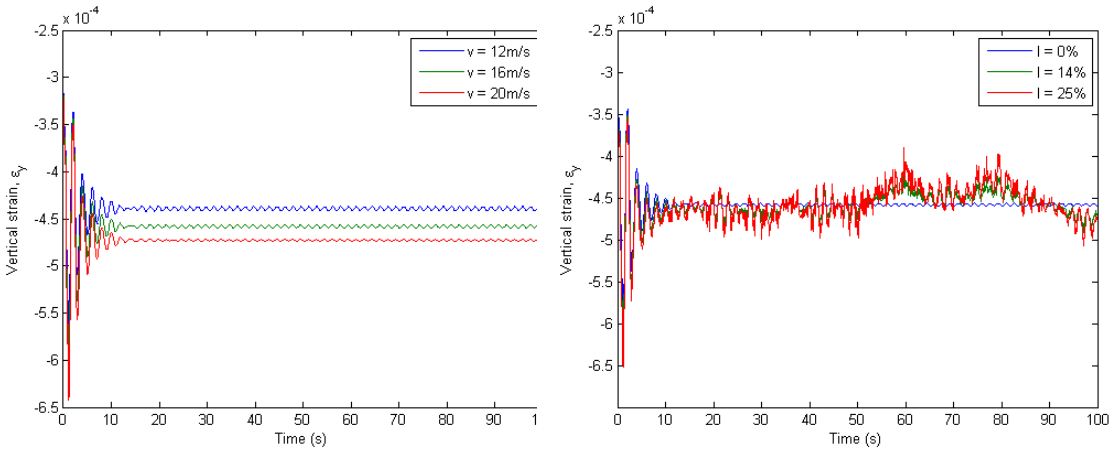

(a) Variable Wind Speed, $\varepsilon_{1,y}$ (b) Variable Turbulence Intensity, $\varepsilon_{1,y}$

Figure 5.9: Vertical Strain $\varepsilon_{1,y}(t)$, Variable Wind Speed & Variable Turbulence

5.2.3.2 Parked Conditions

The strain histories experienced in the parked condition can be found through applying loads generated for load case LC10. Circumferential, vertical and shear strain are given in Figure 5.10, along with the same histories compare to the LC1 strains.

The mean strain in the case of the vertical and circumferential strain is higher in the operating condition than in the parked condition. However, the mean strain in shear is highest in the parked condition. This is attributed to the fact that the tower will deform differently in this condition as compared to the operating condition with high bending and thrust applied at the tower top.

5.3 Hybrid Towers - Sensitivity Analysis

Two of the structural models constructed have been used in this part of the review. The exact, analytical model of the tower was used to evaluate the free vibration response KPIs. The 11 DOF GBFE model was used to evaluate the forced response KPIs.

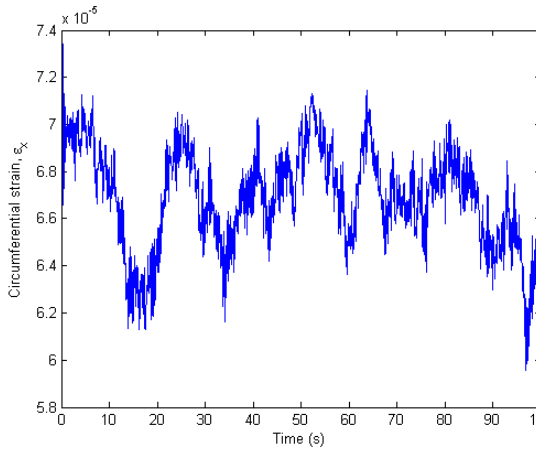

(a) Time v $\varepsilon_{1,x}$, LC10

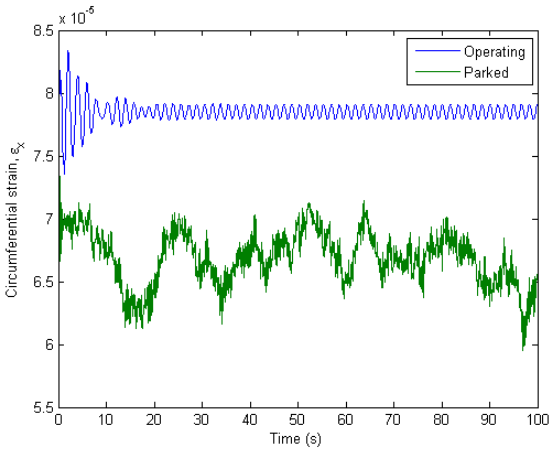

(b) Time v $\varepsilon_{1,x}$, LC1 & LC10

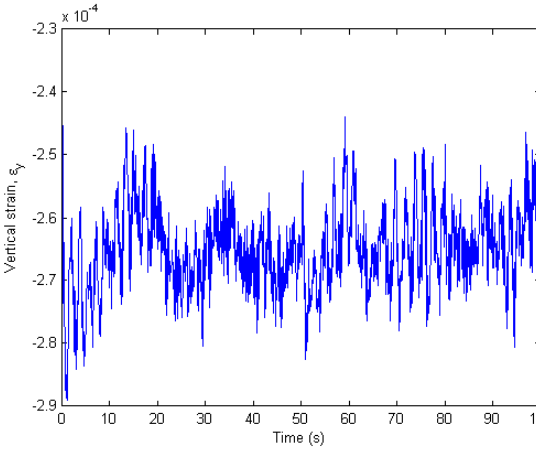

(c) Time v $\varepsilon_{1,y}$, LC10

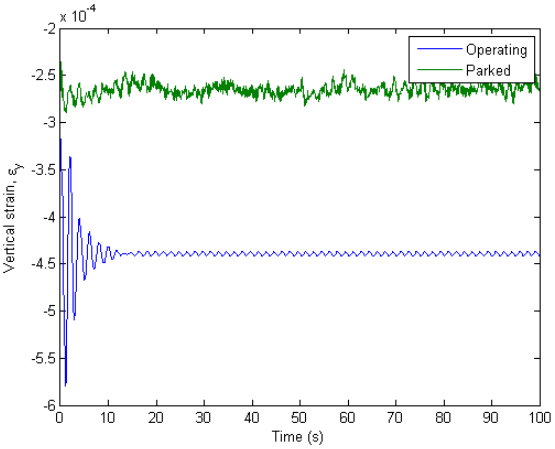

(d) Time v $\varepsilon_{1,y}$, LC1 & LC10

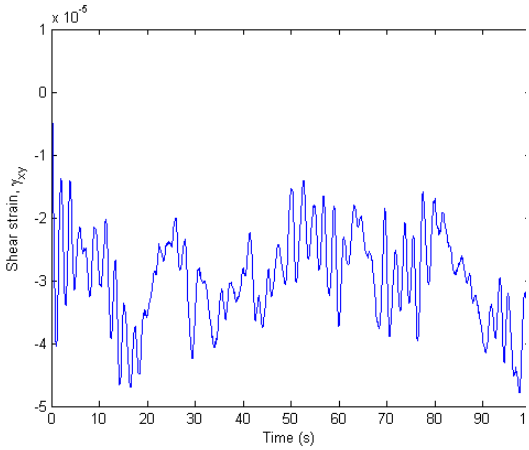

(e) Time v $\gamma_{1,xy}$, LC10

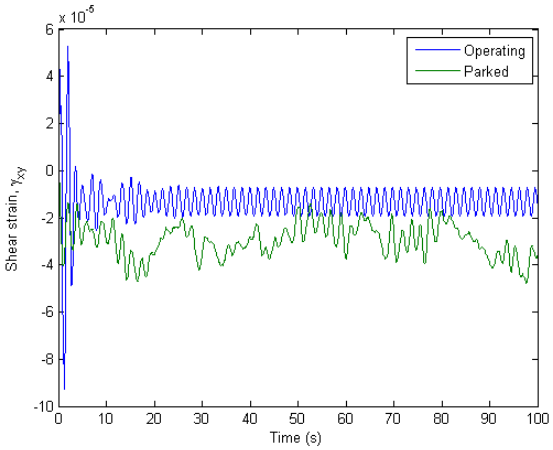

(f) Time v $\gamma_{1,xy}$, LC1 & LC10

Figure 5.10: Vertical, Circumferential & Shear Strain $\varepsilon_1(t)$, Operating (LC 1) & Parked (LC 10) Conditions

x_i, Inputs	Symbol	Units	x_i^{LB}	x_i^{UB}
x_1, Diameter Concrete	D_c	m	7.5	15
x_2, Thickness Concrete	t_c	m	0.1	0.4
x_3, Diameter Steel	D_s	m	4	6
x_4, Thickness Steel	t_s	m	0.02	0.03
x_5, Interface Height/Tower Height	h_{int}/H	%	0.2	0.8
x_6, Tower Top Mass	M_{nac}	kg	0	0.6

Table 5.3: KPI Design Variables

5.3.1 Design Parameters & Response Key Performance Indicators

A select number of fundamental design parameters are used in order to make some initial findings as to their respective influence on the response characteristics. These are listed in Table 5.4.

Key inputs were selected to represent the more fundamental design choices available in the design of a hybrid concrete-steel tower. Five geometrical parameters were chosen including the diameters of the respective portions of the tower and the thicknesses of these shells. Also included is the height of the concrete-steel interface. Finally, a sixth parameter to represent the mass of the nacelle as a percentage of the overall tower mass was included as this is expected to have a significant influence on the response characteristics of such a tower. The list of variables and range of each variable is provided in Table 5.3. It is noted that there are many more design properties which could have been included – for example, real towers would normally include some taper of the tower diameter as well as a taper of the shell thickness with increasing height. There would also be some prestressed and non-prestressed steel reinforcement in the concrete section of tower to ensure cracking of the concrete did not occur. Whilst these effects would have some effect on the response of the tower, they have been omitted for the purposes of this initial review.

Response KPI	Symbol	Units
1st Natural Frequency	ω_1	rad s^{-1}
2nd Natural Frequency	ω_2	rad s^{-1}
3rd Natural Frequency	ω_3	rad s^{-1}
displacement	$u_{N,X}$	m
velocity	$\frac{du_{N,X}}{dt}$	m/s
acceleration	$\frac{d^2u_{N,X}}{dt^2}$	m/s^2
Concrete Mass	M_c	kg
Steel Mass	M_s	kg
Total Tower Mass	M_{Tower}	kg

Table 5.4: Response KPIs

5.3.2 Design of Experiment/Model Configuration

There are six design parameters to be varied in modelling the performance of the tower. Therefore there are six dimensions to the domain being considered. If design combinations were found by taking points at each of the upper and lower limits of each dimension only, there would be $2^6 = 64$ combinations required. If a mid-point input was included, this would lead to $3^6 = 729$ combinations. Another method of ensuring a desired uniform spread of sampling points across the six dimensions chosen, without the need to sub-divide each dimension, is to use the statistical point sampling method known as the Latin Hypercube algorithm, as used by Olsson et al. [2003]. This method was used here to generate a total of 2000 configurations using the six input parameters.

The implementation of this sampling method is carried out using an embedded MATLAB function. A pre-defined number of 2000 configurations was taken as an input, as well as defining six dimensions to the hypercube. The result is 2000 randomly distributed but entirely unique points within the domain.

5.3.3 Forced Response Applied Loading

Load case LC 4 is used in the sensitivity analysis. The rotor is operational and working at a rated speed of $\Omega = 12.1rpm$. Generalised loading values are evaluated using

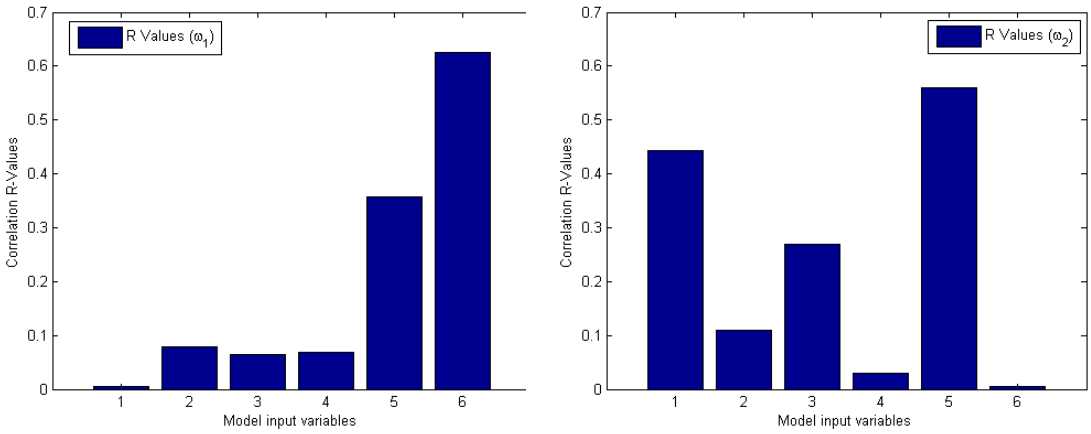

(a) Correlation values, ω_1

(b) Correlation values, ω_2

Figure 5.11: Absolute Values of Correlations between Input Variables & Selected Free Vibration Responses (ω_1, ω_2)

methods outlined in Chapter 4 (Aerodynamic Loading).

5.3.4 Key Performance Indicator Results

5.3.4.1 Free Vibration

Free vibration response KPIs are evaluated for each tower configuration using the exact closed form expressions developed in Chapter 3. Figure 5.11 gives a graphical representation of the correlation values of the ω_1 and ω_2 responses in absolute terms. From the correlation plots the factor which has the most significant impact on the first natural frequency, ω_1, is the tower top mass, M_{nac} (x_6). An increase in the ratio of top mass to tower mass will lead to a decrease in natural frequency. The interface height relative to the height of the tower, h_{int}/H (x_5) also seems to have a significant impact, with an increase in interface height yielding an increase in frequency. Other input parameters do not appear to have a significant impact on the first natural frequency.

The second natural frequency, ω_2, is most strongly impacted by the interface height (x_5). An increase in interface height relative to total height will lead to a decrease in

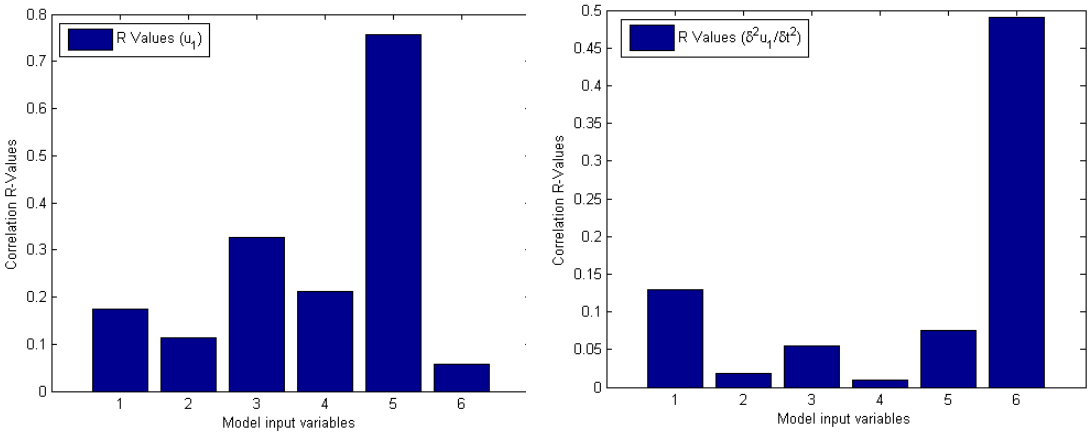

(a) Correlation values, $u_{N,X}$

(b) Correlation values, $\frac{d^2u_{N,X}}{dt^2}$

Figure 5.12: Absolute Values of Correlations between Input Variables & Selected Forced Vibration Responses $u_{N,X}$, $\frac{d^2u_{N,X}}{dt^2}$

this response KPI. Beyond this, there is a reasonably strong relationship between the second frequency and the base diameter (x_1) and to a lesser extent the upper, steel diameter (x_3). Increases in these input values will yield an increase in frequency.

5.3.4.2 Forced Vibration

Forced vibration response KPIs are evaluated for each tower configuration using the 11 DOF GBFE model.

The tower top displacement, $u_{N,X}$ is strongly correlated to the interface level. There is a weak relationship between the displacement and the tower top mass. A moderate relationship exists between the displacement and the diameter and thicknesses of the lower and upper segments.

Figure 5.12 graphically demonstrates the correlation values in absolute terms for the displacement and acceleration indicators.

In terms of velocity $\frac{du_{N,X}}{dt}$ and acceleration $\frac{d^2u_{N,X}}{dt^2}$, the tower top mass has a significant influence. The interface height to total height ratio has a strong relationship with

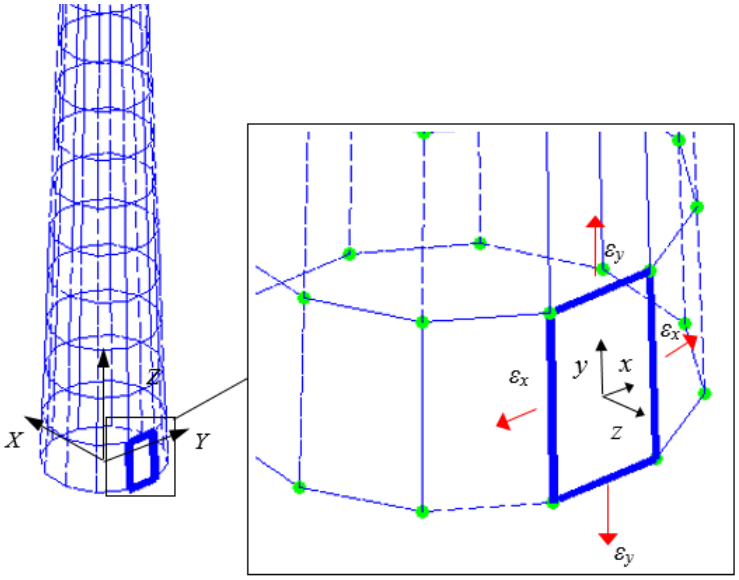

Figure 5.13: Local Shell Element Strain & Axes Convention

the velocity but a relatively weak relationship with acceleration. The tower segment diameters have somewhat of an influence on the velocity and acceleration signals. The tower thicknesses have a negligible impact on the forced vibration responses compared to other inputs listed above.

5.4 Key Design Parameters – Forced Vibration Response

Global responses are generated using the 11 DOF GBFE model. Local strain responses are found using the 11 DOF LSFE model. The element chosen for review is the first of the towers N elements and is denoted $\{\varepsilon_1\}^T = [\varepsilon_{1,x}, \varepsilon_{1,y}, \gamma_{1,xy}]$. This local finite element is located such that the plane of the element is normal to the tower fore-aft degree of freedom and parallel to the side-side degree of freedom. The element is shown in more detail in Figure 5.13.

Tower Properties	Symbol	Units	Tower 2	Tower 3	Tower 4	Tower 5
Tower Height	H	m	100	100	100	100
Base Diameter	D_c	m	8.8	8.8	8.8	8.8
Base Shell	t_c	mm	350	350	350	350
Top Diameter	D_s	m	3	3	3	3
Top Shell	t_s	mm	25	25	25	25
Interface lvl	h_{int}	m	20	40	60	80
Interface Dia	D_{int}	m	6.5	6.5	6.5	6.5
Fore-aft freq	f_1	Hz	0.550	0.647	0.678	0.671
Tower Top Mass	M_{nac}	kg	296,740	296,740	296,740	296,740
Tower Mass	M_{Tower}	kg	720,844	1,032,273	1,343,701	1,655,130
Mass Ratio	$\frac{M_{nac}}{M_{Tower}}$	-	0.41	0.29	0.22	0.18
Conc damping	ξ_c	-	0.05	0.05	0.05	0.05
Steel damping	ξ_s	-	0.02	0.02	0.02	0.02
Conc stength	f_{ck}	MPa	50	50	50	50

Table 5.5: Hybrid Towers 2-5; Geometrical and Material Properties

5.4.1 Hybrid Concrete-Steel Interface Level

Loadcase LC5 was used to run simulations for each tower which is based on a mean hub height wind speed, $\bar{v}$ of 16m/s and a turbulence level, I of 14%. In this case, a series of hybrid tower configurations will be used with varying properties in line with Table 5.5.

The global displacement and acceleration data is presented in Figure 5.14. Fore-aft tower top displacement and acceleration is represented in the time and frequency domain. The mean tower top displacement reduces with increasing hybrid interface height. From the Fast Fourier Transform (FFT) plot of this data, it is clear that the amplitude of vibration about the mean also reduces with increase interface height, as represented by the decrease in the peak at this frequency. The first peak represents the natural frequency of the tower and is the dominant frequency in all cases. The FFT plot also shows that the first peak moves to the right with increasing interface height. This indicates that the stiffness of the tower is increasing. The second peak in the FFT plots does not change location with increasing interface height. This peak represents the 3P rotational frequency of the rotor.

The global acceleration has a mean value of $\frac{d^2u_{N,X}}{dt^2} = 0m/s^2$, which is unaffected by changing tower properties. The amplitude of acceleration changes and increases with increasing interface height. The acceleration FFT plot shows the change in location of the first peak, coinciding with the change in tower natural frequency.

When considering the results of this review in terms of global response to the sensitivity analysis previously carried out, the results are as expected in light of the sensitivity analysis results. There is a significant reduction in mean displacement with increase in interface height. In addition, there is a reduction in vibration amplitude. The acceleration variation is not as pronounced as the displacement variation. The relationship with tower natural frequency was identified in this assessment and was as expected when considering the results of the sensitivity analysis carried out using the exact model.

Local strain signals are presented in the time and frequency domain in Figure 5.15 for an element at the base of the tower. The time history of vertical shear strain is similar to that of the fore-aft displacements in terms of individual signals and the change in strain with changing interface height. A notable difference is the frequency content of the strain signals compared to the fore-aft displacement signals. There are more peaks in the FFT of vertical strain signals, which are as a result of deformation of the tower due to various forcing functions both at the top of the tower and along its height, as well as excitement from frequencies of each of the model components. The coincidence of the fore-aft model frequency with the first blade flapwise frequency can be seen in the case of the vertical strain signal in particular, where there is a peak in energy of the signal at this frequency at both 60m and 80m interface levels.

The FFT of the circumferential, $\varepsilon_{1,x}$ signal also shows a number of peaks in energy at various frequencies. These peaks are at multiples of the rotational frequency of the rotor (1P and 3P) as well as the natural frequencies of the tower and blades.

The shear strain signal has a mean of close to zero over the time history studied. There are fewer dominant frequencies in the case of these signals, which could be attributed

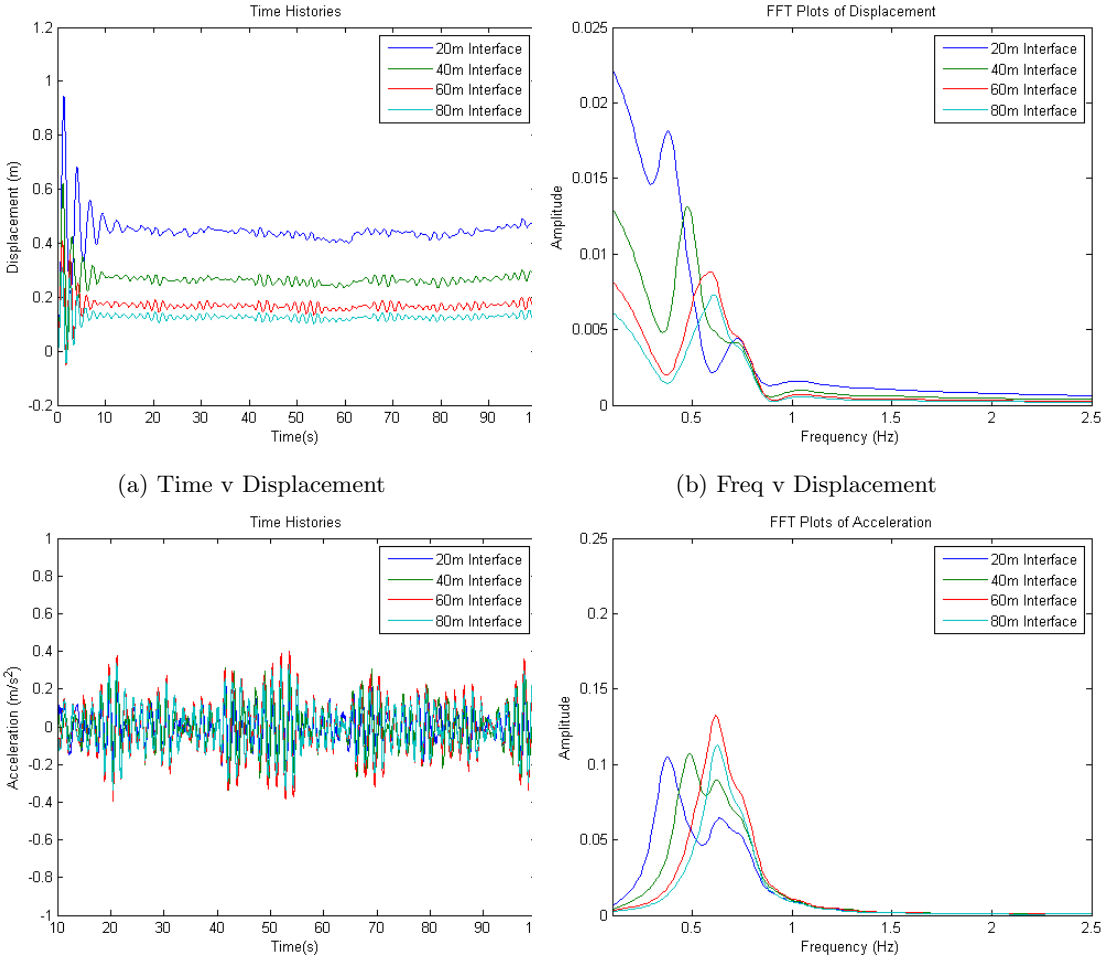

(a) Time v Displacement

(b) Freq v Displacement

(c) Time v Acceleration

(d) Freq v Acceleration

Figure 5.14: Fore-aft Displacement & Acceleration $u_{N,X}(t), u_{N,X}(f), \frac{d^2u_{N,X}(t)}{dt^2}, \frac{d^2u_{N,X}(f)}{dt^2}$, Varied Concrete/Steel Interface Levels (20m, 40m ,60m & 80m)

Tower Properties	Symbol	Units	Tower 6	Tower 7	Tower 8	Tower 9
Tower Height	H	m	100	100	100	100
Base Diameter	D_c	m	8.8	8.8	8.8	8.8
Base Shell	t_c	mm	350	350	350	350
Top Diameter	D_s	m	3	3	3	3
Top Shell	t_s	mm	25	25	25	25
Interface lvl	h_{int}	m	60	60	60	60
Interface Dia	D_{int}	m	6.5	6.5	6.5	6.5
Fore-aft freq	f_1	Hz	0.606	0.651	0.683	0.696
Tower Top Mass	M_{nac}	kg	537,480	403,110	268,740	134,370
Tower Mass	M_{Tower}	kg	1,343,701	1,343,701	1,343,701	1,343,701
Mass Ratio	$\frac{M_{\text{nac}}}{M_{\text{Tower}}}$	-	0.40	0.30	0.20	0.10
Conc damping	ξ_c	-	0.05	0.05	0.05	0.05
Steel damping	ξ_s	-	0.02	0.02	0.02	0.02
Conc stength	f_{ck}	MPa	50	50	50	50

Table 5.6: Hybrid Towers 6-9; Geometrical and Material Properties

to the fact that the shear strain of this element is more affected by multiples of the 3P (0.63Hz, 1.26Hz, ...) frequency than the 1P (0.21Hz, 0.42Hz, ...) frequency.

5.4.2 Tower Top Mass

Four models were constructed in order to assess the implications on forced response characteristics when varying the mass at the top of the tower. The properties of the tower were held constant for each of these models, with the tower top mass varied from 10% to 40%. Details are provided in Table 5.6.

The displacement time history provided in fig 5.16 shows that whilst there is some variation in the amplitude of vibration as a result of varying the tower top mass, there is no change in the mean fore-aft displacement. In this case, there is an increase in the amplitude of vibration with a decrease in tower top mass. From the FFT plot, it is evident that the dominant frequency of vibration changes with the change in tower top mass. Increasing the mass results in a decrease in the dominant frequency. Multiples of the 3P rotor frequency are evident but not significant on the FFT plots.

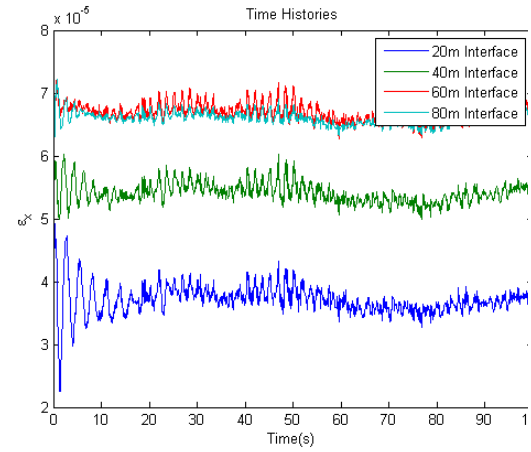

(a) Time v $\varepsilon_{1,x}$

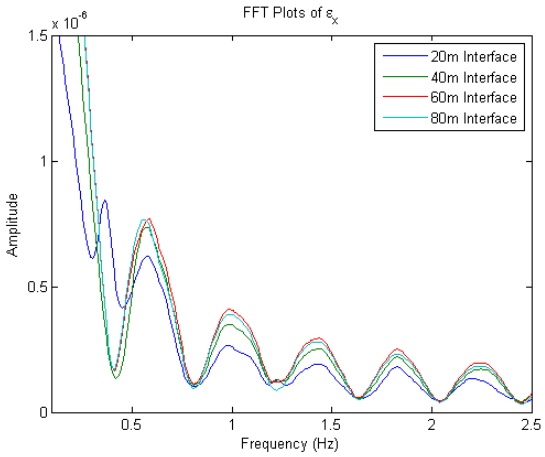

(b) Freq v $\varepsilon_{1,x}$

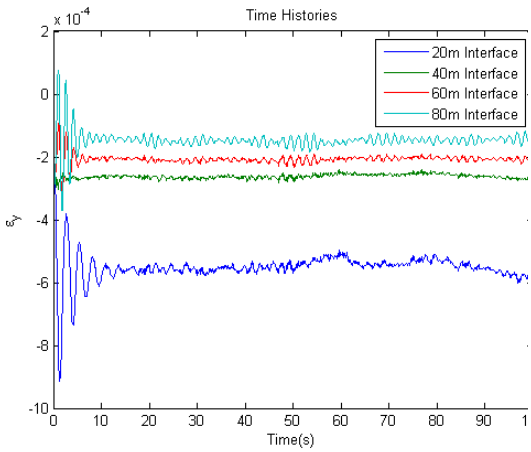

(c) Time v $\varepsilon_{1,y}$

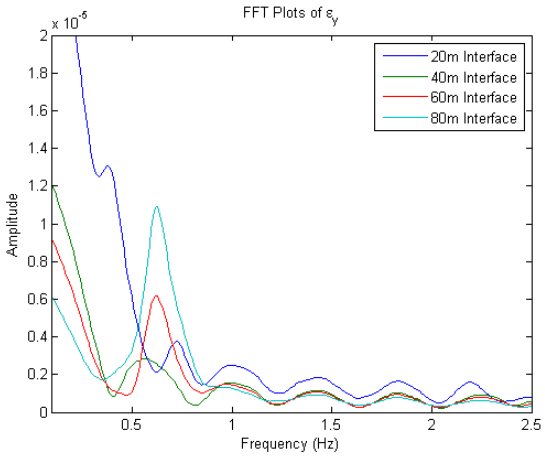

(d) Freq v $\varepsilon_{1,y}$

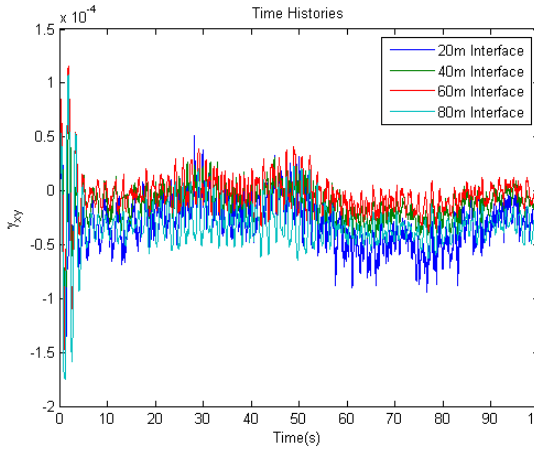

(e) Time v $\gamma_{1,xy}$

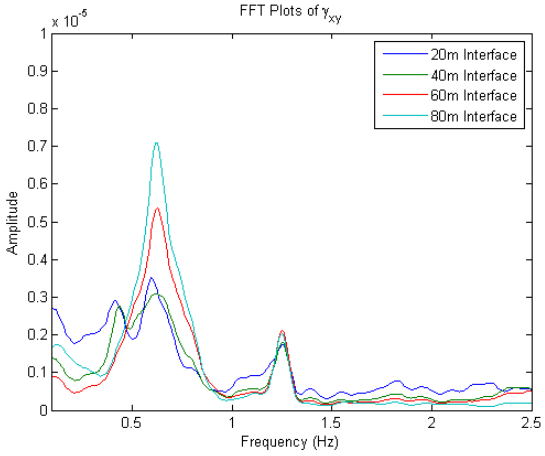

(f) Freq v $\gamma_{1,xy}$

Figure 5.15: Vertical Strain $\varepsilon_1(t), \varepsilon_1(f)$, Varied Interface Levels (20m, 40m ,60m & 80m)

The acceleration time history and FFT plots display the same properties as the displacement time history and FFT plots in terms of change in amplitude and frequency of vibration, without a change in the mean acceleration values. The change in amplitude of the acceleration is more pronounced than the change in amplitude of the displacement. This is evident in the time history plots and relative size of FFT peaks.

Local strain time histories and FFT plots are presented in Figure 5.17. There is clearly an increase in vertical and circumferential strain with increasing mass. The mean strain is expected to be the same for each model, however the varying level of mean strain can be explained due to the vertical load induced by the tower top mass.

5.5 Influence of Structural Damping

One distinct characteristic of hybrid towers to be studied is the nature of the varying structural damping afforded by the two material types. The influence of structural damping is to be considered using both 11 DOF models, the GBFE model and LSFE model. The ability to include separate structural damping properties for the concrete and steel portions of the tower, afforded by these models will be put to use to this end.

It is noted that damping is generally not prescribed in any detail in the literature. For example, IEC 61400 recommends that all towers have a structural damping ratio of 1%. AWEA and ASCE recommend a value of 5% be used which includes both aerodynamic and structural damping, regardless of tower construction.

Structural damping ratios were assigned to the steel and concrete as per Table 5.7. In the case of Hybrid Towers 10, 11 and 12, damping ratios vary from model to model but are consistent between the concrete and the steel elements. Hybrid Tower 4 incorporates separate damping ratios of 5% for concrete and 2% for steel to represent anticipated values.

Loadcase LC9 was used to run simulations for each tower which is based on a mean hub height wind speed, $\bar{v}$ of 20m/s and a turbulence level, I of 25%.

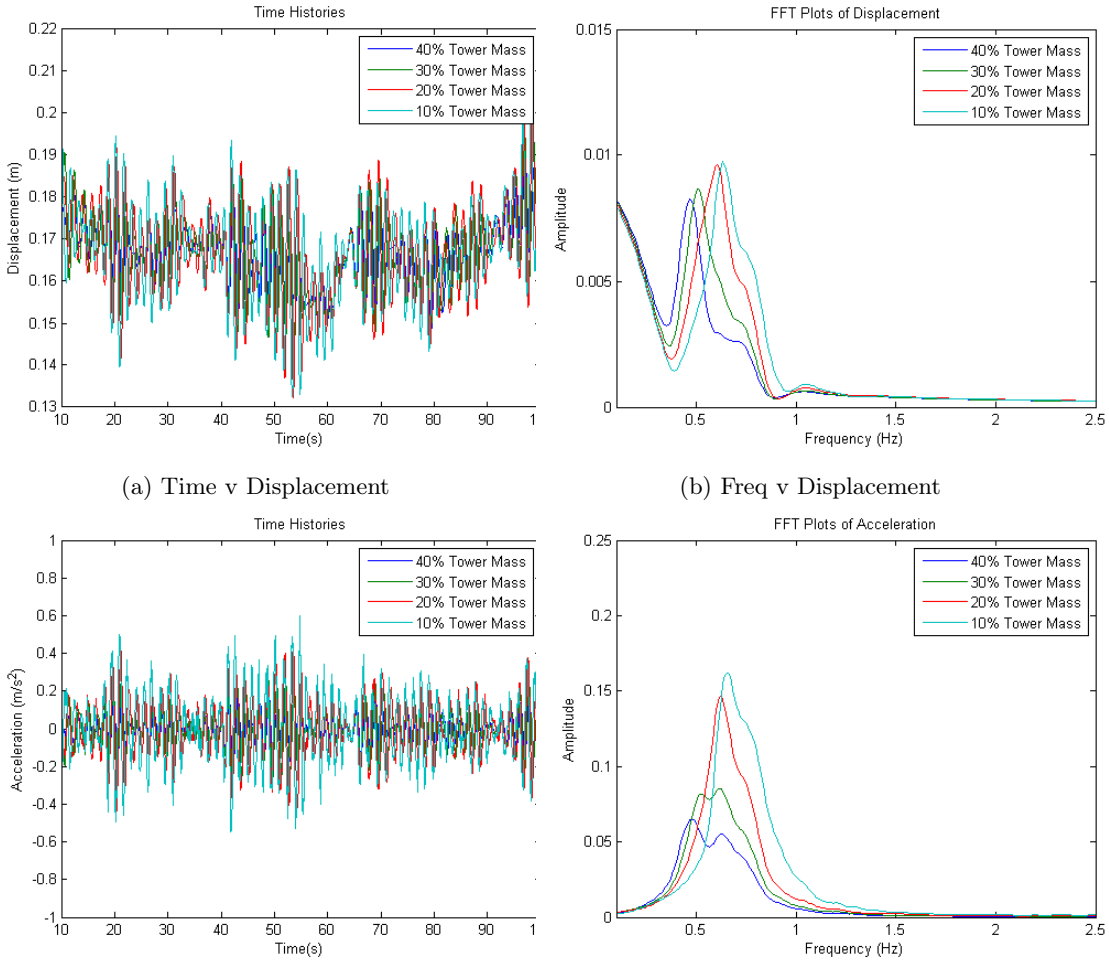

(a) Time v Displacement

(b) Freq v Displacement

(c) Time v Acceleration

(d) Freq v Acceleration

Figure 5.16: Fore-aft Displacement $u_{N,X}(t), u_{N,X}(f), \frac{d^2u_{N,X}(t)}{dt^2}, \frac{d^2u_{N,X}(f)}{dt^2}$, Varied Nacelle/Tower Mass Proportion (10%, 20%, 30% & 40%)

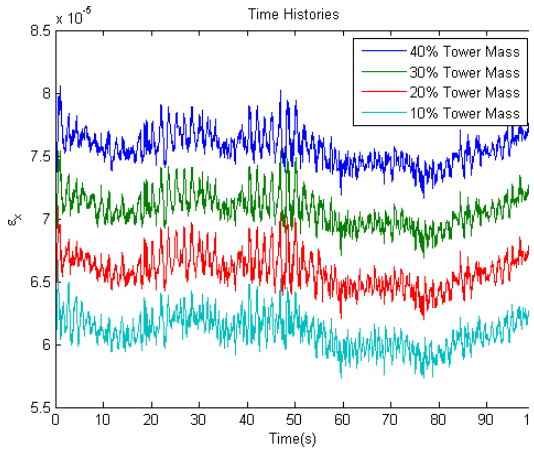

(a) Time v $\varepsilon_{1,x}$

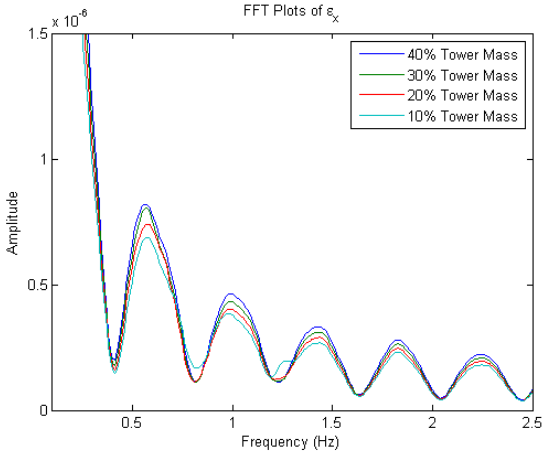

(b) Freq v $\varepsilon_{1,x}$

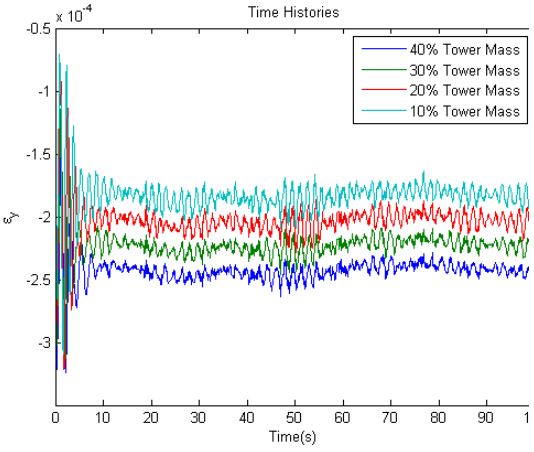

(c) Time v $\varepsilon_{1,y}$

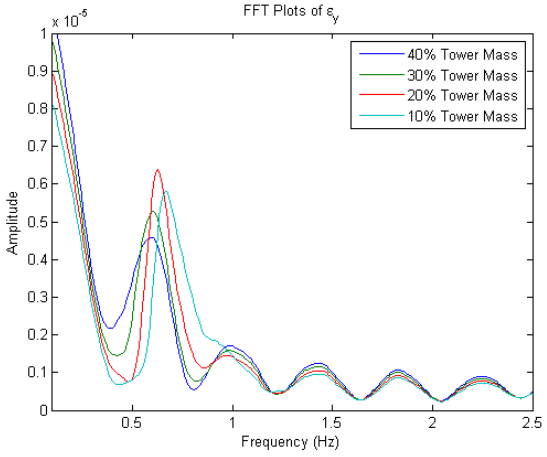

(d) Freq v $\varepsilon_{1,y}$

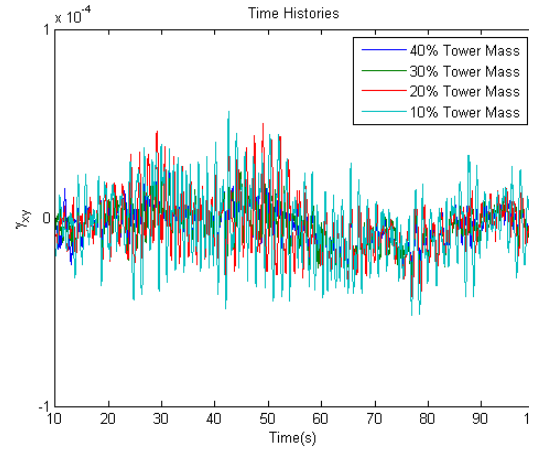

(e) Time v $\gamma_{1,xy}$

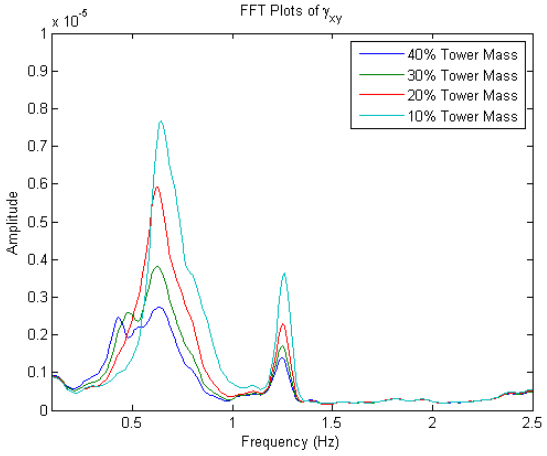

(f) Freq v $\gamma_{1,xy}$

Figure 5.17: Vertical, Circumferential & Shear Strain $\varepsilon_1(t), \varepsilon_1(f)$, Varied Nacelle/Tower Mass Proportion (10%, 20%, 30% & 40%)

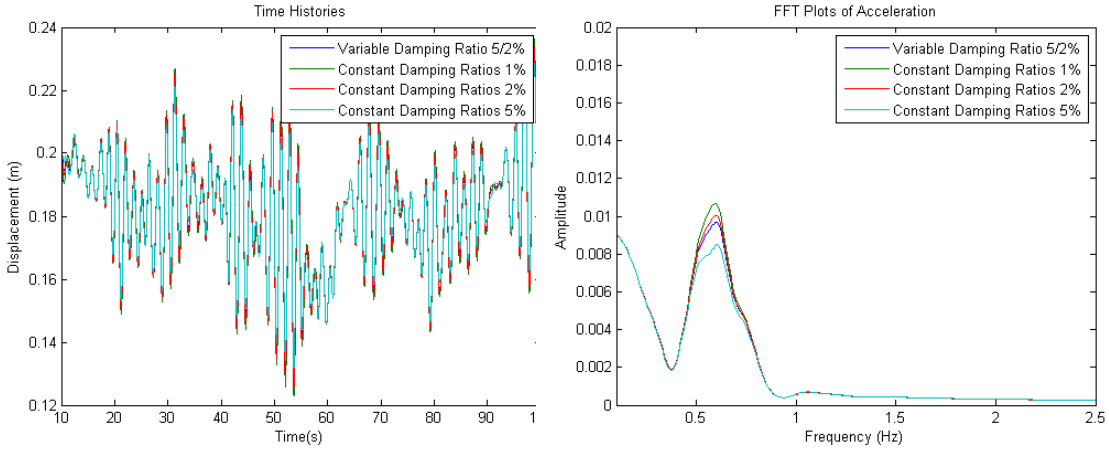

(a) Time v Displacement

(b) Freq v Displacement

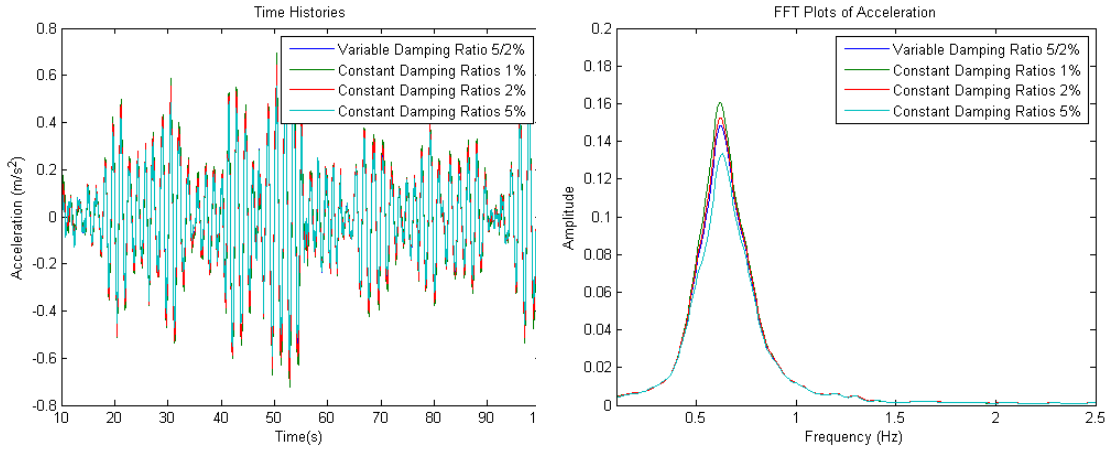

(c) Time v Acceleration

(d) Freq v Acceleration

Figure 5.18: Fore-aft Displacement $u_{N,X}(t), u_{N,X}(f)$, $\frac{d^2u_{N,X}(t)}{dt^2}$, $\frac{d^2u_{N,X}(f)}{dt^2}$, Varied Structural Damping (1%, 2%, 5% & Mixed)

Tower Properties	Symbol	Units	Tower 4	Tower 10	Tower 11	Tower 12
Tower Height	H	m	100	100	100	100
Base Diameter	D_c	m	8.8	8.8	8.8	8.8
Base Shell	t_c	mm	350	350	350	350
Top Diameter	D_s	m	3	3	3	3
Top Shell	t_s	mm	25	25	25	25
Interface lvl	h_{int}	m	60	60	60	60
Interface Dia	D_{int}	m	6.5	6.5	6.5	6.5
Fore-aft freq	f_1	Hz	0.678	0.678	0.678	0.678
Tower Top Mass	M_{nac}	kg	296,740	296,740	296,740	296,740
Tower Mass	M_{Tower}	kg	1,343,701	1,343,701	1,343,701	1,343,701
Mass Ratio	$\frac{M_{\text{nac}}}{M_{\text{Tower}}}$	-	0.22	0.22	0.22	0.22
Conc damping	ξ_c	-	0.05	0.01	0.02	0.05
Steel damping	ξ_s	-	0.02	0.01	0.02	0.05
Conc stength	f_{ck}	MPa	50	50	50	50

Table 5.7: Hybrid Towers 4, 10-12; Geometrical and Material Properties

There is a small but distinguished difference between the displacement and acceleration time histories (fig 5.18) between the four models in terms of the amplitude of response. Peaks in the FFT plots are larger for models with lowest damping ratios which emphasise the increase in amplitude of vibration. Where variable damping is introduced, there is a change in response as compared to models with constant damping properties.

From inspection of the local strain responses given in Figure 5.19, it is clear that by varying the damping properties there is a small but noticeable change in the amplitude of response. This is most apparent from review of the FFT plots of strain in each direction. There is a decrease in peak strain in the initial, transient part of each signal with an increase in damping ratio.

5.6 Influence of Concrete Compressive Strength

There is a defined relationship between the characteristic compressive strength of concrete, f_{ck} and the uncracked Youngs Modulus, E_{mod} of concrete. This relationship has been defined in Eurocode 2 (British Standards Institution [2004]) and is given in Eq.

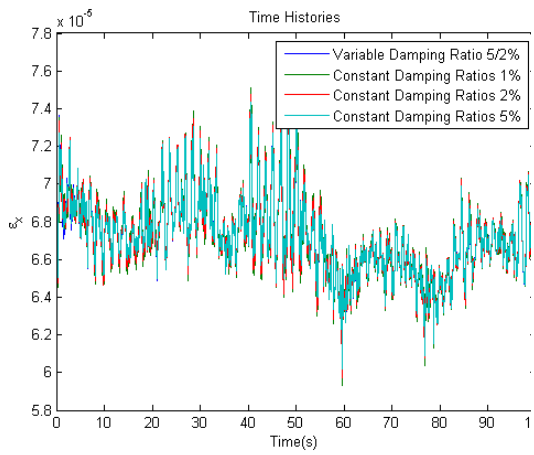

(a) Time v $\varepsilon_{1,x}$

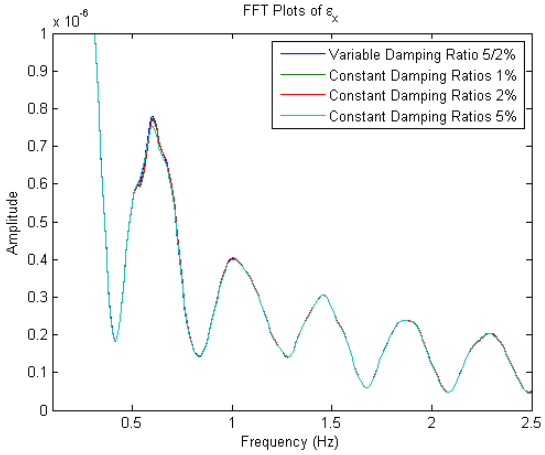

(b) Freq v $\varepsilon_{1,x}$

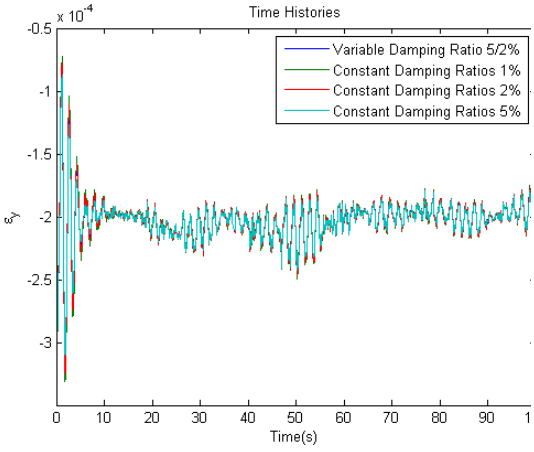

(c) Time v $\varepsilon_{1,y}$

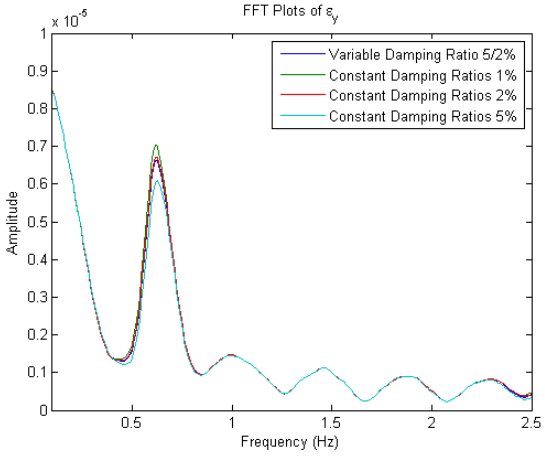

(d) Freq v $\varepsilon_{1,y}$

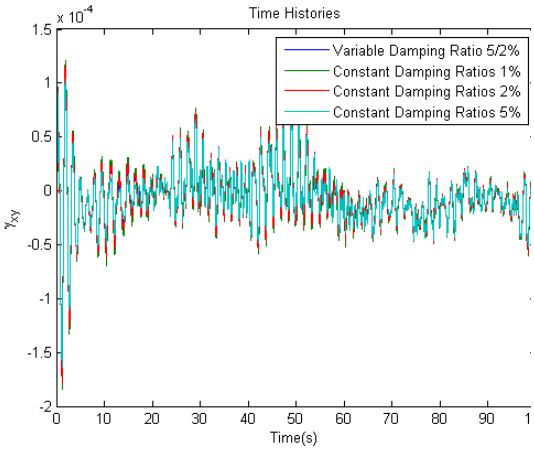

(e) Time v $\gamma_{1,xy}$

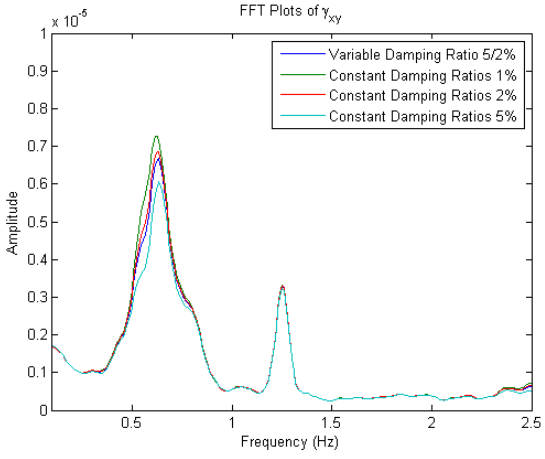

(f) Freq v $\gamma_{1,xy}$

Figure 5.19: Vertical, Circumferential & Shear Strain $\varepsilon_1(t), \varepsilon_1(f)$, Varied Structural Damping (1%, 2%, 5% & Mixed)

Tower Properties	Symbol	Units	Tower 5	Tower 13	Tower 14
Tower Height	H	m	100	100	100
Base Diameter	D_c	m	8.8	8.8	8.8
Base Shell	t_c	mm	350	350	350
Top Diameter	D_s	m	3	3	3
Top Shell	t_s	mm	25	25	25
Interface lvl	h_{int}	m	80	80	80
Interface Dia	D_{int}	m	6.5	6.5	6.5
Fore-aft freq	f_1	Hz	0.671	0.654	0.680
Tower Top Mass	M_{nac}	kg	296,740	296,740	296,740
Tower Mass	M_{Tower}	kg	1,655,130	1,655,130	1,655,130
Mass Ratio	$\frac{M_{\text{nac}}}{M_{\text{Tower}}}$	-	0.18	0.18	0.18
Conc damping	ξ_c	-	0.05	0.05	0.05
Steel damping	ξ_s	-	0.02	0.02	0.02
Conc stength	f_{ck}	MPa	50	30	70

Table 5.8: Hybrid Towers 5, 13-14; Geometrical and Material Properties

5.1

$$f_{cm} = f_{ck} + 8(N/mm^2)$$
$$E_{mod} = 22 \times \left(\frac{f_{cm}}{10}\right)^{0.3} \tag{5.1}$$

In Eq. 5.1, the term f_{cm} refers to the mean compressive strength of concrete, whereas f_{ck} refers to the characteristic compressive strength. In order to understand the effect of compressive strength, three different hybrid towers were reviewed. The compressive strength, f_{ck}, was varied between 30MPa and 70MPa. A summary of the properties of each tower is given in Table 5.8. A hybrid interface height of 80m was chosen for each tower with a view to identifying the impact of compressive strength as clearly as possible. Loadcase LC7 was used to run simulations for each tower which is based on a mean hub height wind speed, $\bar{v}$ of 12m/s and a turbulence level, I of 25%.

Global tower top displacement and acceleration responses were collected using the 11 DOF GBFE model and are presented in Figure 5.20. From review of the time history plot of displacement, there is clearly a variance in mean tower top displacement due to

the change in concrete compressive strength. The frequency domain plot shows a small increase in amplitude of vibration with increase in compressive strength. Therefore, while there is a change in mean displacement, there is only a marginal change in the amplitude.

Local strain time histories and FFT plots are presented in Figure 5.21. There is an increase in the vertical and circumferential strain experienced at the given finite element with increase in compressive strength. The change in amplitude of vertical and circumferential strain is marginal only. However, there is a significant change in the peak shear strain as compressive strength increases. This is evident from both the time history and FFT plots for this component.

There was also a small change in the first fore-aft frequency of the model with the change in concrete compressive strength. Natural frequency increased from 0.671 Hz to 0.680Hz with the increase in compressive strength.

5.7 Influence of Prestress

An exercise was carried out to review the effects of imposing prestressed tendons on a concrete tower.

The tower configuration used was based on an example tower put forward by Lanier [2005] as a possible fully concrete wind turbine tower designed to support a 5MW turbine. Three variations of this tower were studied, with properties given in Table 5.9. The shell thickness varies from 762mm at the base to 457mm at the top. The concrete characteristic compressive strength is given as 48 MPa. Although not provided in the literature, a density of 2450 kg/m^3 and a Poisson's ratio of 0.15 are assumed for the concrete.

Post-tensioned tendons are to be unbonded to the surrounding concrete. The tendons are defined by the NREL as having a modulus of elasticity of 196.5 GPa and a yield stress of 1860 MPa. Concrete is modelled using a non-linear stress–strain relationship

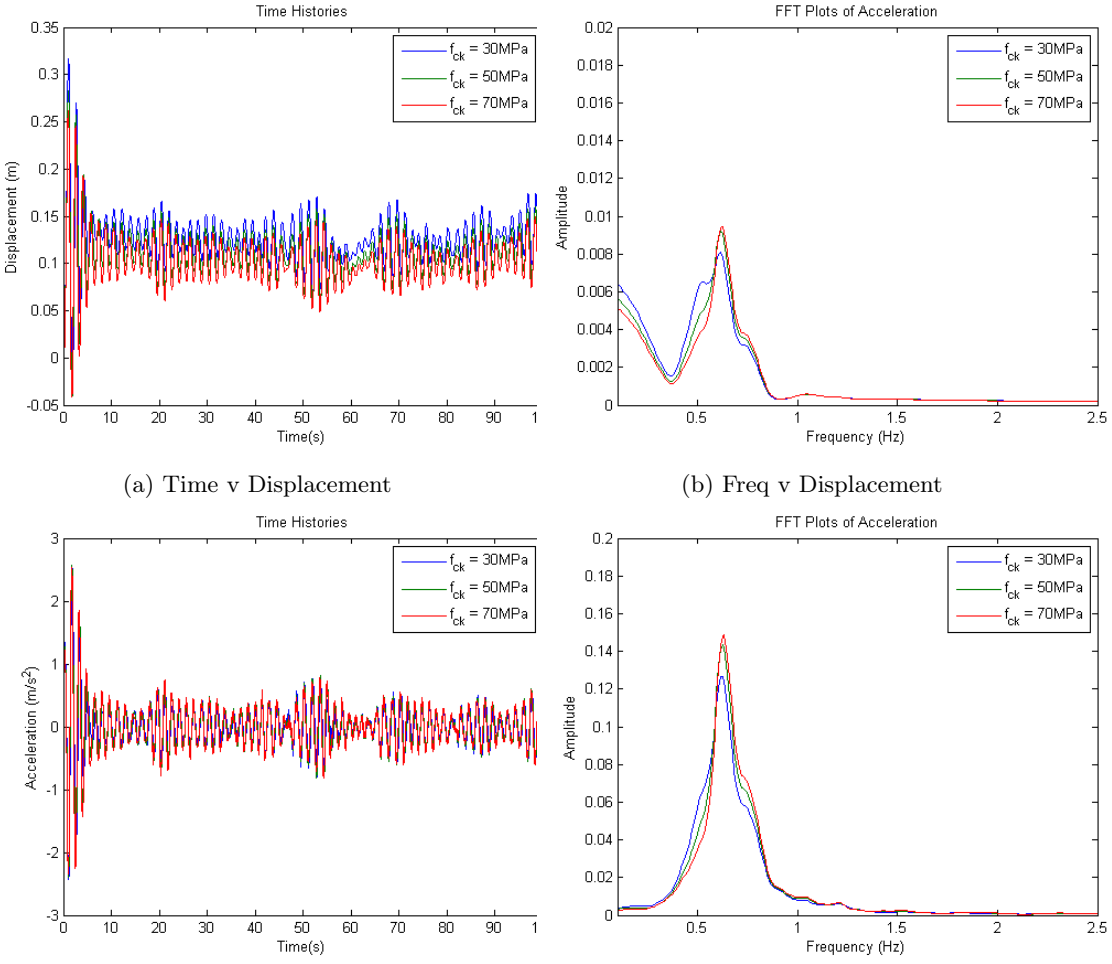

(a) Time v Displacement

(b) Freq v Displacement

(c) Time v Acceleration

(d) Freq v Acceleration

Figure 5.20: Fore-aft Displacement $u_{N,X}(t), u_{N,X}(f)$, $\frac{d^2u_{N,X}(t)}{dt^2}$, $\frac{d^2u_{N,X}(f)}{dt^2}$, Varied Concrete Compressive Strength (30MPa, 50MPa & 70MPa)

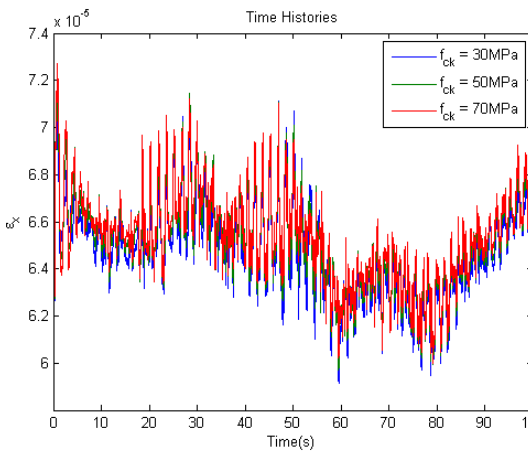

(a) Time v $\varepsilon_{1,x}$

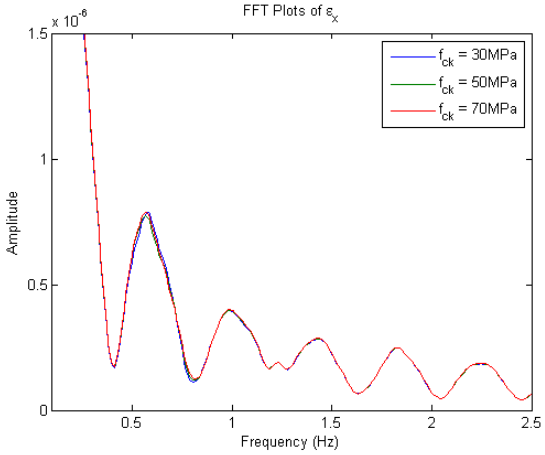

(b) Freq v $\varepsilon_{1,x}$

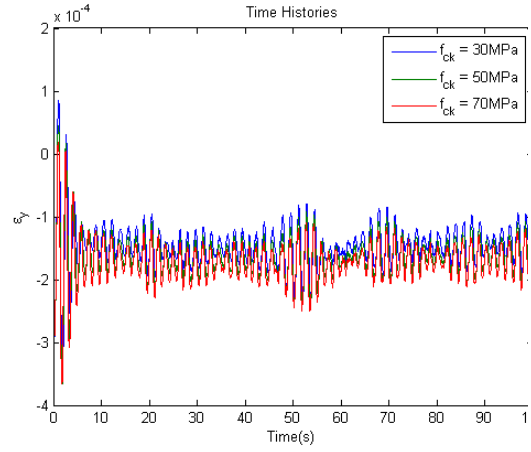

(c) Time v $\varepsilon_{1,y}$

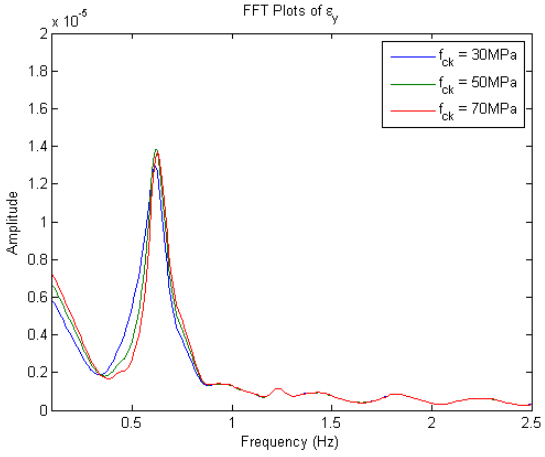

(d) Freq v $\varepsilon_{1,y}$

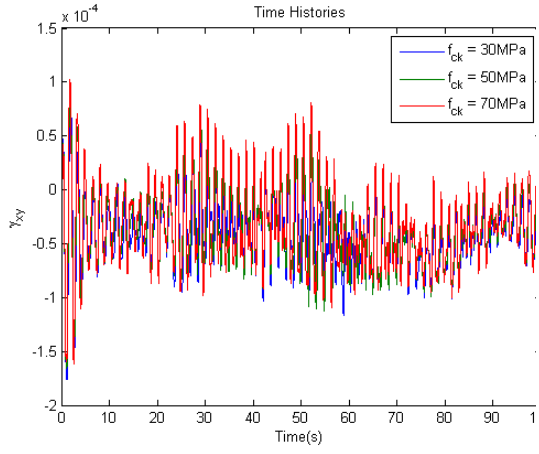

(e) Time v $\gamma_{1,xy}$

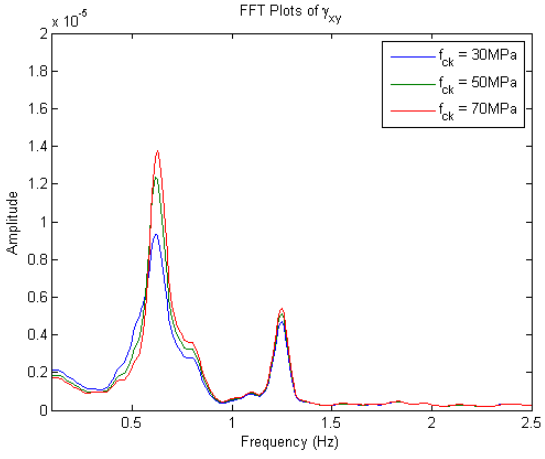

(f) Freq v $\gamma_{1,xy}$

Figure 5.21: Vertical, Circumferential & Shear Strain $\varepsilon_1(t), \varepsilon_1(f)$, Varied Concrete Compressive Strength (30MPa, 50MPa & 70MPa)

Tower Properties	Symbol	Units	Tower 15	Tower 16	Tower 17
Tower Height	H	m	100m	100m	100m
Base Diameter	D_c	m	7.62m	7.62m	7.62m
Base Shell	t_c	mm	762-467mm	762-467mm	762-467mm
Top Diameter	D_s	m	3.68m	3.68m	3.68m
Top Shell	t_s	mm	-	-	-
Interface lvl	h_{int}	m	-	-	-
Interface Dia	D_{int}	m	-	-	-
Fore-aft freq	f_1	Hz			
Tower Top Mass	M_{nac}	kg	480,000	480,000	480,000
Tower Mass	M_{Tower}	kg	2,775,832	2,775,832	2,775,832
Mass Ratio	$\frac{M_{\text{nac}}}{M_{\text{Tower}}}$	-	0.17	0.17	0.17
Conc damping	ξ_c	-	0.05	0.05	0.05
Steel damping	ξ_s	-	-	-	-
Conc stength	f_{ck}	MPa	30	48	70

Table 5.9: Hybrid Towers 15-17; Geometrical and Material Properties

in the case of the free vibration analysis, and post-tensioned tendons are modelled using an elastic–perfectly plastic relationship. Non-pre-stressed reinforcement has not been included in the model. Losses have been incorporated in terms of friction, anchorage and elastic deformation losses during construction. Long-term losses including creep, shrinkage and relaxation have also been included.

Where a non-linear relationship for concrete was used, an iterative Newton–Raphson algorithm was used to check the shell strain level after initial tendon anchorage and, if necessary, update shell element stiffness matrices using secant moduli such that the FE strain and the corresponding concrete stress were in agreement.

Pre-stress force is applied as a proportion of the critical buckling load of the tower, which was estimated using a Rayleigh–Ritz energy formulation and an assumed deflected shape at the point of buckling, P_{crit}.

5.7.1 Prestress Force

Figure 5.22 shows the variation of the first and second natural frequency of the tower with varying levels of applied prestress and for three different compressive strengths. Both linear and non-linear concrete constitutive properties are used, with non-linear behaviour modelled using a non-linear stress–strain relationship put forward by Hognestad [1951].

The increase in prestress force results in a marginal net decrease in the frequency of the tower. The induced compression within the concrete shell leads to a 'softening' of the shell elements, whereas the induced tension in the prestressed tendons leads to a 'stiffening' in these bar elements. In combination, a net 'softening' is experienced. The models with linear concrete properties show a linear reduction in stiffness with increasing prestress. The largest decrease is experienced by the concrete with 30 MPa compressive strength. The non-linear models show a change in the rate of reduction of stiffness with increasing prestress. A reduction in stiffness of approximately 3.5% is experienced by the concrete with 30 MPa compressive strength in this case at a prestress level of 60% of the critical buckling load, whereas a reduction of approximately 2% only is experienced in the case of the linear model. The softening effect seen on the first natural frequency is also present in the case of the second natural frequency however to a lesser extent.

In order to review the implications of prestress in terms of local and global responses to a forced simulation, hybrid tower 15 was subjected to load case LC 7. Two different levels of prestress were applied to the tower. Initially, zero prestress was applied and the responses gathered. Next a prestress of 60% of the critical buckling load was applied and results gathered.

The time history and FFT responses are presented in Figure 5.23. There is a negligible change in the tower top displacement or acceleration in the fore-aft direction as a result of applying the prestress. The slight change in natural frequency of the tower has been

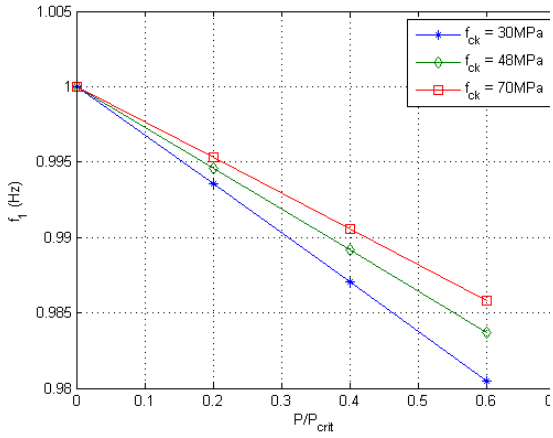

(a) Linear Model, P/P_{crit} vs f_1

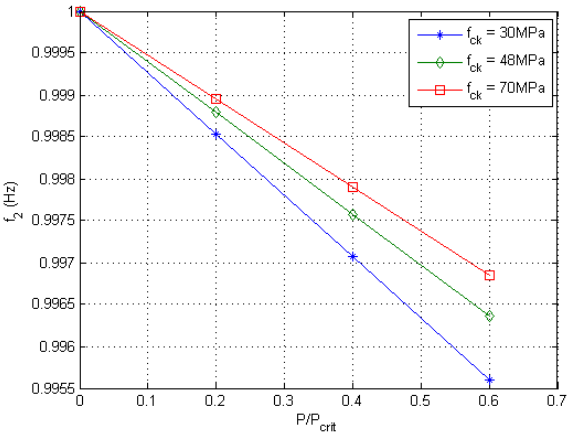

(b) Linear Model, P/P_{crit} vs f_2

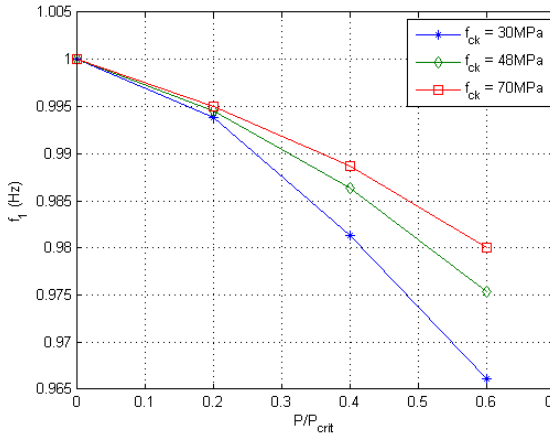

(c) Non-Linear Model, P/P_{crit} vs f_1

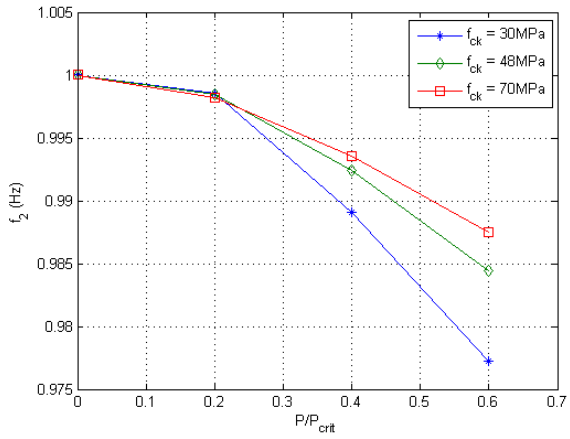

(d) Non-Linear Model, P/P_{crit} vs f_2

Figure 5.22: Change in Free Vibration Responses with Prestress Force Ratio $P(f)/P_{crit}$, Varied Concrete Constitutive Model

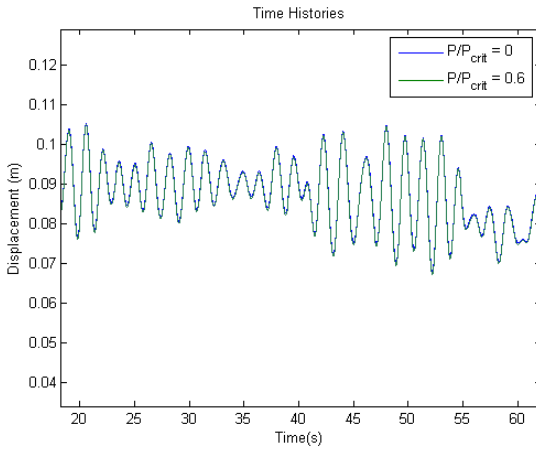

(a) Time v $u_{N,X}$

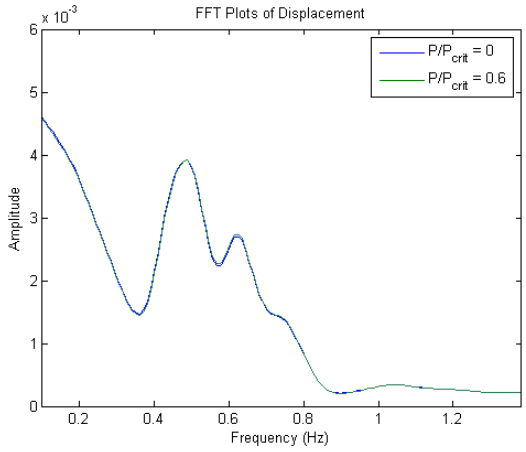

(b) Freq v $u_{N,X}$

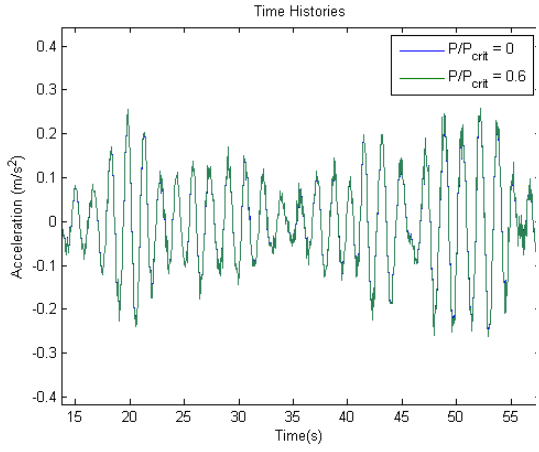

(c) Time v $\frac{d^2 u_{N,X}}{dt^2}$

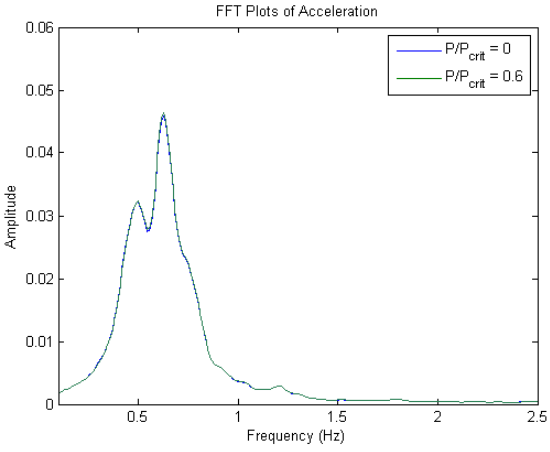

(d) Freq v $\frac{d^2 u_{N,X}}{dt^2}$

Figure 5.23: Fore-aft Displacement $u_{N,X}(t), u_{N,X}(f)$, $\frac{d^2 u_{N,X}(t)}{dt^2}$, $\frac{d^2 u_{N,X}(f)}{dt^2}$, With & Without Prestress Force ($P/P_{crit} = 0.6$)

detected by the FFT plot, however there is no appreciable change in the mean or peak displacement or acceleration.

At a local level, there is a much more appreciable change in the strain response as a result of the presence of a prestress force. This is evident in the strain response for shell element 1, $\{\varepsilon_1\}^T = [\varepsilon_{1,x}, \varepsilon_{1,y}, \gamma_{1,xy}]$, in each direction in the time domain. In the frequency domain, there is little change in the response characteristics. The mean strain in each direction is affected by the presence of prestress. These results can be seen in Figure 5.24.

5.7.2 Time Dependencies

Figure 5.25 shows a plot of the first natural frequency versus pre-stress force for both the linear and non-linear concrete model, with results shown for each point in time considered. Prestress was considered immediately after prestress application, 1 year, 10 years and 30 years after prestress application, with a reduction in prestress experienced over time due to various mechanisms. It can be seen that with increasing pre-stress, there is a relative softening of the tower stiffness. The maximum softening for any given load is experienced immediately after pre-stress is applied. When time-dependent losses were taken into account, the pre-stress force reduced, and so some recovery in stiffness occurred. Softening is more pronounced in the case of the non-linear concrete model.

The time history and FFT responses are presented in Figure 5.26. There is a negligible change in the tower top displacement or acceleration in the fore-aft direction as a result of the change in prestress over time. There is no distinguishable change in the acceleration signal or the frequency of response in terms of displacement or acceleration.

At a local level, the change in response is far more apparent due to the change in prestress over time. This is evident in the strain response for shell element 1, $\{\varepsilon_1\}^T = [\varepsilon_{1,x}, \varepsilon_{1,y}, \gamma_{1,xy}]$, in the vertical and circumferential directions but not to any extent in terms of shear strain. The change in response is evident in the time and frequency

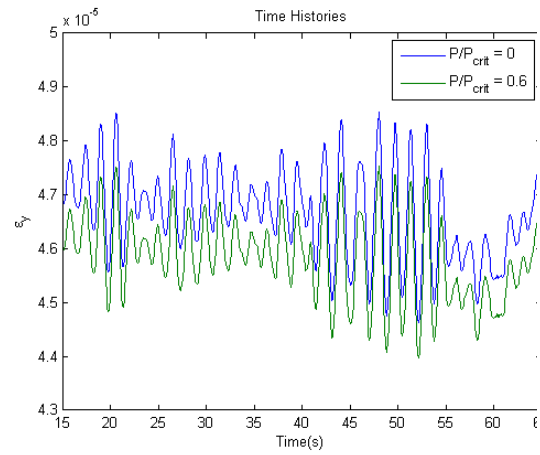

(a) Time v $\varepsilon_{1,x}$

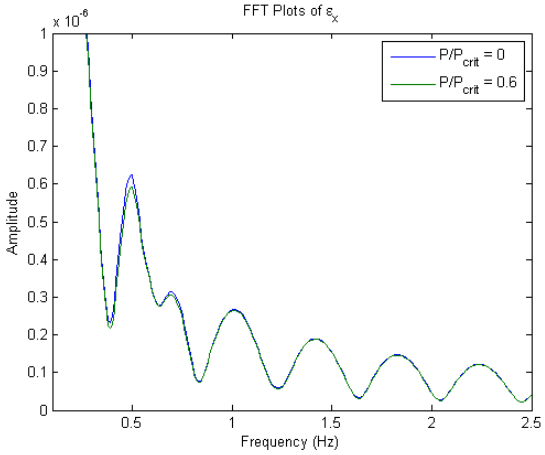

(b) Freq v $\varepsilon_{1,x}$

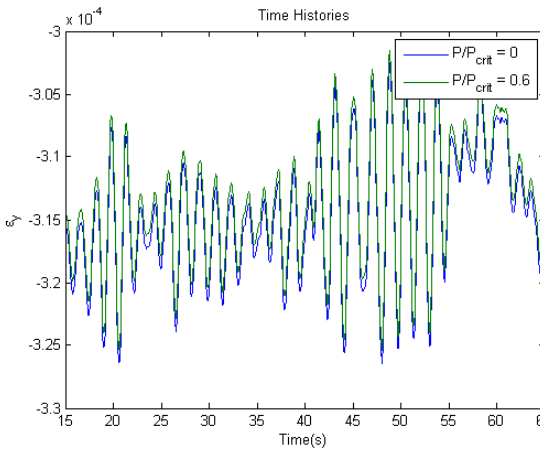

(c) Time v $\varepsilon_{1,y}$

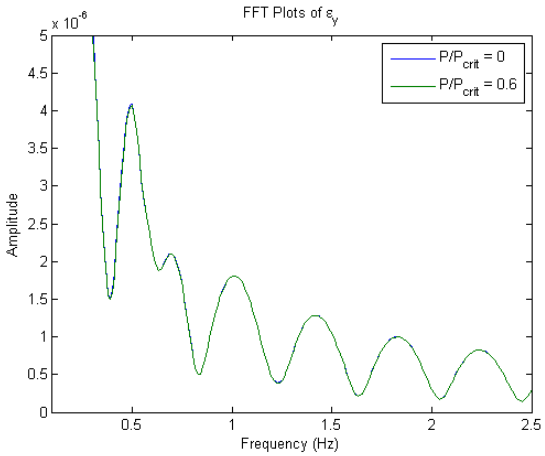

(d) Freq v $\varepsilon_{1,y}$

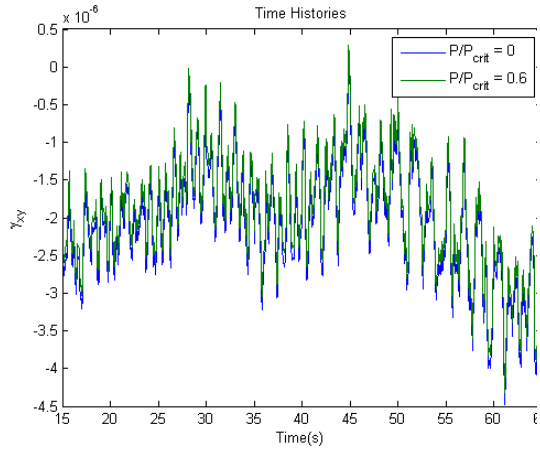

(e) Time v $\gamma_{1,xy}$

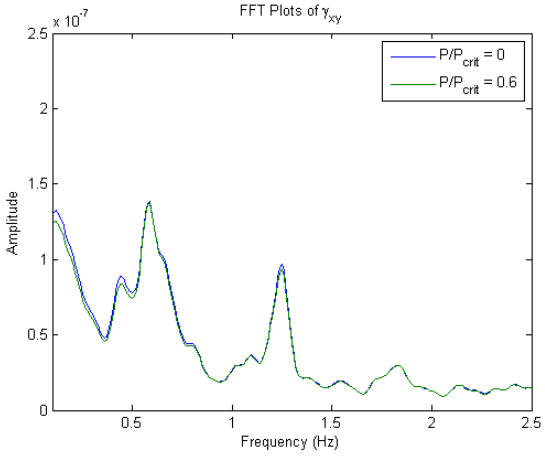

(f) Freq v $\gamma_{1,xy}$

Figure 5.24: Vertical, Circumferential & Shear Strain $\varepsilon_1(t), \varepsilon_1(f)$, With & Without Prestress Force ($P/P_{crit} = 0.6$)

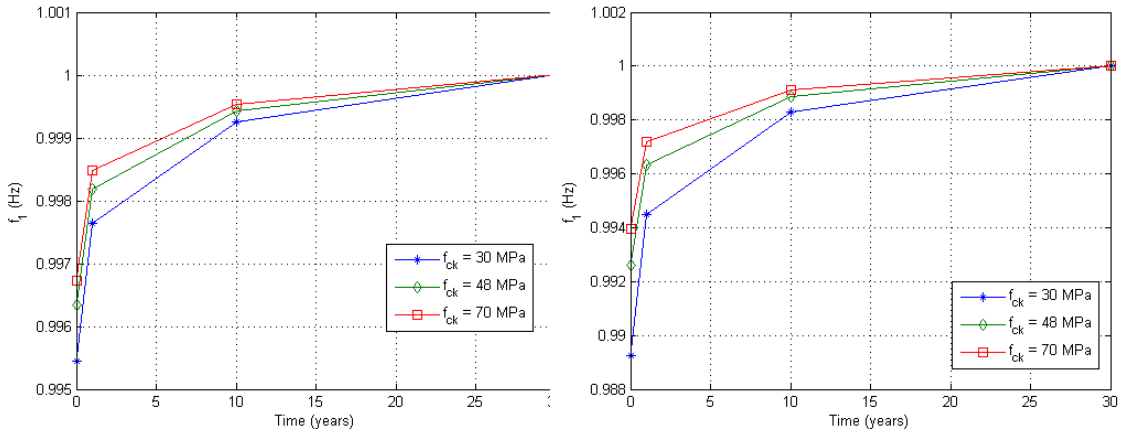

(a) Linear Model; Time vs f_1

(b) non-Linear Model; Time vs f_1

Figure 5.25: Change in Free Vibration Response with Time; Variable Concrete Compressive Strength

domain. As prestress force reduces over time, the result is a decrease in the mean vertical and circumferential strain. These results can be seen in Figure 5.27.

5.7.3 Constitutive Model

Where the constitutive relationship of the concrete was varied by changing from a linear to non-linear description, the result in terms of the natural frequency response was that towers with non-linear properties experienced a greater net level of softening. This is outlined in Figure 5.28 where tower 15, which was composed of concrete with a characteristic compressive strength, f_{ck} of 30 MPa concrete, using both linear and non-linear properties.

5.8 Conclusions

In this Chapter, a review was carried out of the effect of various types of operating conditions, magnitudes of wind speeds and magnitudes of turbulence on the generalised loadings to be applied to any forced simulation. Both operating and parked conditions were considered.

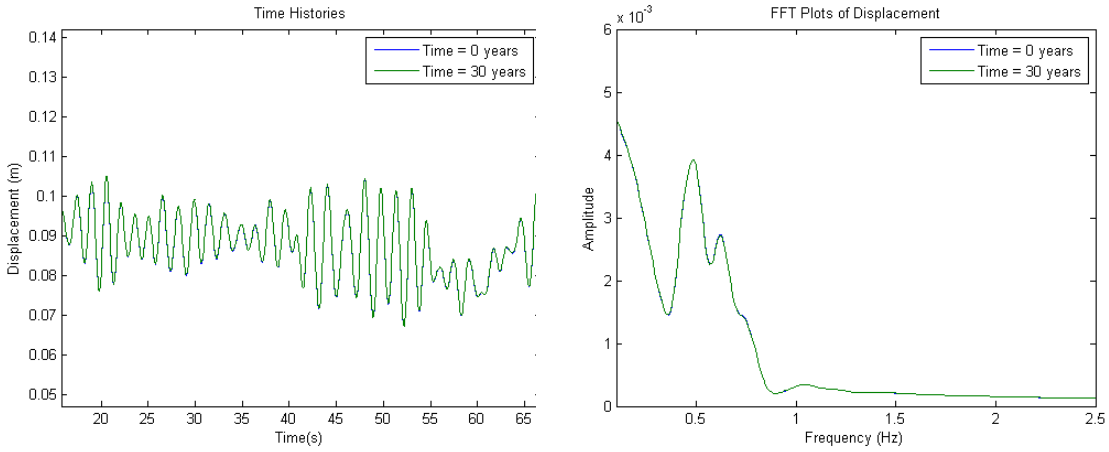

(a) Time v $u_{N,X}$

(b) Freq v $u_{N,X}$

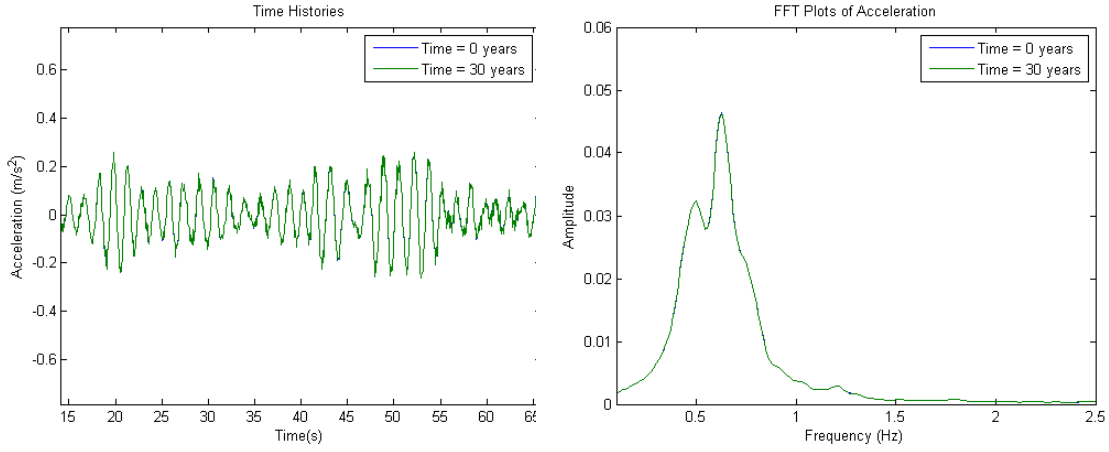

(c) Time v $\frac{d^2u_{N,X}}{dt^2}$

(d) Freq v $\frac{d^2u_{N,X}}{dt^2}$

Figure 5.26: Fore-aft Displacement $u_{N,X}(t), u_{N,X}(f), \frac{d^2u_{N,X}(t)}{dt^2}, \frac{d^2u_{N,X}(f)}{dt^2}$, Immediately after Prestressing & 30 years after Prestressing (significant losses in force)

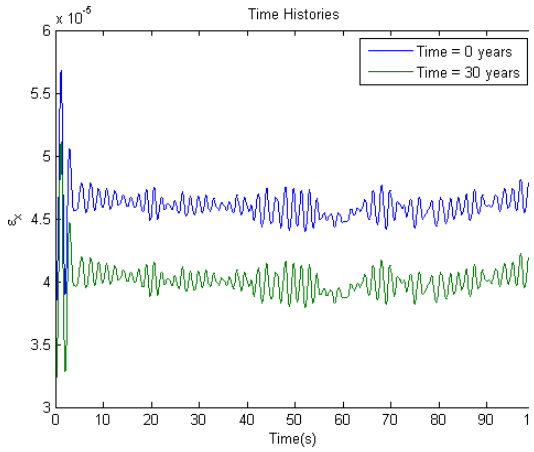

(a) Time v $\varepsilon_{1,x}$

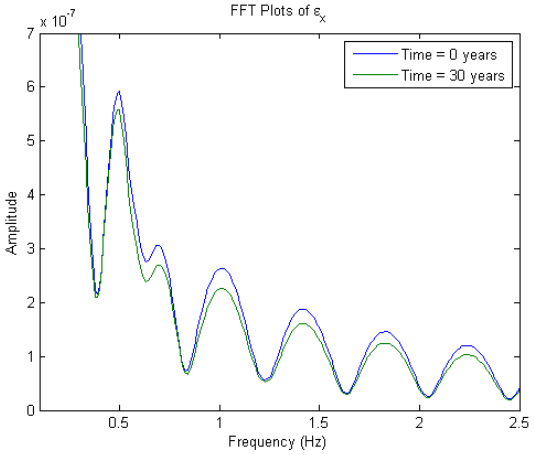

(b) Freq v $\varepsilon_{1,x}$

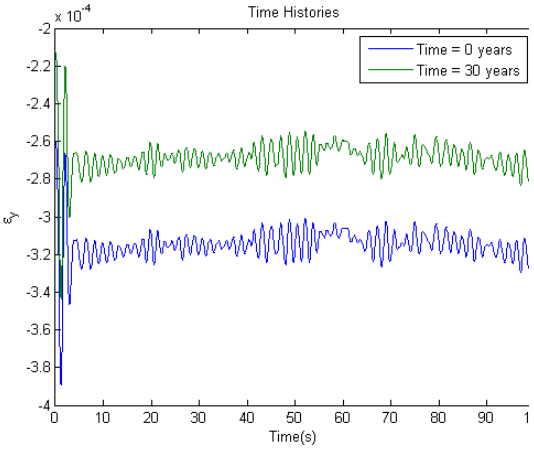

(c) Time v $\varepsilon_{1,y}$

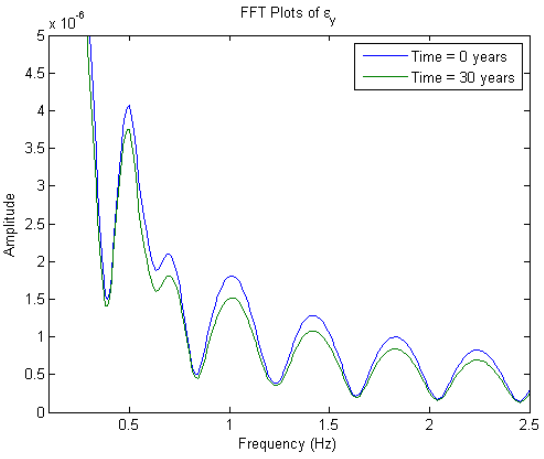

(d) Freq v $\varepsilon_{1,y}$

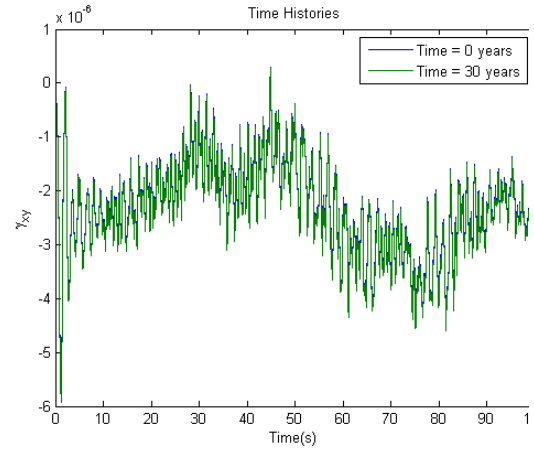

(e) Time v $\gamma_{1,xy}$

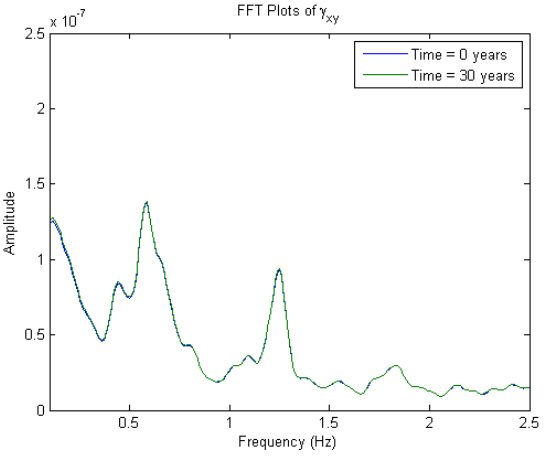

(f) Freq v $\gamma_{1,xy}$

Figure 5.27: Vertical, Circumferential & Shear Strain $\varepsilon_1(t), \varepsilon_1(f)$, Immediately after Prestressing & 30 years after Prestressing (significant losses in force)

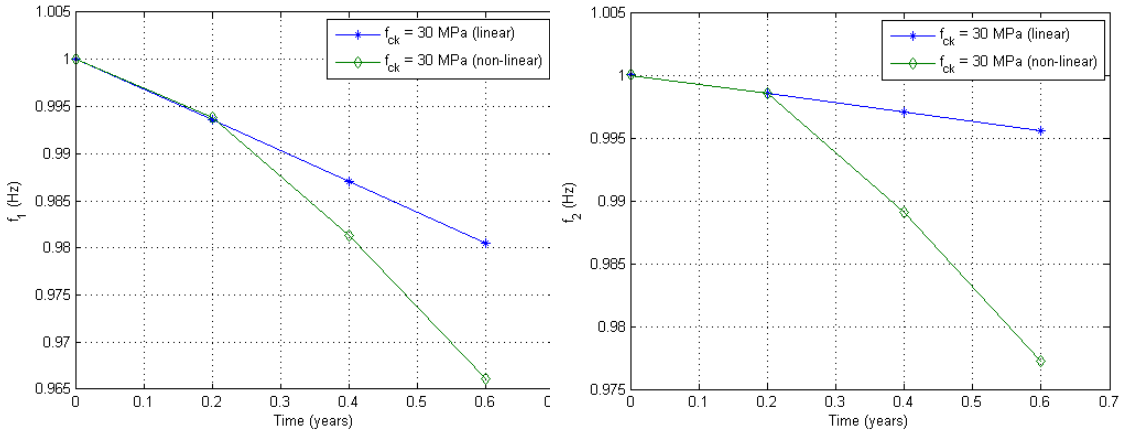

(a) P/P_{crit} vs f_1 (b) P/P_{crit} vs f_2

Figure 5.28: Change in Free Vibration Responses with Prestress Force Ratio $P(f)/P_{crit}$, Linear & Non-Linear Concrete Constitutive Model

Local strain signals in each principal direction were reviewed using the 11 DOF LSFE model for an element at the base of the tower. For the element considered, the local vertical direction, $\varepsilon_{1,y}$, exhibits the highest magnitude of strain. In a sensitivity analysis of impact of various design variables, the exact analytical model was used to assess free vibration and the 11 DOF GBFE model was used in assessing forced vibration. The nacelle mass had the most significant impact on the first natural frequency of the tower. The hybrid interface height was also strongly correlated to the first natural frequency. The mean global displacement was not impacted by the tower top mass, however the acceleration was strongly impacted. Hybrid interface height was strongly correlated with the displacement but to a lesser extent on the velocity and acceleration response.

The forced vibration response was reviewed in more detail in the time and frequency domains to assess the impact of the changing interface height, tower top mass, concrete compressive strength, prestress level and damping parameters. Again, global and local responses have been reviewed.

Chapter 6

Optimisation of Hybrid Concrete-Steel Towers

6.1 Introduction

This chapter will encompass a number of different areas of optimisation relevant to the Thesis. A methodology will be outlined which will allow for the optimisation of a defined objective associated with these hybrid towers. Generalisation of simulation data extracted based on a defined design of experiment programme of simulations, will be carried out using Artificial Neural Networks (ANNs) machine learning applications.

Then, this methodology will be used to optimise hybrid towers in terms of individual objective functions. Specific complexities in the field of wind turbines include the highly dynamically coupled nature of the flexible components of the turbine (e.g. blade-tower interaction), fluid-structure interaction between wind field and vibrating turbine, soil-structure interaction, variable geometry and material composition and rotating turbine blades. Constraints can also be widely varying including implicit and explicit structural constraints, noise, environmental constraints, geographical constraints and construction and operational issues.

Ma and Meng [2014] optimised a prestressed concrete tower consisting of stiffened concrete shell elements and prestressing tendons using a Genetic Algorithm. The tower is designed to support a 5MW turbine and is to be 100m tall. The cross sectional shape and tendon numbers were optimised. Inbuilt in the algorithm was the use of the finite element package Abaqus. The objective function used was the cost of the tower, which was written using the design variables. Yıldırım and Özkol [2010] optimised a tubular steel wind turbine tower used to support a 1.5MW wind turbine using a Genetic Algorithm. Given the steel material, constraints included stress limitations to avoid local shell buckling. The objective function in this work was the tower mass which was to be minimised. The design variables were the shell thicknesses required to satisfy constraints at intervals of 1m over the tower height of 52m. In the case of both of these works the objective functions, variables and constraints are well defined by the authors and optimised towers are presented. However, the authors do not explain how dynamic effects such as dynamic tower top displacements due to interaction between the optimised tower and the turbine are included in the result.

Karpat [2013] published a paper presenting a tool for the optimization of a wind turbine tower, making use of another form of Evolutionary optimization method known the particle swarm optimization (PSO) algorithm. Using the tool developed, the author was able to improve on the design by Uys et al. [2007] both in terms of tower mass and cost.

Cai et al. [2012] presented a paper identifying an optimisation method for the design of blades using the PSO algorithm combined with Finite Element Method. The Finite Element (FE) model is built into the PSO routine and activated in testing any set of variables, where the FE model generates stresses and deflection values at predefined locations around the blade so that constraint conditions can be checked. This work is interesting as it shows both the effectiveness of the Evolutionary Algorithm adopted as well as the integration of an FE model into the overall routine.

Metamodels or Artificial Neural Networks (ANN) are to be used currently. An ANN

is a tool which can be built and trained to take a set of input variables and process them in order to generate output data. The name neural network is taken from its basis of having a configuration and internal processing ability likened to that of the human brain including neurons and connecting circuits. Modern ANNs are said to have developed from pioneering works by McCulloch and Pitts (1943), with their application in civil engineering beginning in the 1980s (Flood and Kartam [1994]). In this thesis, such a network will be used to generalize the results of a large number of wind turbine tower dynamic simulations. In the literature, this tool has been successfully applied in a range of engineering applications.

6.2 Non-Linear Programming

6.2.1 Formulation of Constrained Non-Linear Programming (NLP) Problem

The problem in question is the optimisation of a wind turbine tower, which is a vibrating tower structure, subject to a multitude of implicit and explicit nonlinear constraints. The problem is therefore a constrained problem in terms of mathematical optimisation and can be written as a Non-Linear Programming (NLP) problem as given in Eq. 6.1.

$$\begin{aligned} &\text{Minimise} \quad f(x), \quad \text{subject to} \\ &\qquad g_j(x) \geq 0, \quad \text{and} \quad j = 1, 2, \cdots, J \\ &\qquad h_k(x) = 0, \quad \text{and} \quad k = 1, 2, \cdots, K \\ &\qquad x_i^{LB} \leq x_i \leq x_i^{UB}, \quad \text{and} \quad i = 1, 2, \cdots, N \end{aligned} \tag{6.1}$$

In this form, the terms $g_j(x)$ and $h_k(x)$ refer to the inequality and equality constraints to be imposed on the solution. For example, implicit constraints such as the tower natural frequency will need to satisfy some inequality expression where it will need to be above or below a set measure. Lower and upper bounds x_i^{LB}, x_i^{UB} are imposed on the design variables as also provided in Eq. 6.1.

6.2.2 Optimisation Algorithms

Given the non-continuous nature of feasible objectives and constraints in this problem and the multi-modal nature of the solution, an optimisation approach consisting of a hybrid of a non-traditional Evolutionary Algorithm and a more traditional Direct Search algorithm was used here. A Genetic Algorithm was utilised to find near-optimum solutions, with these solutions then used as a start point with a Pattern-Search algorithm which found the global optimum results. In order to simulate this behaviour of reproducing more optimal solutions in any given domain, Evolutionary Algorithms have been developed in the past number of decades (Lagaros and Karlaftis [2015]). The Evolutionary Algorithm chosen is the Genetic Algorithm, which is designed to mimic natural selection behaviour in terms of survival of the fittest in order to generate an optimum solution. Initially genetic descriptions are selected at random and the fitness of each member is tested. Next, population members or chromosomes are ranked according to their fitness and, on this basis, fitter members are used in genetic operations to produce the next generation of the population with the intention being to continually improve on fitness.

Direct Search methods are also suited to this form of problem where the objective function is not continuous and so not differentiable (Deb [2012]). The algorithm assesses the fitness of a mesh of points (known as polling of mesh points) located around a single 'current' point. Where a point being polled is found to have a better fitness than the 'current' point, the polling is found to be successful and the point with best fitness then becomes the 'current' point. After polling is complete, the algorithm changes the mesh size for the next step such that the mesh is converging or diverging around a 'current' point. An established approach is to factor the mesh size by 2 for a successful poll and by 0.5 for an unsuccessful poll.

6.2.3 Transformation to Unconstrained NLP Problem

There are a number of numerical methods available for dealing with nonlinear constraints in genetic optimisation problems, such as the Augmented Lagrangian Algorithm put forward by Conn et al. [1991]. A simplification can be made in terms of handling non-linear constraints to improve the computational effort required. These nonlinear constraints are instead incorporated by transforming the constrained problem to an unconstrained problem using additional penalty terms in the description of the objective function. The transformed unconstrained optimisation problem is written below and includes the objective to be optimised plus constraint penalty terms.

$$
\begin{aligned}
\text{Minimise} \quad & F(x,R) = f(x) + R\left(\sum_{j=1}^{J}|P_j(x)| + \sum_{k=1}^{K}|P_k(x)|\right), \\
& \text{Where} \\
& x \in X \\
& P_j(x) = \begin{cases} \frac{g_j(x)}{\text{Lim}_j(x)}, & \text{if } g_j(x) \leq 0 \\ 0, & \text{otherwise} \end{cases} \\
& P_k(x) = \begin{cases} \frac{h_k(x)}{\text{Lim}_k(x)}, & \text{if } h_k(x) \neq 0 \\ 0, & \text{otherwise} \end{cases}
\end{aligned}
\tag{6.2}
$$

In Eq. 6.2, R is a large penalty number assigned to each constraint and $P(x)$ is a measure of violation of a constraint from its allowable value, for example stress or displacement. Lim_j refers to a location on the boundary of the feasible space in the domain, beyond which the solution is infeasible. Gen and Cheng [1996] refers to this form of penalty inclusion as a dynamic penalty in that it allows for a measure of violation to be factored into the scale of the penalty imposed. The penalty quantity reverts to a zero value when there is no violation of a particular constraint at the point $\{x\}$ under consideration. Deb [2012] describes this in his text on the subject of optimisation as an exterior penalty

Objective	$f(x)$
Maximise Frequency	$\omega_1(x)$
Minimise Displacement	$u_{N,X}(x)$
Minimise Stress Utilisation Ratios	$\sum_{i=1}^{4} w_i \frac{\sigma_{h,i}}{\sigma_{h,adm}}$
Minimise Levelised Cost of Energy	$\mathrm{LCoE}(x)$
Minimise Climate Change Potential	$\mathrm{CCP}(x)$
Minimise Tower Mass	$M_{\mathrm{Tower}}(x)$

Table 6.1: Structural & Non-Structural Objective Functions, $f(x)$

method as it is only infeasible points which are penalised.

6.2.4 Definition of Objective Functions

The objective functions which have been targeted for optimisation throughout this chapter are given in Table 6.1. A seminal piece of work by Negm and Maalawi [2000] optimised a wind turbine tower of varying cross section and numbers of vertical segments using five different objective functions. The authors found that minimisation of the weighted sum of the system natural frequencies gave a balanced design where exact frequency placement is possible, leading to a balance between limiting vibrations and mass. A similar outcome is targeted here by minimising the weighted sum of stress utilisation ratios.

Minimisation of mass and cost is well documented in the literature. Works such as those by Taylor and Agbayani and Yang and Zhu [2015] are examples of minimisation of mass of steel towers. Minimisation of cost can be achieved at a structural level, wind farm level and also when expressed as the cost of energy. Ashuri et al. [2014] presented work describing the minimisation of the cost of energy in off-shore applications. Both the Annual Energy Production (AEP) and cost will increase with larger turbine assemblies so an optimum 'levelised' cost is desirable.

6.3 Definition of Constraints

6.3.1 Geometrical Constraints

Geometrical constraints will be imposed on the tower geometry initially in terms of assigning lower and upper limits for each variable and next by enforcing decreasing diameter and thickness values with increasing tower height. These constraints are given in Eq. 6.3.

$$\begin{aligned} g_1(x) &= x_1 - x_2 \geq 0 \\ g_2(x) &= x_2 - x_3 \geq 0 \\ g_3(x) &= x_4 - x_5 \geq 0 \\ g_4(x) &= x_6 - x_7 \geq 0 \end{aligned} \tag{6.3}$$

With reference to practical construction limitations, the upper limit on the steel shaft diameter has been taken to be 4.5m. In addition, a maximum steel plate thickness of 60mm has been chosen. Producing plates of higher thickness is possible but will attract a premium in terms of cost. A lower limit of 200mm has been chosen for the shell thickness. This is so as to ensure sufficient cover can be provided for both reinforcement and prestressing tendons where these are to be encased. These bounds are listed in Eq. 6.4.

$$\begin{aligned} x &\in X \\ x^{LB} &= \{2, 1.75, 1.5, 0.2, 0.2, 0.01, 0.01, 20H\} \\ x^{UB} &= \{6, 2.25, 2, 0.6, 0.4, 0.06, 0.03, 80H\} \end{aligned} \tag{6.4}$$

6.3.2 Global Structural Constraints

The fundamental frequency of the tower structure is critical to the overall wind turbine design. Traditionally, wind turbine towers have been designed to be stiff-stiff, which is where their frequency is in excess of the highest frequency load application ($3P$). However, this is not normal practice for turbines of the height considered here (Lavassas et al. [2003]). In this case, a soft-stiff design is considered appropriate, which is where the towers frequency lies between both reference frequencies. Here the constraints used will be the $1P$ and $3P$ frequencies, with a safety margin of 10% included.

The maximum displacement of the tower in the fore-aft direction, $u_{N,X}$, is to be limited to a value of 1% of the tower height. This limit has been used in the literature (Ma and Meng [2014]) as a reasonable limit in order to avoid excessive displacement of the tower which would negatively impact the tower and overall turbine assembly.

A maximum allowable tower top rotation in the pitching direction , $\theta_{N,Y}$, of 5 degrees is imposed on the tower. This is imposed to avoid interference between the turbine blades and the tower. These response constraints are given in Eq. 6.5.

$$\begin{aligned} g_5(x) &= f_n - \left(1.1 \times 1P\right) \geq 0 \\ g_6(x) &= \left(0.9 \times 3P\right) - f_n \geq 0 \\ g_7(x) &= \frac{H}{100} - u_{N,X} \geq 0 \\ g_8(x) &= 5^o - \theta_{N,Y} \geq 0 \end{aligned} \tag{6.5}$$

6.3.3 Local Structural Constraints

In terms of the concrete segments, stress limitations are required to ensure that the maximum compression resulting from the summation of bending, dead weight and pre-stressing forces does not exceed the design compression capacity of the concrete in any given segment. In tension, in order to avoid any cracking in the concrete under service

loading, a condition of zero net tension is imposed. Limitations on compression stress are based on Eurocode 2 (British Standards Institution [2004]). Any prestressed tendons included in the optimisation routine will be deemed to be acting at their limiting design yield stress. As the number of tendons is not explicitly included within the vector of design variables, $\{x\}$, the optimisation routine will vary the number of tendons required in order to offset any tension developed in the concrete through bending of the tower. The designed number of tendons will be the minimum required to offset induced tension. An upper limit of 15MPa was chosen for concrete prestress.

With regards to the stress within the steel segments at the top of the tower, there is a need to limit stress here both to avoid yielding of the material but also to avoid local shell buckling. A constant height between stiffeners was taken as 7.5m as a reasonable height. Constraints in terms of material stress are outlined in Eqs. 6.6 and 6.7.

$$\begin{aligned} g_9(x) &= \sigma_{adm,c} - \sigma_{h_o,c} - \sigma_{pt,c} \geq 0 \\ g_{10}(x) &= \sigma_{adm,c} - \sigma_{h_{int},c} - \sigma_{pt,c} \geq 0 \\ g_{11}(x) &= \sigma_{adm,s} - \sigma_{h_{int},s} \geq 0 \\ g_{12}(x) &= \sigma_{adm,s} - \sigma_{H,s} - \sigma_{pt,c} \geq 0 \end{aligned} \tag{6.6}$$

Where

$$\begin{aligned} \sigma_{adm,c} &= 0.6 f_{ck} \\ \sigma_{adm,s} &= min\big(f_y, f_{\text{buckle}}\big) \\ \sigma_{pt,c} &= 15MPa \end{aligned} \tag{6.7}$$

A limit is to be placed on the fatigue life of both the steel and concrete portions of the tower of a minimum 20 years. The fatigue life of the concrete must be assessed under the special condition of the concrete being under a permanent state of compression. Recent work in the literature (Lantsoght et al. [2016]) has given a good description of different methods available. Methods are available from Eurocode 2 (British Standards

Institution [2004]) and fib Model Code 2010 (fib International [2013]). The authors suggest the model proposed in fib Model Code is more accurate in the case of high strength concrete as used here. Therefore this code was adopted and fatigue life checked using Rainflow counting of stress time histories and the application of a 'Palmgren-Miner' damage hypothesis. Fatigue life calculation of the steel plated part of the tower has been calculated using the procedure set out in Eurocode 3, Part1-9, British Standards Institution [1993].

$$
\begin{aligned}
g_{13}(x) &= 1 - \sum_{i=1}^{N} \frac{n_{h_o,c,i}}{N_{c,i}} = 1 - D_{h_o,c} \geq 0 \\
g_{14}(x) &= 1 - \sum_{i=1}^{N} \frac{n_{h_{int},c,i}}{N_{c,i}} = 1 - D_{h_{int},c} \geq 0 \\
g_{15}(x) &= 1 - \sum_{i=1}^{N} \frac{n_{h_{int},s,i}}{N_{s,i}} = 1 - D_{h_{int},s} \geq 0 \\
g_{16}(x) &= 1 - \sum_{i=1}^{N} \frac{n_{H,s,i}}{N_{s,i}} = 1 - D_{H,s} \geq 0
\end{aligned}
\tag{6.8}
$$

Where fatigue damage accumulated over the lifetime of the turbine for either segment, as found using Palgren-Miner hypothesis, $\sum_{i=1}^{N} \frac{n_{H_h,i}}{N_i}$, must be less than unity in order for fatigue life constraint to be satisfied. Fatigue life constraints are listed in Eq. 6.8.

6.4 Methodology for the Optimisation of Hybrid Tower

The methodology proposed incorporates the 11 DOF LSFE model and incorporates both local and global structural responses and constraints. In-built Artificial Neural Network meta-models are trained using selected design inputs such that dynamic responses of towers can be assessed through the numerical optimisation routine. The use of this non-linear generalisation technique is distinct from the use of a computationally expensive dynamic MDOF model embedded within the optimisation routine, without the loss of dynamic response data and data accuracy. A flowchart of how the methodology is constructed is given in fig 6.1.

A two-part optimisation algorithm (GA followed by PS) is used such that the benefits of each algorithm can be exploited, thus ensuring improved optima. There are examples in the literature where this approach has been taken, with authors defining the approach as 'cascading' algorithms and either using existing algotihms in series or modifying algorithms prior to combining (Garg [2016], Zhang et al. [2005]).

6.4.1 Generalisation of Free and Forced Vibration Properties

6.4.1.1 Discrete Sampling of Design Variable Domain

In order to find a suitable sample size in terms of the sampling rate of the overall eight-dimensional domain of the geometrical design variables, an assessment was carried out by taking various sample sizes and comparing respective results in a formal manner.

The fundamental fore-aft frequency, f_n, of the at-rest turbine was selected as an indicator for the purposes of comparing sample sizes. The principle of the Central Limit Theorem (CLT) was applied in order to compare spreads of fundamental frequency outputs for any given sample size. The workings of this principle is widely provided in texts on the subject of the use of statistics (Walpole et al. [1993]). For each sample size, 100 independent and equally spread samples were taken from the domain and the fundamental frequency was found for each of the points within each sample. The statistical point sampling method known as the Latin Hypercube algorithm was used to ensure an even spread of data points across the eight-dimensions of the vector domain. According to the CLT, by taking the mean of each sample and then assessing the dispersion of means of all samples, an assessment can be made as to how representative the sample size is of the entire domain. The distribution of means of independent and equally dispersed samples within any function will tend to be normal, regardless of the probability distribution of the underlying function itself. This property will be used here in order to assess samples of size 5n, 10n, 20n and 30n (40, 80, 160 and 240 respectively) for $x \in \mathbb{R}^n$.

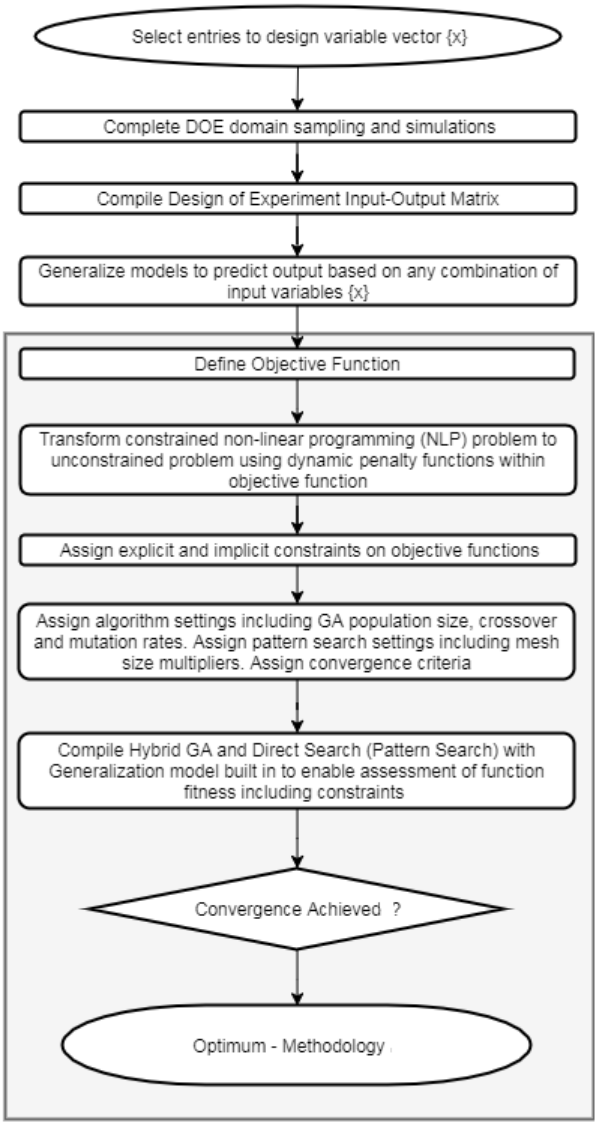

Figure 6.1: Optimisation Methodology Flowchart - From Definition of Objective, through Generalisation of Responses to Compiling Optimisation Algorithm

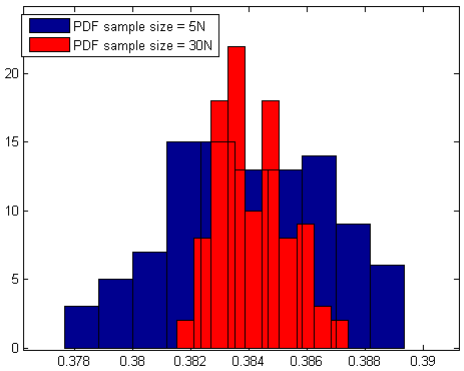

(a) Sample Results Histogram, Various Sample Sizes

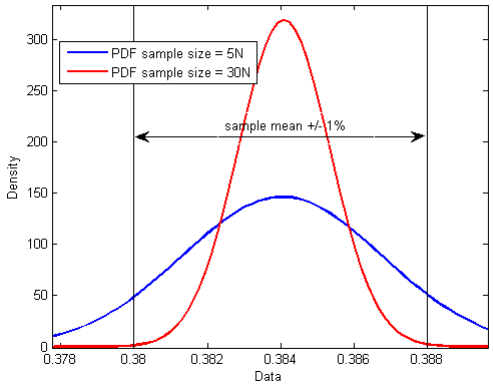

(b) Sample Results PDF, Various Sample Sizes

Figure 6.2: Generalisation of Response Properties - Comparison of Domain Sample Sizes using Central Limit Theorem

The mean fundamental frequency for each set of sample sizes was found to be 0.384 Hz. With increasing sample size, the spread of mean values decreased and the density function converged about the mean. Histogram and Probability Density Functions (PDF) are provided in fig 6.2 for the 5n and 30n sample sizes to illustrate this fact. The PDF plots show that for a sample size of 30n, there is a greater than 95% probability that the frequency mean will be within 1% of the actual mean. Based on this assessment of the domain representation found by taking 30n sample points ($30 \times 8 = 240$), this sample size was adopted in fitting models for the remainder of this chapter.

6.4.1.2 Integration of 11 DOF LSFE Model

The 11 DOF LSFE model is used in this methodology as it is capable of providing free and forced response characteristics for any given tower configuration (based on design variable quantities).

DO Optimisation	v (m/s)	I (%)	LC	H(m)
1	12	14	4	100
2	16	14	5	100
3	20	14	6	100
4	16	14	5	100
5	16	14	5	125
6	16	14	5	150

Table 6.2: Design Optimisation Load Cases 1-6

6.4.1.3 Meta Modelling – Artificial Neural Networks

Feed-forward Artificial Neural Networks (ANNs) will be used as a means of predicting the response of the MDOF model.

Mini and Sowmya [2012] presented a paper on the subject of neural network use to predict the fatigue strength of fibre-reinforced composite materials. The authors noted that the neural networks employed had a distinct advantage over curve for surface equation fitting techniques in generalizing results based on inputs owing to their ability to capture highly non-linear patterns and where a large number of input variables are to be considered. This is important in the case of generalizing the behaviour of the wind turbine towers proposed here.

Rafiq et al. [2001] wrote on the subject of neural network design for engineering applications. A practical example of a reinforced concrete slab is presented. The authors provide useful guidance on how to design the configuration of the network and also how to pre-process data to be used in the training phase. Their work showed how ANNs can be trained to provide a design result to a high level of accuracy, once properly designed and trained, in place of time consuming and computationally expensive traditional techniques.

6.4.2 Design of Experiment

A series of experiments were designed to vary input parameters in finding simulation free and forced vibration responses. The exposure condition of mean hub height wind speed, $\bar{v}$ was varied by way of using different load cases, as defined in Table 6.2. In addition, the hub height of the tower was varied. The input vector to the ANNs, $\{\bar{x}\}^T \in \mathbb{R}^{11}$ is given as $\{\bar{x}\}^T = [x^T, \bar{v}, I, H]$.

Sample values for the design variables were chosen using the statistical point sampling method known as the Latin Hypercube algorithm, using a sample size 240 to sample the domain.

6.4.3 ANN Output, Configuration Training

The target quantities to be predicted by the ANNs can be grouped in four broad categories, including - the peak displacement and rotation responses for each of the tower top degrees of freedom, Z_u, the frequencies associated with each of the turbine degrees of freedom, Z_ω the peak shell stresses, Z_σ and the fatigue damage expectancy of the concrete and steel, Z_D. Therefore, it was decided to configure and train four seperate ANNs for each to predict these responses. The contents of each output layer, Z, are identified in Eq. 6.9. Table 6.3 identifies the configuration of each ANN required to predict each output layer. The notation $A - B - C$ refers to the number of neurons in the input, hidden and output layers respectively.

$$\begin{aligned}
\{Z_\omega\}^T &= [\omega_1, \omega_2, \cdots, \omega_{11}] \\
\{Z_u\}^T &= [u_{N,X}, u_{N,Y}, u_{N,Z}, \cdots, \theta_{N,Z}] \\
\{Z_\sigma\}^T &= [\sigma_{h_o,c}, \sigma_{h_{int},c}, \sigma_{h_{int},s}, \sigma_{H,s}] \\
\{Z_D\}^T &= [D_{h_o,c}, D_{h_{int},c}, D_{h_{int},s}, D_{H,s}]
\end{aligned} \tag{6.9}$$

DO	Z_ω	Z_u	Z_σ	Z_D
1 2 3	11-66-11	11-66-5	11-66-4	11-66-4
4 5 6	11-66-11	11-66-5	11-66-4	11-66-4

Table 6.3: Feed-Forward Artificial Neural Network Layer Architecture/Configuration

Baum [1988] proposed a theorem for the minimum number of neurons required in the first hidden layer of a multi-layered feed-forward network. This stated that the minimum number of neurons in this layer is equal to the number of training data sets divided by the number of input neurons. The output layer is a function of previous layers, which are assigned a weighting and bias function on the basis of the network training process.

Figure 6.3 outlines the construction of each feed-forward ANN in terms of the application of weights and bias quantities. Through iteratively testing different combinations of weights and bias quantities and comparing the input-output relationship as the performance of the ANN, values of W_{ij}, V_{jk}, b_{wj} and b_{vk} can be optimised to give the final ANN.

$$\begin{aligned} Y_j &= \sum_{i=1}^{I} W_{ij} X_i + b_{wj} \\ Z_k &= \sum_{j=1}^{J} V_{jk} Y_j + b_{vk} = \sum_{j=1}^{J} V_{jk} \Big(\sum_{i=1}^{I} W_{ij} X_i + b_{wj} \Big) + b_{vk} \end{aligned} \tag{6.10}$$

Figure 6.4 includes training performance and regression information for a selection of ANNs trained. In all cases, a high correlation of determination (R^2) regression value was obtained.

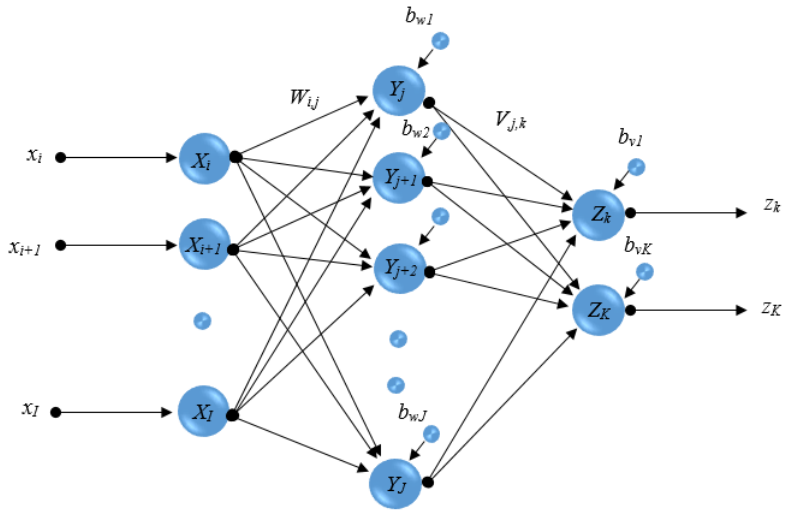

Figure 6.3: Typical Feed-Forward Artificial Neural Network Architecture/Configuration Graphic

6.4.4 Hybrid Genetic Algorithm-Pattern Search Optimisation Algorithm

A flowchart of the GA/PS algorithm is given in fig 6.5. The broad extents of the Genetic Algorithm, Pattern Search Algorithm and Artificial Neural Network functions are evident from the flowchart. The ANNs can be accessed by both the GA and PS phases of the optimisation. Once convergence has been reached by the GA phase, this point is taken as the initial 'current' point in the PS phase.

6.5 Hybrid Tower Optimisation

Objective functions are initially formulated as single objective problems. These are separated into structural and non-structural objective functions. The algorithm settings used in the optimisations carried out in this chapter are given in Table 6.4.

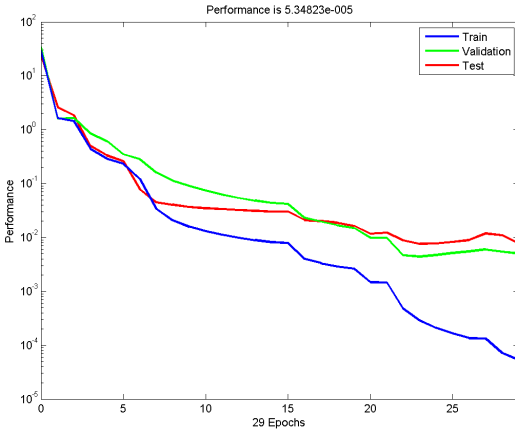

(a) Training Performance, Z_u

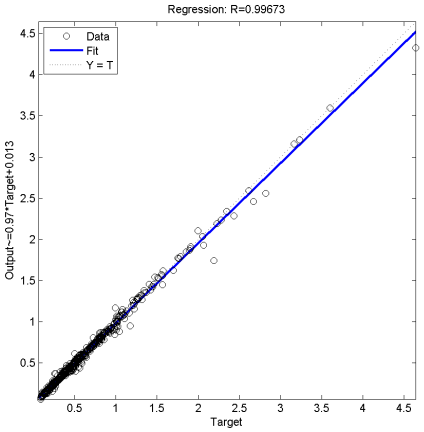

(b) Regression, Z_u

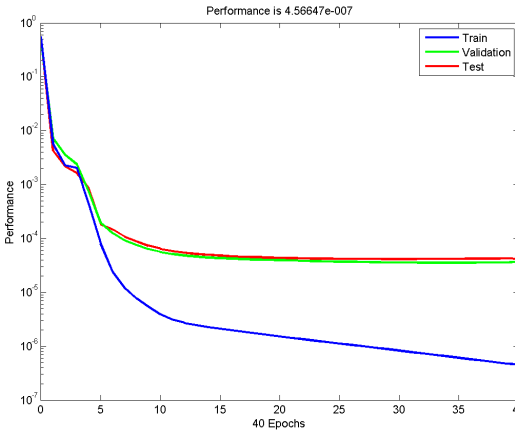

(c) Training Performance, Z_ω

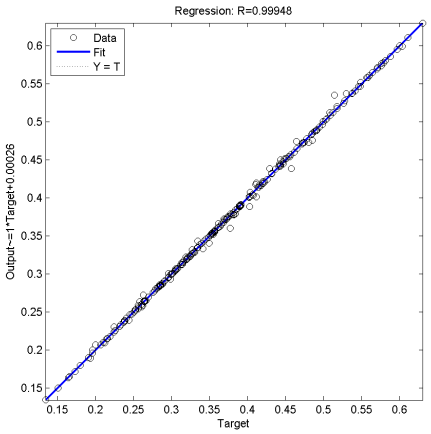

(d) Regression, Z_ω

Figure 6.4: Typical Feed-Forward Artificial Neural Network Training and Regression Plots

Algorithm settings	Genetic Algorithm	Pattern Search
population	200	-
crossover	0.8	-
migration	0.2	-
elite retention	0.05	-
generations	100	-
polling order	-	consecutive
mesh expansion factor	-	2
mesh contraction factor	-	0.5
mesh tolerance	-	1.00E-06
generations	-	100

Table 6.4: GA/PS Algorithm Initialisation Parameters

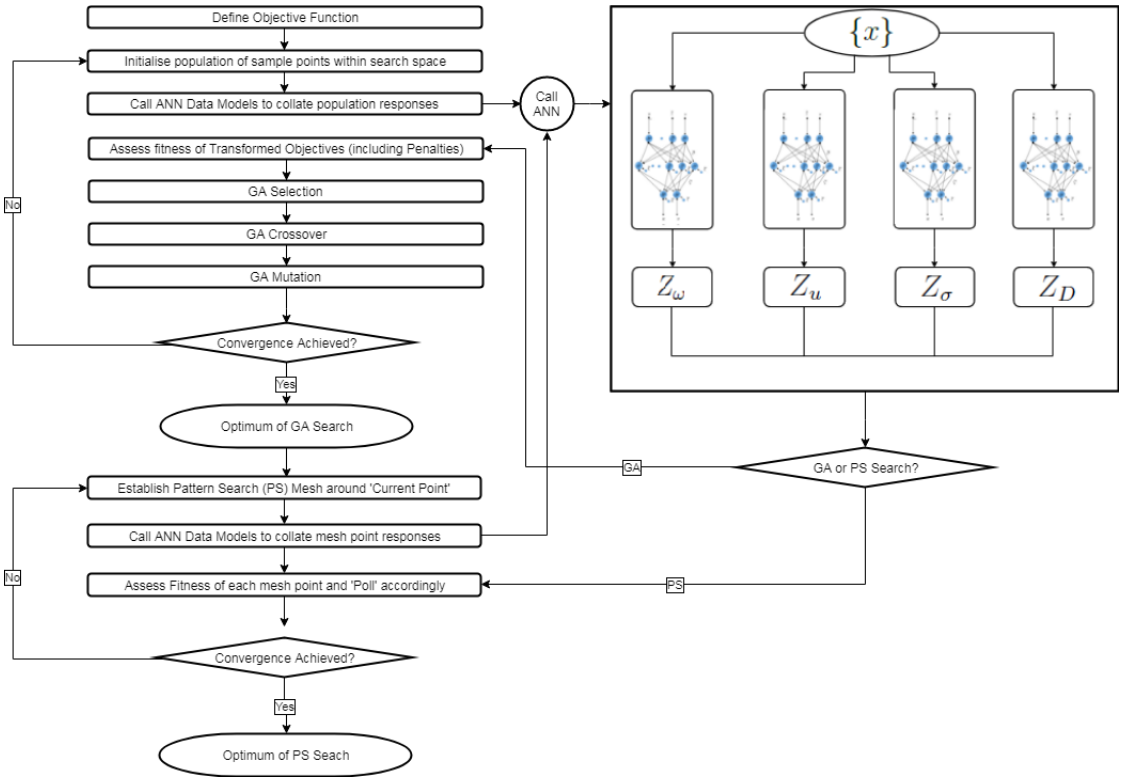

Figure 6.5: Flowhart of Genetic Algorithm/Pattern Search (GA/PS) Optimisation Algorithm, including Artifical Neural Networks

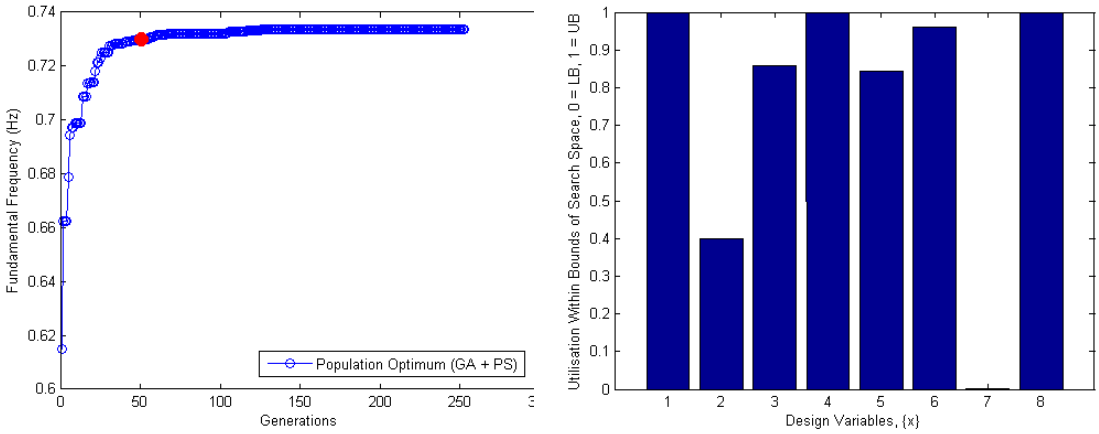

(a) Population Optimum (b) Variable Utilisation within Bounds

Figure 6.6: $max(f(x))$, Natural Frequency Objective Optimisation

6.5.1 Structural Objective Functions

Structural objective functions were optimised using a single load case, LC 5, with a view to understanding the effects of the input design variables on the optimum value of the objective. All of the explicit and implicit geometrical and structural constraints are imposed on the optimisation algorithm, with the exception of constraining the objective function itself.

6.5.1.1 Natural Frequency

Fundamental frequency was to be maximised using the hybrid GA-PS optimisation algorithm.

Algorithm iterations and final results are given in fig 6.6. The transformed unconstrained optimisation problem is defined in Eq, 6.11.

$$\text{Maximise} \quad F(x,R) = |-\omega_1 - R\left(\sum_{j=1}^{J}|P_j(x)| + \sum_{k=1}^{K}|P_k(x)|\right)| \tag{6.11}$$

An optimum, maximum frequency was found of 0.734 Hz. This optimum value was

-	LB	ω_1	$u_{N,X}$	$\sum_{i=1}^{4} w_i \frac{\sigma_{h,i}}{\sigma_{h,adm}}$	UB
LC	-	5	5	5	-
$\bar{v}(m/s)$	-	16	16	16	-
$I(\%)$	-	14	14	14	-
$H(m)$	-	100	100	100	-
$x_1(m)$	2.000	6.000	5.802	5.021	6.000
$x_2(m)$	1.750	2.250	2.250	2.091	2.250
$x_3(m)$	1.500	1.929	1.699	2.000	2.000
$x_4(m)$	0.200	0.600	0.600	0.377	0.600
$x_5(m)$	0.200	0.369	0.400	0.377	0.400
$x_6(m)$	0.010	0.058	0.060	0.060	0.060
$x_7(m)$	0.010	0.010	0.029	0.030	0.030
$x_8(m)$	20.000	80.000	77.226	80.000	80.000
$\sigma_{h_o,c}(MPa)$	0	20.509	21.138	25.116	$0.6f_{ck}$
$\sigma_{h_{int},c}(MPa)$	0	24.709	28.599	23.690	$0.6f_{ck}$
$\sigma_{h_{int},s}(MPa)$	0	84.311	124.923	84.607	$min(f_y, f_{\text{buckle}})$
$\sigma_{H,s}(MPa)$	0	277.009	169.358	119.251	$min(f_y, f_{\text{buckle}})$
$D_{h_o,c}$	0	0.000	0.000	0.000	1
$D_{h_{int},s}$	0	0.000	0.000	0.000	1
ω_1(Hz)	0.232	0.734	0.691	0.570	0.570
$u_{N,X}$(m)	0	0.243	0.064	0.195	H/100

Table 6.5: Optimum Design Variables (x), Structural Objectives

found after 251 iterations of the algorithm. The 'best' function values are provided for the optimisation. A coloured marker is given to show where the algorithm switches from GA to PS. Table 6.5 provides the design variable solution and the fitness of this point within the search domain in terms of explicit and implicit constraints.

The optimum solution was found where the concrete interface height was at its highest possible value of 80%. All other design variables were close to their respective upper bounds with the exception of the hybrid interface diameter and the steel shell thickness.

6.5.1.2 Fore-Aft Displacement

Fore-aft displacement was set as an objective to be minimised. Algorithm iterations and final results are given in Figure 6.7. The transformed unconstrained problem is

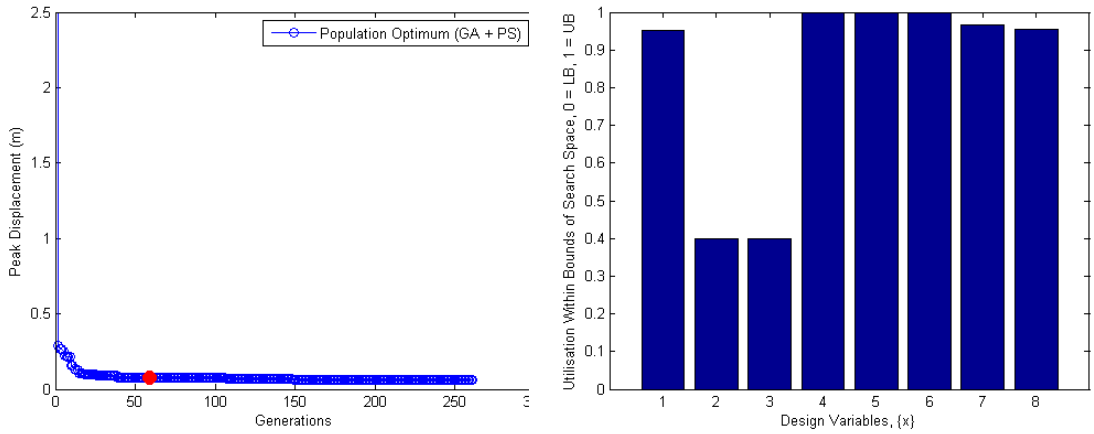

(a) Population Optimum (b) Variable Utilisation within Bounds

Figure 6.7: $min(u_{N,X}(x))$, Displacement Objective Optimisation

defined in Eq, 6.12.

$$\text{Minimise} \quad F(x,R) = u_{N,X} + R\left(\sum_{j=1}^{J}|P_j(x)| + \sum_{k=1}^{K}|P_k(x)|\right) \tag{6.12}$$

In this case, an optimum value was found of 0.064m after 259 iterations of the algorithm. There were some similarities here between the locations of the optimum solution compared to the optimum in the case of the natural frequency. In this case, the optimum occurred close to the upper bound in terms of variable x_8, hybrid interface level.

6.5.1.3 Stress Utilisation Ratio

Stress utilisation is to be minimised. This is carried out as a means of over-designing the tower by designing cross sections which will be well within stress limits but where other responses will be allowed to be close to their constraint boundaries. Weighting factors were set to be equal for each segment considered and such that their sum was equal to 1.

Algorithm iterations and final results are given in fig 6.8. The transformed uncon-

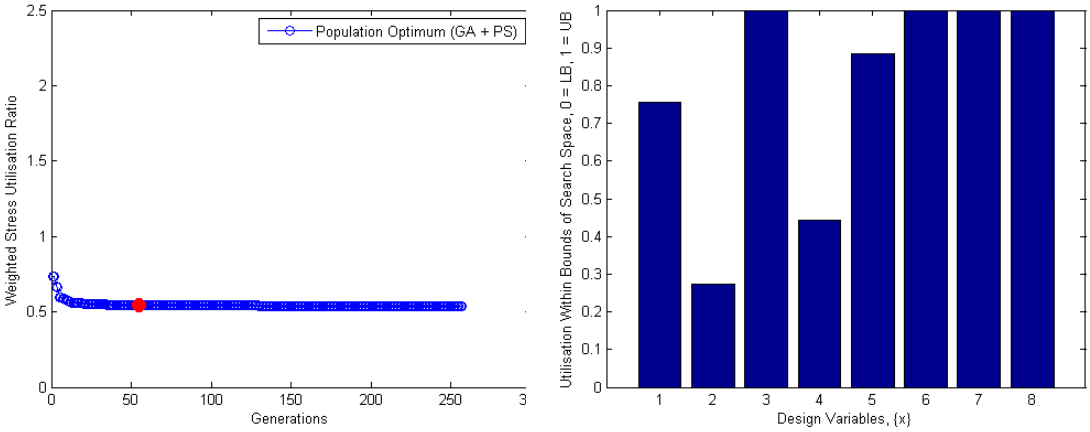

(a) Population Optimum (b) Variable Utilisation within Bounds

Figure 6.8: $min(\sum_{i=1}^{4} w_i \frac{\sigma_{h,i}(x)}{\sigma_{h,adm}})$, Stress Utilisation Objective Optimisation

strained optimisation problem is defined in Eq, 6.13.

$$\begin{aligned} \text{Min; } F(x,R) &= \sum_{i=1}^{4} w_i \frac{\sigma_{h,i}}{\sigma_{h,adm}} + R\left(\sum_{j=1}^{J} |P_j(x)| + \sum_{k=1}^{K} |P_k(x)|\right) \\ h &\in (h_o, h_{int}, H) \\ i &\in (c, s) \end{aligned} \tag{6.13}$$

An optimum solution was found in this case after 253 iterations of the algorithm, at a value of 0.51. From review of Table 6.5, the effects of trying to balance and minimise stress levels for each segment of tower can be seen. Stress utilisation in particular in the case of the steel sections are lower than those where other structural objectives were optimised. One common feature between all of the structural objectives was the tendancy for the algorithm to move towards the region in the domain where the hybrid interface level was close to its upper bound. The same could be said of the base diameter variable (x_1).

$C_{c,i}, C_{co_2,i}$ $i \in (c, s, or, pr)$	$C_{c,i}(euro/tonne)$	$C_{co_2,i}(kgCO_2eq/m^3)$
Concrete	400	439
Prestressed Reinforcement	7000	20017.5
Ordinary Reinforcement	1050	20017.5
Mild Steel	2400	20017.5

Table 6.6: Design Optimisation Material Cost & Embodied Energy Co-efficients

6.5.2 Non-Structural Objective Functions

Non-structural objective functions to be optimised include the Levelised Cost of Energy (LCoE), Climate Change Potential and Mass. Co-efficients used in the formulations are given in Table 6.6. Monetary cost per unit is based on current market rates in Ireland for the supply and construction of each component. Embodied energy cost co-efficients have been taken from the ecoinvent database (Frischknecht and Rebitzer [2005]).

6.5.2.1 Levelised Cost of Energy

Levelised Cost of Energy (LCoE) is typically measured as a function of the total cost of energy production (including capital and fixed operational and maintenance costs) and the energy yield, and is expressed in units of €/kW. On the basis that fixed operational and maintenance costs will be constant for all towers studied, LCoE is expressed here as a ratio of the Tower Capital Cost (TCC), divided by Annual Energy Production (AEP) of the turbine at the location and elevation under consideration. Expressions for LCoE, AEP and TCC are given in Eq. 6.14. The term $P_t(v)$ refers to the power available at a particular wind speed, v, which can be taken directly from the power curve of the NREL baseline turbine. The total number of hours in the year when the turbine is expected to be in operation is given as h_{year} and this has been given as 4000 hours. The probability of occurrence of a particular wind speed $f(v)$, is found using a Weibull distribution curve, taken at a sample site in the midlands within Ireland (Weibull scale and shape values, $c = 9 - 9.8$, $k = 2.4 - 2.5$). The LCoE was optimised initially for a 100m high hybrid tower exposed to Load Case LC 2. The transformed unconstrained

objective function is given in Eq. 6.15

$$\begin{aligned} LCoE(x) &= \frac{TCC(x)}{AEP} \\ AEP &= h_{year}\int_0^{\infty} P_t(v)f(v)dv \\ TCC(x) &= C_{c,c}Vol_c\gamma_c + \\ & C_{c,s}Vol_s\gamma_s + C_{c,or}Vol_{or}\gamma_{or} + C_{c,pr}Vol_{pr}\gamma_{pr} \end{aligned} \tag{6.14}$$

The subscripts 'c','s','or' and 'pr' refer to concrete, steel, ordinary reinforcement and prestressed reinforcement respectively. The terms $C_{c,i}, i \in (c, s, or, pr)$ are provided in Table 6.6 and relate to cost per unit mass.

$$\text{Min;}F(x, R) = LCoE(x) + R\left(\sum_{j=1}^{J}|P_j(x)| + \sum_{k=1}^{K}|P_k(x)|\right) \tag{6.15}$$

The algorithm used was the combined GA+PS algorithm, with settings used as provided in Table 6.4. The result of this optimisation was for an optimised objective of LCoE of €402/kW and a Total Capital Cost (TCC) of €808,305 for the tower. This optimum value was found after 175 iterations of the algorithm. Figure 6.9 provides plots of the objective function vs the iteration value. Table 6.7 provides the design variable solution and the fitness of this point within the search domain in terms of explicit and implicit constraints.

Figure 6.9 also contains plots of the breakdown of the LCoE in terms of the contributions of the constituent parts of the tower including reinforced concrete, prestressed reinforcement, ordinary reinforcement and mild steel. This breakdown indicates that the most significant contributions are made by the concrete and prestressed reinforcement. Mild steel and ordinary reinforcement also contribute to the total LCoE but to a far less significant extent. Finally, fig 6.9 provides a bar plot of the design variable entries, x_1 to x_8. The vertical axis of this plot is a normalised scale intended to show the range of available search space in the dimension of each variable, with a value of

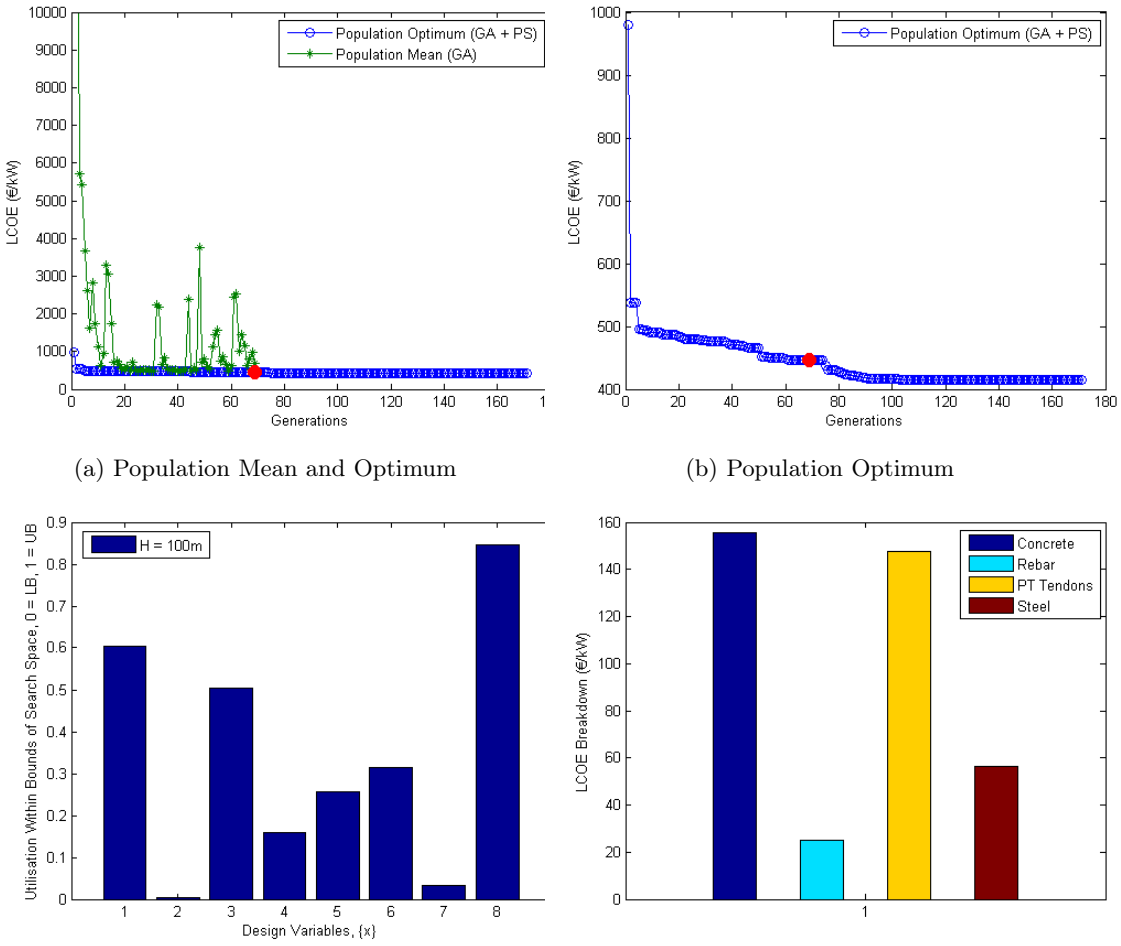

(a) Population Mean and Optimum

(b) Population Optimum

(c) Variable Utilisation within Bounds

(d) LCoE Breakdown/Component

Figure 6.9: $min(LCoE(x))$, Levelised Cost of Energy Objective Optimisation

zero indicating the lower bound and a value of unity indicating the upper bound. Based on this plot, the hybrid interface variable is closest to its upper bound, at 85%. Tower base and top diameters are at 60% and 50% respectively. Shell thickness values are in the range of 15% to 32% of the range.

In order to consider the implications of a varying mean wind speed, $\bar{v}$, two further optimisations were carried out on a tower of 100m in height. These are given in Table 6.7 as DO 1 and DO 3 and include mean hub height wind speeds of 12m/s and 20m/s to be compared to the initial optimisation at $\bar{v} = 16m/s$.

In the case of a varying mean wind speed, an LCoE of €384/kW for the hybrid tower was found in the case of DO 1 after a total of 164 iterations of the algorithm. The highest LCoE value was found in the case of DO 3 at €409/kW. The implications of varying the wind speed can be seen in terms of the utilisation of the available search space for each design variable. Increasing the wind speed has led to a modest increase in some of the design variables including the hybrid interface level and the shell thickness of the concrete and steel at the interface level. However, there is a significant increase in the diameter of the tower top and the shell thickness at the base of the tower. The increase in values of design variables is as a result of the increase in wind speed and was brought about by the algorithm to ensure that constraints such as tower top displacement and material stress levels were satisfied at all times.

In order to consider the implications of a varying tower height, a further two optimisations were carried out on towers of 125m and 150m. These are also given in Table 6.7 as DO 5 and DO 6. Loadcase LC 5 was again used for these tower heights which consists of a mean hub height wind speeds of 16m/s and turbulence intensity of $I = 14\%$.

LCoE values were found to be €402/kW, €569/kW and €856/kW for towers of heights 100m, 125m and 150m respectively. Increasing the tower height has had significant implications for the utilisation of each of the design variables. All variables from x_1 to x_7 have seen increases, whereas variable x_8 has decreased. An LCoE breakdown is provided for each tower height in fig 6.10. The contribution of mild steel increases significantly on increasing the height. This is due to the fact that the interface level is decreasing as a percentage of the tower height, such that tubular steel provides a greater proportion of the tower.

6.5.2.2 Climate Change Potential

Although not traditionally considered as an objective function in the design and optimisation of a structural member, Total Embodied Energy (TEE) or Climate Change Potential (CCP), measured in gCO_2 eq. or $gCO_2eq./kW$, has been given significant

-	DO1	DO2	DO3	DO5	DO6
LC	4	5	6	5	5
$\bar{v}$ (m/s)	12	16	20	16	16
$I(\%)$	14	14	14	14	14
$H(m)$	100	100	100	125	150
$x_1(m)$	4.283	4.415	4.741	4.692	4.926
$x_2(m)$	1.750	1.755	1.994	1.798	1.990
$x_3(m)$	1.669	1.752	1.978	1.798	1.990
$x_4(m)$	0.252	0.264	0.254	0.314	0.395
$x_5(m)$	0.250	0.251	0.245	0.303	0.395
$x_6(m)$	0.023	0.026	0.025	0.040	0.044
$x_7(m)$	0.011	0.011	0.010	0.012	0.025
$x_8(m)$	70.000	70.783	65.974	75.222	82.518
ω_1(Hz)	0.390	0.403	0.427	0.285	0.235
$u_{N,X}$(m)	0.690	0.639	0.559	0.664	0.539
$\sigma_{h_o,c}(MPa)$	30.000	28.676	27.859	30.000	30.000
$\sigma_{h_{int},c}(MPa)$	30.000	29.183	28.727	30.000	30.000
$\sigma_{h_{int},s}(MPa)$	262.120	234.847	229.597	262.878	297.858
$\sigma_{H,s}(MPa)$	271.928	255.726	243.831	302.920	217.214
$D_{h_o,c}$	0.000	0.000	0.000	0.000	0.000
$D_{h_{int},s}$	0.000	0.000	0.000	0.000	0.000
TCC (€)	772324.169	808,305	823,753	1,236,888	1,985,531
AEP (kW)	2,010	2,010	2,010	2,173	2,317
LCoE (€/kW)	384	402	410	569	857

Table 6.7: Optimised Design Variables (x), Structural Response Values & Levelised Cost of Energy

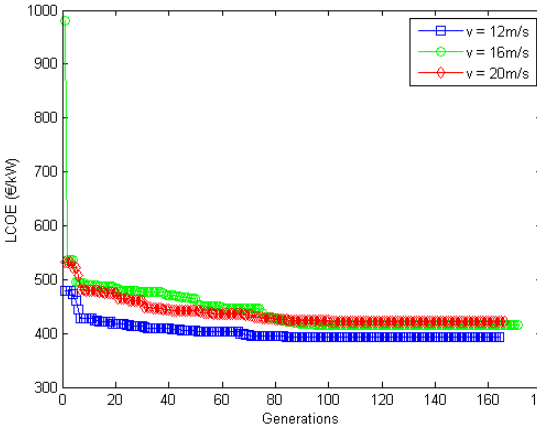

(a) Varying $\bar{v}$, Iteration vs Optimium

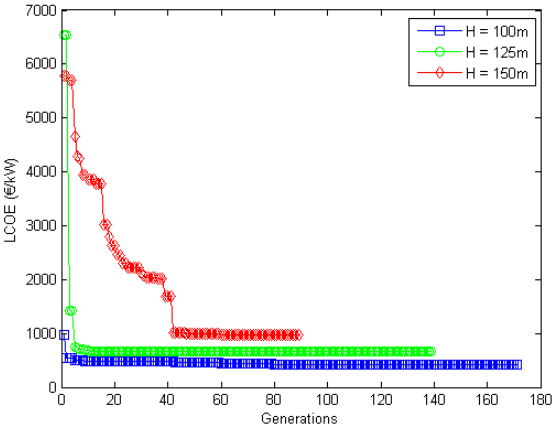

(b) Varying H, Iteration vs Optimium

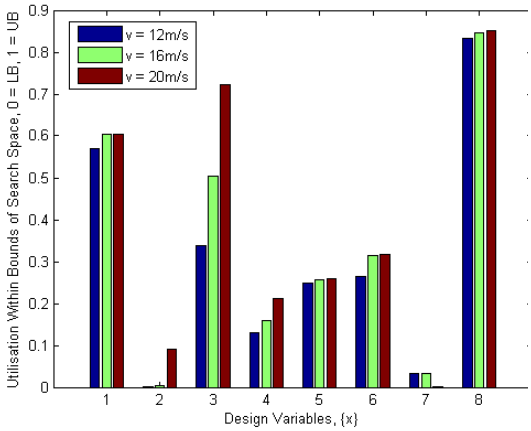

(c) Varying $\bar{v}$, Utilisation within Bounds

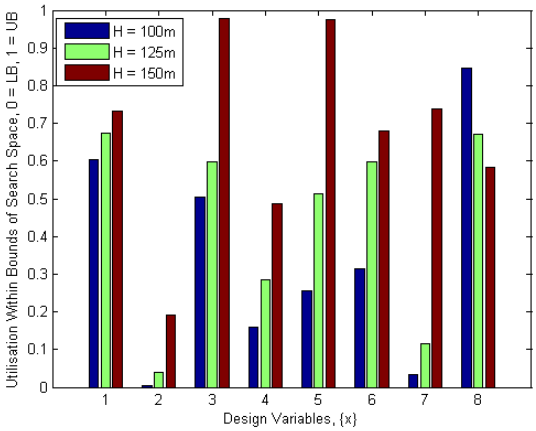

(d) Varying H, Utilisation within Bounds

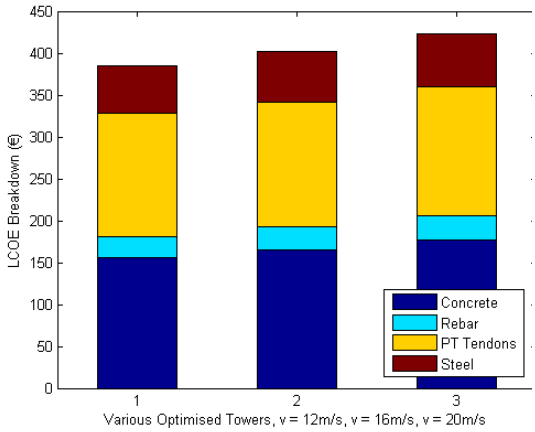

(e) Varying $\bar{v}$, LCoE Breakdown

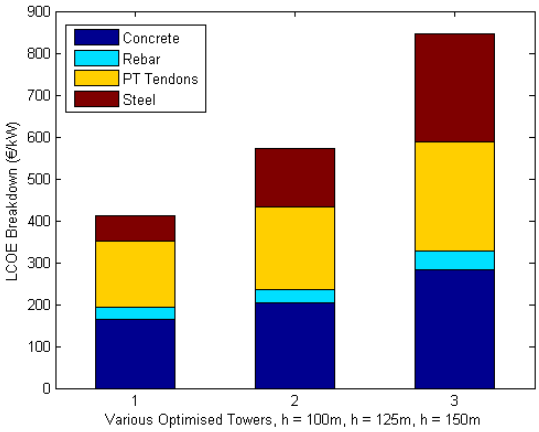

(f) Varying H, LCoE Breakdown

Figure 6.10: $min(LCoE(x))$, Levelised Cost of Energy Objective Optimisation - Variable Wind Speed (a), (c) & (e) & Tower Height (b), (d) & (f)

,

attention in the research recently.

Embodied energy has been considered in various guises in the literature. It has been studied to compare one renewable energy technology to another, to select appropriate components for overall assemblies and as an objective function which is to be minimised in the design of technologies.

Rashedi et al. [2012] optimised materials for various parts of a turbine assembly using the embodied energy as an objective. Life cycle costs of wind turbines were considered by Gallagher et al. [2017] where the Circular Economy was the central focus. Gallagher et al. [2017] carried out a Life-Cycle Assessment (LCA) of solar photovoltaic, hydro and wind systems with a view to comparing their relative performance. Circular Economy objectives were applied to each technology to compare their performance over a 100 year lifespan. The authors demonstrated that wind turbines had a particularly high demand for iron and steel, particularly the towers, and as a result scored poorly compared to other technologies in terms of indicators such as Climate Change Potential (CCP) and Abiotic Resource Depletion Potential (ARDP). The use of hybrid concrete-steel towers is given as an example of a measure which could be used to reduce ARDP.

In this case, Climate Change Potential (CPP) of hybrid towers, measured in $kgCO_2eq./kW$ is set as an objective which is to be minimised. The CCP is measured as the Total Embodied Energy divided by the AEP. The transformed, unconstrained problem is given in Eq. 6.16. Expressions for CCP and TEE are given in Eq. 6.17.

$$\begin{aligned} \text{Min; } F(x,R) &= CCP(x) + R\left(\sum_{j=1}^{J}|P_j(x)| + \sum_{k=1}^{K}|P_k(x)|\right) \\ CCP(x) &= \frac{TEE(x)}{AEP} \end{aligned} \tag{6.16}$$

$$\begin{aligned} TEE(x) = {} & C_{co_2,c}Vol_c + \\ & C_{co_2,s}Vol_s + C_{co_2,or}Vol_{or} + C_{co_2,pr}Vol_{pr} \end{aligned} \tag{6.17}$$

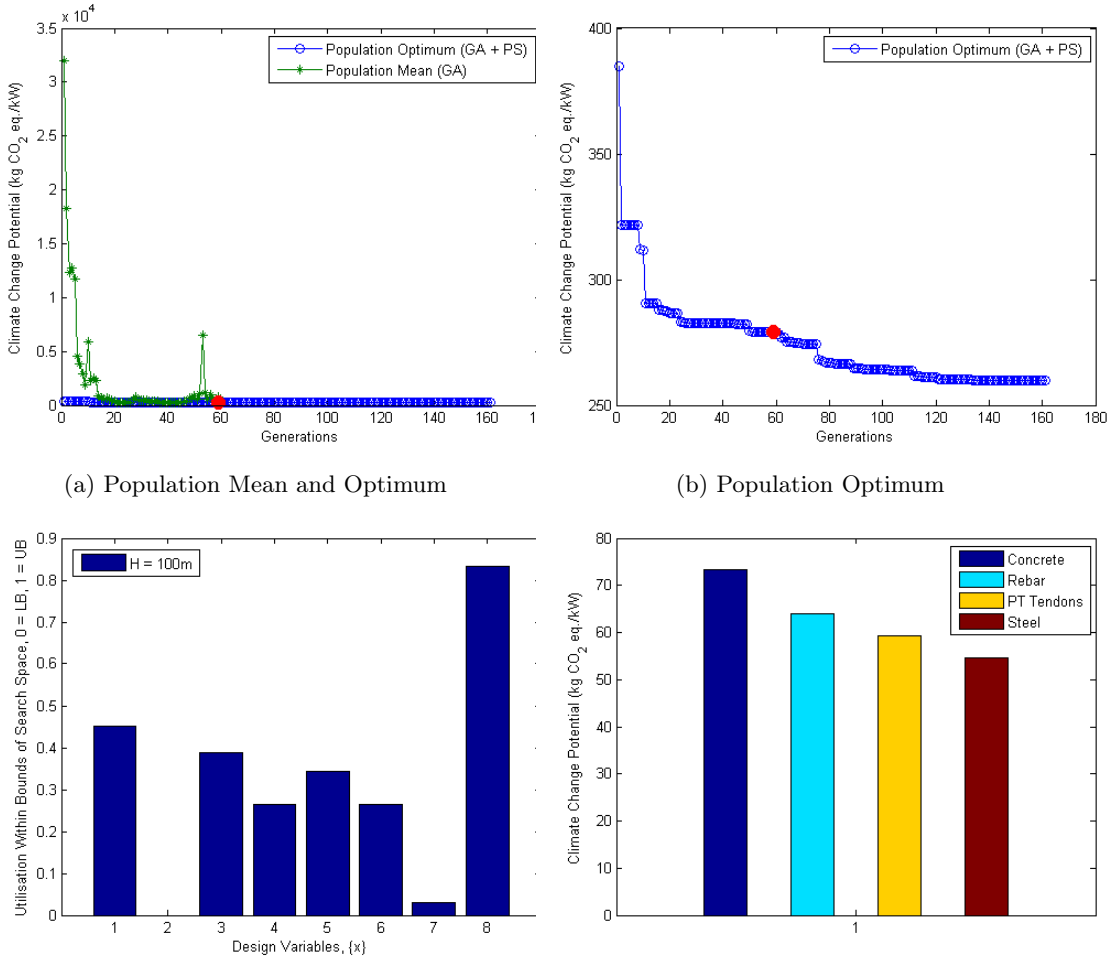

(a) Population Mean and Optimum

(b) Population Optimum

(c) Variable Utilisation within Bounds

(d) CCP Breakdown/Component

Figure 6.11: $min(CCP(x))$ Climate Change Potential Objective Optimisation

The terms $C_{co_2,i}, i \in (c, s, or, pr)$ are provided in Table 6.6 and relate to embodied energy per unit volume.

Climate Change Potential was optimised initially for a 100m high hybrid tower exposed to Load Case LC 5. The algorithm and settings used are the same as those used for LCoE optimisation. The result of this optimisation was for an optimised objective of CCP of 264 $kgCO_2eq./kW$ and a Total Embodied Energy of 499,394 $kgCO_2eq$. An optimum value was found after 165 iterations of the algorithm. Figure 6.11 provides plots of the objective function vs the iteration value.

Figure 6.11 also contains plots of the breakdown of the CCP in terms of the contributions of the constituent parts of the tower – reinforced concrete, prestressed reinforcement, ordinary reinforcement and mild steel. This breakdown indicates that the most significant contribution to embodied energy is made by the concrete. Mild steel makes a lower contribution in terms of the composition of this tower at approximately half that of concrete, despite the fact that the optimal interface height is found to be 78m. Finally, fig 6.11 provides a bar plot of the design variable entries, x_1 to x_8. The vertical axis of this plot is a normalised scale intended to show the range of available search space in the dimension of each variable, with a value of zero indicating the lower bound and a value of unity indicating the upper bound. Based on this plot, the hybrid interface variable is closest to its upper bound, at 82%. Tower base and top diameters are at 45% and 38% respectively. Shell thickness values are typically in the range of 28% to 35% of the range, with an exception being the top of the steel shell which is at only 3%.

In order to consider the implications of a varying mean wind speed, $\bar{v}$, two further optimisations were carried out on a tower of 100m in height in line with the exercise carried out in the case of LCoE. The results of these three optimisation runs are given in Table 6.8 as well as fig 6.12. In the case of a varying mean wind speed, a CCP of 248 $kgCO_2eq./kW$ for the hybrid tower was found in the case of DO 1 after a total of 160 iterations of the algorithm. The highest CCP value was found in the case of DO 3 at 286 $kgCO_2eq./kW$. The implications of varying the wind speed can be seen in terms of the utilisation of the available search space for each design variable.

The implications of a varying tower height are also considered in terms of CCP. The results of these three optimisation runs are given in Table 6.8 as well as fig 6.12. CCP values were found to be 264, 389 and 596 $kgCO_2eq./kW$ for towers of heights 100m, 125m and 150m respectively. Increasing the tower height has had significant implications for the utilisation of each of the design variables. All variables from x_1 to x_7 have seen increases, whereas variable x_8 has decreased. A CCP breakdown is provided for each tower height in fig 6.12. The contribution of mild steel increases significantly on

-	DO1	DO2	DO3	DO5	DO6
LC	4	5	6	5	5
$\bar{v}$ (m/s)	12	16	20	16	16
$I(\%)$	14	14	14	14	14
$H(m)$	100	100	100	125	150
$x_1(m)$	3.803	4.149	3.848	4.475	5.041
$x_2(m)$	1.750	1.750	1.750	1.768	1.983
$x_3(m)$	1.694	1.624	1.729	1.694	1.981
$x_4(m)$	0.306	0.296	0.358	0.337	0.384
$x_5(m)$	0.269	0.279	0.300	0.304	0.384
$x_6(m)$	0.023	0.025	0.027	0.032	0.044
$x_7(m)$	0.011	0.012	0.011	0.019	0.025
$x_8(m)$	70.000	70.000	70.000	85.892	85.086
ω_1(Hz)	0.377	0.396	0.402	0.307	0.240
$u_{N,X}$(m)	0.709	0.687	0.747	0.544	0.518
$\sigma_{h_o,c}(MPa)$	30.000	30.000	30.000	30.000	30.000
$\sigma_{h_{int},c}(MPa)$	30.000	30.000	30.000	30.000	30.000
$\sigma_{h_{int},s}(MPa)$	260.600	275.096	270.858	292.320	294.437
$\sigma_{H,s}(MPa)$	272.087	277.547	282.849	253.495	215.312
$D_{h_o,c}$	0.000	0.000	0.000	0.000	0.000
$D_{h_{int},s}$	0.000	0.000	0.000	0.000	0.000
$TEE(kgCO_2eq.)$	499394.404	531,804	574,384	814,730	1,346,234
$AEP(kW)$	2,010	2,010	2,010	2,173	2,317
$CCP(kgCO2eq./kW)$	248	265	286	375	581

Table 6.8: Optimised Design Variables (x), Structural Response Values & Climate Change Potential

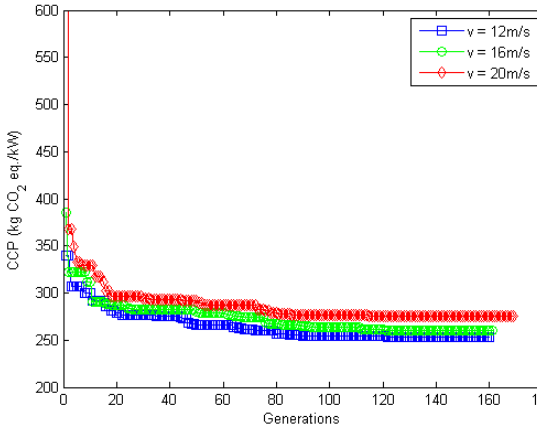

(a) Varying $\bar{v}$, Iteration vs Optimium

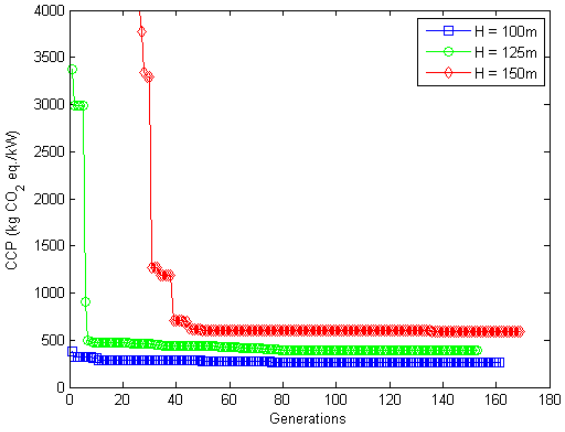

(b) Varying H, Iteration vs Optimium

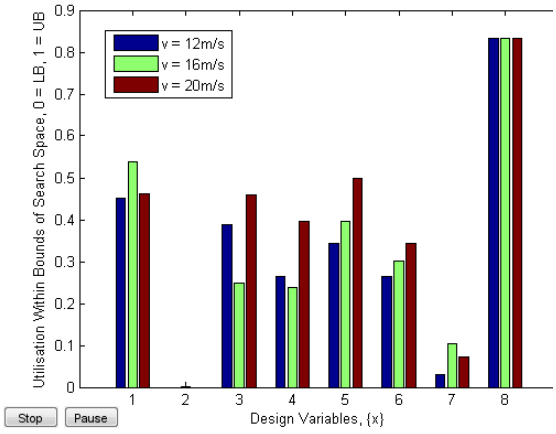

(c) Varying $\bar{v}$, Utilisation within Bounds

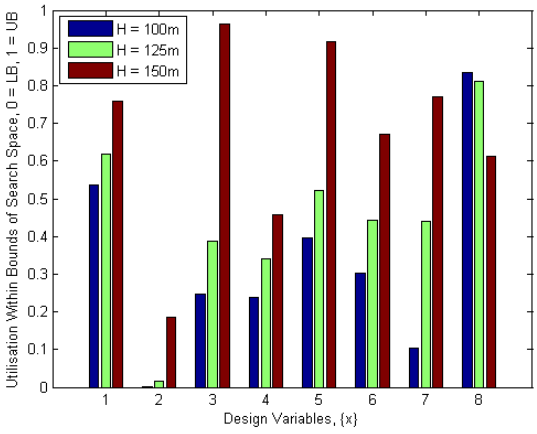

(d) Varying H, Utilisation within Bounds

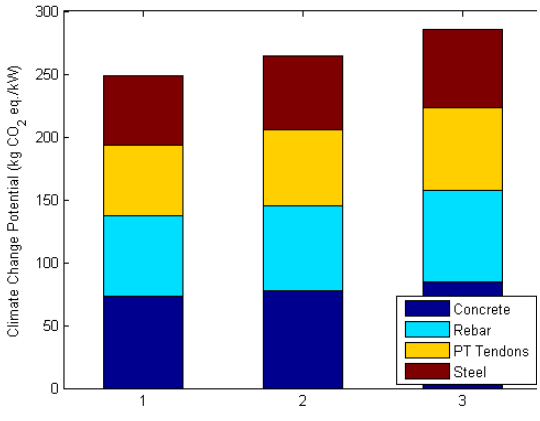

(e) Varying $\bar{v}$, CCP Breakdown

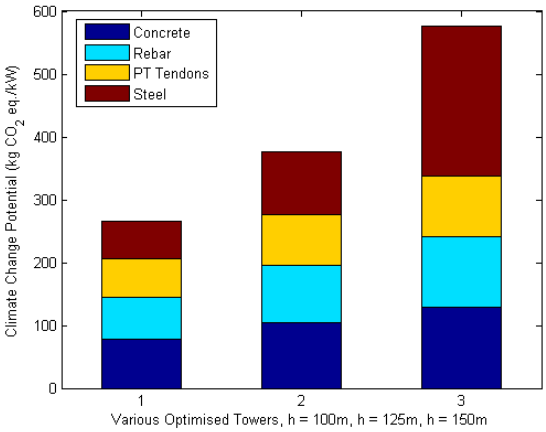

(f) Varying H, CCP Breakdown

Figure 6.12: $min(CCP(x))$, Climate Change Potential Objective Optimisation - Variable Wind Speed (a), (c) & (e) & Tower Height (b), (d) & (f)

increasing the height. This is due to the fact that the interface level is decreasing as a percentage of the tower height, such that tubular steel provides a greater proportion of the tower.

6.5.2.3 Tower Mass

The total mass of a structure has traditionally been set as the objective function when seeking to optimise cost. This is primarily due to the fact that a single material would be present and so minimising mass is a direct means of minimising cost. Although this is not the case in terms of hybrid towers, minimising the mass is a useful exercise as mass may be a limiting factor in terms of transport, cranage or foundation design.

Mass was optimised initially for a 100m high hybrid tower exposed to Load Case LC 5. The transformed unconstrained optimisation problem is given in Eq. 6.18

$$\text{Minimise} \quad F(x,R) = M_{Tower} + R\left(\sum_{j=1}^{J}|P_j(x)| + \sum_{k=1}^{K}|P_k(x)|\right) \tag{6.18}$$

The result of this optimisation was for an optimised objective of mass of 809,892 kg. An optimum value was found after 138 iterations of the algorithm. Figure 6.13 provides plots of the objective function vs the iteration value. Table 6.9 provides the design variable solution and the fitness of this point.

Figure 6.13 also contains plots of the breakdown of the mass in terms of the contributions of the constituent parts of the tower – reinforced concrete, prestressed reinforcement, ordinary reinforcement and mild steel. This breakdown indicates that the most significant contribution to mass is made by the concrete. Mild steel makes a lower contribution in terms of the composition of this tower at approximately half that of concrete, whilst ordinary and prestressed reinforcement account for very little of the mass. Finally, fig 6.13 provides a bar plot of the design variable entries, x_1 to x_8. The vertical axis of this plot is a normalised scale intended to show the range of available search space in the

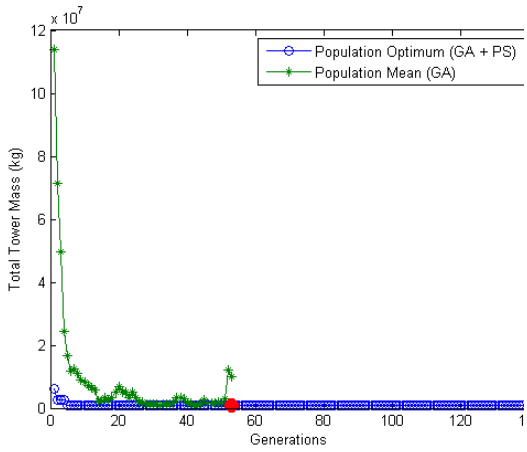

(a) Population Mean and Optimum

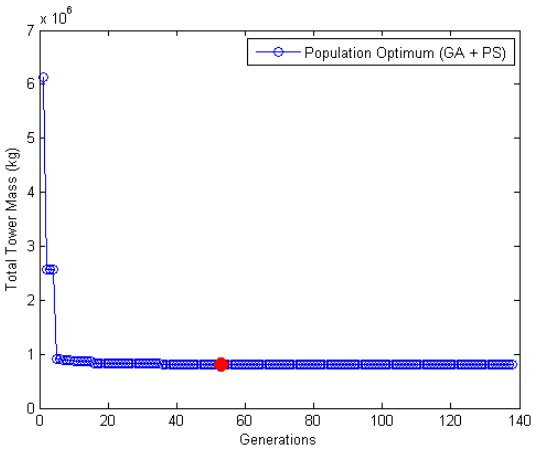

(b) Population Optimum

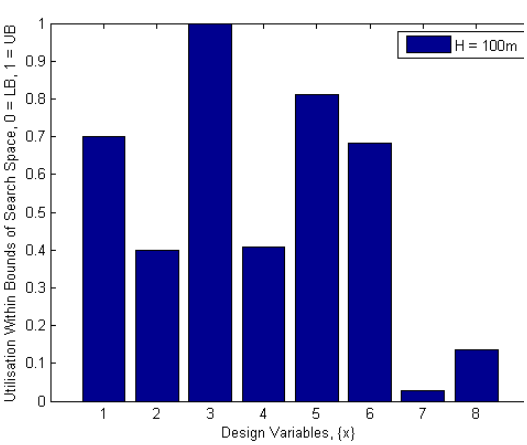

(c) Variable Utilisation within Bounds

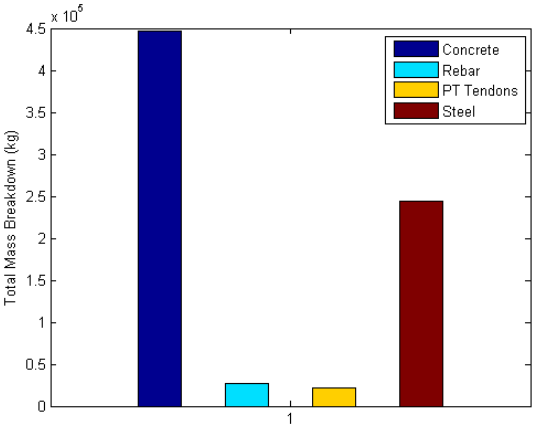

(d) Mass Breakdown/Component

Figure 6.13: $min(M_{Tower}(x))$, Tower Mass Objective Optimisation

dimension of each variable, with a value of zero indicating the lower bound and a value of unity indicating the upper bound. Unlike the case of LCoE and CCP, in this case the hybrid interface level was close to its lower bound, showing the preference for steel as opposed to the heavier concrete. The design variables of steel top diameter and steel shell thicknesses are close to their upper bound positions which is expected given the low interface level and the need for relatively large diameters and thicknesses to give an overall compliant tower.

In order to consider the implications of a varying mean wind speed, $\bar{v}$, two further optimisations were carried out on a tower of 100m in height in line with the exercise carried out in the case of LCoE. The results of these three optimisation runs are given in Table 6.9 as well as fig 6.14. In the case of a varying mean wind speed, a total mass of 740,022 kg for the hybrid tower was found in the case of DO 1 after a total of 145 iterations of the algorithm. The highest mass value was found in the case of DO 3 at 878,917 kg. The implications of varying the wind speed can be seen in terms of the utilisation of the available search space for each design variable.

The implications of a varying tower height are also considered in terms of total mass. The results of these three optimisation runs are given in Table 6.9 as well as fig 6.14. Mass values were found to be 809,812 kg, 1,345,914 kg and 1,966,568 kg for towers of heights 100m, 125m and 150m respectively. Increasing the tower height has had significant implications for the utilisation of each of the design variables. By increasing the tower height, the interface height required to ensure feasible solutions rose, such that in the case of a 150m high tower, the interface was at the mid-point between the upper and lower bound. The breakdown in mass per component highlights the contributions of the concrete and mild steel as compared to the rebar.

6.5.3 Multi-Objective Optimisation

There are a number of established methods available in terms of finding Pareto Optimal solutions where carrying out multi-objective optimisations, with two of the more popular

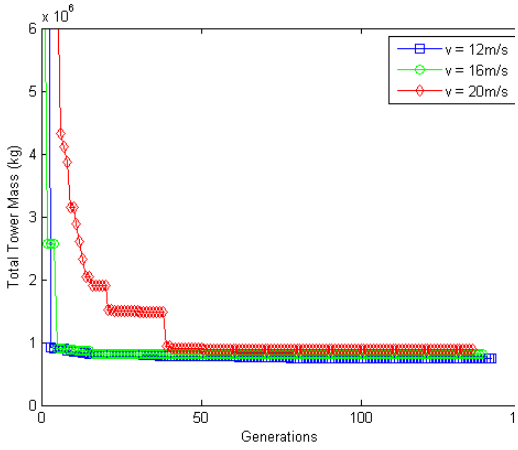

(a) Varying $\bar{v}$, Iteration vs Optimium

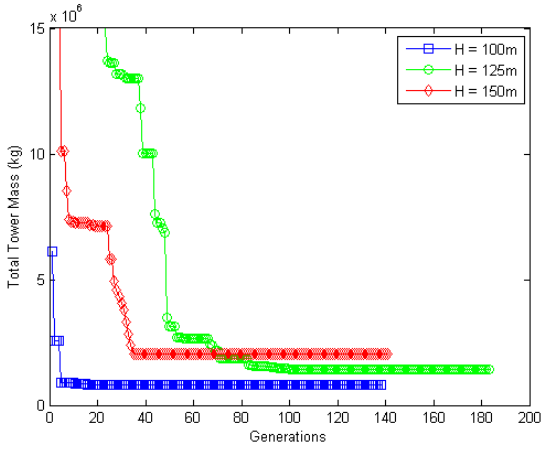

(b) Varying H, Iteration vs Optimium

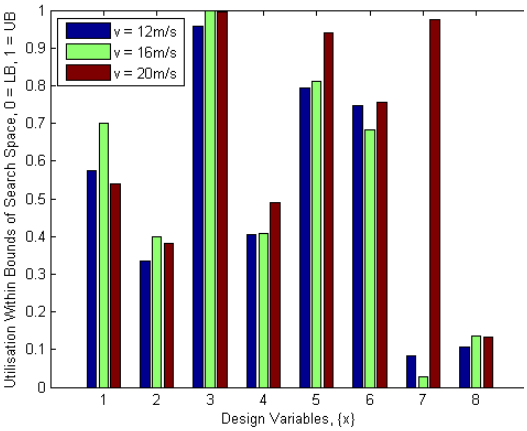

(c) Varying $\bar{v}$, Utilisation within Bounds

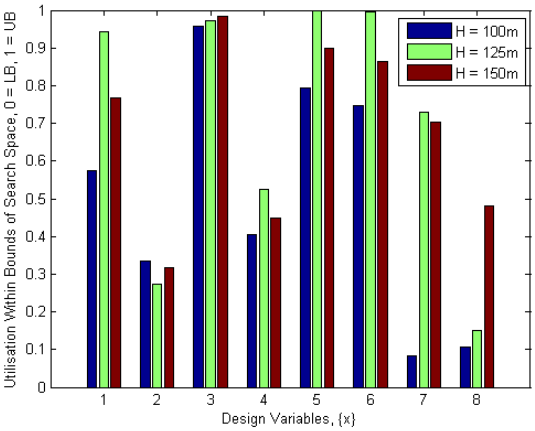

(d) Varying H, Utilisation within Bounds

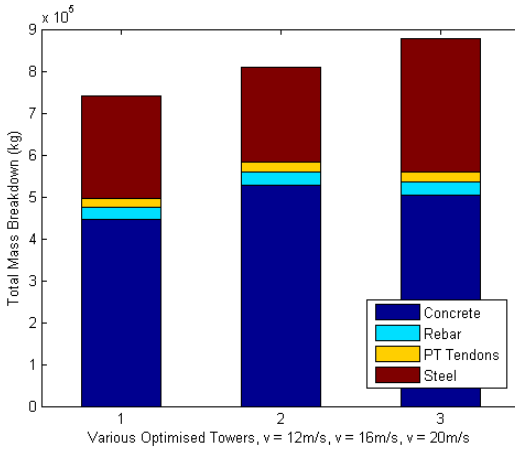

(e) Varying $\bar{v}$, Mass Breakdown

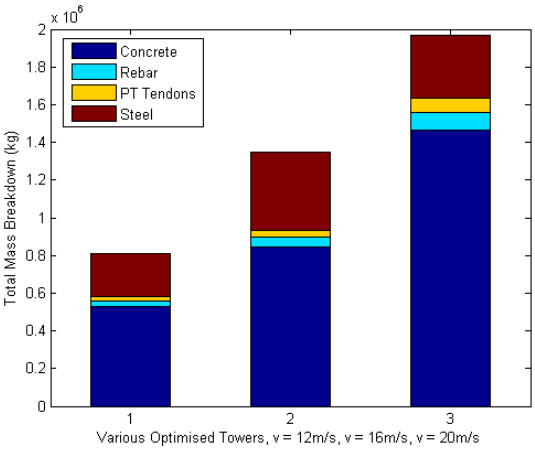

(f) Varying H, Mass Breakdown

Figure 6.14: $min(M_{Tower}(x))$, Tower Mass Objective Optimisation - Variable Wind Speed (a), (c) & (e) & Tower Height (b), (d) & (f)

-	DO1	DO2	DO3	DO5	DO6
LC	4	5	6	5	5
$\bar{v}$ (m/s)	12	16	20	16	16
$I(\%)$	14	14	14	14	14
$H(m)$	100	100	100	125	150
$x_1(m)$	4.295	4.801	4.156	5.773	5.773
$x_2(m)$	2.167	2.250	2.227	2.093	2.093
$x_3(m)$	1.979	1.999	1.998	1.987	1.987
$x_4(m)$	0.362	0.363	0.396	0.410	0.410
$x_5(m)$	0.359	0.362	0.388	0.400	0.400
$x_6(m)$	0.047	0.044	0.048	0.060	0.060
$x_7(m)$	0.012	0.011	0.029	0.025	0.025
$x_8(m)$	26.373	28.191	27.908	36.244	36.244
ω_1(Hz)	0.295	0.303	0.324	0.295	0.295
$u_{N,X}$(m)	1.000	1.000	1.000	0.805	0.805
$\sigma_{h_o,c}(MPa)$	25.818	25.070	27.245	24.850	24.850
$\sigma_{h_{int},c}(MPa)$	29.850	29.858	30.000	29.421	29.421
$\sigma_{h_{int},s}(MPa)$	196.646	219.074	217.259	205.192	205.192
$\sigma_{H,s}(MPa)$	191.972	229.357	98.006	157.445	157.445
$D_{h_o,c}$	0.000	0.000	0.000	0.000	0.000
$D_{h_{int},s}$	0.000	0.000	0.000	0.000	0.000
Mass (kg)	740,022	809,892	878,917	1,345,914	1,345,914

Table 6.9: Optimised Design Variables (x), Structural Response Values & Tower Mass

being the weighted method and the ϵ-constraint method. The weighted method is an intuitive means of weighting several objectives before combining each into one overall objective which is to be optimised.

The ϵ-constraint method incorporates multiple objective functions by retaining a single objective to be optimised and restricting all other objectives to some defined constraint, ϵ, along the Pareto front, $\{\epsilon\}^T = [\epsilon_1, \epsilon_2, \cdots, \epsilon_M]$. The formulation for this method is given in Eq. 6.19, where there are M objectives.

$$\begin{aligned} \text{Minimise} \quad & F(x) = f_o(x) \quad \text{subject to} \\ & [f_1(x), \cdots, f_{o-1}(x), f_{o+1}(x), \cdots, f_M(x)] \leq \epsilon_m \\ & g_j(x) \geq 0, \quad \text{and} \quad j = 1, 2, \cdots, J \\ & h_k(x) = 0, \quad \text{and} \quad k = 1, 2, \cdots, K \\ & x_i^{LB} \leq x_i \leq x_i^{UB}, \quad \text{and} \quad i = 1, 2, \cdots, N \end{aligned} \tag{6.19}$$

The ϵ-constrained method is used in this work as it provides some advantages over the weighted method. Advantages include the ability to ensure uniformly spread points along the Pareto front and the ability to find Pareto optimal points along even convex fronts, which is not true of the weighted sum method. Mavrotas [2009] noted that in the weighting method the scaling of the objective functions has a significant effect on results in terms of Pareto front results. Therefore, we need to scale the objective functions to a common scale before forming the weighted sum. This is not the case in the ϵ-constraint method. Where considering two objectives, one objective is simply formulated as a constraint on the other objective and included as thus within a single objective.

In order to implement the exterior point method described in Section 6.2.3 above, the constrained multi-objective formulation must first be transformed to an unconstrained

problem. This is carried out as follows in Eq. 6.20.

$$\begin{aligned}
&\text{Minimise} \quad F(x,R) = f_o(x) + R\left(\sum_{j=1}^{J}|P_j(x)| + \sum_{k=1}^{K}|P_k(x)| + \sum_{m=1}^{M}|P_m(x)|\right), \\
&\text{Where} \\
&x \in X \\
&P_m(x) = \begin{cases} \frac{f_m(x)}{\epsilon_m}, & \text{if } f_m(x) \geq \epsilon_m \\ 0, & \text{if } m = o \\ 0, & \text{otherwise} \end{cases}
\end{aligned} \tag{6.20}$$

In Eq. 6.20, $P_j(x)$ and $P_k(x)$ are as defined in Eq. 6.2. The penalty term $P_m(x)$ has been introduced to account for points within the search space where the value of one of the constrained objective functions exceeds its assigned constraint, ϵ_m.

6.5.3.1 Multi-Objective Optimisation using Analytical Tower Model

Chapter 3 describes how the natural frequency can be found using an analytical definition of the hybrid tower. Transcendental equations are solved, with the roots of these equations being the unknown β quantity from Eq. 3.12. This equation is re-arranged to give the n^{th} natural frequency, ω_n as given in Eq. 6.21.

$$\omega_n = \left(\frac{\beta_n^4 E_c I_c}{\rho_c A_c}\right)^{0.5} \tag{6.21}$$

This model will now be used within a multi-objective optimisation exercise, where the fundamental frequency, w_1 is set as an objective.

Five variables can be used with the analytical model, including the hybrid interface height, h_{int} the diameters of the lower and upper sections (D_c, D_s) and the shell thicknesses of the upper and lower sections (t_c, t_s). All other values such as material prop-

Description	Value	Unit
Nacelle Mass, ($M_{nacelle}$)	240000	kg
Hub Mass, (M_{hub})	56780	kg
Tower Height, (H)	100	m
Concrete Density, (ρ_c)	2450	kg/m^3
Steel Density, (ρ_s)	8500	kg/m^3
Steel Youngs Modulus, (E_s)	2.05E+13	N/m^2
Concrete Youngs Modulus, (E_c)	3.50E+10	N/m^2

Table 6.10: Multi-Objective Optimisation - Analytical Model Material Properties

erties and densities are pre-defined and given in Table 6.10

Upper and lower limits were chosen for these five variables as defined in Eq. 6.22.

$$\begin{aligned} x &\in X \\ x^{LB} &= \{2, 1.5, 0.2, 0.01, 20\} \\ x^{UB} &= \{6, 3.0, 0.6, 0.06, 80\} \end{aligned} \tag{6.22}$$

A multi-objective optimisation will be carried out by maximising the fundamental frequency, whilst constraining two of the design variables using the ϵ-constraint method. This exercise will allow for examination of the relationships between any two variables and the optimum frequency. Owing to the nature of the tower model, implicit structural constraints are not evaluated. Constraints are imposed in terms of ϵ-constraints on design variables only.

The transformed, unconstrained multi-objective formulation is thus given as per Eq. 6.23.

$$\begin{aligned} \text{Minimise} \quad & F(x, R) = \omega_1(x) + R\left(\sum_{m=1}^{2} |P_m(x)|\right), \\ & P_m(x) = \begin{cases} \frac{x_m}{\epsilon_m}, & \text{if } x_m \geq \epsilon_m \\ 0, & \text{otherwise} \end{cases} \end{aligned} \tag{6.23}$$

The results of these simulations are given below in fig 6.15. Visually, these are useful images as they provide an insight into the relative significance of variables when seeking the maximum possible natural frequency. Results are given as normalised frequency values.

In comparing the relative influence of these variables on the optimum natural frequency, the following observations are made – 1. Maximum frequency occurs at or close to the maximum of each of the two variables set as objectives and 2. Some of the relationships are approximately linear when comparing two variables however others are highly non-linear, for example the relationship between the concrete diameter and the hybrid interface height.

6.5.3.2 LCoE vs Natural Frequency

The objectives of LCoE and fundamental fore-aft frequency were considered in a multi-objective optimisation, using the ϵ-constraint method. In this case, the objective of frequency was set as a constraint and the objective of LCoE was to be optimised in a single objective problem, with the formulation given in Eq. 6.25.

$$\begin{aligned} &\text{Minimise} \quad F(x,R) = LCoE(x) + R\left(\sum_{j=1}^{J}|P_j(x)| + \sum_{k=1}^{K}|P_k(x)| + |P_m(x)|\right), \\ &\qquad \text{Where} \\ &\qquad x \in X \\ &\qquad P_m(x) = \begin{cases} \frac{\omega_1(x)}{\epsilon_1}, & \text{if } \omega_1(x) \geq \epsilon_1 \\ 0, & \text{otherwise} \end{cases} \end{aligned} \tag{6.24}$$

A range of equally spaced natural frequency values were selected in the range 0.2Hz to 0.9Hz and an optimum minimum LCoE was then found for each natural frequency value. Figure 6.16 identifies the optimum fitness found for the selected objectives, in the case of optimisation cases DO1 to DO3, where wind speeds vary.

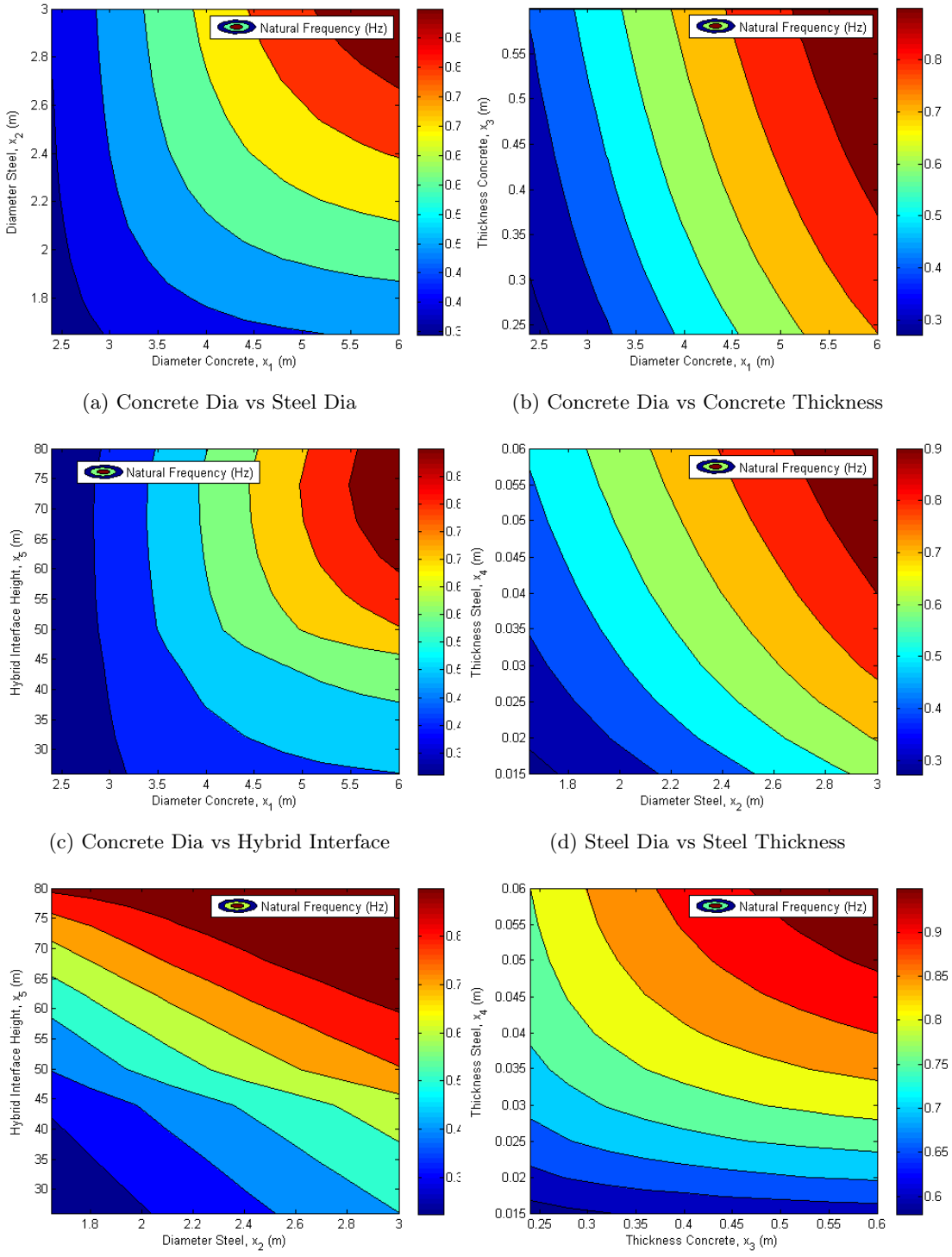

(a) Concrete Dia vs Steel Dia

(b) Concrete Dia vs Concrete Thickness

(c) Concrete Dia vs Hybrid Interface

(d) Steel Dia vs Steel Thickness

(e) Steel Dia vs Hybrid Interface

(f) Thickness Conc vs Thickness Steel

Figure 6.15: $max(\omega_1(x))$, Optimised Natural Frequency with Selected Constrained Objectives

The results indicate a generally increasing LCoE with increasing natural frequency. However, the minimum LCoE was found for each wind speed at 0.3Hz as opposed to the lower value of 0.2Hz. This occurred as at 0.2Hz, other constraints such as tower top displacement forced the solution to a higher LCoE value than that found at 0.3Hz. At 0.9Hz, the LCoE is approximately ten times greater than the LCoE at 0.3Hz for all wind speeds. This demonstrates the trade-off between cost and stiffness, indicating a significant premium associated with increasing the stiffness of the tower in this range.

6.5.3.3 LCoE vs Hybrid Concrete-Steel Interface Level

The objectives of LCoE and hybrid interface level were considered in a multi-objective optimisation, using the ϵ-constraint method. In this case, the objective of hybrid interface height was set as a constraint and the objective of LCoE was to be optimised in a single objective problem. A range of equally spaced hybrid interface values were selected in the range 20m to 80m and an optimum minimum LCoE was then found for each interface value.

$$\begin{aligned} \text{Minimise} \quad & F(x,R) = LCoE(x) + R\Bigg(\sum_{j=1}^{J}|P_j(x)| + \sum_{k=1}^{K}|P_k(x)| + |P_m(x)|\Bigg), \\ & \text{Where} \\ & x \in X \\ & P_m(x) = \begin{cases} \frac{h_{int}}{\epsilon_1}, & \text{if } h_{int} \geq \epsilon_1 \\ 0, & \text{otherwise} \end{cases} \end{aligned} \tag{6.25}$$

Figure 6.16 identifies the optimum fitness found for the selected objectives, in the case of optimisation cases DO1 to DO3, where wind speeds vary.

The results indicate a generally decreasing LCoE with increasing hybrid interface height. An overall optimum LCoE was found in the case of each wind speed at a hybrid interface level of between 70m and 80m.

6.5.3.4 Embodied Energy vs Hybrid Concrete-Steel Interface Level

The objectives of CCP and hybrid interface level were considered in a multi-objective optimisation, using the ϵ-constraint method. In this case, the objective of hybrid interface height was set as a constraint and the objective of CCP was to be optimised in a single objective problem. The formulation for this problem is given in Eq. 6.26. A range of equally spaced hybrid interface values were selected in the range 20m to 80m and an optimum minimum CCP was then found for each interface value.

$$\begin{aligned} &\text{Minimise} \quad F(x,R) = CCP(x) + R\Bigg(\sum_{j=1}^{J}|P_j(x)| + \sum_{k=1}^{K}|P_k(x)| + |P_m(x)|\Bigg), \\ &\text{Where} \\ &x \in X \\ &P_m(x) = \begin{cases} \frac{h_{int}}{\epsilon_1}, & \text{if } h_{int} \geq \epsilon_1 \\ 0, & \text{otherwise} \end{cases} \end{aligned} \tag{6.26}$$

Figure 6.16 identifies the optimum fitness found for the selected objectives, in the case of optimisation cases DO1 to DO3, where wind speeds vary.

The results indicate a generally decreasing CCP with increasing hybrid interface height. An overall optimum CCP was found in the case of each wind speed at a hybrid interface level of between 70m and 80m.

6.6 Conclusions

This chapter has outlined a methodology for the optimisation of hybrid concrete-steel wind turbine towers, incorporating the generalisation of free and forced vibration results of such towers using a configuration of Artificial Neural Networks, which are embedded within an optimisation algorithm which itself is a hybrid of a Genetic Algorithm and a Pattern Search Algorithm.

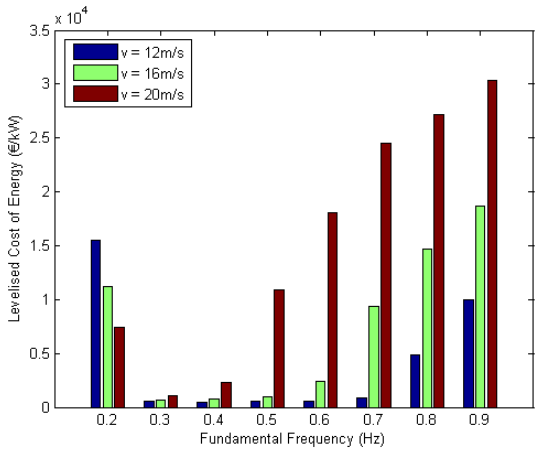

(a) Multi-objective Optimisation, LCoE vs Natural Frequency

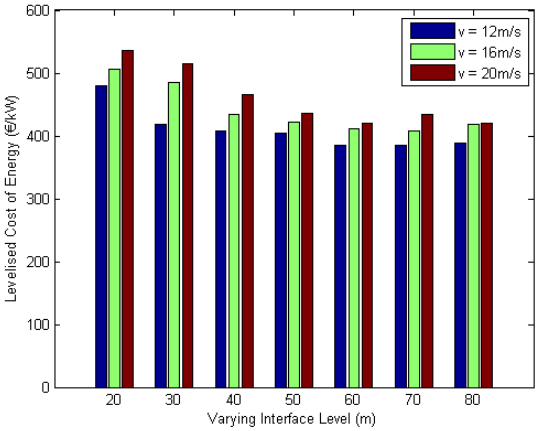

(b) Multi-objective Optimisation, LCoE vs Interface Height

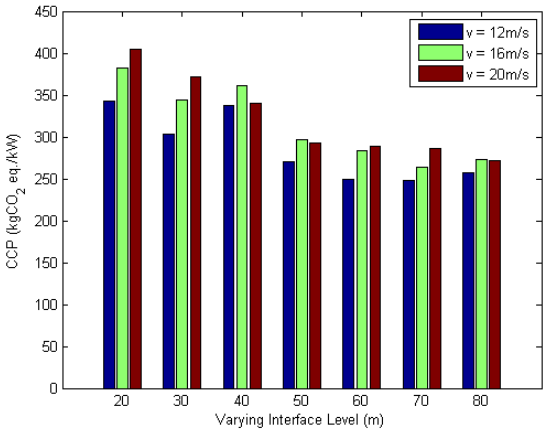

(c) Multi-objective Optimisation, CCP vs Interface Height

Figure 6.16: Multi-objective Optimisation, Selected Constrained Objectives

Structural objective functions were optimised using the 11 DOF LSFE turbine model proposed in Chapter 4, including natural frequency, displacement and stress utilisation. Levelised Cost of Energy (LCoE) was set as an objective and was minimised for a series of load cases and hub heights. The Climate Change Potential (CPP) was also set as an objective to be minimised and followed similar patterns to the LCoE in terms of sensitivity to change in wind speed and height. The total mass of the tower was set as an objective function to be minimised. Multi-objective optimisation was carried out using the ϵ-constraint method and using the 11 DOF LSFE Model as well as the analytical tower model developed in Chapter 3.

The methodology outlined allowed for optimisation of the dynamically sensitive tower structure in a computationally efficient manner by embedding a data-driven model within the optimisation routine. Conclusions were drawn in terms of the optimum hybrid towers under varying design scenarios. These conclusions are described in more detail in Chapter 8.

Chapter 7

Applications in Condition Monitoring and Large Scale Spatial Analysis

7.1 Introduction

This chapter will examine two distinct areas of application of the structural models developed in the previous chapters. The first application is in the area of Structural Health Monitoring (SHM). Given the capacity of the Local Shell FE (LSFE) tower model in terms of adopting and detecting local changes in shell properties, the model will be used to detect localised damage at various locations and under various load conditions. A Discrete Wavelet Transform (DWT) signal processing technique will be used to process response spatial signals to this end.

The second application will be the use of the 11 DOF models in a more holistic sense by coupling it to a Geographical Information Systems (GIS) software application to represent structural and response characteristics spatially.

7.2 Damage Detection using Wavelet Transformation

One established principle in detecting damage to structures is to monitor global response (and vibration) signals to detect a change in the signal characteristics. However, in the case of wind turbines, and as a consequence of the varying load and operating conditions, changes in the vibration characteristics of components are not necessarily indicative of a fault occurrence or structural damage. As such, local damage detection can prove to be more successful than a global detection approach.

Wavelet transformation can be seen as being an extension of the Fourier transform, being a modern means of decomposing a temporal or spatial signal. Chang and Chen [2004] presented a paper proposing the use of a spatial based wavelet approach in order to detect the location of a crack in a rotating blade. They found that the distributions of wavelet coefficients can identify the crack location by showing a peak at the position of the cracking. Law et al. [2006] studied the use of wavelets from the point of view of assessing the sensitivity of the wavelet coefficient from structural responses with respect to system parameters.

In this work, strain and acceleration signals will be extracted from each node of the finite element mesh, creating a spatially varying set of signals. These spatial signals are then to be transformed using the Discrete Wavelet Transform (DWT) signal processing technique. Decomposed co-efficients will then be found for low and high frequency components. The high frequency components of these signals will be used to identify the change in slope from one finite element to the next.

In terms of the background to wavelet transformation, continuous functions are typically transformed, with a continuous wavelet transform of a function $f(x)$ defined as per Eq. 7.1.

$$W_f(a,b) = \frac{1}{\sqrt{|a|}}\psi^*\left(\frac{x-b}{a}\right)dx \tag{7.1}$$

Where b is a translation parameter, a is a scale parameter, $f(x)$ is the input signal expressed spatially and which is to be transformed, $\psi*$ is the complex conjugate of the basis wavelet function ψ. Finally, W_f is the wavelet transform which is to be found.

A discrete version of this transformation is to be employed in this proposal, given the discretised finite element results and thus signal. The signal can now be decomposed into a series as per Eq. 7.2, where the scale and translation parameters are discretized in a binary format.

$$\begin{aligned} d_{j_o,k} &= \int f(x)\psi_{j_o,k}(x)dx, \qquad d_{j,k} = \int f(x)\psi_{j,k}(x)dx \\ a &= 2^j \\ b &= 2j^j k \\ j &\geq j_o, j, k \in Z \end{aligned} \tag{7.2}$$

Where $d_{j_o,k}$ & $d_{j,k}$ are the approximate and detailed wavelet co-efficients and Z denotes a set of defined positive integers. In this work, the Daubechies wavelet of order 10 and Level 1 is used to decompose the strain and acceleration signals.

7.2.1 Static Strain Signals

7.2.1.1 Tower Numerical Model

In this application, the tower will be modelled using the Local Shell Finite Element (LSFE) model. In this case, the full stiffness matrices where each of the N nodal DOF (6 DOF per node) are represented, $[K_{l,T}] \in \mathbb{R}^{6N \times 6N}$, will be used in terms of the application of static load.

Loading will be applied to the tower top and global, nodal responses are extracted using

Wind Speed, $\bar{v}$ (m/s)	Thrust (kN)
7	370.927
8	450.605
9	534.139
10	617.821
11	699.506
12	771.966
13	833.871

Table 7.1: BEM Thrust vs Wind Speed, $\bar{v}$

the relationship previously given in Chapter 4, Section 6.

$$\begin{aligned} \{D_l\} &= [K_{l,T}]^{-1}\{R\} \\ \{D_l\}, \{R\} &\in \mathbb{R}^{6N\times 1} \end{aligned} \tag{7.3}$$

Local finite element strain signals, $\{\varepsilon\}^T = [\varepsilon_x, \varepsilon_y, \gamma_{xy}]$ may be generated using local shell responses. The proposed wind turbine flexible model has been instantiated using the specifications of the NREL 5-MW baseline reference wind turbine blades described by Jonkman et al..

7.2.1.2 Load Definition

Strain signals are to be extracted from the model initially where loading is applied statically. The load to be applied to the tower will be a lateral tower top load which will simulate the loading applied by the rotor. The Blade Element Momentum (BEM) method is used to determine a suitable load for this thrust, whereby the aerodynamic properties of an airfoil (rotor blade) are utilised in tandem with the prevailing wind speeds and blade rotational speed to generate nodal drag and lift loadings acting on elements of the blades. A description of the BEM is given in Chapter 4 of this thesis. The algorithm was run a number of times to assess the variation of load at different normal operating wind speeds. The results are provided in Table 7.1.

7.2.1.3 Damage Detection

A wind turbine tower is subjected here to a lateral load of 500kN as noted above. The geometry of this tower is approximately based upon a conceptual hybrid tower put forward by the Concrete Centre (Tricklebank et al. [2007]) for a 100m hub height. The hybrid tower has a base and top diameter of 12m and 3m respectively. The concrete-steel interface height is taken as 70m above ground level. The shell thickness taken for the lower concrete segment is 350mm and 24mm for the upper steel shell. The concrete compressive strength is given as 50MPa. Although not provided in the literature, a density of 2450 kg/m^3 and a Poisson's ratio of 0.15 is assumed for the concrete. A density of 7850 kg/m^3 and a Poisson's ratio of 0.30 is assumed for the steel segment.

After having applied the lateral load of 500kN, a series of loads increasing from 370kN to 833kN (representing prevalent wind speeds, $\bar{v}$ of 7m/s to 13m/s) were applied to the tower top. This was carried out to investigate any change in the strain pattern as a result of the increase in load for the undamaged tower. It was found that after normalising the strain at each load level that there was no change in pattern and so this pattern is independent of the load intensity. Fig 7.2 shows the undeflected and deflected shape of the overall tower, before and after having imposed the tower top lateral load.

Damaged circumferential locations were next simulated by reducing a given finite shell element's planar stiffness. This was carried out at three locations. On each occasion, the vertical strain signal, ε_y, was extracted from all nodes around the interface circumference and this was processed with a discrete wavelet transformation as discussed above. Fig 7.1 shows the strain signals of the undamaged circumference overlaid with the damaged circumference appropriate for each damaging event. It can be seen that the change in strain profile is marginal but nonetheless is present in the region around the damaged finite element.

It was found that after transforming the strain signal of the damaged towers that this led to a visible change in the pattern of the detail component of the wavelet transform. In

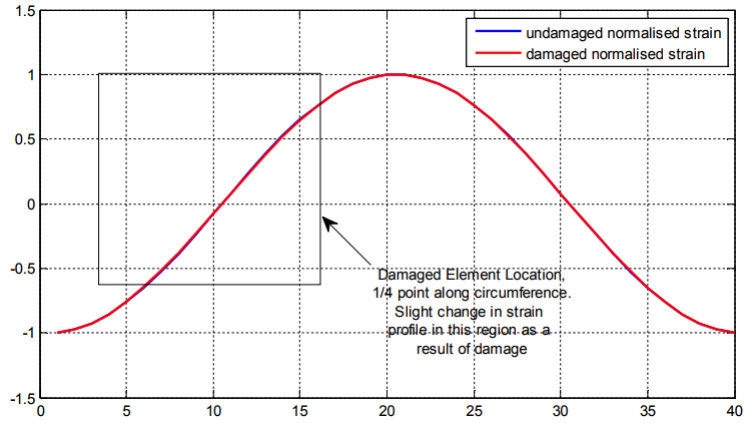

(a) Damaged Location 1

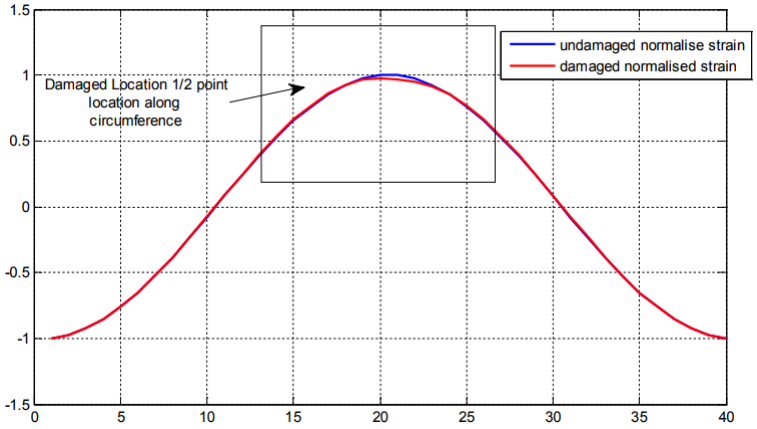

(b) Damaged Location 2

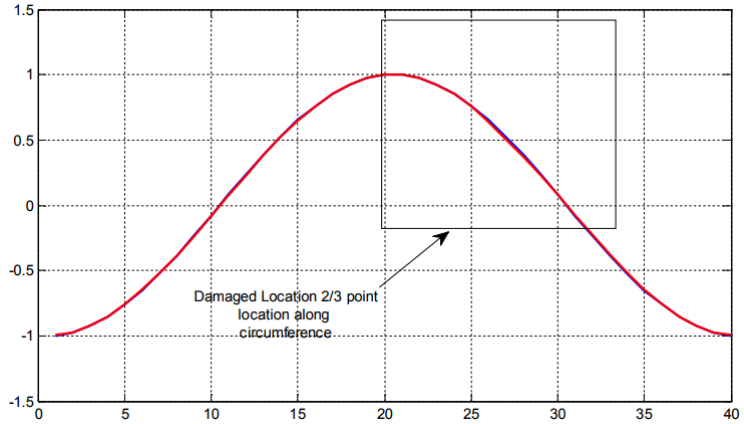

(c) Damaged Location 3

Figure 7.1: Circumferential Strain Profile $\varepsilon_{n,y}(X, Y, Z)$, Static Tower Top Loading, Locations 1-3

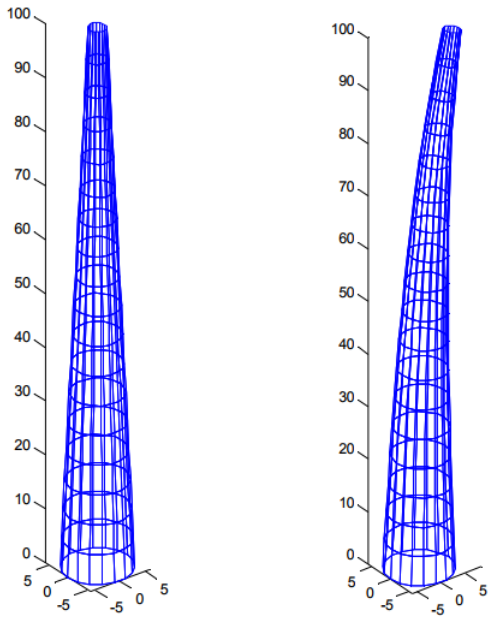

Figure 7.2: Tower Displaced Shape $D_T(X, Y, Z)$, Static Tower Top Loading, LSFE Tower Model

order to highlight where a change in the peaks has occurred, the component quantities for the damaged and undamaged states were combined. The results are presented in fig 7.3. Here the damaged locations are clearly evident by the new peaks which represent the arithmetic difference between the damaged and undamaged coefficients.

7.2.2 Dynamic Strain & Acceleration Signals

7.2.2.1 Tower Numerical Model

In the case of dynamic simulations, a combination of a reduced order numerical model derived from the LSFE tower model and the NREL aeroelastic code FAST will be used. The tower will initially be modelled using the LSFE model but will then be reduced to 5 DOF to simulate translational and rotational degrees of freedom at the top of the tower.

Prior to applying the loads, the tower FE model, with N nodes, is reduced from $6N$ DOF to 5 DOF through the use of three dimensional shape functions. These shape

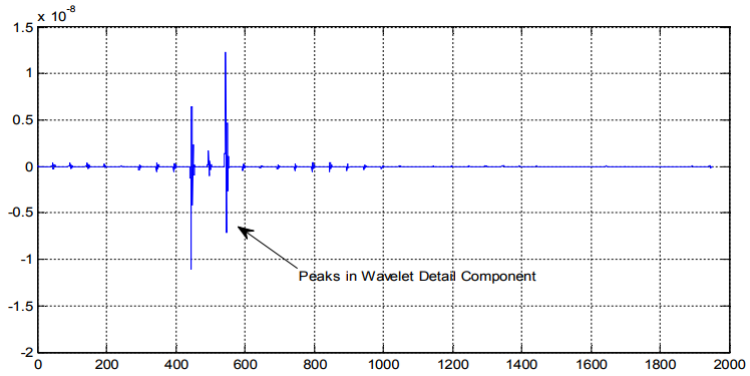

(a) Damaged Location 1

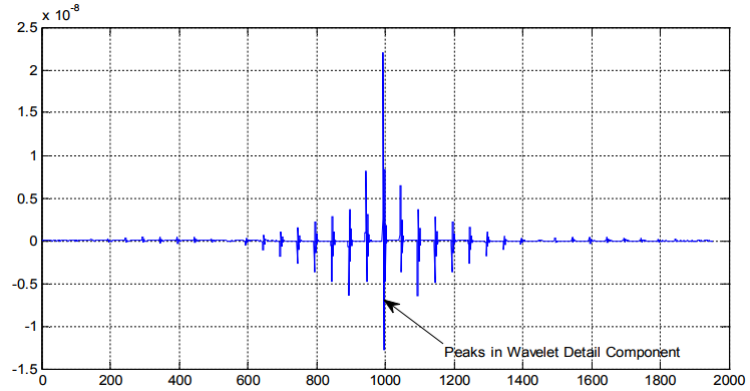

(b) Damaged Location 2

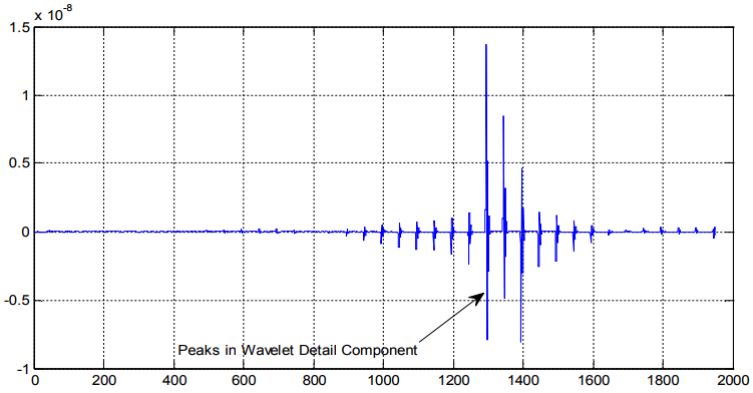

(c) Damaged Location 3

Figure 7.3: DWT Detail Component Differences $d_{dam} - d_{undam}$, Static Tower Top Loading, Locations 1-3

functions have previously been introduced in Chapter 4. Fig 7.4 identifies the 5 DOF directions to be used. A shape function matrix, $[S] \in \mathbb{R}^{6N\times 5}$, is written as follows and includes five distinct shape function vectors, as per Eq. 7.4.

$$S = \begin{bmatrix} \vdots & \vdots & \vdots & \vdots & \vdots \\ s_{fa} & s_{tilt} & s_{ss} & s_{roll} & s_{tor} \\ \vdots & \vdots & \vdots & \vdots & \vdots \end{bmatrix} \tag{7.4}$$

Where, in Eq. 7.4, shape functions for fore-aft, tilting, side-side, rolling and torsional motion are included, $s_{fa}, s_{tilt}, s_{ss}, s_{roll}, s_{tor} \in \mathbb{R}^{6N}$.

This model is essentially equivalent to the tower portion of the 11 DOF LSFE turbine model EOM matrices, without the interaction from blade elements. The dynamic equations of motion and unknown responses, $q(t), \dot{q}(t), \ddot{q}(t)$ can be written as per Eq. 7.5 to Eq. 7.7.

$$\Big([S]^T[M_{l,T}][S]\Big)\ddot{q}(t) + \Big([S]^T[C_{l,T}][S]\Big)\dot{q}(t) + \Big([S]^T[K_{l,T}][S]\Big)q(t) = Q(t) \tag{7.5}$$

$$[M_{TR}]\ddot{q}(t) + [C_{TR}]\dot{q}(t) + [K_{TR}]q(t) = Q(t) \tag{7.6}$$

$$q^T(t) = \begin{bmatrix} q_{fa} & q_{tilt} & q_{ss} & q_{roll} & q_{tor} \end{bmatrix} \tag{7.7}$$

Where reduced order matrices for stiffness $[K_{TR}] \in \mathbb{R}^{5\times 5}$, mass $[M_{TR}] \in \mathbb{R}^{5\times 5}$, and damping $[C_{TR}] \in \mathbb{R}^{5\times 5}$ replace the original stiffness, mass and damping matrices of size $[K_{l,T}], [M_{l,T}], [C_{l,T}] \in \mathbb{R}^{6N\times 6N}$.

Local finite element nodal responses may be gathered through the principle of superposition and through the relationships defined in Chapter 4, Section 6.

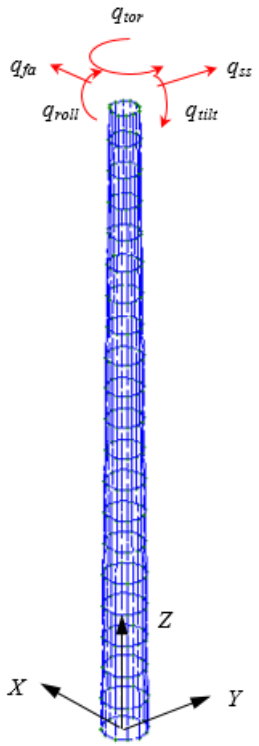

Figure 7.4: DWT Tower DOF (Reduced from $6N$ to 5) $q_j, j \in [fa, ss, tilt, roll, tor]$, Dynamic Tower Loading

Earthquake	Year	Location	Magnitude (M_w)	PGA (g)
Northridge	1994	California	6.7	0.18

Table 7.2: Sample Seismic Ground Motions, Northridge California, 1994

Loadcase LC	$\bar{v}$ (m/s)	I (%)	$\Omega_r(rpm)$	Earthquake
11	12	10	12.1	t = 250
12	12	10	0	t = 0

Table 7.3: Forced Simulation Loadcases LC 11 & LC 12

7.2.2.2 Load Definition

In this study the combined effects of turbulent aerodynamic loads and seismic loads on multi-megawatt onshore wind turbines has been studied. One earthquake record has been downloaded from the United States Geological Survey (USGS) archive for the purposes of this study. Pertinent data from the earthquake is summarised in Table 7.2.

The full field wind field, characterised by a mean wind speed at hub height of 12m/s, takes account of specially correlated turbulence, and the vertical wind shear. The numerical simulations are carried out considering a 10% turbulence intensity. To estimate the aerodynamic loads, the horizontal (downwind) wind speeds are utilized from the three dimensional wind speeds offered by TurbSim.

Two load cases were considered, which are termed LC11 and LC 12. One consists of an operational turbine, with an earthquake introduced at a time instant of t = 250s. The second consists of a parked turbine with an earthquake present from the beginning of the simulation. Pertinent information about both load cases is given below in Table 7.3.

Forcing functions in terms of the F_x, tower top fore-aft force are given in fig 7.5 for LC11. The position of the earthquake initiation can be observed. Simulations are carried out using the NREL baseline turbine and the aero-elastic code FAST with the above seismic and aerodynamic loading as input. These loads are then applied to the finite element model of the tower using the input, $Q(t)$ in the equations of motion.

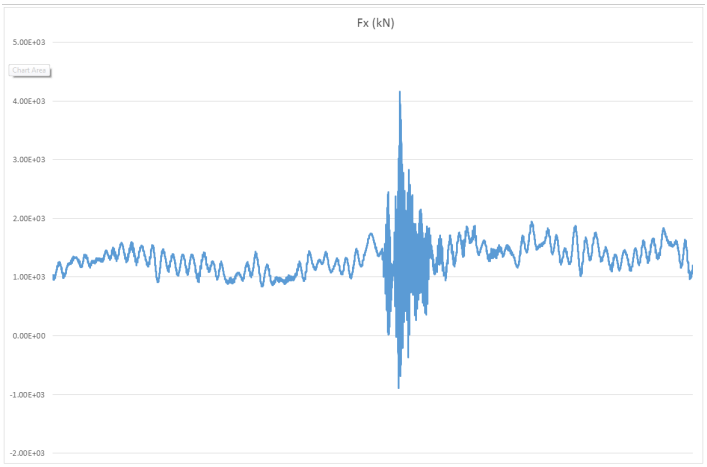

Figure 7.5: Tower Fore-Aft Load $F_x(t)$, LC11

$$Q^T(t) = \begin{bmatrix} F_x & M_y & F_y & M_x & 0 \end{bmatrix} \tag{7.8}$$

7.2.2.3 Dynamic Loading & Detection - Strain

Damaged circumferential locations were simulated by reducing a given finite shell element's planar stiffness. This was carried out at a location at the base of the tower. Initially, damage was considered for the simulation associated with LC11 at 20% and 50% in terms of loss of stiffness. Fig 7.6 identifies the time varying strain component for the damaged finite element.

Next, strain profiles were considered in one dimension (around damaged circumference) and two dimensions (review of both circumferential and vertical profiles). These plots are provided in fig 7.7 for a time instant before and after the earthquake initiation.

Finally, the circumferential strain profiles were processed using the DWT technique and the decomposed signals compared in terms of damaged and undamaged models. From these profiles, damage can be clearly detected. Plots of the overlaid decomposed signals are given in fig 7.7.

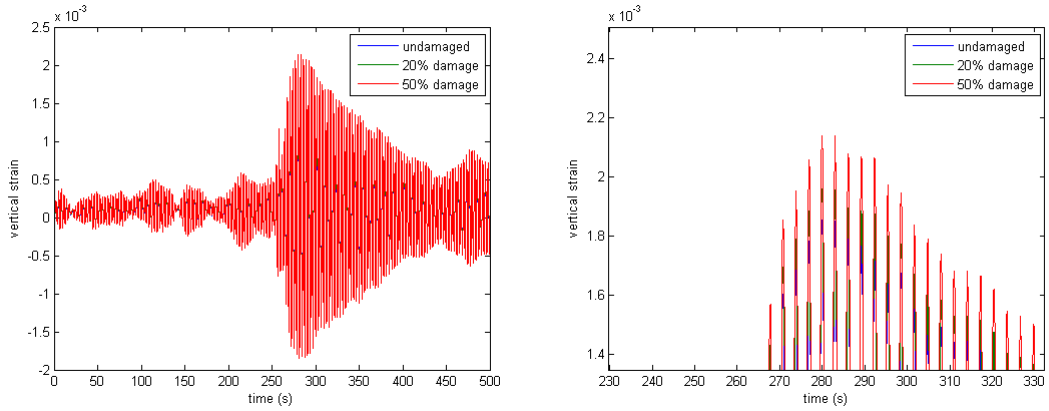

Figure 7.6: Vertical Strain $\varepsilon_{1,y}$, Dynamic Tower Loading, Damaged & Undamaged Time Histories

7.2.2.4 Dynamic Loading & Detection - Acceleration

In practical terms, detection of damage through the use of acceleration signals is desirable as tri-axial accelerometers may be affixed to the structure at one point only, without the need for fixing some reference or base-point, which would be the case in terms of strain or displacement. Accelerometers will also offer a higher level of accuracy compared to strain gauges adding to why they may be favoured.

Acceleration signals were considered at the physical nodes of the damaged finite element. In this case, LC11 was applied to the model and damage was considered to extents of 5%, 10%, 20% and 50% at time instants 116s and 280s, before and after the initiation of the seismic loading. Results are presented in fig 7.8 which show the acceleration signals of damaged towers (50% loss in stiffness) at the above time instants, in the vertical (Z) direction at all nodes of the tower. A change in the acceleration pattern over the surface of the tower can be detected on close observation in both cases.

After processing acceleration signals using the DWT technique, the decomposed detail components of damaged and undamaged signals are overlaid and presented in fig 7.8 in terms of the varying magnitude around the damaged circumference. Damage can be clearly observed, where the magnitude of peaks are pronounced at the damaged finite

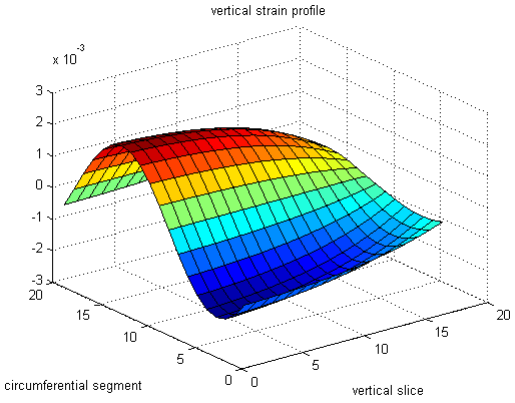

(a) LC 11, Undamaged ε_y (surface)

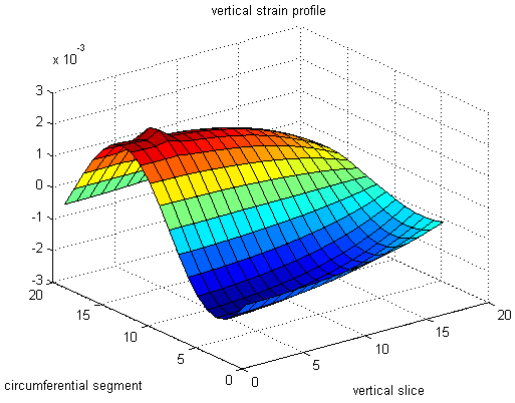

(b) LC 11, 50% Damaged ε_y (surface)

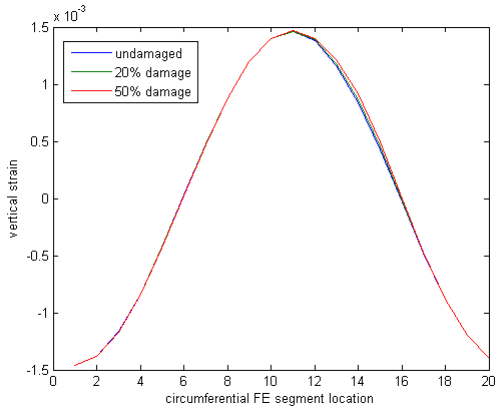

(c) LC 11, ε_y (circumference), t = 116.8

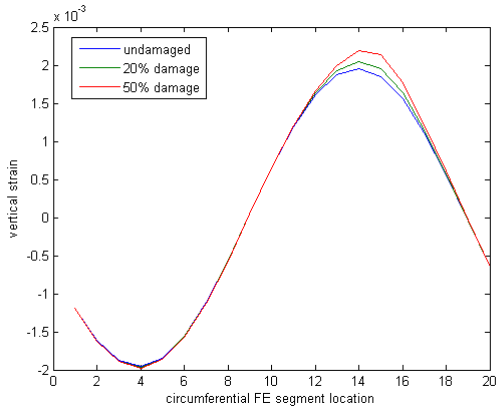

(d) LC 11, ε_y (circumference), t = 280

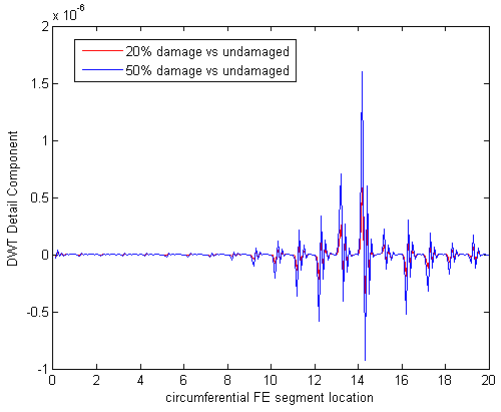

(e) LC 11, DWT (circumference), t = 116.8

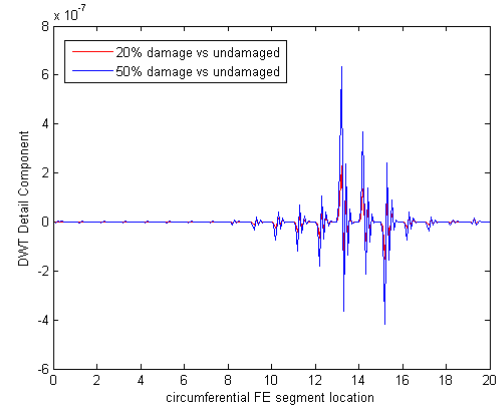

(f) LC 11, DWT (circumference), t = 280

Figure 7.7: Vertical Strain over Tower Surface ε_y (Damaged & Undamaged), Vertical Strain around Tower Circumference ε_y (Damaged & Undamaged), and DWT of Vertical Strain around Tower Circumference (Damaged & Undamaged)

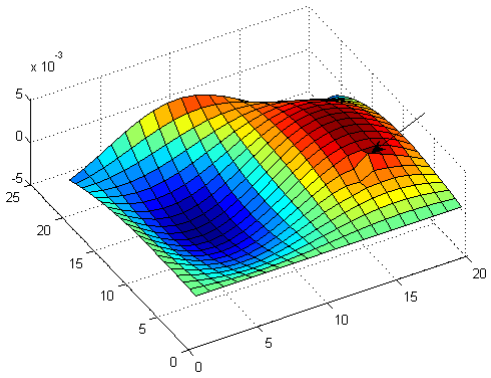

(a) $\frac{d^2u}{dz^2}$ (surface), t = 116.8s

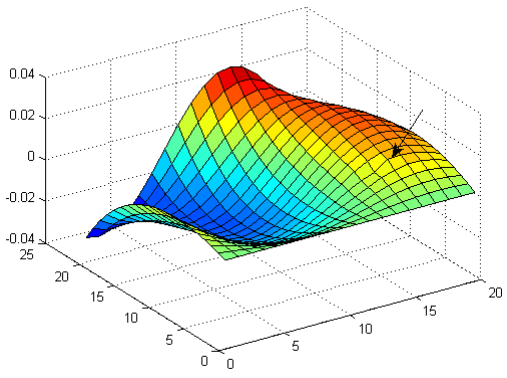

(b) $\frac{d^2u}{dz^2}$ (surface), t = 280s

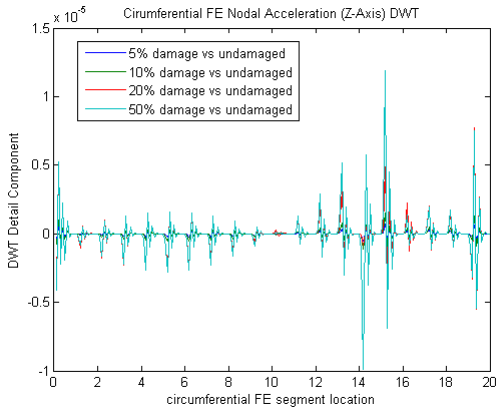

(c) LC 11, DWT (circumference), t = 116.8s

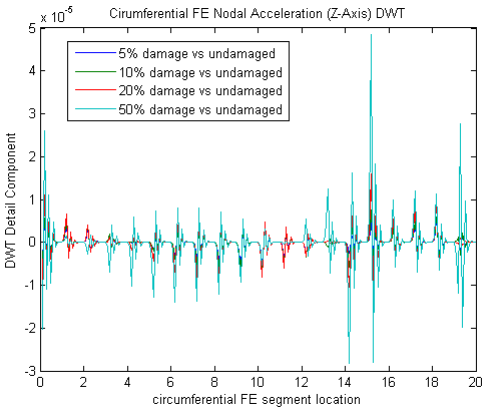

(d) LC 11, DWT (circumference), t = 280s

Figure 7.8: Vertical Acceleration over Tower Surface $\frac{d^2u_Y}{dz^2}$ (Damaged, t = 116.8s, t = 280s) and DWT Detailed Components of Vertical Acceleration over Tower Surface

element location.

7.3 Applications in Geographical Information System (GIS) Environment

7.3.1 Introduction

The performance of the baseline 5MW NREL wind turbine (Jonkman et al.) is to be represented spatially under key structural performance criteria such as tower top displacement, tower shell stress and tower fatigue life. Each of the criteria listed can be evaluated directly by the 11 DOF model responses or by taking the responses and carrying out some post-processing.

7.3.2 GIS Current Practise

ArcGIS software is to be used in this work to cater for the GIS requirements of the work. This software is widely used in areas such as spatial planning and the management of infrastructure and assets around the world.

In the area of wind energy, GIS software is well established in studying acceptable locations for wind farms when assessed against various criteria, the most popular being energy production. An example of this is where Grassi et al. [2014] presented a paper where they calculated energy production whilst including the wake effect experienced by turbines which are clustered. Siyal et al. [2015] used GIS to conduct a 'Wind Energy Assessment' in Sweden, whilst considering geographic and environmental restrictions. The authors then went on to quantify available energy from suitable sites and draw conclusions on the implications for Sweden's wind energy potential. Latinopoulos and Kechagia [2015] put forward a GIS based framework for the evaluation of site suitability to wind farm development based both on siting criteria (environmental, social etc...) and the idea of measuring this site suitability using a 'Suitability Index' which is to be presented spatially.

In terms of other engineering applications, Pilla and Broderick [2015] presented a GIS model on the subject of 'personal exposure to particulate matter' experienced by Dublin commuters. She and Sarshar [1999] presented a paper outlining a bridge management system proposal based on a GIS platform. Information and business modelling is used to support the development of this GIS based bridge management tool.

.

7.3.3 Spatial Input Parameters in GIS Environment

In order to meet the goal of representing performance in a spatial sense, turbine loading parameters must be represented spatially and in terms of working in a GIS environment, inputs are made available as raster image files. As such, it was decided to examine data made available by the SEAI within its wind atlas mapping project (Standen et al.). Data available includes various statistical information relating to wind speeds, $\bar{v}(m/s)$. Mean wind speed as well as Weibull co-efficients of wind speed distribution are available to view and download as raster files. Fig 7.9 shows the spatial representation of the mean wind speed, $\bar{v}$, across the Republic of Ireland, at an elevation of 100m above ground level. A portion of this image has been overlain by the extent of Co. Galway as this area will be reviewed in some detail.

In order to generate a stochastic, turbulent time history for assessing the performance of the turbine, the mean hub-height wind speed is required and this is available through the raster images provided by the SEAI, used in conjunction with the Power Law as given in Eq. 7.9. Mean wind speed as a function of height, $\bar{v}(h)$ can be found using the Power Law, which states

$$\bar{v}(h) = \bar{v}(h_{\text{ref}})(\frac{h}{h_{\text{ref}}})^{\alpha} \tag{7.9}$$

Where $\bar{v}_{\text{ref}}$ is the mean wind speed at a reference height and α is the shear exponent

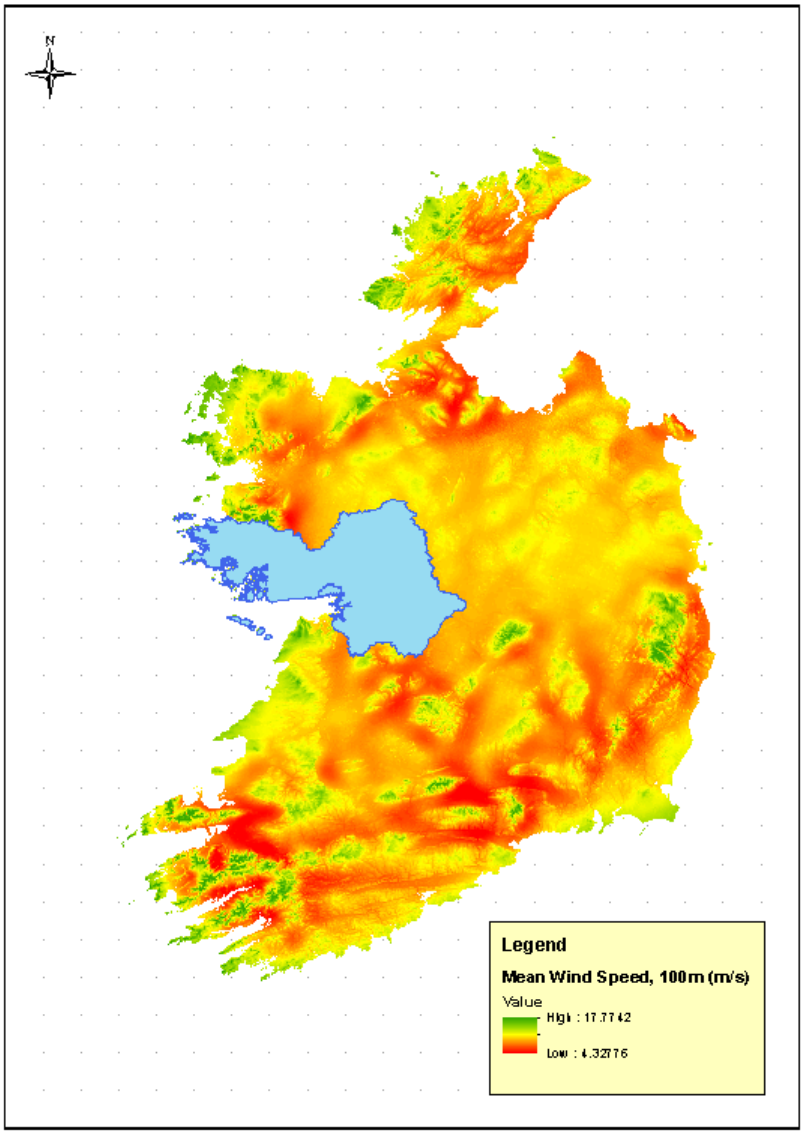

Figure 7.9: Mean wind speed $\bar{v}(t)$ across Republic of Ireland, 100m Elevation

value. At the time of writing, raster images were available from the SEAI as files of the prevailing wind speeds at heights of 20m, 30m, 40m, 50m, 75m, 100m, 125m and 150m. By re-arranging the expression given in Eq. 7.9 to read as per Eq. 7.10, values for α can be found. The reference height is taken to be 20m.

$$\alpha = \left(ln \frac{\bar{v}(h)}{\bar{v}(h_{\text{ref}})} \right) \times \left(\frac{h}{h_{\text{ref}}} \right)^{-1} \tag{7.10}$$

This expression can be utilised with the 'Map Algebra' geoprocessing tool within ArcGIS, along with the rasters for mean wind speeds at relevant elevations, to produce a raster image of the shear exponent values. This is presented in fig 7.10. Raster images of hub height wind speed and shear exponent are included.

In terms of making observations on these spatial images, hub-height wind speeds tend to be highest at coastal areas and at areas of high altitude (north-western areas). Low wind speeds are noted in sheltered areas adjacent to higher altitude sites. The converse can be said of the shear exponent spatial imagery, where low shear is evident in coastal areas and at high altitude. This is intuitive and suggests low wind speeds in areas close to ground level in these areas as compared to the higher level wind speeds.

7.3.3.1 11 DOF LSFE Model Simulations & Results

Wind speed time histories are required for the purposes of running forced simulations with the 11 DOF model. The Kaimal Power Spectrum Density (PSD) put forward in IEC 61400 (International Electrotechnical Commission [2005]) is to be used. The PSD description is given in Eq. 7.11

$$PSD(f) = \frac{4\sigma_w^2 L_w / v(h_{\text{hub}})}{(1 + 6f L_w / v(h_{\text{hub}}))^{\frac{5}{3}}} \tag{7.11}$$

Where f represents the frequency in Hz, L_w is an integral scale length (m) defined in

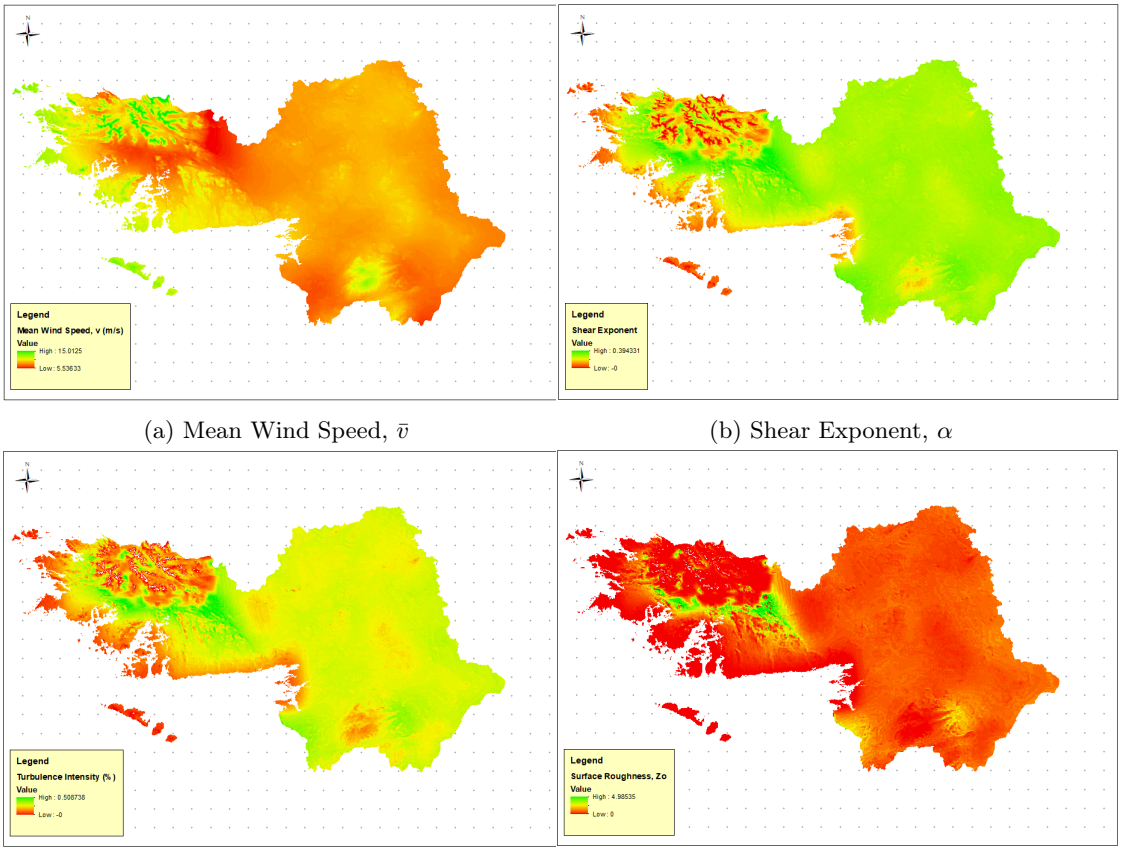

(a) Mean Wind Speed, $\bar{v}$

(b) Shear Exponent, α

(c) Turbulence Intensity, $I(\%)$

(d) Surface Roughness, $z_o(m)$

Figure 7.10: Hub Height Exposure Conditions $\bar{v}$, α, $I(\%)$ and $z_o(m)$, Co. Galway

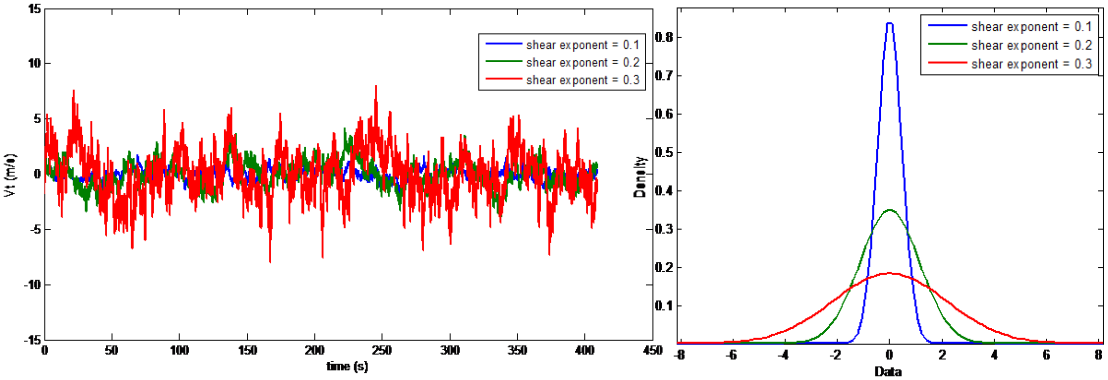

(a) Time Histories

(b) PDFs

Figure 7.11: Example of Varying Turbulent Wind Speeds ($\bar{v}_t$) with Shear Exponent (α)

IEC 61400 and σ_w^2 is the variance in wind speed. The variance will be based on the location-specific shear exponent and is found as follows in Eq. 7.12

$$\begin{aligned} \sigma_w &= v(h_{\text{hub}}) \times \frac{1}{log\left(\frac{h_{\text{ref}}}{z_o}\right)} \\ z_o &= \frac{h \times h_{\text{ref}}}{e^{\frac{1}{\alpha}2}} \end{aligned} \tag{7.12}$$

Where z_o is the roughness length. Images for roughness length and turbulence intensity (I) are included in fig 7.10. In these equations, 100m and 20m are used as heights from which the shear exponent was calculated. The fluctuating or turbulent component is derived by finding the inverse fourier transform (IFT) of the wind speed PSD defined above. The turbulent wind component is assumed to be constant over the swept path of the rotor and is calculated at the hub height, H.

A plot is provided in fig 7.11 of generated turbulent wind speeds ($\bar{v}_t$) found by taking the IFT of the wind speed PSD. Plots are given for the turbulence based on varying shear exponents, showing how higher levels of surface shear experienced by wind leads to higher turbulence in the time history. The probability distribution functions of these time histories are also given in fig 7.11.

Once simulations were carried out according to a predefined 'Design of Experiment' range of input parameters, key output quantities were collected. These include the peak tower top loading quantities as well as response quantities including the peak fore-aft displacement, tower stress and strain quantities. Contour plots of some of the peak tower top load and peak tower responses are given in fig 7.12.

Mean wind speeds were varied from 5 to 15 m/s and shear exponent was varied from 0.01 to 0.25. A total of 99 simulations were carried out across the two equally divided dimensions.

7.3.3.2 Multivariate Regression

Multivariate linear regression analyses can be used to generalise an input-output relationship where a set of known outputs are available with a corresponding set of input parameters, subject to achieving an appropriate level of model fit. In this case, it is carried out in order to generalise both the loading quantities and the response quantities.

Multi-variable linear regression analyses have been widely used in the literature. For example, Harte and Basu [2012] used linear regression to predict stiffness matrix co-efficients associated with the foundation of a wind turbine structure. A series of input parameters, some of which were, horizontal force, bending moment, soil stiffness and foundation diameter, were used to generate such stiffness co-efficients.

$$Q_i(\bar{v}, \alpha, z_o, I) = c_{Q_i,0} + c_{Q_i,\bar{v}}\bar{v} + c_{Q_i,\alpha}\alpha + c_{Q_i,z_o}z_o + c_{Q_i,I}I \tag{7.13}$$

The general expression for the mean generalised tower top loading is given in Eq. 7.13 as a function of the defined variables. The input variables are the wind speed, shear exponent, turbulence intensity and surface roughness. This expression can be re-written in matrix form, identifying each simulation combination of input variables as per Eq. 7.14 and a linear regression analysis carried out on these equations to determine the

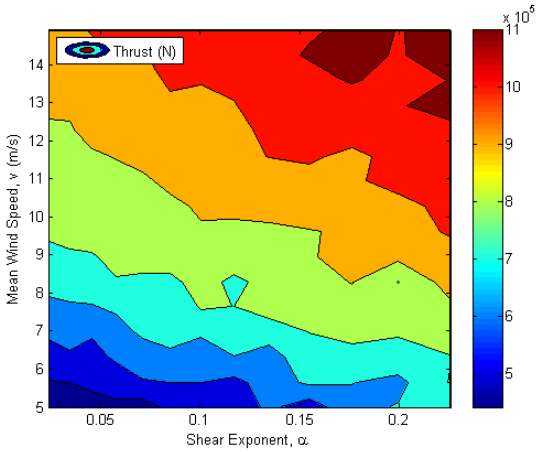

(a) Thrust, q_7 (kN)

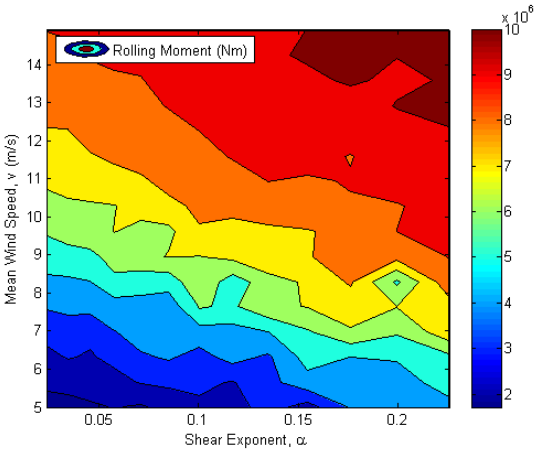

(b) Rolling Moment q_{10} (kNm)

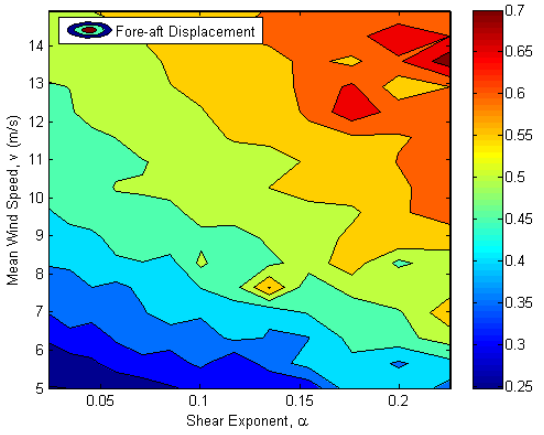

(c) Fore-aft displacement, $u_{N,X}$ (m)

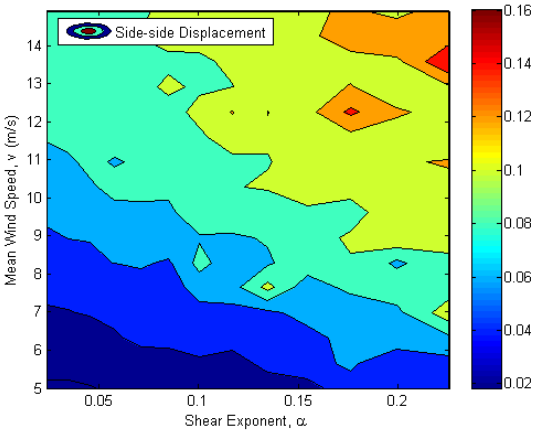

(d) Side-side displacement, $u_{N,Y}$ (m)

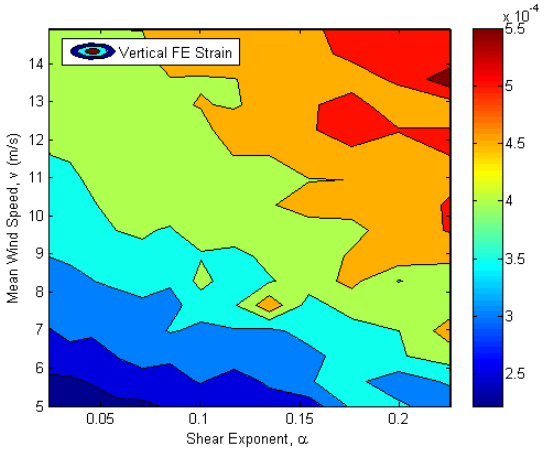

(e) Vertical strain, ε_y

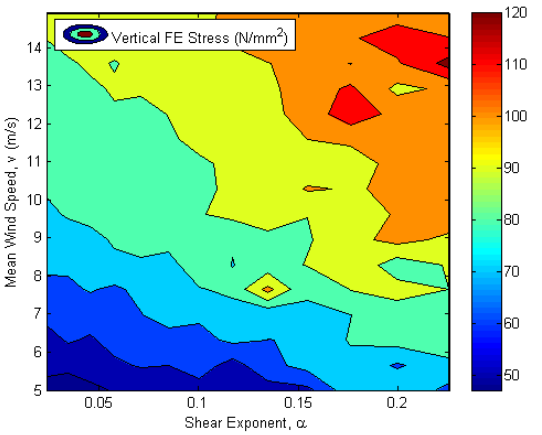

(f) Vertical stress, $\sigma_y(N/mm^2)$

Figure 7.12: Multivariate Regression Simulations Tower Loadings (q_7, q_{10}) & Responses

unknown c_{Q_i} co-efficient values. This formulation may be made for each of the loading quantities $Q_i \in \left[Q_7, Q_8, Q_9, Q_{10}, Q_{11}\right]$. The linear regression analysis exercise was carried out using the software MS EXCEL for each formulation. A total of 5 regression analyses were carried out for the loading quantities.

$$\begin{Bmatrix} Q_{i,11} \\ Q_{i,12} \\ Q_{i,13} \\ Q_{i,14} \\ \vdots \\ Q_{i,98} \\ Q_{i,99} \end{Bmatrix} = \begin{bmatrix} 1 & \bar{v}_{11} & \alpha_{11} & z_{o,11} & I_{11} \\ 1 & \bar{v}_{12} & \alpha_{12} & z_{o,12} & I_{12} \\ 1 & \bar{v}_{13} & \alpha_{13} & z_{o,13} & I_{13} \\ 1 & \bar{v}_{14} & \alpha_{14} & z_{o,14} & I_{14} \\ \vdots & \vdots & \vdots & \vdots & \vdots \\ 1 & \bar{v}_{98} & \alpha_{98} & z_{o,98} & I_{98} \\ 1 & \bar{v}_{99} & \alpha_{99} & z_{o,99} & I_{99} \end{bmatrix} \begin{Bmatrix} c_{Q_i,o} \\ c_{Q_i,\bar{v}} \\ c_{Q_i,\alpha} \\ c_{Q_i,z_o} \\ c_{Q_i,I} \end{Bmatrix} \tag{7.14}$$

Next, a similar set of regression analyses were completed for three identified responses of fore-aft displacement, vertical strain and vertical stress, $d_i \in \left[u_{N,X}, \varepsilon_y, \sigma_y\right]$. Eq. 7.13 can be re-written in terms of these response quantities as per Eq. 7.15.

$$d_i(\bar{v}, \alpha, z_o, I) = c_{d_i,0} + c_{d_i,\bar{v}}\bar{v} + c_{d_i,\alpha}\alpha + c_{d_i,z_o}z_o + c_{d_i,I}I \tag{7.15}$$

Similarly, Eq. 7.14 can also be re-written as per Eq. 7.16.

$$\begin{Bmatrix} d_{i,11} \\ d_{i,12} \\ d_{i,13} \\ d_{i,14} \\ \vdots \\ d_{i,98} \\ d_{i,99} \end{Bmatrix} = \begin{bmatrix} 1 & \bar{v}_{11} & \alpha_{11} & z_{o,11} & I_{11} \\ 1 & \bar{v}_{12} & \alpha_{12} & z_{o,12} & I_{12} \\ 1 & \bar{v}_{13} & \alpha_{13} & z_{o,13} & I_{13} \\ 1 & \bar{v}_{14} & \alpha_{14} & z_{o,14} & I_{14} \\ \vdots & \vdots & \vdots & \vdots & \vdots \\ 1 & \bar{v}_{98} & \alpha_{98} & z_{o,98} & I_{98} \\ 1 & \bar{v}_{99} & \alpha_{99} & z_{o,99} & I_{99} \end{bmatrix} \begin{Bmatrix} c_{d_i,o} \\ c_{d_i,\bar{v}} \\ c_{d_i,\alpha} \\ c_{d_i,z_o} \\ c_{d_i,I} \end{Bmatrix} \tag{7.16}$$

Fig 7.13 provides a regression plots of the target quantities of peak tower top displace-

-	Q_7(kN)	Q_8(kNm)	Q_9(kN)	Q_{10}(kNm)
$c_{Q_i,0}$	264,649	-933,161	-9,768	-1,611,379
$c_{Q_i,\bar{v}}$	47,842	93,569	926	710,437
$c_{Q_i,\alpha}$	219,756	-791,653	60,407	3,670,356
c_{Q_i,z_o}	-1,672	-245,550	-262	-73,021
$c_{Q_i,I}$	754,540	14,415,930	2,099	9,375,322
R^2	0.933	0.872	0.913	0.923

Table 7.4: Loading Linear Regression Co-efficients & Performance

-	$u_{N,X}(m)$	ϵ_y	$\sigma_y(N/mm^2)$
$c_{d_i,0}$	0.115	0.000149	31.759
$c_{d_i,\bar{v}}$	0.147	0.000005	1.107
$c_{d_i,\alpha}$	0.029	0.000019	4.075
c_{d_i,z_o}	-0.206	0.000542	115.081
$c_{d_i,I}$	0.004	0.000009	2.004
R^2	0.927	0.842	0.842

Table 7.5: Response Linear Regression Co-efficients & Performance

ment set against the output quantities of the multi-variable linear regression models.

7.3.4 Loading and Responses in GIS Environment

By taking the multivariate regression models and the rasters representing exposure conditions, it is possible to create raster images of both the tower top generalised load and the model responses to this load. This is possible using the 'Map Algebra' tool within the ArcGIS software package and the resulting GIS raster images are presented in fig 7.14.

Using the same tool, it is possible to present images of the response characteristics listed above including the fore aft displacement, base vertical strain and base vertical stress. These images are presented in fig 7.15. Fig 7.15 also contains a plot of the maximum available power (MW) resource available, when considering the mean wind speed across this area. This is calculated according to Eq. 7.17, neglecting turbine specific power

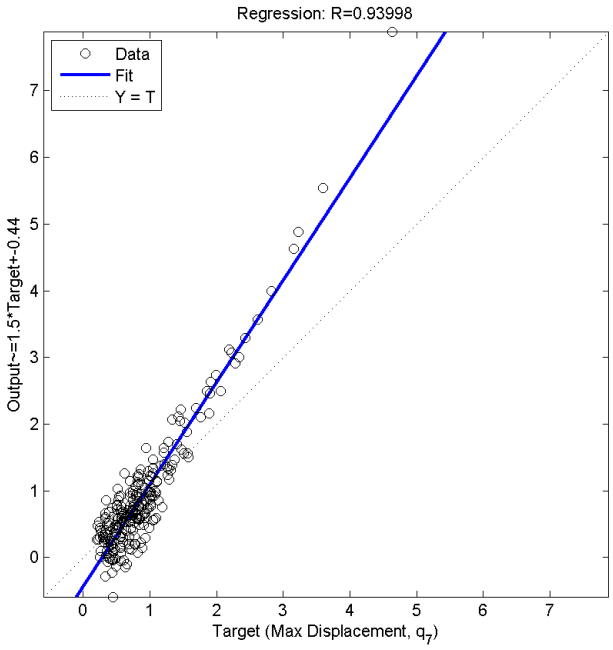

Figure 7.13: Multivariate Linear Regression Plot, $u_{N,x}$

co-efficients (C_p).

$$\text{Power(wind)} = \frac{1}{2} A_r \rho_a \bar{v}^3 \tag{7.17}$$

7.3.5 Multi-Criteria Decision Making in GIS Environment

GIS software has been successfully used to carry out multi-criteria analyses for assessing suitable locations for wind farm development in the literature (Latinopoulos and Kechagia [2015]). Authors have assessed suitability based on a range of criteria including technical issues such as wind speed and power output and social and environmental issues such as proximity to wildlife habitats and proximity to urban centres. Using GIS software, areas seen as infeasible or exhibiting some level of performance outside of a predetermined selection threshold level can be excluded. An example of this practice is given here in terms of selection within thresholds under criteria such as turbulence

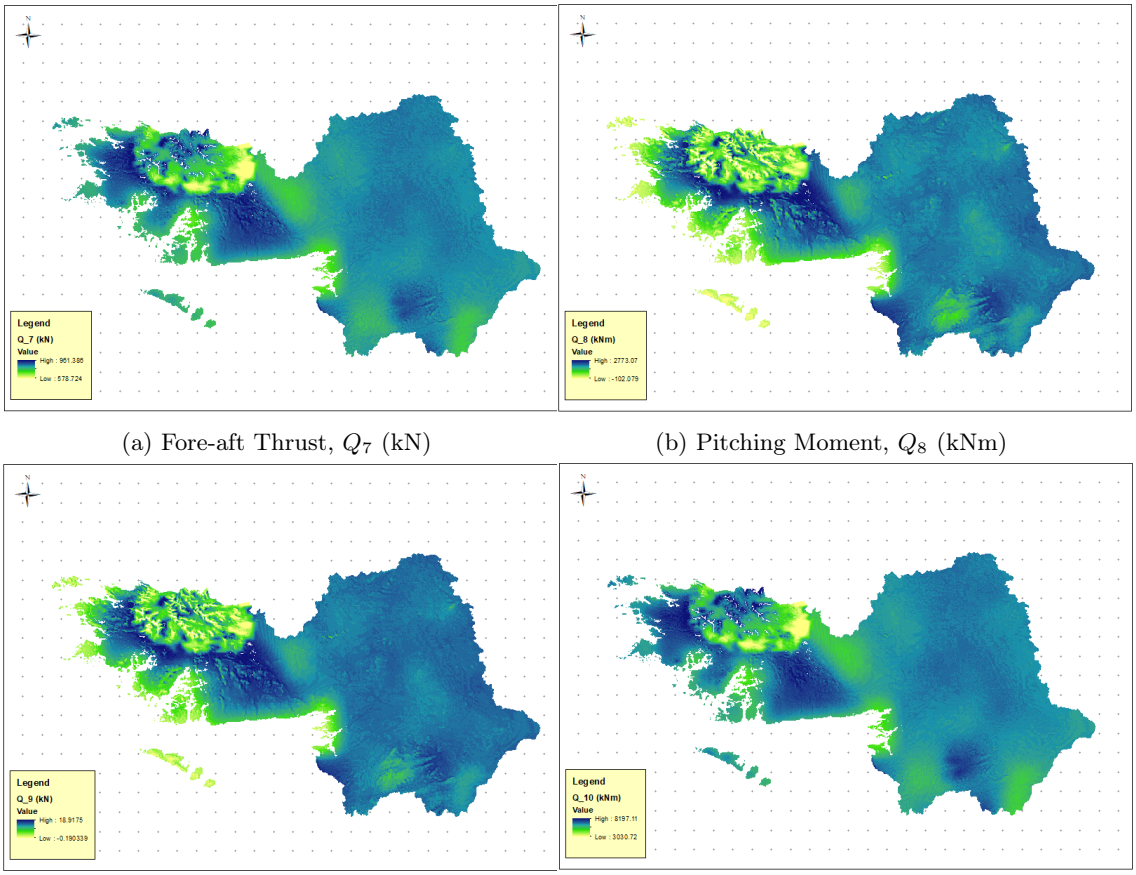

(a) Fore-aft Thrust, Q_7 (kN)

(b) Pitching Moment, Q_8 (kNm)

(c) Side-side Force, Q_9 (kN)

(d) Rolling Moment, Q_{10} (kNm)

Figure 7.14: Example of Tower Loading Presented Spatially in GIS Environment

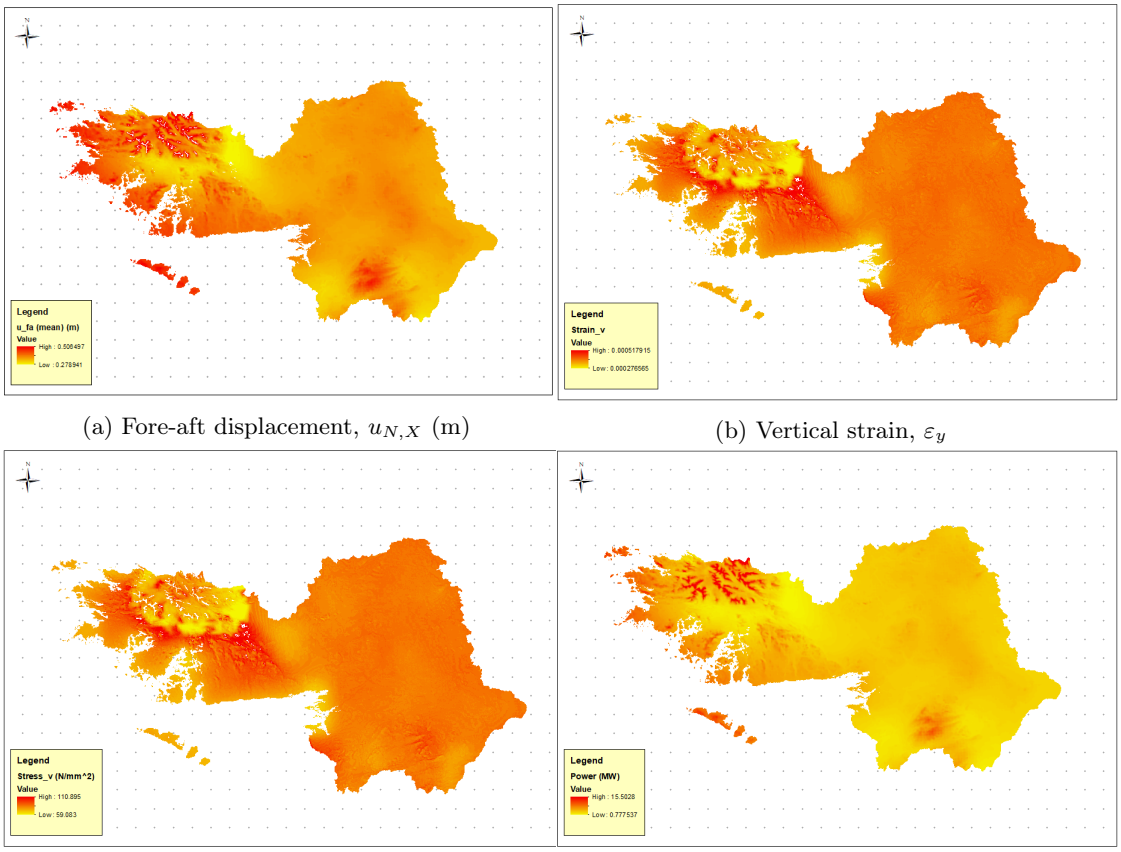

(a) Fore-aft displacement, $u_{N,X}$ (m)

(b) Vertical strain, ε_y

(c) Vertical stress, $\sigma_y(N/mm^2)$

(d) Power (MW)

Figure 7.15: Example of Tower Responses & Power Presented Spatially in GIS Environment

Criteria	Lower Threshold	Upper Threshold
Turbulence Intensity (%)	0	20
Power Availability (MW)	2	∞

Table 7.6: MCDM Criteria Threshold

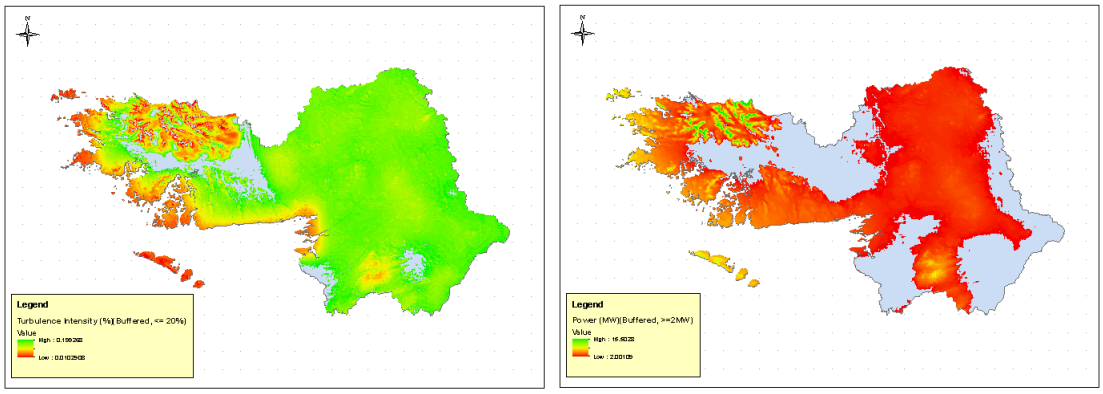

(a) Limited Turbulence Intensity, I (b) Limited Power Yield

Figure 7.16: Limiting Criteria (Infeasible Zones Identified) Presented Spatially in GIS Environment for Turbulence Intensity & Power

level and wind resource.

The upper limit of 20% placed on turbulence intensity may be adopted where designers are seeking to limit the extent of vibrations the turbine would be exposed to. The effect of this exclusion can be seen in the raster image presented in fig 7.16. Infeasible areas are detected on the western side of the county and to a lesser extent to the south. A lower threshold of 2MW was imposed on the power resource. Wind farm developers may set some lower threshold on sites suitable for development. Selecting 2MW has the effect of excluding a large portion of the lands in question in the centre and south of the county.

The Weighted Linear Combination (WLC) method is widely used in GIS applications (Malczewski [2000]) in assessing site suitability where multiple criteria are fed into the decision making process. In this case, an exercise is carried out where two structural performance criteria which were observed to be conflicting in a geographical sense, are to be considered jointly using the WLC method. These criteria include the mean tower top

displacement in the fore-aft direction and the standard deviation of this displacement.

The total score given to each location within the domain is calculated using the expression given in Eq. 7.18.

$$SPI = B_{SPI} \times \sum_{i=1}^{I} w_i x_i \tag{7.18}$$

Where w_i is a normalized weight for each performance criteria, such that $\sum w_i = 1$ and where x_i is the normalised score given to each criteria. Normalised scores for x_i in the range 0 to 1 are found using the relationship from Eq. 7.19.

$$x_i = \frac{d_i - d_{i,min}}{d_{i,max} - d_{i,min}} \tag{7.19}$$

In Eq. 7.18, B_{SPI} refers to a Boolean value of either 1 or 0 and will be used to determine if the site is within acceptable limitations. In a general sense, if the site is infeasible for any of the structural criteria given, this value for B_{SPI} will default to 0. In this case, upper or lower limits were not chosen for either of the chosen performance criteria and as such, B_{SPI} will be set to a value of 1.

Assigning weightings to each of the criteria is dependent on the perceived value of a criteria relative to the others. Various methods have been used in GIS applications in the literature, including Saaty Matrices, Pairwise Comparison and Swing Weights Technique as described by Malczewski [2000]. Caterino et al. [2009] presented an overview of some MCDM methods in a paper comparing such methods for suitability to upgrade of buildings sensitive to seismic damage. Here the Swing Weights Technique is used given its simplicity and intuitive basis. Table 7.7 shows the relative importance assigned to each of the criteria to be considered. These values are all subjective and at the discretion of any given designer. In order to assess how altering the preference of one criteria over the other affects the spatial result, four cases were examined.

-	case 1		case 2		case 3		case 4	
-	$\bar{u}_{N,X}$	$\sigma_{u_{N,X}}$	$\bar{u}_{N,X}$	$\sigma_{u_{N,X}}$	$\bar{u}_{N,X}$	$\sigma_{u_{N,X}}$	$\bar{u}_{N,X}$	$\sigma_{u_{N,X}}$
Relative Importance (%)	100	0	100	50	50	100	0	100
Weightings, w_i	1	0	0.66	0.33	0.33	0.66	0	1

Table 7.7: MCDM Weightings, Case 1 Focusing on Mean Displacement, Case 2 Focusing on Standard Deviation of Displacement

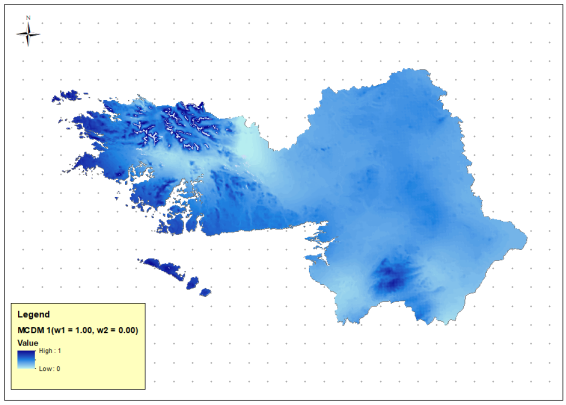

(a) Case 1

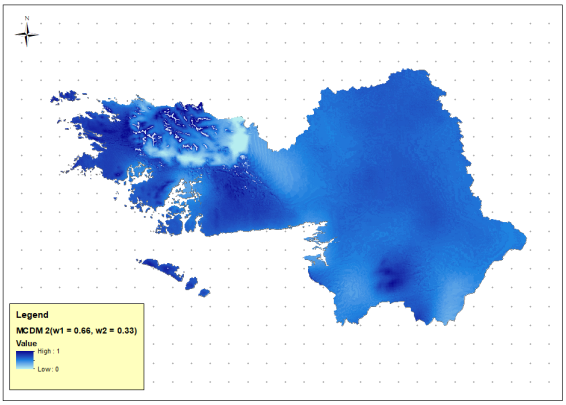

(b) Case 2

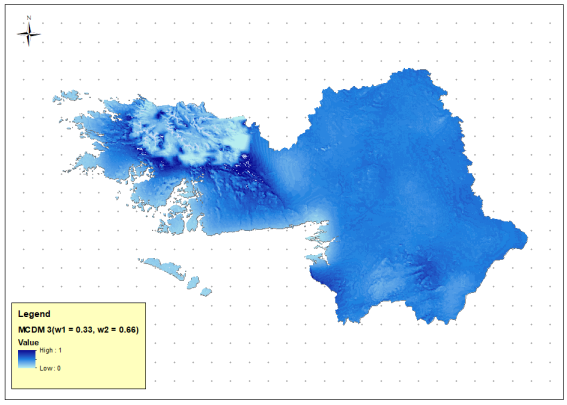

(c) Case 3

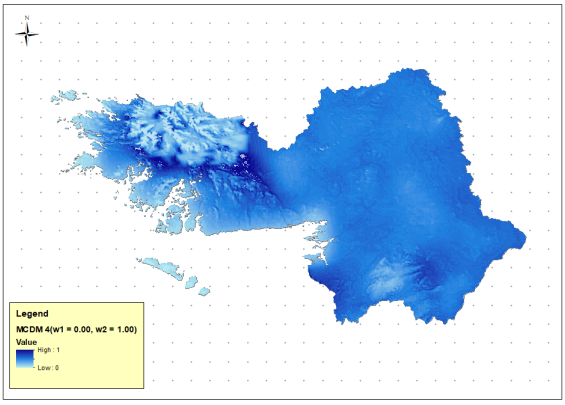

(d) Case 4

Figure 7.17: Results of MCDM Presented Spatially in GIS Environment, Cases 1 - 4, 1 = Optimal Areas

The results of the four cases of the MCDM analyses are presented in fig 7.17, with regions where results are close to unity offering optimal conditions. The two extremes of these cases (case 1 and case 4) are clearly very different in that optimal regions with scores approaching unity are in different locations. High mean wind speeds are evident in local regions in the northwest of the region and as such, these regions are preferred in case 1. Moving to case 2, these regions are favoured, but the overall extent of optimal or high scoring regions have increased to take in areas to the south and east. In case 3, optimal areas are now appearing in areas separate to those seen in cases 1 and 2, where the deviation in displacement is becoming more favoured over the mean displacement.

7.4 Conclusions

A method was proposed to utilise spatial strain and acceleration signals as a means of damage detection around the shell of the finite element model of wind turbine tower, with response signals processed with the Discrete Wavelet Transform (DWT) signal processing technique. This method was shown to be robust under various conditions.

GIS spatial images were presented to represent aerodynamic loading and tower responses generated using BEM and the 11 DOF structural models described earlier in the thesis. By generalising the loading and response quantities as a function of spatially distributed environmental exposure conditions, it is possible to plot these loading and response quantities spatially.

Chapter 8

Conclusions

8.1 Development of Numerical & MDOF Models

A number of numerical models were developed to describe the structure of a hybrid concrete-steel wind turbine tower with nacelle and hub mass at its top. An exact, analytical model was developed using classical beam bending theory with boundary and compatibility conditions imposed to generate a system of homogeneous linear equations with non-trivial solutions.

An approximate, finite element model of the tower was constructed using modified Euler-Bernoulli beam elements to describe out-of-plane translation and rotation of each beam node. This was given the name Global Beam Finite Element model (GBFE) as responses generated are in terms of global nodal responses. Following this, a high-fidelity shell model of the tower was developed using Reissner-Mindlin shell finite elements. This was given the name Local Shell Finite Element model (LSFE) as responses are available in terms of local elemental strain response. These elements were four-noded bi-linear elements, taking their name from the polynomial degree of elemental interpolation functions. Each element node consisted of two in-plane (membrane) degrees of freedom and three out-of-plane (plate) degrees of freedom. Once elements are transformed to a global tower co-ordinate system and transposed to the global system stiffness and mass

matrices, each node offers 6 DOF. This model is extended to incorporate geometric and material non-linearity to account for initial-stress conditions imposed by a pre-tension within the concrete portion of the tower.

Chapter 4 introduces the concept and procedure of formulating reduced order dynamic MDOF models for the wind turbine which include Finite Element and Euler-Lagrangian principles. The FE structural models developed for the towers are incorporated into the MDOF model by reducing each tower model to 5 DOF using global interpolation functions. Tower finite element displacement vectors are expressed as functions of the reduced order tower DOFs' and the global interpolation functions. Total Potential and Kinetic Energy formulations are described for the model. Absolute velocity expressions for the blades, accounting for the influence of the tower motion, are then included in the Kinetic Energy expressions. Differentiation of Lagrange's equation is carried out with respect to each model DOF, with the result that system equations of motion are determined.

The concept of generalised loading is to be applied to various degrees of freedom of the MDOF structural models previously proposed. The generalised loading was found for each DOF through the use of the principle of Virtual Work, in the case of the aerodynamic loading to be applied to the blade DOFs' and the tower DOFs'. The physical loading generated by the rotor, through the rotating blades has been numerically determined using the BEM method. Drag and lift forces are calculated for the blade aerfoil in an iterative manner and on the basis of a number of assumptions in terms of the behaviour of the wind field and its interaction with the rotor blades. Loading acting on the tower is calculated using the drag co-efficient of the cylindrical shape of the tower. In both cases, the assumed shapes of vibration are used in the Virtual Work formulation to find generalised loading time-histories which can be applied to the structural models.

Forcing function comparison in terms of the primary direction of tower top thrust, showed an increase in mean applied load with an increase in mean wind speed, $\bar{v}$. Although there was no increase in the mean applied thrust with increase in turbulence

intensity, I, there was a significant increase in the amplitude of applied load. When comparing the parked and operating conditions, although the rotor is inactive in the parked condition, this condition resulted in similar generalised fore-aft load, $Q_7(t)$ to the operating condition.

8.2 Global and Local Responses

Global tower top responses were examined and compared to each other for operating and parked conditions. Responses are compared in both the temporal and frequency domains. Local strain signals in each principal direction were reviewed using the 11 DOF LSFE model for an element at the base of the tower. For the element considered, the local vertical direction, $\varepsilon_{1,y}$, exhibits the highest magnitude of strain. Strain signals showed similarities to global tower top deformation signals however differences were found, particularly in the frequency content. This is attributed to the fact that the strain at any point in time is a combination of the effects of the global displacements in each global DOF direction at that point in time. This is significant as it is an example of the complex relationship between local strain and global deformation and how local strain signals cannot be extracted or extrapolated from global response signals only. An initial sensitivity analysis was carried out using key design variables used in the design of a hybrid tower including hybrid interface height, concrete diameter and shell thickness, steel diameter and shell thickness and the tower top mass.

The exact analytical model was used to assess free vibration and the 11 DOF GBFE model was used in assessing forced vibration. The nacelle mass had the most significant impact on the first natural frequency of the tower. The hybrid interface height was also strongly correlated to the first natural frequency. The mean global displacement was not impacted by the tower top mass, however the acceleration was strongly impacted. Hybrid interface height was strongly correlated with the displacement but to a lesser extent on the velocity and acceleration response.

The forced vibration response was reviewed in more detail in the time and frequency

domains to assess the impact of the changing interface height and tower top mass. Increasing the hybrid interface level for the tower configurations led to a significant decrease in the mean tower top displacement, peak displacement and first fore-aft frequency. At a local finite element level, the increase in interface height impacted the strain responses. The influence of tower top mass was shown in the time and frequency domain. Increasing the tower top mass to tower mass ratio had a significant effect on the amplitude of acceleration of the tower top. The change in this factor had no impact on the mean displacement and only a slight impact on the peak displacement. At a local level, there were changes in the mean vertical and circumferential strain as a result of changes in tower top mass. This is as a result of the increased vertical load imposed on the tower. There was is a small but distinguished difference between the displacement and acceleration time histories between towers where structural damping properties were varied, in terms of the amplitude of response. These changes in response signals were evident at a global and local level. The compressive strength of the concrete portion of a tower configuration was varied. The result was an increase in overall tower stiffness, leading to a decrease in mean tower top displacement but an increase in the amplitude of displacement about the mean, as well as an increase in amplitude of acceleration about the mean acceleration.

The 11 DOF LSFE model with incorporation of prestressed tendons was used to assess the implications of prestress. The first and second natural frequency of the tower was slightly reduced when introducing and increasing a prestress in the tendons. This net reduction in frequency is as a result of 'softening' of the concrete shell despite the beneficial 'stiffening' of the vertical tendons. The global forced vibration response of the tower showed insignificant change as a result of the introduction of prestress. There was very evident change in the strain response profiles with increase in prestress. This is as a result of the imposed strain due to the prestressing operation.

8.3 Tower Optimisation

A methodology has been proposed for the optimisation of hybrid concrete-steel wind turbine towers. This methodology incorporates the generalisation of free and forced vibration results of such towers using a configuration of Artificial Neural Networks, which are embedded within an optimisation algorithm which itself is a hybrid of a Genetic Algorithm and a Pattern Search Algorithm.

Structural objective functions were optimised using the 11 DOF LSFE turbine model proposed in Chapter 4. Fundamental fore-aft frequency was maximised, peak tower displacement was minimised, as was a weighted sum of concrete and steel stress utilisation ratios. Optimum solutions in terms of each selected objective were found when the design variable describing concrete-steel interface level was close to its upper limit. Nonetheless, other design variables differed between objectives, suggesting the objectives are not exactly correlated.

Levelised Cost of Energy (LCoE) was set as an objective and was minimised for a series of load cases and hub heights. Varying the mean wind speed from 12m/s to 20m/s resulted in a moderate increase in LCoE. Increasing the hub height from 100m to 150m resulted in a significant increase in LCoE. Concrete and prestressed reinforcement contributed most significantly to the breakdown of LCoE.

The Climate Change Potential (CCP) was also set as an objective to be minimised and followed similar patterns to the LCoE in terms of sensitivity to change in wind speed and height. The height of concrete in the optimum 100m tower at 16m/s was 70m. Contributions to the overall CCP are much more equally spread than was the case in LCoE, with each contributing similar amounts. The total mass of the tower was set as an objective function to be minimised. In this case, the variable describing concrete-steel interface was forced close to its lower-bound. In terms of breakdown of contributions by material type, concrete contributes significantly more than steel to total mass, despite the concrete height being only 28.19m.

Multi-objective optimisation was carried out using the ϵ-constraint method. The LCoE and fundamental natural frequency were set as objectives to be optimised. The results indicate a generally increasing LCoE with increasing natural frequency. Finally, the exact analytical tower model was incorporated into the optimisation methodology proposed and the exact natural frequency was optimised as part of a multi-objective optimisation exercise. Contour plots were generated to represent the optimised frequency as a function of the two other objectives. In all cases, maximum stiffness was found at or close to the upper limit of the other two objectives. Some relationships showed approximately linear change in stiffness by varying either parameter, whereas other relationships were highly non-linear.

8.4 Applications in Local and Global Spatial Analyses

A method was proposed to utilise spatial strain and acceleration signals as a means of damage detection around the shell of the finite element model of wind turbine tower. The method proposed includes sampling both strain and acceleration signals around each node of the finite element mesh to create spatial signals which can then be processed. Processing involved passing the signals through the Discrete Wavelet Transform (DWT) signal processing technique. The spatial signals were all transformed and coefficients were found for low and high frequency components.

Simulations were carried out to assess the robustness of the method under varying loading conditions including aerodynamic and seismic load and including operational and parked conditions. Under all scenarios of strain and acceleration signals, by combining the coefficients for the high frequency component in terms of taking the undamaged and relevant damaged co-efficients, it can be seen that the region of damage can be clearly identified. This proved to be the case for both strain signals and acceleration signals.

GIS spatial images were presented to represent aerodynamic loading and tower responses generated using BEM and the 11 DOF structural models described earlier in the thesis. By generalising the loading and response quantities as a function of spatially distributed

environmental exposure conditions, it is possible to plot these loading and response quantities spatially. It was also shown that Multi-Criteria Decision Making applications can be carried out using spatial images and by combining both traditional objectives such as power output with structural criteria such as displacement.

8.5 Future Research Potential

There is potential now to extend the numerical models presented in this thesis as well as extend their application. There is potential to expand the description of the wind turbine to include relatively highly discretised finite element models of the blades and hub. These elemental models may then be reduced in order in a similar way as the tower model for inclusion in a MDOF model. In this way, local strain signals may be extracted for the blades and hub in the same manner.

The reduced order models developed could be extended to include descriptions of soil-structure interaction at the turbine foundations. This would allow for review of the implications of various soil types on the local strain response signals. In the same way, there is an opportunity to also incorporate control devices such as passive or active tuned mass dampers to review their implications on the structural response at a local level.

In terms of structural health monitoring, the method proposed of using Spatial DWT of the strain or acceleration signal could be a powerful means of locating damage around any location on the shell of the wind turbine tower. Similarly, the method could be expanded to include blades. This work can be extended to include experimental works where physical strain acceleration signals may be extracted.

Experimental works may be carried out as a direct extension of the numerical modelling completed here. Scale models of tubular towers could be exposed to excitation and the local response compared to the responses collected from the reduced order models prepared in this work.

This thesis has considered hybrid towers where the concrete and steel portions of the tower are connected only at an interface location. Future work might consider hybrid cross sections, which have been developed for other applications in structural engineering. For example, steel tubes which are lined with concrete to form a composite cross section may be studied. Hybrid tubular and lattice towers have been constructed and could be reviewed in detail. Models developed here could be used directly where possible, or alternate models developed where required.

Various objective functions have been optimised using the framework proposed, including the non-structural objectives of Levelised Cost of Energy (LCoE) and Climate Change Potential (CCP). Given the fact that cost and embodied energy factors are entirely dependent on site specific conditions and market conditions (embodied energy/cost of fabrication, transport, erection etc...), there is merit in extending the studies carried out to look at the influence location plays on optimum hybrid towers in terms of LCoE and CCP.

References

Thomas Ackermann and Lennart Söder. Wind energy technology and current status: a review. *Renewable and Sustainable Energy Reviews*, 4(4):315–374, 2000. 1, 3

S Adhikari and S Bhattacharya. Dynamic analysis of wind turbine towers on flexible foundations. *Shock and Vibration*, 19(1):37–56, 2012. 53

Nestor A Agbayani and Rolando E Vega. The rapid evolution of wind turbine tower structural systems: A historical and technical overview. In *Structures Congress 2012*, pages 1201–1212. ASCE, 2012. 45

Mohammad AlHamaydeh and Saif Hussain. Optimized frequency-based foundation design for wind turbine towers utilizing soil–structure interaction. *Journal of the Franklin Institute*, 348(7):1470–1487, 2011. 37

Turaj Ashuri, Michiel B Zaaijer, Joaquim RRA Martins, Gerard JW Van Bussel, and Gijs AM Van Kuik. Multidisciplinary design optimization of offshore wind turbines for minimum levelized cost of energy. *Renewable Energy*, 68:893–905, 2014. 41, 170

NM Auciello. Transverse vibrations of a linearly tapered cantilever beam with tip mass of rotary inertia and eccentricity. *Journal of Sound and Vibration*, 194(1):25–34, 1996. 50, 52

NM Auciello and A Ercolano. Exact solution for the transverse vibration of a beam

a part of which is a taper beam and other part is a uniform beam. *International Journal of Solids and Structures*, 34(17):2115–2129, 1997. 52

Eric B Baum. On the capabilities of multilayer perceptrons. *Journal of Complexity*, 4 (3):193–215, 1988. 179

N Bazeos, GD Hatzigeorgiou, ID Hondros, H Karamaneas, DL Karabalis, and DE Beskos. Static, seismic and stability analyses of a prototype wind turbine steel tower. *Engineering Structures*, 24(8):1015–1025, 2002. 36, 70

Ji-hong BI, Hong-peng REN, and Yuan-biao YIN. Seismic analysis of pre-stressed reinforced concrete wind-turbine tower. *Journal of Tianjin University*, 2:007, 2011. 48

Gunjit S Bir. *User's Guide to BModes (Software for Computing Rotating Beam Coupled Modes)*. National Renewable Energy Laboratory Golden, CO, 2005. 64, 99, 293

British Standards Institution. *Eurocode 3: Design of Steel Structures: Part 1-9: Fatigue*. British Standards Institution, 1993. xx, 82, 174

British Standards Institution. *Eurocode 2: Design of Concrete Structures: Part 1-1: General Rules and Rules for Buildings*. British Standards Institution, 2004. 82, 86, 148, 173

FJ Brughuis. Large wind turbines: the higher the better. *Advanced Tower Systems BV Netherlands EWEC*, 2006. 47

Xin Cai, Jie Zhu, Pan Pan, and Rongrong Gu. Structural optimization design of horizontal-axis wind turbine blades using a particle swarm optimization algorithm and finite element method. *Energies*, 5(11):4683–4696, 2012. 37, 166

N Caterino, I Iervolino, Gaetano Manfredi, and Edoardo Cosenza. Comparative analysis of multi-criteria decision-making methods for seismic structural retrofitting. *Computer-Aided Civil and Infrastructure Engineering*, 24(6):432–445, 2009. 242

Tommy HT Chan and TH Yung. A theoretical study of force identification using prestressed concrete bridges. *Engineering Structures*, 22(11):1529–1537, 2000. 80

Chih-Chieh Chang and Lien-Wen Chen. Damage detection of cracked thick rotating blades by a spatial wavelet based approach. *Applied Acoustics*, 65(11):1095–1111, 2004. 214

Xiao Chen, Chuanfeng Li, and Jianzhong Xu. Failure investigation on a coastal wind farm damaged by super typhoon: A forensic engineering study. *Journal of Wind Engineering and Industrial Aerodynamics*, 147:132–142, 2015. 43

Anil K Chopra. *Dynamics of Structures*, volume 3. Prentice Hall New Jersey, 1995. 36, 98, 276

RW Clough and J Penzien. *Dynamics of Structures*. McGraw-Hill, New York, 1993. 22, 95

Gino Bertollucci Colherinhas, Marcus Vinicius Girão Morais, Maura Angélica Milfont Shzu, and Suzana Moreira Ávila. Genetic optimization analysis of wind tower vibrations controlled by a pendulum tmd. *Revista Interdisciplinar de Pesquisa em Engenharia-RIPE*, 2(13):103–119, 2016. 7, 41

Concrete Society. *Technical Report 43 — Post-Tensioned Concrete Floors Design Handbook, 2nd Edition*. The Concrete Society, 2005. 86

Andrew R. Conn, Nicholas I. M. Gould, and Philippe Toint. A globally convergent augmented lagrangian algorithm for optimization with general constraints and simple bounds. *SIAM Journal on Numerical Analysis*, 28(2):545–572, 1991. 169

Robert D Cook et al. *Concepts and Applications of Finite Element Analysis*. John Wiley & Sons, 2007. 22, 83, 267, 270

Richard Courant et al. Variational methods for the solution of problems of equilibrium and vibrations. *Bull. Amer. Math. Soc*, 49(1):1–23, 1943. 22

Danish Wind Industry Association. A wind energy pioneer: Charles f. brush. *Danish Wind Industry Association*, 8, 2010. xix, 3

Kalyanmoy Deb. *Optimization for Engineering Design: Algorithms and Examples*. PHI Learning Pvt. Ltd., 2012. 38, 168, 169

Dywidag Systems International. Prefabricated dywidag tendons secure innovative ats hybrid wind tower. https://www.dsiunderground.at/en/projects/project-details/article/innovative-ats-hybrid-wind-tower-germany.html. Accessed: 17-01-2019. 48

Staffan Engström, Tomas Lyrner, Manouchehr Hassanzadeh, Thomas Stalin, and John Johansson. Tall towers for large wind turbines. *Report from Vindforsk project*, 342: 50, 2010. 122

European Wind Energy Association. *Wind Energy-The Facts: a Guide to the Technology, Economics and Future of Wind Power*. Routledge, 2012. 5, 6

fib International. *fib Model Code for Concrete Structures 2010*. Ernst & Song, 2013. 174

Breiffni Fitzgerald, Biswajit Basu, and Søren RK Nielsen. Active tuned mass dampers for control of in-plane vibrations of wind turbine blades. *Structural Control and Health Monitoring*, 20(12):1377–1396, 2013. 94, 111

Ian Flood and Nabil Kartam. Neural networks in civil engineering. i: Principles and understanding. *Journal of Computing in Civil Engineering*, 8(2):131–148, 1994. 167

Rolf Frischknecht and Gerald Rebitzer. The ecoinvent database system: a comprehensive web-based lca database. *Journal of Cleaner Production*, 13(13-14):1337–1343, 2005. 188

Ivar Fylling and Petter Andreas Berthelsen. Windopt: an optimization tool for floating support structures for deep water wind turbines. In *ASME 2011 30th International*

Conference on Ocean, Offshore and Arctic Engineering, pages 767–776. American Society of Mechanical Engineers, 2011. 41

John Gallagher, Biswajit Basu, Maria Browne, Alan Kenna, Sarah McCormack, Francesco Pilla, and David Styles. Adapting stand-alone renewable energy technologies for the circular economy through eco-design and recycling. *Journal of Industrial Ecology*, 2017. 194

Harish Garg. A hybrid pso-ga algorithm for constrained optimization problems. *Applied Mathematics and Computation*, 274:292 – 305, 2016. 175

CG Gebhardt and BA Roccia. Non-linear aeroelasticity: An approach to compute the response of three-blade large-scale horizontal-axis wind turbines. *Renewable Energy*, 66:495–514, 2014. 21

Mitsuo Gen and Runwei Cheng. A survey of penalty techniques in genetic algorithms. In *Evolutionary Computation, 1996., Proceedings of IEEE International Conference on*, pages 804–809. IEEE, 1996. 169

Global Wind Energy Council. Global wind energy outlook 2006. 2006. 5

Global Wind Energy Council. Global wind report: Annual market update 2017. 2017. xix, 5, 6

Stefano Grassi, Sven Junghans, and Martin Raubal. Assessment of the wake effect on the energy production of onshore wind farms using gis. *Applied Energy*, 136:827–837, 2014. 228

Lanhui Guo, Chia-Ming Uang, Ahmed Elgamal, Ian Prowell, and Sumei Zhang. Pushover analysis of a 53 m high wind turbine tower. *Advanced Science Letters*, 4(3):656–662, 2011. 43

John F Hall, Christine A Mecklenborg, Dongmei Chen, and Siddharth B Pratap. Wind energy conversion with a variable-ratio gearbox: design and analysis. *Renewable Energy*, 36(3):1075–1080, 2011. 16

Martin Otto Laver Hansen, Jens Nørkær Sørensen, S Voutsinas, Niels Sørensen, and H Aa Madsen. State of the art in wind turbine aerodynamics and aeroelasticity. *Progress in Aerospace Sciences*, 42(4):285–330, 2006. 20, 111

M Harte and B Basu. Foundation impedance and tower transfer functions for offshore wind turbines. *Proceedings of the Institution of Mechanical Engineers, Part K: Journal of Multi-body Dynamics*, 2013. 95, 96, 111

Michael Harte and Biswajit Basu. Soil-foundation models and tower transfer functions for offshore wind turbines. In *53rd AIAA/ASME/ASCE/AHS/ASC Structures, Structural Dynamics and Materials Conference*, page 1417, 2012. 234

Reinhard Harte and Gideon PAG Van Zijl. Structural stability of concrete wind turbines and solar chimney towers exposed to dynamic wind action. *Journal of Wind Engineering and Industrial Aerodynamics*, 95(9):1079–1096, 2007. 48

Eivind Hognestad. *Study of combined bending and axial load in reinforced concrete members*. University of Illinois at Urbana Champaign, College of Engineering. Engineering Experiment Station., 1951. 155

Y Hu, C Baniotopoulos, and J Yang. Effect of internal stiffening rings and wall thickness on the structural response of steel wind turbine towers. *Engineering Structures*, 81: 148–161, 2014. 70

Yong Huang and Xian-Fang Li. A new approach for free vibration of axially functionally graded beams with non-uniform cross-section. *Journal of Sound and Vibration*, 329 (11):2291–2303, 2010. 52

International Electrotechnical Commission. Iec 61400-1: Wind turbines part 1: Design requirements. *International Electrotechnical Commission*, 2005. 12, 42, 231

Bonnie J Jonkman. *TurbSim User's Guide: Version 1.50*. National Renewable Energy Laboratory Golden, Colorado, 2009. xxi, 110

Jason Jonkman, Sandy Butterfield, Walter Musial, and George Scott. *Definition of a 5-MW Reference Wind Turbine for Offshore System Development*. National Renewable Energy Laboratory Golden, Colorado. 96, 122, 216, 228

Jason M Jonkman and ML Buhl Jr. *FAST User's Guide*. National Renewable Energy Laboratory Golden, Colorado. 119

Fatih Karpat. A virtual tool for minimum cost design of a wind turbine tower with ring stiffeners. *Energies*, 6(8):3822–3840, 2013. 39, 41, 166

A Kenna and B Basu. Damage detection in wind turbine towers using a finite element model and discrete wavelet transform of strain signals. In *Journal of Physics: Conference Series*, volume 628. IOP Publishing, 2015a. 70

A Kenna and B Basu. A finite element model for pre-stressed or post-tensioned concrete wind turbine towers. *Wind Energy*, 18(9):1593–1610, 2015b. 81

Arnold D Kerr. On the dynamic response of a prestressed beam. *Journal of Sound and Vibration*, 49(4):569–573, 1976. 80

Adolf Kirchhoff et al. *Die Homerische Odyssee*. Wilhelm Hertz, 1879. 52

Larisse Klein. Transverse vibrations of non-uniform beams. *Journal of Sound and Vibration*, 37(4):491–505, 1974. 52

Slawomir Koziel and Xin-She Yang. *Computational Optimization, Methods and Algorithms*, volume 356. Springer, 2011. 38

Andrew Kusiak, Zijun Zhang, and Mingyang Li. Optimization of wind turbine performance with data-driven models. *Sustainable Energy, IEEE Transactions on*, 1(2): 66–76, 2010. 39, 41

Hyo-Gyoung Kwak and Filip C Filippou. *Finite Element Analysis of Reinforced Concrete Structures under Monotonic Loads*. Department of Civil Engineering, University of California Berkeley, CA, USA, 1990. 81, 82

Nikos D Lagaros and Matthew G Karlaftis. Life-cycle cost structural design optimization of steel wind towers. *Computers & Structures*, 2015. 42, 168

MW Lanier. Evaluation of design and construction approaches for economical hybrid steel/concrete wind turbine towers. Technical report, Technical Report. Golden: National Renewable Energy Laboratory, 2005. 7, 47, 151

Eva O.L. Lantsoght, Cor van der Veen, and Ane de Boer. Proposal for the fatigue strength of concrete under cycles of compression. *Construction and Building Materials*, 107:138 – 156, 2016. 173

D Latinopoulos and K Kechagia. A gis-based multi-criteria evaluation for wind farm site selection. a regional scale application in greece. *Renewable Energy*, 78:550–560, 2015. 228, 238

I Lavassas, G Nikolaidis, P Zervas, E Efthimiou, IN Doudoumis, and CC Baniotopoulos. Analysis and design of the prototype of a steel 1-mw wind turbine tower. *Engineering Structures*, 25(8):1097–1106, 2003. 36, 70, 172

SS Law and ZR Lu. Time domain responses of a prestressed beam and prestress identification. *Journal of Sound and Vibration*, 288(4):1011–1025, 2005. 80

SS Law, XY Li, and ZR Lu. Structural damage detection from wavelet coefficient sensitivity with model errors. *Journal of Engineering Mechanics*, 132(10):1077–1087, 2006. 214

Seunug-Min Lee, Dae-Yong Kwon, Yong-Chun Kim, Shi Wei, Hyun-Chul Park, and Chin-Wha Chung. Analysis of load on the hybrid tower and cost effectiveness of the wind turbine. *Journal of the Korean Society for New and Renewable Energy*, 6(4): 50–60, 2010. 47

Yeon-Seung Lee, José A González, Ji Hyun Lee, Young Il Kim, KC Park, and Soonhung Han. Structural topology optimization of the transition piece for an offshore wind turbine with jacket foundation. *Renewable Energy*, 85:1214–1225, 2016. 42

Kai Long and Ji Xiu Wu. Research on the door buckling strength of turbine tower of hawts. In *Applied Mechanics and Materials*, volume 268, pages 1239–1243. Trans Tech Publ, 2012. 70

HongWang Ma and Ran Meng. Optimization design of prestressed concrete wind-turbine tower. *Science China Technological Sciences*, 57(2):414–422, 2014. 165, 172

Triantafyllos K Makarios, Evangelos Efthymiou, and Charalampos C Baniotopoulos. On the torsional–translational response of wind turbine structures. *Arabian Journal for Science and Engineering*, pages 1–9, 2015. 70

Jacek Malczewski. On the use of weighted linear combination method in gis: common and best practice approaches. *Transactions in GIS*, 4(1):5–22, 2000. 241, 242

James F Manwell, Jon G McGowan, and Anthony L Rogers. *Wind Energy Explained: Theory, Design and Application*. John Wiley & Sons, 2010. 1, 2, 14

Qibo Mao. Free vibration analysis of multiple-stepped beams by using adomian decomposition method. *Mathematical and Computer Modelling*, 54(1):756–764, 2011. 60

George Mavrotas. Effective implementation of the ε-constraint method in multi-objective mathematical programming problems. *Applied Mathematics and Computation*, 213(2):455–465, 2009. 204

Madhavan K Mini and Manne Sowmya. Neural network paradigms for fatigue strength prediction of fiber-reinforced composite materials. *International Journal of Advanced Structural Engineering*, 4(1):7, 2012. 178

Saeed Moaveni. *Finite Element Analysis: Theory and Application with ANSYS*. Pearson Education India, 2003. 74

PJ Murtagh, B Basu, and BM Broderick. Simple models for natural frequencies and mode shapes of towers supporting utilities. *Computers & Structures*, 82(20):1745–1750, 2004. 53

PJ Murtagh, B Basu, and BM Broderick. Along-wind response of a wind turbine tower with blade coupling subjected to rotationally sampled wind loading. *Engineering Structures*, 27(8):1209–1219, 2005. 21, 44

S Naguleswaran. A direct solution for the transverse vibration of euler-bernoulli wedge and cone beams. *Journal of Sound and Vibration*, 172(3):289–304, 1994. 52

S Naguleswaran. Natural frequencies, sensitivity and mode shape details of an euler–bernoulli beam with one-step change in cross-section and with ends on classical supports. *Journal of Sound and Vibration*, 252(4):751–767, 2002. 50, 60

Hani M Negm and Karam Y Maalawi. Structural design optimization of wind turbine towers. *Computers & Structures*, 74(6):649–666, 2000. 41, 170

Anders Olsson, Göran Sandberg, and Ola Dahlblom. On latin hypercube sampling for structural reliability analysis. *Structural Safety*, 25(1):47–68, 2003. 135

Anatoly Perelmuter and Vitalina Yurchenko. Parametric optimization of steel shell towers of high-power wind turbines. *Procedia Engineering*, 57:895–905, 2013. 37, 41

Francesco Pilla and Brian Broderick. A gis model for personal exposure to pm10 for dublin commuters. *Sustainable Cities and Society*, 15:1–10, 2015. 229

B Posiadała. Free vibrations of uniform timoshenko beams with attachments. *Journal of Sound and Vibration*, 204(2):359–369, 1997. 50, 52

M Premalatha, Tasneem Abbasi, SA Abbasi, et al. Wind energy: Increasing deployment, rising environmental concerns. *Renewable and Sustainable Energy Reviews*, 31: 270–288, 2014. 6

Aidan Quilligan, A O'Connor, and V Pakrashi. Fragility analysis of steel and concrete wind turbine towers. *Engineering Structures*, 36:270–282, 2012. 47, 95

MY Rafiq, G Bugmann, and DJ Easterbrook. Neural network design for engineering applications. *Computers & Structures*, 79(17):1541–1552, 2001. 178

Gireesh Kumar V Ramachandran, Henrik Bredmose, Jens Nørkær Sørensen, and Jørgen Juncher Jensen. Fully coupled three-dimensional dynamic response of a tension-leg platform floating wind turbine in waves and wind. *Journal of Offshore Mechanics and Arctic Engineering*, 136(2):020901, 2014. 21

A Rashedi, Idapalapati Sridhar, and King Jet Tseng. Multi-objective material selection for wind turbine blade and tower: Ashby's approach. *Materials & Design*, 37:521–532, 2012. 194

Robert W Righter. *Wind Energy in America: A History*. University of Oklahoma Press, 1996. 3

M Saiidi, B Douglas, and S Feng. Prestress force effect on vibration frequency of concrete bridges. *Journal of Structural Engineering*, 120(7):2233–2241, 1994. 80

P Schaumann and F Wilke. Current developments of support structures for wind turbines in offshore environment. *Fourth International Conference on Advances in Steel Structures*, pages 1107–1114, 2005. 20

TH She and M Sarshar. A geographic information system (gis)–based bridge management system. *Computer-Aided Civil and Infrastructure Engineering*, 14(6):417–427, 1999. 229

Silvio Simani. Overview of modelling and advanced control strategies for wind turbine systems. *Energies*, 8(12):13395–13418, 2015. 94

Shahid Hussain Siyal, Ulla Mörtberg, Dimitris Mentis, Manuel Welsch, Ian Babelon, and Mark Howells. Wind energy assessment considering geographic and environmental restrictions in sweden: A gis-based approach. *Energy*, 83:447–461, 2015. 228

A Staino and B Basu. Dynamics and control of vibrations in wind turbines with variable rotor speed. *Engineering Structures*, 56:58–67, 2013. 111

Jessica Standen, Clive Wilson, and Simon Vosper. *Remodelling the Irish National Onshore and Offshore Wind Atlas Version 2.0*. Sustainable Energy Authority of Ireland. 229

Hamid Taghavifar, Aref Mardani, and Ashkan Haji Hosseinloo. Appraisal of artificial neural network-genetic algorithm based model for prediction of the power provided by the agricultural tractors. *Energy*, 93:1704–1710, 2015. 40

Trevor R Taylor and Nestor A Agbayani. Design optimization of tubular steel towers for utility-scale wind turbines. In *Structures Congress 2015*, pages 1748–1759. 170

AH Tricklebank, B Magee, and PH Halberstadt. Concrete towers for onshore and offshore wind farms. *The Concrete Centre: Surrey*, 2007. 19, 47, 217

A Uściłowska and JA Kołodziej. Free vibration of immersed column carrying a tip mass. *Journal of Sound and Vibration*, 216(1):147–157, 1998. 52

P.E. Uys, J. Farkas, K. Jármai, and F. van Tonder. Optimisation of a steel tower for a wind turbine structure. *Engineering Structures*, 29(7):1337 – 1342, 2007. 166

Jan van der Tempel and David-Pieter Molenaar. Wind turbine structural dynamics–a review of the principles for modern power generation, onshore and offshore. *Wind Engineering*, 26(4):211–222, 2002. 53

Frank J Vecchio. Nonlinear finite element analysis of reinforced concrete membranes. *ACI Structural Journal*, 86(1):26–35, 1989. xx, 82

Ronald E Walpole, Raymond H Myers, Sharon L Myers, and Keying Ye. *Probability and Statistics for Engineers and Scientists*, volume 5. Macmillan New York, 1993. 175

Jianhong Wang, Datong Qin, and Teik C Lim. Dynamic analysis of horizontal axis wind turbine by thin-walled beam theory. *Journal of Sound and Vibration*, 329(17): 3565–3586, 2010. 21

Xiangguo Wu, Jing Yang, and Issa B Mpalla. Preliminary design and structural responses of typical hybrid wind tower made of ultra high performance cementitious composites. *Structural Engineering and Mechanics*, 48(6):791–807, 2013. 48

Liu Xiong, Li Gangqiang, Chen Yan, Ye Zhiquan, and Tian Peng. Dynamic response analysis of the tubular tower of horizontal axis wind turbines [j]. *Acta Energiae Solaris Sinica*, 4:004, 2010. 64

CHEN Yan, LUO Zhen, LIU Xiong, and Ye Zhiquan. Coupling analysis of rotor and tower of horizontal axis wind turbine. *Acta Energiae Solaris Sinica*, 33(10):1648–1654, 2012. 64

Hezhen Yang and Yun Zhu. Robust design optimization of supporting structure of offshore wind turbine. *Journal of Marine Science and Technology*, 20(4):689–702, 2015. 42, 170

Xin-She Yang, Slawomir Koziel, and Leifur Leifsson. Computational optimization, modelling and simulation: recent trends and challenges. *Procedia Computer Science*, 18: 855–860, 2013. 37, 39

Serdar Yıldırım and İbrahim Özkol. Wind turbine tower optimization under various requirements by using genetic algorithm. *Engineering*, 2(08):641, 2010. 166

Frederik Zahle, Carlo Tibaldi, David R Verelst, Robert Bitche, and Christian Bak. Aero-elastic optimization of a 10 mw wind turbine. In *33rd Wind Energy Symposium*, 2015. 41

Chaoyong Zhang, Peigen Li, Yunqing Rao, and Shuxia Li. A new hybrid ga/sa algorithm for the job shop scheduling problem. In Günther R. Raidl and Jens Gottlieb, editors, *Evolutionary Computation in Combinatorial Optimization*. Springer Berlin Heidelberg, 2005. 175

Zili Zhang, Søren RK Nielsen, Frede Blaabjerg, and Dao Zhou. Dynamics and control

of lateral tower vibrations in offshore wind turbines by means of active generator torque. *Energies*, 7(11):7746–7772, 2014. 94, 96

Zili Zhang, Biswajit Basu, and Søren RK Nielsen. Tuned liquid column dampers for mitigation of edgewise vibrations in rotating wind turbine blades. *Structural Control and Health Monitoring*, 22(3):500–517, 2015. 21

Jie Zhu, Xin Cai, Pan Pan, and Rongrong Gu. Multi-objective structural optimization design of horizontal-axis wind turbine blades using the non-dominated sorting genetic algorithm ii and finite element method. *Energies*, 7(2):988–1002, 2014. 37

Appendix A

A.1 Numerical Integration - Gauss Quadrature

In order to generate the co-efficients of stiffness matrices, $k_{i,j}$ in the case of planar elements, it is necessary to integrate the shape functions over the area of the element. Whilst this can be achieved easily in the case of rectangular elements, where elements are of irregular shape and have been transformed to another co-ordinate system, a numerical method known as Quadrature, or more specifically, Gauss quadrature can be employed. As outlined in Cook et al. [2007], an integral having limits $x = x_1$ and $x = x_2$ can be transformed to an integral having limits $\zeta = -1$ and $\zeta = 1$ such that

$$I = \int_{x_1}^{x_2} f dx = \int_{-1}^{1} \phi d\zeta \tag{A.1}$$

Where the function $f = f(x)$, has been transformed to $\phi = \phi(\zeta)$. The method then assigns weightings to function values at specific sampling locations with the intention of minimising the numerical integration error and allowing for the integrand value to be found as

$$I = \int_{-1}^{\phi} d\zeta \approx W_1\phi_1 + W_2\phi_2 + \cdots + W_n\phi_n \tag{A.2}$$

Table A.1: Gauss - Quadrature Sampling Point Locations

Order n	Sampling point locations ζ_i	Weight factors W_i
1	0	2
2	$\pm 1 \frac{}{\sqrt{3}}$	1
3	$\pm\sqrt{0.6}$	$\frac{5}{9}$

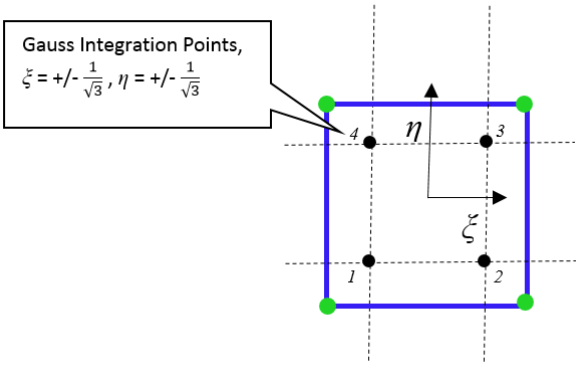

Figure A.1: Gauss - Quadrature Sampling Point Locations

Where in this case, n refers to the order of the rule. In the case of the 2 dimensional element at hand, where $[N] = [N](\zeta, \eta)$, the method locates sampling points in two dimensions and assigns weights so as to allow for numerical summation. A generalisation of the procedure in two dimensions for the shape function $[N]_i$ reads

$$I = \int_{-1}^{1}\int_{-1}^{1} [N]_i(\zeta,\eta)d\zeta d\eta \approx \sum_j \sum_k W_j W_k [N]_i(\zeta_j, \eta_k) \tag{A.3}$$

The number of sampling points in the case of the 2D element was chosen here to be four, such that the order is said to be 2. Table A.1 provides the sampling point locations and weighting factors relevant to other orders of Gauss quadrature integration. The sampling point locations chosen for the quadrilateral element are shown in Figure A.1.

A.2 Jacobian Matrix

As a consequence of transforming the co-ordinate system of a finite element from a Cartesian c-ordinate system to some local system whose axis need not be parallel to the Cartesian axis, it is necessary to review any derivatives present in the elementary stiffness matrix integral for that element.

$$[k] = t \int [B]^T [E][B] dx dy \tag{A.4}$$

In the case of a planar element such as a membrane or plate element, derivatives in Cartesian co-ordinates are present to represent the area of the element. From review of Eq. A.4, some method is required to transform from dx to $d\zeta$ and dy to $d\eta$. In vector calculus, a matrix known as the Jacobian matrix exists and can be used here to achieve the required transformation. In the case of a function $\phi = \phi(\zeta, \eta)$, the transformation can be achieved through the following representations.

$$\begin{aligned} \frac{\partial \phi}{\partial \zeta} &= \frac{\partial \phi}{\partial x}\frac{\partial x}{\partial \zeta} + \frac{\partial \phi}{\partial y}\frac{\partial y}{\partial \zeta} \\ \frac{\partial \phi}{\partial \eta} &= \frac{\partial \phi}{\partial x}\frac{\partial x}{\partial \eta} + \frac{\partial \phi}{\partial y}\frac{\partial y}{\partial \eta} \end{aligned} \tag{A.5}$$

or

$$\begin{Bmatrix} \frac{\partial \phi}{\partial \zeta} \\ \frac{\partial \phi}{\partial \eta} \end{Bmatrix} = [J] \begin{Bmatrix} \frac{\partial \phi}{\partial x} \\ \frac{\partial \phi}{\partial y} \end{Bmatrix}$$

(A.6)

where $[J]$ is known as the Jacobian matrix.

A.3 Strain-Displacement Matrix Derivation

The strain-displacement matrix is an essential component in the numerical assembly of an element stiffness matrix. A stiffness matrix expression in a general sense reads

$$[k] = \int [B]^T [E][B] dV \tag{A.7}$$

The determination of the make-up of this matrix is entirely dependent on the complexity of the element at hand, however it will consistently be used as a means of relating the element displacements to strain through a number of simple expressions.

$$\{\varepsilon\} = [\partial]\{u\} = [B]\{d\} \tag{A.8}$$

$$\{u\} = [N]\{d\} \tag{A.9}$$

Hence

$$[B] = [\partial][N] \tag{A.10}$$

Deriving the strain-displacement matrix can be carried out for bar, beam and membrane/plate elements. Cook et al. [2007] describes this matrix as being a product of three rectangular matrices, which originate in the conversion of displacements and their

derivatives to the element strains.

$$\{\varepsilon\} = \begin{Bmatrix} \varepsilon_x \\ \varepsilon_y \\ \gamma_{xy} \end{Bmatrix} = \begin{Bmatrix} \frac{\partial u}{\partial x} \\ \frac{\partial v}{\partial y} \\ \frac{\partial u}{\partial y} + \frac{\partial v}{\partial x} \end{Bmatrix} = \begin{bmatrix} 1 & 0 & 0 & 0 \\ 0 & 0 & 0 & 1 \\ 1 & 0 & 0 & 0 \\ 0 & 1 & 1 & 0 \end{bmatrix} \begin{Bmatrix} \frac{\partial u}{\partial x} \\ \frac{\partial u}{\partial y} \\ \frac{\partial v}{\partial x} \\ \frac{\partial v}{\partial y} \end{Bmatrix}$$

(A.11)

$$\begin{Bmatrix} \frac{\partial u}{\partial x} \\ \frac{\partial u}{\partial y} \\ \frac{\partial v}{\partial x} \\ \frac{\partial v}{\partial y} \end{Bmatrix} = \begin{bmatrix} [J]^{-1} & \\ & [J]^{-1} \end{bmatrix} \begin{Bmatrix} \frac{\partial u}{\partial \zeta} \\ \frac{\partial u}{\partial \eta} \\ \frac{\partial v}{\partial \zeta} \\ \frac{\partial v}{\partial \eta} \end{Bmatrix} \tag{A.12}$$

$$\begin{Bmatrix} \frac{\partial u}{\partial \zeta} \\ \frac{\partial u}{\partial \eta} \\ \frac{\partial v}{\partial \zeta} \\ \frac{\partial v}{\partial \eta} \end{Bmatrix} = \begin{bmatrix} \frac{\partial N_1}{\partial \zeta} & 0 & \frac{\partial N_2}{\partial \zeta} & 0 & \frac{\partial N_3}{\partial \zeta} & 0 & \frac{\partial N_4}{\partial \zeta} & 0 \\ \frac{\partial N_1}{\partial \eta} & 0 & \frac{\partial N_2}{\partial \eta} & 0 & \frac{\partial N_3}{\partial \eta} & 0 & \frac{\partial N_4}{\partial \eta} & 0 \\ 0 & \frac{\partial N_1}{\partial \zeta} & 0 & \frac{\partial N_2}{\partial \zeta} & 0 & \frac{\partial N_3}{\partial \zeta} & 0 & \frac{\partial N_4}{\partial \zeta} \\ 0 & \frac{\partial N_1}{\partial \eta} & 0 & \frac{\partial N_2}{\partial \eta} & 0 & \frac{\partial N_3}{\partial \eta} & 0 & \frac{\partial N_4}{\partial \eta} \end{bmatrix} \{d\} \tag{A.13}$$

The three rectangular matrices in the above three expressions are thus multiplied to find the $[B]$ matrix for a membrane element with three strain quantities. In the case of the membrane portion of the stiffness matrix, with 8DOF, this will be an 8 x 3 matrix, which in turn will be pre and post multiplied by the 3 x 3 material constitutive matrix from Eq. A.7.

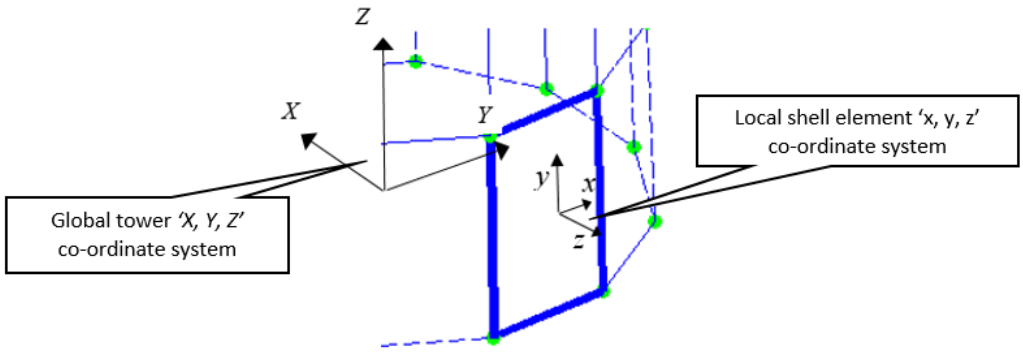

Figure A.2: Global and Local Shell Element Axes Orientation

A.4 Transformation Matrix

Where local elemental axes are not aligned with the global structure axis, prior to assembling the global matrices each local finite element matrix must be transformed to the global system by way of a geometric transformation which accounts for the differences in angle between the local element axis and the global structure axis.

The global and local axis orientation can be seen in Figure A.2. The transformation of an elemental stiffness matrix, $[k]$ to the global structure axes system (XYZ) is achieved by using an axes transformation matrix $[\Gamma]$.

In establishing this matrix, consideration is given to the difference between the angles of each axes system as discussed in the following manner. Vector quantities can be defined initially for each of the local axis directions, named here as $\overline{X}$, $\overline{Y}$ and $\overline{Z}$, by taking account of the Cartesian co-ordinates of each element. Vector quantities of the global axes named here as X, Y and Z can be found in a similar way by taking global node locations along these axes. Vector algebra is used to construct a transformation

matrix for each shell element.

$$[\Gamma]_{24x24} = \begin{bmatrix} [TT]_{3x3} & & & & & & & & \\ & [TT]_{3x3} & & & & & & & \\ & & [TT]_{3x3} & & & & & & \\ & & & [TT]_{3x3} & & & & & \\ & & & & [TT]_{3x3} & & & & \\ & & & & & [TT]_{3x3} & & & \\ & & & & & & [TT]_{3x3} & & \\ & & & & & & & [TT]_{3x3} & \\ & & & & & & & & [TT]_{3x3} \end{bmatrix} \tag{A.14}$$

$$[TT]_{3*3} = \begin{bmatrix} \overline{X}X & \overline{X}Y & \overline{X}Z \\ \overline{Y}X & \overline{Y}Y & \overline{Y}Z \\ \overline{Z}X & \overline{Z}Y & \overline{Z}Z \end{bmatrix} \tag{A.15}$$

Each entry to the $[TT]$, 3 x 3 matrix is found using the following expression

$$\bar{i}j = \frac{i \cdot j}{\|i\|\|j\|} \tag{A.16}$$

Appendix B

B.1 FEM Free Vibration Analyses

In order to evaluate the damping co-efficients a_0 and a_1, it is necessary to define the damping ratios relevant to the frequency range of interest - ζ_1 and ζ_2, and this makes Eq. 3.59 frequency dependent.

$$2\zeta_n = \frac{a_0}{\omega_n} + a_1\omega_n \tag{B.1}$$

$$\begin{bmatrix} \frac{1}{\omega_1} & \omega_1 \\ \frac{1}{\omega_2} & \omega_2 \end{bmatrix} \begin{Bmatrix} a_0 \\ a_1 \end{Bmatrix} = \begin{Bmatrix} 2\zeta_1 \\ 2\zeta_2 \end{Bmatrix} \tag{B.2}$$

The construction of the damping matrix for any forced vibration analysis is thus dependent on knowledge of the modes of free vibration of the structure. As the term 'free' vibration suggests, this is a theoretical state of the structure whereby zero damping exists and there is no energy dissipated through a response cycle. In addition, there are no external forces applied on the structure in this condition, such that the expression for the equation of motion (EOM) of a structure can be simplified by omitting any damping or external force. The EOM for the Global Beam FE (GBFE) model constructed in

B.

Chapter 3, Section 3 is used here as an example.

$$[M_{g,T}]\{\ddot{u}\} + [K_{g,T}]\{u\} = 0 \tag{B.3}$$

A text on the subject by Chopra [1995] outlines how this equation can be re-written in terms of the vibration frequencies and mode shapes which thus allow for solutions to these quantities. The displacement and acceleration vectors can be re-written as

$$\{u\} = \{\phi\}_n sin\omega t \tag{B.4}$$

$$\{\ddot{u}\} = -\omega^2\{\phi\}_n sin\omega t \tag{B.5}$$

Substituting Eq. B.4 and B.5 back into Eq. B.3 thus yields the eigenproblem

$$\big([K_{g,T}] - \omega^2[M_{g,T}]\big)\{\phi\} = 0 \tag{B.6}$$

In order for a non-trivial solution to exist whereby the mode shapes, which are represented by ϕ are non-zero quantities, the determinant of the per-multiplied matrix must equate to zero and thus yield the natural frequencies of the system. A number of mathematical methods are available to solve the eigenproblem given here. In terms of engineering applications however, there is a need to focus on methods which can provide the eigenpairs of both frequency and mode shape, which is a demanding problem computationally. Some well-established methods in achieving this purpose include Transformation methods, Determinant Search methods, and Subspace Iteration.

The solution to the eigenproblem presented here for a GBFE model for example in

terms of ω and ϕ, where the structure has 5N DOF provides solutions in the form of

$$\phi = \begin{bmatrix} \phi_{1,1} & \phi_{1,2} & \cdots & \phi_{1,5N} \\ \phi_{2,1} & \phi_{2,2} & \cdots & \phi_{2,5N} \\ \vdots & \vdots & \ddots & \vdots \\ \phi_{5N,1} & \phi_{5N,2} & \cdots & \phi_{5N,5N} \end{bmatrix} \tag{B.7}$$

$$\omega^2 = \begin{bmatrix} \omega_1^2 & & & \\ & \omega_2^2 & & \\ & & \ddots & \\ & & & \omega_{5N}^2 \end{bmatrix} \tag{B.8}$$

Appendix C

C.1 Global Matrix Assembly - GBFE & LSFE Models

The book-keeping and transformation steps carried out to establish the global model matrices for the LSFE model, broadly include the following -

1. Define the basic geometric and material properties of the tower such as its diameter at critical points (base, hybrid interface and top), its shell thickness and its height.

2. Define the nodal locations around the circumference of the tower and vertically along its height. This is a function of the required FE mesh density,

3. Define a matrix containing the global nodal geometric locations around the tower shell, for example a matrix of size $N \times 3$, where each row describes the X, Y, Z cartesian co-ordinates of node n, $(1 \leq n \leq N)$. The total number of nodes will be equal to the number of vertical tower divisions multiplied by a factor of the circumferential divisions, $N = \text{vertical} \quad \text{divisions} \times (\text{seg} + 1) = N_{\text{els}} + \text{seg}$. Fig C.1 gives an indication of these properties of the shell discretisation.

4. Define a matrix containing the global nodes associated with each local finite element, for example a matrix of size $N_{\text{els}} \times 4$, where each row describes the global node numbers associated with a given element i, $(1 \leq i \leq N_{\text{els}})$

5. Create local shell element stiffness and mass matrices using membrane and plate co-efficients in the case of both.

$$[k] \in \mathbb{R}^{20\times 20} = [k_m] \oplus [k_p] = \begin{bmatrix} [k_m] & [0] \\ [0] & [k_p] \end{bmatrix} \tag{C.1}$$

$$[m] \in \mathbb{R}^{20\times 20} = [m_m] \oplus [m_p] = \begin{bmatrix} [m_m] & [0] \\ [0] & [m_p] \end{bmatrix} \tag{C.2}$$

6. Re-arrange local element stiffness $[k]$ and mass $[m]$ matrices such that nodal degrees of freedom are grouped together, with 6 DOF per node. This step introduces zero terms to elemental matrices associated with a 'drilling' DOF $\theta_{i,z}, i \in [1,2,3,4]$. The result is for a displacement vector as follows

$$\{d\}^T = [u_{1,x}, u_{1,y}, u_{1,z}, \theta_{1,x}, \theta_{1,y}, \theta_{1,z}, u_{2,x}, \cdots, u_{4,z}, \theta_{4,x}, \theta_{4,y}, \theta_{4,z}] \tag{C.3}$$

7. Transform each local element stiffness and mass matrix to its global structure equivalent by way of transformation matrices $[\Gamma]$. Local nodal geometry from step 3 is used to define transformation matrices.

$$[K] \in \mathbb{R}^{24\times 24} = [\Gamma]^T [k] [\Gamma] \tag{C.4}$$

8. Assemble the global matrices by taking local matrix quantities for each global DOF and using assigning co-efficients to their global nodal locations.

$$[K_{l,T}] \in \mathbb{R}^{6N\times 6N} = \sum_{i=1}^{N_{\text{els}}} [K] \tag{C.5}$$

$$[M_{l,T}] \in \mathbb{R}^{6N\times 6N} = \sum_{i=1}^{N_{\text{els}}} [M] \tag{C.6}$$

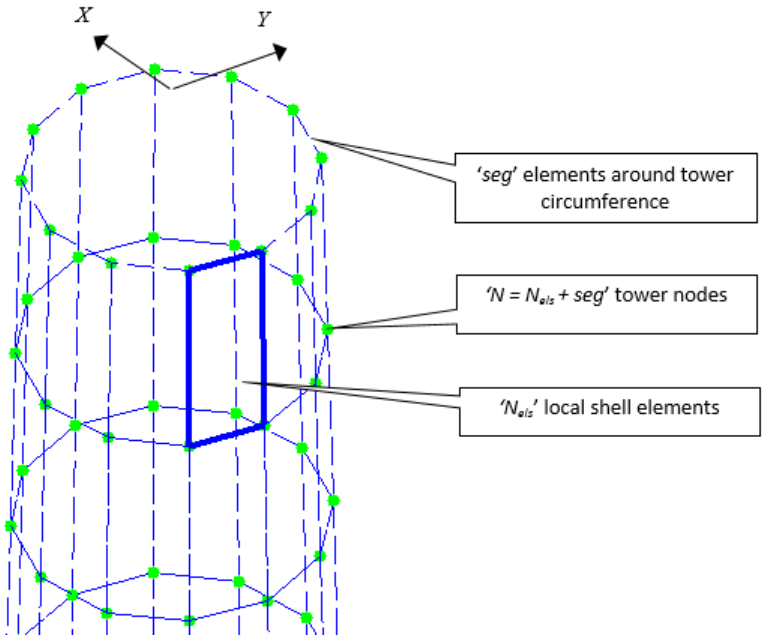

Figure C.1: LSFE Model Tower 3D Elemental and Nodal Discretisation Properties

These steps are detailed to suit the LSFE model, however are also applicable in the case of the GBFE model.

Steps 1-4 above are elementary but require careful book-keeping practice. The three dimensional Cartesian co-ordinates of the nodes from step 3 are used in defining the local axes vectors which are then used in defining transformation matrices. The matrix of global node numbers are then used to define location matrix non-zero locations, which are in turn used in populating the global matrices.

Step 5 includes creating the local elemental matrices using various interpolation functions and numerical integration as per chapter three. Step 6 involves re-arranging the local matrices. This is carried out for two reasons. First, in order to transform the local matrices to the structure global axes, degrees of freedom associated with each node are to be grouped for ease of constructing the transformation matrix. Second, a zero term is to be entered for the in-plane rotation degree of freedom, $\theta_{i,z}$. This is commonly known as a 'drilling' degree of freedom. This would lead to a singular stiffness matrix were it

not for the fact that a transformation is to be carried out. Including a zero term allows for transformation to take place and for a stiffness to be allocated for rotation about the global Z axis. A re-arranged local element matrix, $[k] \in \mathbb{R}^{24\times24}$ takes the following form.

$$[k] \in \mathbb{R}^{24\times24} = \begin{bmatrix} [k_m]_{1,1} & [k_m]_{1,2} & 0 & 0 & 0 & 0 & [k_m]_{1,3} & [k_m]_{1,4} & \cdots & 0 \\ [k_m]_{2,1} & [k_m]_{2,2} & 0 & 0 & 0 & 0 & [k_m]_{2,3} & [k_m]_{2,4} & \cdots & 0 \\ 0 & 0 & [k_p]_{1,1} & [k_p]_{1,2} & [k_p]_{1,3} & 0 & 0 & 0 & \cdots & 0 \\ 0 & 0 & [k_p]_{2,1} & [k_p]_{2,2} & [k_p]_{2,3} & 0 & 0 & 0 & \cdots & 0 \\ 0 & 0 & [k_p]_{3,1} & [k_p]_{3,2} & [k_p]_{3,3} & 0 & 0 & 0 & \cdots & 0 \\ 0 & 0 & 0 & 0 & 0 & 0 & 0 & 0 & \cdots & 0 \\ [k_m]_{3,1} & [k_m]_{3,2} & 0 & 0 & 0 & 0 & [k_m]_{3,3} & [k_m]_{3,4} & \cdots & 0 \\ [k_m]_{4,1} & [k_m]_{4,2} & 0 & 0 & 0 & 0 & [k_m]_{4,3} & [k_m]_{4,4} & \cdots & 0 \\ \vdots & \vdots & \vdots & \vdots & \vdots & \vdots & \vdots & \vdots & \ddots & \vdots \\ 0 & 0 & 0 & 0 & 0 & 0 & 0 & 0 & \cdots & 0 \end{bmatrix} \tag{C.7}$$

The translation and rotation degrees of freedom for each node are now grouped together within the matrix.

In the case of the beam model, the local element axes were co-incidental with the global tower axes and as such, no reference was made to axes properties nor required during model formulation. However, the nature of local element axes is a factor in all finite element models and requires consideration where there are elements presented which are orientated in physical space differently to one another.

The methodology of establishing an approximate set of algebraic equations to replace exact differential equations of any structure is based upon establishing nodal degrees of freedom which are related to some structure-wide or global axis system. As such, on solving the algebraic equations, all unknown displacements and rotations will be orientated about this global axis system regardless of the orientation of the local finite

element nodes which they are associated with. This allows for overall structural deformation to be established. Therefore, prior to assembling the global matrices, each local finite element matrix must be transformed to the global system by way of a geometric transformation, as described in Appendix A.

Step 8 of the steps listed involves taking each local element stiffness matrix and apportioning the correct parts of these local matrices to the global matrix. Eq. C.5 and Eq. C.6 can be used to this end.

Appendix D

D.1 MDOF Model System Matrices

$$[M_b] = \begin{bmatrix} \int_0^{R_b} m_b(z)\phi_{b,x}^2(z)dz & 0 \\ 0 & \int_0^{R_b} m_b(z)\phi_{b,y}^2(z)dz \end{bmatrix} \tag{D.1}$$

$$[M_{bt}(\psi_i)] = \begin{bmatrix} \int_0^{R_b} m_b(z)\phi_{b,x}(z)dz & 0 & 0 & 0 & 0 \\ 0 & 0 & \int_0^{R_b} m_b(z)\phi_{b,y}(z)cos(\psi_i)dz & 0 & 0 \end{bmatrix} \tag{D.2}$$

$$[M_{tb}(\psi_i)] = [M_{bt}(\psi_i)]^T \tag{D.3}$$

$$[M_{TB}] = \begin{bmatrix} [M_{TB,X}] & 0 & 0 \\ 0 & [M_{TB,Y}] & 0 \\ 0 & 0 & \frac{1}{2}J_{nac,tor}\{s_{11}\}_{\theta_{N,Z}} \end{bmatrix} \tag{D.4}$$

$$[M_{TB,X}] = \begin{bmatrix} \frac{1}{2}M_{nac}\{s_7\}_{u_{N,X}} + m_b^1 & 0 \\ 0 & \frac{1}{2}J_{nac,tilt}\{s_8\}_{\theta_{N,Y}} \end{bmatrix} \tag{D.5}$$

$$[M_{TB,Y}] = \begin{bmatrix} \frac{1}{2}M_{nac}\{s_9\}_{u_{N,Y}} + m_b^1 & \\ 0 & \frac{1}{2}J_{nac,roll}\{s_{10}\}_{\theta_{N,X}} \end{bmatrix} \tag{D.6}$$

$$m_b^1 = 3\int_0^{R_b} m_b(z)dz \tag{D.7}$$

$$[K_b] = \begin{bmatrix} K_{b,x} + U_{c,x} + U_{g,x} & 0 \\ 0 & K_{b,y} - \Omega_b^2 \int_0^{R_b} m_b(z)\phi_{b,y}^2(z)dz + U_{c,y} + U_{g,y} \end{bmatrix} \tag{D.8}$$

$$K_{b,x} = \int_0^{R_b} EI_{b,x}(z)(\frac{\delta^2\phi_{b,x}(z)}{\delta z^2})^2 dz \tag{D.9}$$

$$K_{b,y} = \int_0^{R_b} EI_{b,y}(z)(\frac{\delta^2\phi_{b,y}(z)}{\delta z^2})^2 dz \tag{D.10}$$

$$U_{g,x} = -\frac{1}{2}gcos(\psi_i)\int_0^{R_b}\left((\frac{\delta\phi_{b,x}}{dz})^2\right)\int_\zeta^{R_b} m_b(z)dz \tag{D.11}$$

$$U_{c,x} = \frac{1}{2}\Omega^2\int_0^{R_b}\left((\frac{\delta\phi_{b,x}(z)}{dz})^2\right)\int_\zeta^{R_b} m_b(z)zdz \tag{D.12}$$

$$U_{g,y} = -\frac{1}{2}gcos(\psi_i)\int_0^{R_b}\left((\frac{\delta\phi_{b,y}}{dz})^2\right)\int_\zeta^{R_b} m_b(z)dz \tag{D.13}$$

$$U_{c,y} = \frac{1}{2}\Omega^2\int_0^{R_b}\left((\frac{\delta\phi_{b,y}(z)}{dz})^2\right)\int_\zeta^{R_b} m_b(z)zdz \tag{D.14}$$

$$[K_{t,b}(\psi_i)] = \begin{bmatrix} 0 & 0 \\ 0 & -\Omega_b^2\int_0^{R_b} m_b(z)\phi_{b,x}(z)cos(\psi_i)dz \\ 0 & 0 \\ 0 & 0 \end{bmatrix} \tag{D.15}$$

$$[C_b] = \begin{bmatrix} \frac{2(\zeta_{s,b}+\zeta_{AD,b})}{\omega_{b,x}} K_{b,x} & 0 \\ 0 & \frac{2\zeta_{s,b}}{\omega_{b,y}} K_{b,y} \end{bmatrix} \tag{D.16}$$

$$[C_{tb}(\psi_i)] = \begin{bmatrix} 0 & 0 \\ 0 & -2\Omega_b \int_0^{R_b} m_b(z)\phi_{b,y}(z) sin(\psi_i) dz \\ 0 & 0 \\ 0 & 0 \end{bmatrix} \tag{D.17}$$

Appendix E

E.1 Analytical Model, Uniform Tower Properties Mode Shapes

In classical beam bending theory, boundary conditions are typically defined based on the shape (or derivatives of the shape) of vibration at beam supports. In the case of a cantilever beam, for its first mode of vibration, there are known boundary conditions of zero displacement and zero rotation at the fixed support, and zero bending and shear force at the free end of the beam. These are commonly written in the following form.

$$\phi(0) = 0 \tag{E.1}$$

$$\frac{d\phi(0)}{dz} = 0 \tag{E.2}$$

$$-EI\frac{d^2\phi(L)}{dz^2} = 0 \tag{E.3}$$

$$-\frac{d}{dz}EI\frac{d^2\phi(L)}{dz^2} = 0 \tag{E.4}$$

By applying these conditions to the fourth-order Euler-Bernoulli expression for the motion of a cantilever beam, it is possible to show that non-trivial solutions exist only if

$$\cosh(\beta_n L)\cos(\beta_n L) + 1 = 0 \tag{E.5}$$

This transcendental equation can then be solved numerically to give the roots $\beta_1 L = 1.875, \beta_2 L = 4.694....$ From this, circular frequencies are found from

$$\omega_n = \beta_n^2 \sqrt{\frac{EI}{\rho A}} \tag{E.6}$$

The circular frequencies and mode shapes found for the cantilever beam can also be found for simply supported beams or fully-encastre beams simply by applying the corresponding boundary conditions to each support in terms of relevant displacement, rotation, bending moment or shear force.

Appendix F

F.1 Stress-Stiffening Phenomenon

Stress stiffening is a phenomenon which relates the influence of membrane forces on the lateral deflection associated with bending in an element. In terms of studying the softening behaviour of members under compression, there are a number of ways to approach it from a modelling point of view. In the case of straight elements or plates, such elements are often assumed to sustain compression with only small levels of lateral displacement up to the point of elastic buckling. No large lateral displacements occur during the softening of the member. Buckling will occur where a member converts membrane strain energy into bending strain energy without the increase of any externally applied load. In the study of frames or elements with initial curvatures or expected imperfections, an appropriate approach would be to use large-displacement theory. This involves the use of coupling terms in the stiffness matrices of the elements involved between bending and membrane actions as they will interact through non-linear displacements of the structure. In terms of this Thesis, as the shell elements are used to portray towers which are slender, single member structures and which can be said to be initially straight, it can be said that there is no requirement to use a large-displacement analogy. Softening of the elements will be assumed under the effect of small displacements occurring under any compression condition which the tower or structure can safely withstand.

In terms of the energy in a system with initial stress, the total energy includes strain energy and potential energy of applied loads (W), to do work as explained previously. The strain energy can be divided into components for in-plane and out of plane strains or membrane, U_m and bending strains, U_b.

$$\Pi = U_m + U_b + W \tag{F.1}$$

When the change in total potential energy with respect to the system degrees of freedom is at zero, the system has reached equilibrium. Thus the static equilibrium condition is described as

$$[K_e]\{D\} + [K_{geo}]\{D\}\breve{}\{R\} = \{0\} \tag{F.2}$$

In Eq. F.2, $[K_{geo}]$ refers to a global geometric stiffness matrix. It is therefore seen that the global stiffness is simply the direct sum of the global elastic stiffness and geometric stiffness matrices.

$$[K] = [K_e] + [K_{geo}] \tag{F.3}$$

Appendix G

G.1 NREL 5MW Baseline Turbine

The global structural properties of the NREL rotor and tower are given below in Table G.1

The blade considered is the LM61.5 P2 (manufactured by LM Wind Power), which is 61.5m long and has a total mass of 17,740kg. The radius of the hub is 1.5m such that the total rotor radius is 63m. The shapes of vibration for the blade used within the models ($\phi_{b,i,x}, \phi_{b,i,y}$) are the shapes associated with the first mode of vibration of the blade in the flapwise and edgewise directions. An eigenanalysis of a blade was carried out using the NREL finite element based code BModes (Bir [2005]), with the resulting mode shapes then described using continuous sixth-order polynomial shape functions. The shape functions are given in Figure G.1.

Properties	Units	Values
Max. rated power	MW	5
Rotor orientation, configuration	-	Upwind, 3 blades
Rotor diameter	m	126
Cut-in, rated, cut-out wind speed	m/s	3m/s, 11.4m/s, 25m/s
Cut-in, rated rotor speed	rpm	6.9rpm, 12.1 rpm
Blade length	m	61.5
Overall blade (integrated) mass	kg	17,740
Blade mass moment of inertia	kg m^2	11,776
1st in-plane blade natural frequency	Hz	1.0606
1st out-of-plane blade natural frequency	Hz	0.6767
Blade structural-damping ratio(all modes)	%	0.48%
Hub diameter	m	3
Hub mass	kg	56,780
Nacelle mass	kg	240,000
Tower Height	m	87.6
Tower Overall (integrated) mass	kg	347,460
Tower 1st Fore-Aft mode natural frequency	Hz	0.324
Tower 1st Side-to-Side mode natural frequency	Hz	0.312
Tower structural-damping ratio(all modes)	%	1

Table G.1: NREL 5MW Baseline Turbine - Basic Properties

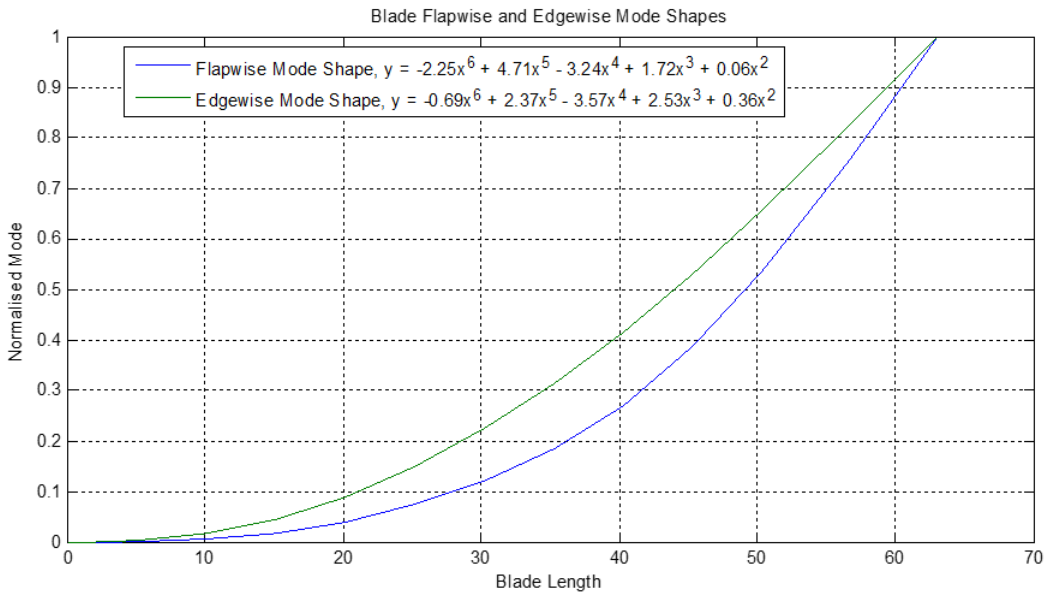

Figure G.1: NREL Baseline Turbine - Blade Mode Shapes